POWER SYSTEM DYNAMIC ENHANCEMENT USING PHASE IMBALANCE SERIES CAPACITIVE COMPENSATION AND DOUBLY FED INDUCTION GENERATOR-BASED WIND FARMS

A Thesis

Submitted to the College of Graduate Studies and Research

in Partial Fulfillment of the Requirements

For the Degree of Master of Science

in the Department of Electrical and Computer Engineering

University of Saskatchewan

Saskatoon, Saskatchewan

By

Jiping Zhang

PERMISSION TO USE

I agree that the Library, University of Saskatchewan, may make this thesis freely available for inspection. I further agree that permission for copying of this thesis for scholarly purpose may be granted by the professor or professors who supervised the thesis work recorded herein or, in their absence, by the Head of the Department or the Dean of the College in which the thesis work was done. It is understood that due recognition will be given to me and to the University of Saskatchewan in any use of the material in this thesis. Copying or publication or any other use of this thesis for financial gain without approval by the University of Saskatchewan and my written permission is prohibited.

Request for permission to copy or to make any other use of the material in this thesis in whole or part should be addressed to:

Head of the Department of Electrical and Computer Engineering

57 Campus Drive

University of Saskatchewan

Saskatoon, Saskatchewan

Canada S7N 5A9

ABSTRACT

Wind energy is among the fastest growing renewable energy technologies in the world that has been increasing by about 30% a year globally. Wind energy has proven to be a clean, abundant and completely renewable source of energy. Owing to the rapidly increasing use of wind power, the aspect of integrating high level of penetrations wind power into the grid is becoming more and more of a reality. Examples of large wind farms in the United States are the 781.5 MW Roscoe wind farm in Texas, the 735.5 MW Horse Hollow Wind Energy Center in Taylor and Nolan County, Texas, the 845 MW Shepherds Flat wind farm in Oregon and the 1550 MW Alta wind farm being developed in California.

As most large wind farms in North America employ Doubly-fed Induction Generator (DFIG) wind turbines, their voltage-sourced converter-based back-to-backs offer independent control of the real and reactive power. The use of these control capabilities have been recently proposed for damping power swings, inter-area oscillations as well as subsynchronous resonance. There is, however, a question that is always associated with the use of voltage-sourced converter -based back-to-back wind farms for damping power system oscillations: what happens when there is no wind? The keyword to the answer is "combined". The potential benefit of using these types of wind farms for damping power system oscillations should always be combined with conventional damping devices (power system stabilizers, thyristor controlled series capacitor, static synchronous series compensator, high voltage dc systems, etc.).

This thesis reports the results of digital time-domain simulation studies that are carried out to investigate the potential use of supplemental controls of DFIG-based wind farms combined with a phase imbalanced hybrid series capacitive compensation scheme for damping power system oscillations. The thesis also addresses the recent concern over the case of large share of wind power generation which results in reducing the total inertia of the synchronous generators and degrading the system transient stability. In this regards, the results of the investigations have shown that in such a case properly designed supplemental controllers for the wind farm converters could be an asset in improving the system transient stability rather than degrading it.

Time-domain simulations are conducted on a benchmark model using the ElectroMagnetic Transients program (EMTP-RV).

ACKNOWLEDGMENTS

TABLE OF CONTENTS

v

LIST OF FIGURES

x

the RSC of wind farm B).

LIST OF TABLES

xiii

LIST OF SYMBOLS

A	blade sweep area (m^2)
C	capacitor
C_f	wind turbine blade design constant
C_p	power coefficient of the blade
C_{TCSC}	fixed capacitor of TCSC
C_s	capacitor of the RC snubber circuit
d	direct axis
E_{fd}	exciter output voltage
E_R	output voltage of the voltage regulator amplifier
E_{ref}	reference voltage of the excitation system
E_{SB}	feedback stabilizing signal of the excitation system
$Fixed\ C$	Transmission lines are series capacitor compensated
e_d, e_q	d- and q- axis stator voltages
e_{fd}	field voltage
GSC	grid side converter
$G_p(s)$	transfer function of a proportional type TCSC supplemental controller
$G_{L\text{-}L}(s)$	transfer function of a lead-lag type TCSC supplemental controller
H	inertia constant
$Hybrid$	Transmission lines are compensated with the hybrid single-phase-TCSC compensation scheme
i_d, i_q	d- and q- axis stator currents
i_{fd}	field winding current
$i_{1d},$	d-axis damper winding current
i_{1q}, i_{2q}	q-axis damper winding currents
IMG	imaginary part of a complex number
J	inertias
K_A	gain of the voltage regulator amplifier
K_E	exciter gain
K_{FE}	feedback stabilizing loop gain of the excitation system

K_G	supplemental controller gain
K_P	proportional controller gain
K_i	integral controller gain
K_1, K_2	constants
k_2	shaft stiffness
L_s, L_r	stator and rotor inductances
L_{TCSC}	fixed inductor of TCSC
L_{ad}	d-axis magnetizing inductance
L_{aq}	q-axis magnetizing inductance
L_d, L_q	d- and q-axis synchronous inductances
L_{ffd}	self-inductance of the field winding
L_{11d}	self-inductance of the d-axis damper winding
L_{11q}, L_{22q}	self-inductances of the q-axis damper winding
M	mutual inductance between rotor and stator
MPT	maximum power tracking point
P	real power
PI	proportional integral
P_{L1} and P_L1	real power flow in transmission line L_1
P_{L2} and P_L2	real power flow in transmission line L_2
P_r, P_g	active power of the RSC and GSC
P_m	mechanical power
$P_{grid-Ref}$	real power reference for GSC
ρ	air density (kgm^{-3})
Q	reactive power
$Q_{grid-Ref}$	reactive power reference for RSC
$Q_{GSC-Ref}$	reactive power reference for GSC
q	quadrature axis
R	rotor radius of the wind turbine
RSC	rotor side converter
R_L	resistance of the series capacitor compensated transmission line
R_a	armature resistance
R_{fd}	field winding resistance

R_{1d}	d-axis damper winding resistance
R_{1q}, R_{2q}	q-axis damper winding resistances
r_s	resistance of the RC snubber circuit
s	Laplace transformation operator
T	superscript to denote matrix transpose
t	time
T_F	forward thyristor
T_R	reverse thyristor
T_A, T_E, T_{FE}	time constants in the excitation system
T_e	electromagnetic torque
T_{ELEC}	air-gap torque
T_m	supplemental controller low-pass filter time constant
T_{MECH}	mechanical torque
T_1, T_2, T_3, T_4	lead-lag network time constants
T_w	washout filter time constant
V_C	voltage across the series capacitor of the compensated transmission line
V_{Cd}, V_{Cq}	voltages across the series capacitor in the d-q reference frame
V_{dc}	dc link capacitor voltage
$V_{dc\text{-}Ref}$	reference signal
V_L	voltage across the inductance of the series capacitor compensated transmission line
V_{Ld}, V_{Lq}	voltages across the inductance in the d-q reference frame
V_R	voltage across the resistance of the series capacitor compensated transmission line
V_{Rd}, V_{Rq}	voltages across the resistance in the d-q reference frame
V_{Rmax}, V_{Rmin}	maximum and minimum ceiling voltages of the excitation system respectively
v_{qg}, v_{dg}	quadrature and direct axis GSC voltages
V_b	infinite-bus voltage
V_s, V_r	stator and rotor side voltages
V_t	generator terminal voltage
V_{td}, V_{tq}	d- and q- axis generator terminal voltages

v_{qr}, v_{dr}	quadrature and direct axis RSC voltages
V_ω	wind speed (m/s)
X_C	series capacitor reactance
X_L	inductive reactance of the series capacitor compensated transmission line
X_{-max}, X_{-min}	maximum and minimum TCSC reactances respectively
X_{order}	dynamic reactance of TCSC
X_{TCSCo}	initial net reactance of TCSC
α	thyristor firing angle
Ψ_d, Ψ_q	d- and q- axis stator flux linkages
Ψ_{fd}	field winding flux linkage
Ψ_{1d}	d-axis damper winding flux linkage
Ψ_{1q}, Ψ_{2q}	q-axis damper winding flux linkages
δ	generator power (load) angle
δ_{21} and del21	generator 2 load angle measured with respect to generator 1 load angle
δ_{31} and del31	generator 3 load angle measured with respect to generator 1 load angle
λ	wind turbine blade tip speed ratio
λ_s, λ_r	stator and rotor side flux linkages
$\lambda_{qm}, \lambda_{dm},$	q- and d- axis magnetizing flux linkages
Ω_m	mechanical angular velocity (rad/s)
ω	angular velocity
$\omega_0 (f_0)$	synchronous frequency (377 rad/sec)
ω_{21}	generator 2 speed measured with respect to generator 1 speed
ω_{31}	generator 3 speed measured with respect to generator 1 speed
0	suffix to denote the initial operating condition
$^{-1}$	superscript to denote matrix inversion

Chapter 1

INTRODUCTION

1.1   Wind Energy

Wind energy is among the fastest growing renewable energy technologies in the world, and that has been increasing by about 30% a year globally. Wind energy has proven to be a clean, abundant and completely renewable source of energy. Owing to the rapidly increasing use of wind power, the aspect of integrating high level of penetrations wind power into the grid is becoming more and more reality. Examples of large wind farms in the United States are the 781.5 MW Roscoe wind farm in Texas, the 735.5 MW Horse Hollow Wind Energy Center in Taylor and Nolan County, Texas, the 845 MW Shepherds Flat wind farm in Oregon and the 1550 MW Alta wind farm being developed in California [1]. The majority of large wind farms around the world employ Doubly Fed Induction Generator (DFIG) wind turbines. In such a type of induction generators, the frequency converter rating is typically 25% to 30% of the generator rated power. This reduced rating in the frequency converter provides an attractive cost saving compared to full-rated converter induction generator wind turbines.

1.2   Series Compensation

Series capacitive compensation of power transmission lines is the most economical way to improve power transfer capability, especially when large amounts of power must be transmitted through long transmission lines.   However, one of the hindering factors for the increased utilization of series capacitive compensation is the potential risk of Subsynchronous Resonance (SSR), where electrical energy is exchanged with turbine-generator shaft systems in a growing manner which can result in shaft damage [2]. Figure 1.1 shows a typical time response of a turbine-generator shaft torsional torque during and after clearing a fault on a series capacitive compensated transmission line in the presence of the SSR phenomenon. It is worth noting here that this shaft is designed to withstand a maximum torsional torque of 4 per unit (on the generator base MVA). Another limitation of series capacitive compensation is its inability to provide adequate damping to power system oscillations after clearing and high-speed reclosing

1

of system faults.   Figure 1.2 shows a typical time response of a generator load angle, measured with respect to a reference generator load angle, during and after clearing a three-phase fault on a series capacitive compensated transmission line. As can be seen from this figure, the oscillations are not completely damped after the first few seconds from fault clearing which results in degrading the power quality of the system.
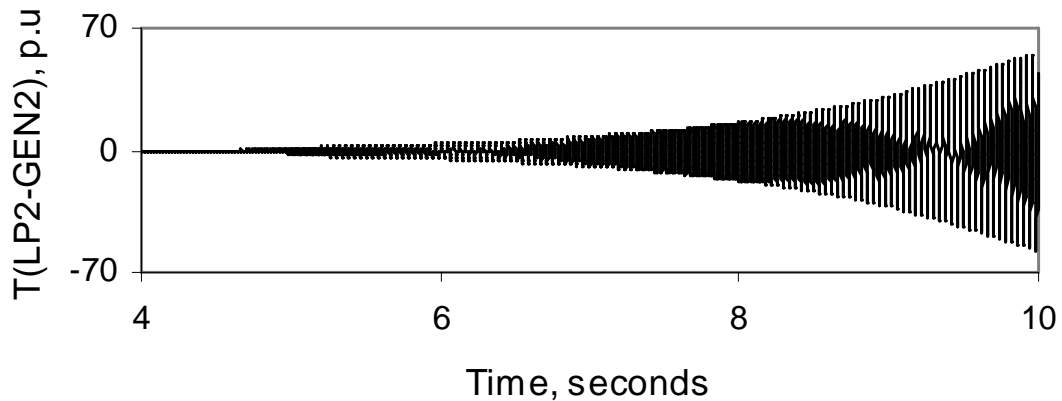
Figure 1.1: Transient time response of a turbine-generator shaft torsional torque during and after clearing a system fault on a series capacitive compensated transmission line.
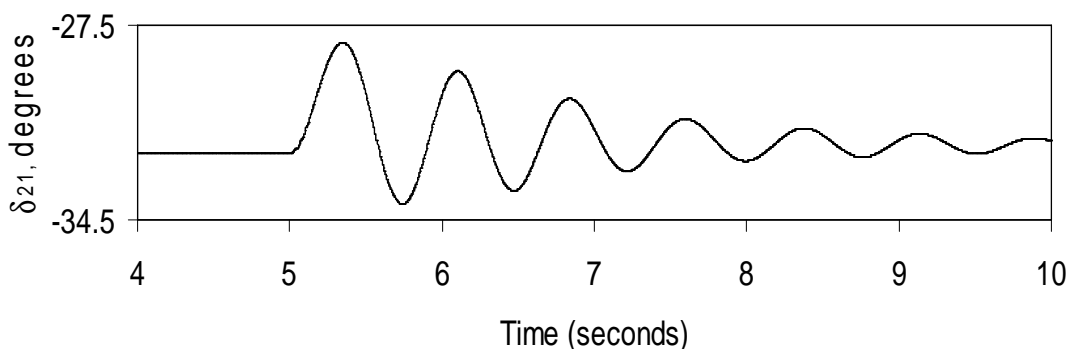
Figure 1.2: Transient time response of a generator load angle, measured with respect to a reference generator load angle, during and after clearing a system fault on a series capacitive compensated transmission line.

1.3   Transmission Line Series Compensation

The main purpose of series compensation in a power system is virtual reduction of line reactance in order to enhance power system stability and increase the loadability of transmission corridors [3]. The principle is based on the compensation of the distributed line reactance by the insertion of a series capacitor. The reactive power generated by the capacitor is continuously proportional to the square of the line current. This means that the series capacitor has a self-

2

regulating effect. When the system loading increases, the reactive power generated by the series capacitor increases as well. The response of the series capacitor is automatic, instantaneous and continuous as long as the capacitor current remains within the specified operating limits. The following are some of the major benefits of incorporating series capacitors in transmission systems:

1.3.1 Increase the power transfer capability by raising the first swing stability limit

A substantial increase in the stability margin is achieved by installing a series capacitor. The series compensation will improve the situation in two ways: it will decrease the initial generator load angle corresponding to a specific power transfer and it will also shift the power-load angle (P-δ) characteristic upwards. This will result in increasing the transient stability margin.

1.3.2 Increase in power transfer

The increase in the power transfer capability as a function of the degree of compensation for a transmission line can be illustrated using the circuit and the vector diagram shown in Figure 1.3. The power transfer on the transmission line is given by:

$$P = \frac{|V_s||V_R|}{X_{line} - X_c} \sin \delta = \frac{|V_s||V_R|}{X_{line}(1-k)} \sin \delta \tag{1.1}$$

where k is the degree of compensation defined as

$$k = \frac{X_c}{X_{line}}$$

The effect on the power transfer when a constant load angle difference is assumed is shown in Figure 1.4. Practical compensation degree range from 20 to 70 percent. Transmission capability increases of more than two times can be obtained in practice.
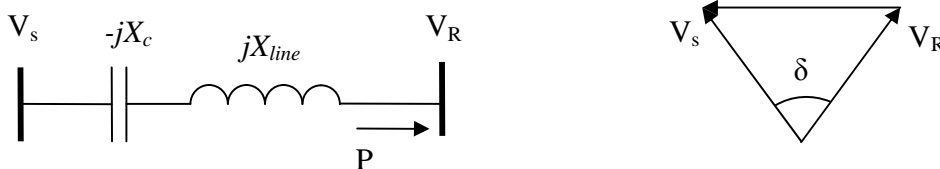
Figure 1.3: Transmission line with series capacitor.

3
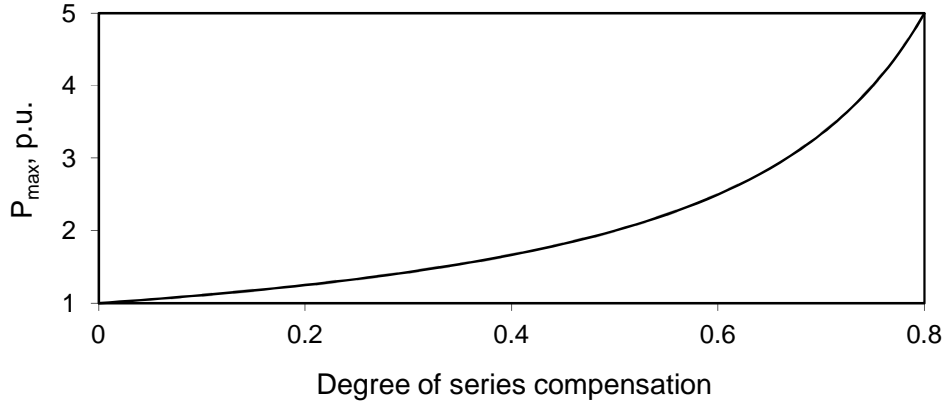
Figure 1.4: Maximum power transmitted over a transmission line as a function of the degree of series compensation ($|V_s| = |V_R| = 1\ p.u.$, $X_{line} = 1\ p.u.$).

1.3.3 Active load sharing between parallel circuits

When two transmission lines are connected in parallel, the natural power sharing between them is dictated by their respective impedances. If the two lines are of different configurations (and consequently of different thermal ratings), their impedances could still be very close. Therefore, the power transmitted in each line will be similar. The voltage drop in both circuits is identical, and therefore, the relationship between the line currents I_{L1} and I_{L2} can be expressed as:

$$I_{L1}Z_{L1} = I_{L2}Z_{L2} \tag{1.2}$$

If overloading the lower thermal rating line, (L_2, Figure 1.5) is to be avoided (i.e., $I_{L2} \leq I_{L2\,max}$), then the full power capacity of the other line, L_1, will never be reached (i.e. $I_{L1} < I_{L1\,max}$). For example, consider the case when L_1 is a four conductor bundle (quad) circuit configuration, whereas L_2 has a two conductor bundle (twin) circuit configuration. If the conductors of the two bundles are identical, then L_1 has twice the rating of L_2. The inductive reactances of the two lines, however, are very close. If a series capacitor is installed in the higher thermal rating line, both transmission lines can operate at their maximum capacity when the appropriate degree of compensation is provided (50% in this case) [4].

4
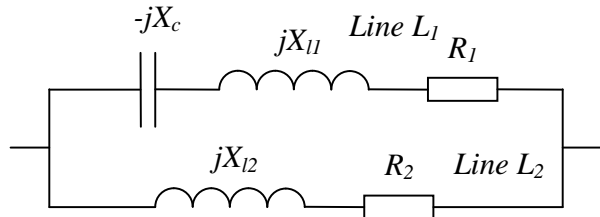
Figure 1.5: Adjusting the power sharing between two parallel lines using a series capacitor.

1.4.   Series Capacitor Location

The optimum location for a single series capacitor bank, in terms of the most effective use of the series capacitive reactance, is at the middle of the transmission line [3]. The "effectiveness", which is based on the distributed parameter theory of transmission lines, is the figure of merit for the reduction of the series inductive reactance by a series capacitor. One Canadian installation that has the capacitors located at the middle of the transmission line is the B.C. Hydro 500 kV system described in [5]. A number of utilities, especially in the U.S., have tended to utilize two series capacitor banks and locate them at the ends of the transmission lines, in order to take advantage of existing land and the availability of service personnel at the line terminals [3]. In some situations, there may be valid reasons (geographical restrictions or specific benefits) for selecting other locations. For example, B.C. Hydro has a 605 Mvar, 500 kV single capacitor bank installed at McLeese substation which is located "nearly" mid-line between Williston and Kelly Lake substations (180 km from Williston and 130 km from Kelly Lake) [6].

1.5.   Power System Oscillations

Many electric utilities world-wide are experiencing increased loadings on portions of their transmission systems, which can, and sometimes do, lead to poorly damped, low-frequency oscillations (0.5 – 2 Hz). These oscillations can severely restrict system operations by requiring the curtailment of electric power transfers as an operational measure. They can also lead to widespread system disturbances if cascading outages of transmission lines occur due to oscillatory power swings, like during the blackout in Western North America on August 10, 1996 [7].

Damping is defined as the energy dissipation properties of a material or a system. Power system oscillations can be damped, when extra energy is injected into the system which is instantaneously decelerated, and/or when extra energy is consumed in the system which is instantaneously accelerated. The damping energy is obtained by the modulation of load or generation for a period of time, typically in the range of five to ten seconds. The damping energy must have the correct phase shift relative to the accelerated/decelerated system as incorrect phase angles can excite the oscillations. Figure 1.6 shows different possibilities to damp power system oscillations [8].
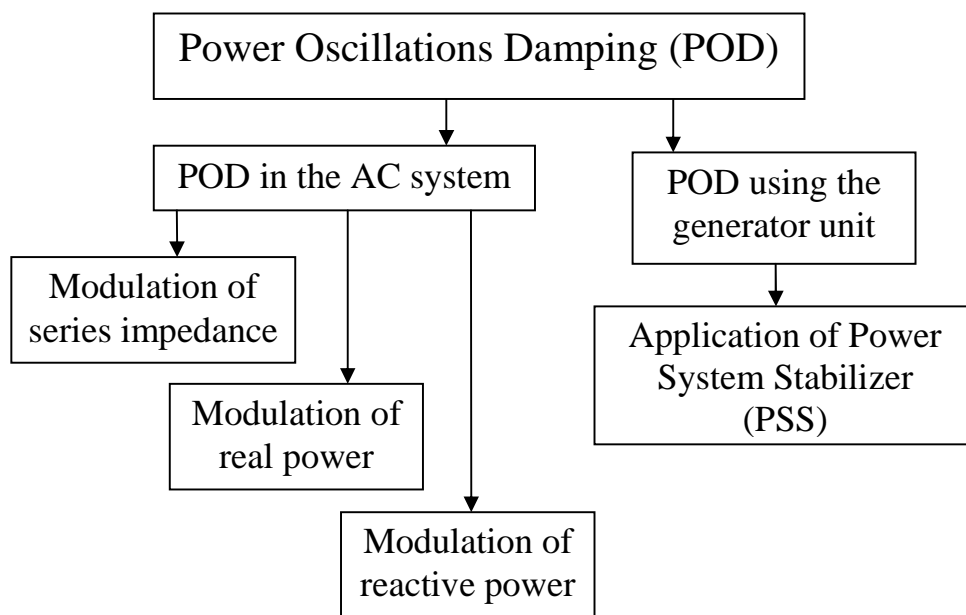
Figure 1.6: Strategies to damp power system oscillations.

1.6. Flexible AC Transmission Systems

All of the above discussed advantages of series compensation can be achieved without the risks of SSR phenomenon if series Flexible AC Transmission Systems (FACTS) devices are used instead of series capacitors. These devices are also able to provide adequate and fast damping to power system oscillations.

FACTS controllers are power electronic based controllers which can influence transmission system voltages, currents, impedances and/or phase angles rapidly [9], [10]. These controllers have the flexibility of controlling both real and reactive power, which could provide

an excellent capability for improving power system dynamics. FACTS technology provides an unprecedented way for controlling transmission grids and increasing transmission capacity.

FACTS controllers may be based on thyristor devices with no gate turn-off (only with gate turn-on), or with power devices with gate turn-off capability. In general, the principal controllers with gate turn-off devices are based on dc to ac converters, which can exchange active and/or reactive power with the ac system. In the studies conducted in this thesis, a series FACTS controller based on thyristor switches is considered. This FACTS controller, shown in Figure 1.7, is called a Thyristor Controlled Series Capacitor (TCSC) [9], [10].
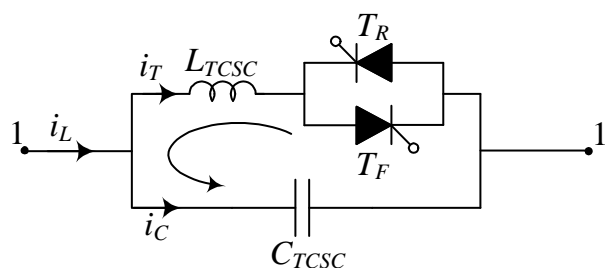
Figure 1.7: A schematic diagram of the TCSC.

The TCSC which will be discussed in details in Chapter 3 has been installed and operated successfully by utilities in several countries. One example of a TCSC installation is the Brazilian North-South interconnection (a 500 kV, 1020 km transmission line with a rated transmitted power of 1300 MW), where a hybrid three-phase-TCSC connects the North and South systems [11], [12]. Such a hybrid three-phase-TCSC, shown in Figure 1.8, consists of five fixed capacitors (distributed equally along the line length) and two TCSC modules (located at the sending and receiving ends). The degree of compensation of the interconnection is 66% (1100 Mvar capacitive), where the fixed capacitors provide 54% and each TCSC module provides 6%. The task of the TCSC modules is purely damping the low-frequency, inter-area power oscillations between the two systems. These oscillations would otherwise provide a hazard to the stability of the interconnected system. The three-phase TCSC and the hybrid three-phase-TCSC which are already employed by several utilities for power flow control and damping low-frequency and SSR oscillations have shown superior performance through field tests, analytical and simulation studies [13] – [27].

1.7 The Hybrid Single-Phase TCSC/SSSC Compensation Schemes

The recently proposed phase imbalanced series capacitive compensation concept has been shown to be effective in enhancing power system dynamics as it has the potential of damping power swing as well as subsynchronous resonance oscillations [28] - [31]. Figure 1.9 shows two schemes for a phase imbalanced capacitive compensation. They are *"hybrid"* series compensation schemes, where the series capacitive compensation in one phase is created using a single-phase TCSC (Scheme I) or a single-phase Static Synchronous Series Compensator (SSSC) (Scheme II) in series with a fixed capacitor (C_c), and the other two phases are compensated by fixed series capacitors (C). The TCSC and SSSC controls are initially set such that their equivalent compensations at the power frequency combined with the fixed capacitor yield a resultant compensation equal to the other two phases. Thus, the phase balance is maintained at the power frequency while at any other frequency, a phase imbalance is created. To further enhance power oscillations damping, the TCSC and SSSC are equipped with supplementary controllers.

Figure 1.8: A three-line diagram of a hybrid three-phase-TCSC.

Scheme I   Scheme II

Figure 1.9: Schematic diagrams of the hybrid series capacitive compensation schemes.

1.8 Research Objective and Scope of the Thesis

As most large wind farms in North America employ DFIG wind turbines, their voltage-sourced converter (VSC)-based back-to-backs (BtBs) offer independent control of the real and reactive power. The use of these control capabilities have been recently proposed for damping power swings, inter-area oscillations as well as subsynchronous resonance [32]-[43]. There is, however, a question that is always associated with the use of VSC-based BtB wind farms for damping power system oscillations: what happens when there is no wind? The keyword to the answer is "combined". The potential benefit of using these types of wind farms for damping power system oscillations should always be combined with conventional damping devices (PSS, Static Synchronous Compensator (STATCOM), TCSC, SSSC, Static Var Compensator (SVC), High Voltage DC (HVDC), etc.). The main objective of this research work is to investigate the potential use of supplemental controls of DFIG-based wind farms combined with Scheme I for damping power system oscillations resulting from large disturbances (mainly transmission line faults) in multi-machine power systems.

There are five chapters in this thesis. The main topics of each chapter are as follows:

Chapter 1 introduces the fundamental benefits of series compensation of transmission lines. Brief introductions to SSR, FACTS controllers and the TCSC are also presented. The objective of the research is also presented in this chapter.

In Chapter 2, the system used for the investigations conducted in this thesis is described and the detailed dynamic models of its individual components are also presented in this chapter.

9

The results of the digital time-domain simulations of a case study for the system during a three-phase fault are presented at the end of this chapter.

Chapter 3 presents a comprehensive description of the TCSC, its three modes of operation and the analysis of its net reactance. The phase imbalanced hybrid single-phase-TCSC compensation scheme (Scheme I) and its modeling in the ElectroMagnetic Transient Program (EMTP-RV) are also presented.

Chapter 4 demonstrates the effectiveness of the supplemental controllers of the hybrid single-phase- TCSC compensation scheme (Scheme I) and the DFIG-based wind farms in damping power system oscillations through time-domain simulation studies. The recent concern over the case of large share of wind power generation which results in reducing the total inertia of the synchronous generators and degrading the system transient stability is also addressed in this chapter.

Chapter 5 summarizes the research described in this thesis and presents some conclusions.

Chapter 2

MODELING OF POWER SYSTEM INCORPORATING DFIG-BASED WIND FARMS FOR LARGE DISTURBANCE STUDIES

2.1 Introduction

In this chapter, the system used for the studies reported in this thesis is described and the mathematical models of its various components are presented. A digital time-domain simulation of a case study of the system during a three-phase fault is presented at the end of this chapter.

2.2 System under Study

The system used in the investigations of this thesis is shown in Figure 2.1. It consists of four large generating stations (G_1, G_2, G_3 and G_4) supplying two load centers (S_1 and S_2) through nine 500 kV transmission lines. Two DFIG-based wind farms, designated as Wind Farms A and B, each comprises 333 - 1.5 MW, 0.575 kV wind turbines is connected via a transformer to buses 7 and 8. The two double-circuit transmission lines L_1 and L_2 are series compensated with fixed capacitor banks located in the middle of the lines. The compensation degree of L_1 and L_2 is 50%. The total installed capacity of the four generating stations and peak load of the system are 5600 MVA and 5387 MVA respectively. Shunt capacitors are installed at buses 4 and 5 to maintain their voltages within 1±0.05 p.u. The EMTP-RV is used as the simulation study tool.

2.3 Power System Modeling

The nonlinear differential equations of the system under study are derived by developing individually the mathematical models which represent the various components of the system, namely the synchronous generator, the excitation system, the transmission line, the system load and the DFIG-based wind turbine and its converter controllers. Knowing the mutual interaction among these models, the whole system of differential equations can be formed.

11
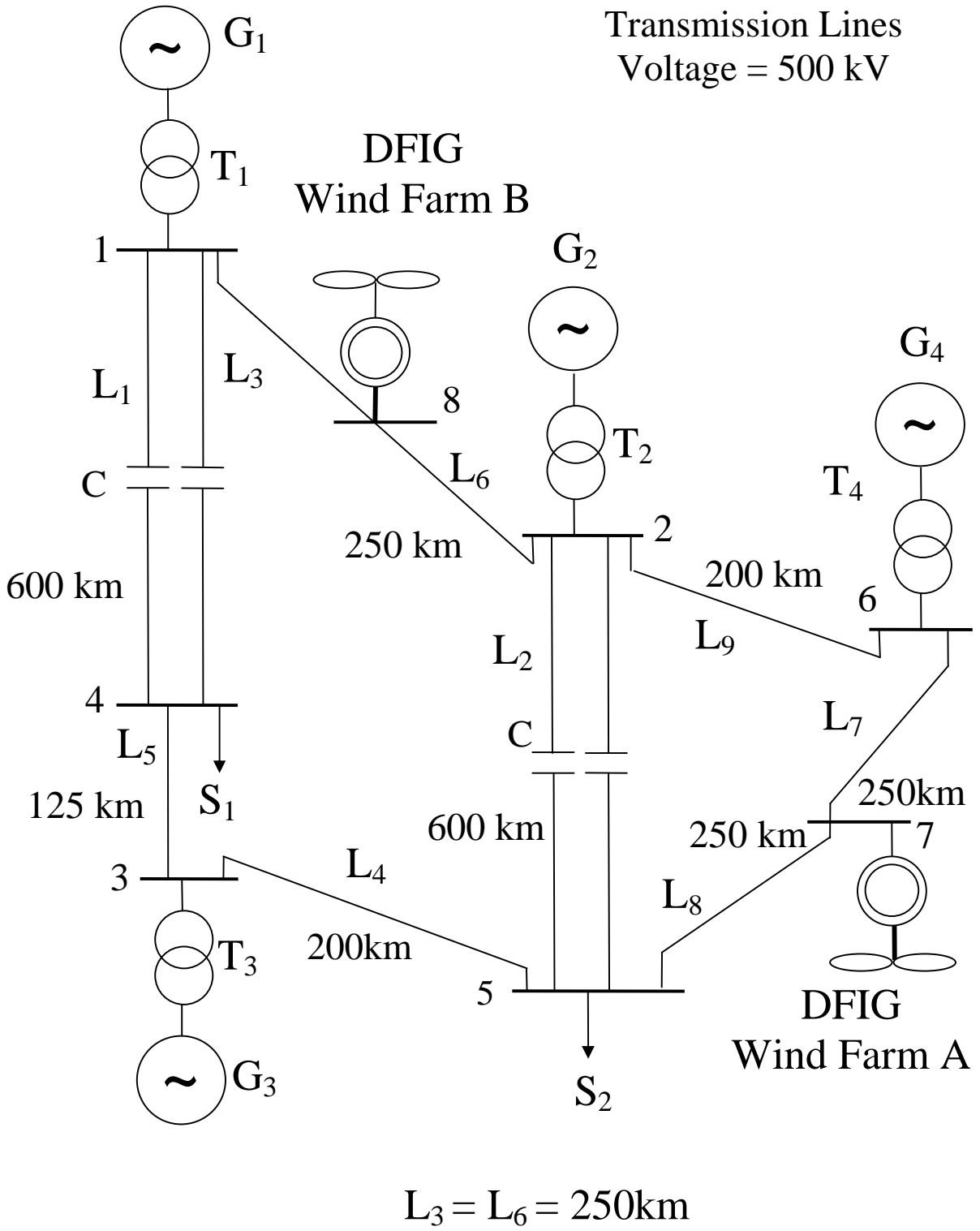
Figure 2.1: System under study.

2.3.1 Modeling of the synchronous generator

In a conventional synchronous machine, the stator circuit consisting of a three-phase winding produces a sinusoidally space distributed magnetomotive force. The rotor of the machine carries the field (excitation) winding which is excited by a dc voltage. The electrical damping due to the eddy currents in the solid rotor and, if present, the damper winding is represented by three equivalent damper circuits; one on the direct axis (d-axis) and the other two on the quadrature axis (q-axis). The performance of the synchronous machine can be described by the equations given below in the d-q reference frame (Figure 2.2) [44]. In these equations, the convention adopted for the signs of the voltages and currents is that v is the impressed voltage at the terminals and that the direction of positive current i corresponds to generation. The sign of the currents in the equivalent damper windings is taken positive when they flow in a direction similar to that of the positive field current.

With time t expressed in seconds, the angular velocity ω expressed in rad/s ($\omega_0 = 377 rad/\sec$) and the other quantities expressed in per unit, the stator equations become:

$$e_d = \frac{1}{\omega_0}\frac{d\Psi_d}{dt} - \frac{\omega}{\omega_0}\Psi_q - R_a i_d \tag{2.1}$$

$$e_q = \frac{1}{\omega_0}\frac{d\Psi_q}{dt} + \frac{\omega}{\omega_0}\Psi_d - R_a i_q \tag{2.2}$$

The rotor equations:

$$e_{fd} = \frac{1}{\omega_0}\frac{d\Psi_{fd}}{dt} + R_{fd} i_{fd} \tag{2.3}$$

$$0 = \frac{1}{\omega_0}\frac{d\Psi_{1d}}{dt} + R_{1d} i_{1d} \tag{2.4}$$

$$0 = \frac{1}{\omega_0}\frac{d\Psi_{1q}}{dt} + R_{1q} i_{1q} \tag{2.5}$$

13

$$0 \quad = \frac{1}{\omega_0} \frac{d\Psi_{2q}}{dt} + R_{2q} i_{2q} \tag{2.6}$$

The stator flux linkage equations:

$$\Psi_d = -L_d i_d + L_{ad} i_{fd} + L_{ad} i_{1d} \tag{2.7}$$

$$\Psi_q = -L_q i_q + L_{aq} i_{1q} + L_{aq} i_{2q} \tag{2.8}$$
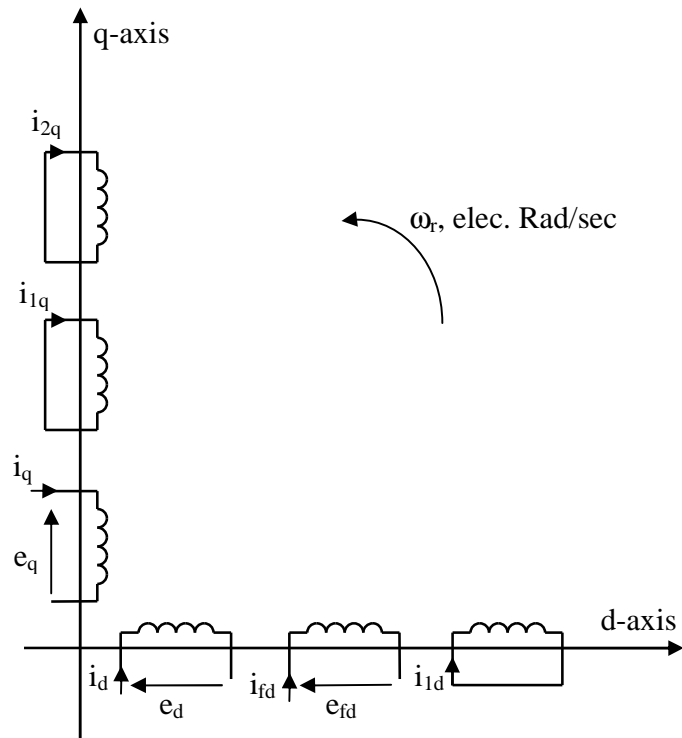
Figure 2.2: Modeling of the synchronous machine in the d-q reference frame.

The rotor flux linkage equations:

$$\Psi_{fd} = L_{ffd} i_{fd} + L_{ad} i_{1d} - L_{ad} i_d \tag{2.9}$$

$$\Psi_{1d} = L_{ad} i_{fd} + L_{11d} i_{1d} - L_{ad} i_d \tag{2.10}$$

$$\Psi_{1q} = L_{11q} i_{1q} + L_{aq} i_{2q} - L_{aq} i_q \tag{2.11}$$

14

$$\Psi_{2q} = L_{aq}i_{1q} + L_{22q}i_{2q} - L_{aq}i_q \tag{2.12}$$

The air-gap torque equation:

$$T_{ELEC} = \Psi_d i_q - \Psi_q i_d \tag{2.13}$$

The overall differential equations which describe the transient performance of the synchronous machine are given by the following matrix equation:

$$\left[\frac{dX_{syn}}{dt}\right] = \left[At_{syn}\right]\left[X_{syn}\right] + \left[Bt_{syn}\right]\begin{bmatrix} V_{td} \\ V_{tq} \\ e_{fd} \end{bmatrix} \tag{2.14}$$

Where

$$\left[X_{syn}\right] = \begin{bmatrix} i_d & i_q & i_{fd} & i_{1q} & i_{1d} & i_{2q} \end{bmatrix}^T$$

$$\left[At_{syn}\right] = [L]^{-1}[Qt]$$

$$\left[Bt_{syn}\right] = [L]^{-1}[Rt]$$

$$[L] = \begin{bmatrix}
-L_d & 0 & L_{ad} & 0 & L_{ad} & 0 \\
0 & -L_q & 0 & L_{aq} & 0 & L_{aq} \\
-L_{ad} & 0 & L_{ffd} & 0 & L_{ad} & 0 \\
0 & -L_{aq} & 0 & L_{11q} & 0 & L_{aq} \\
-L_{aq} & 0 & L_{ad} & 0 & L_{11d} & 0 \\
0 & -L_{aq} & 0 & L_{aq} & 0 & L_{22q}
\end{bmatrix} \tag{2.15}$$

$$[Qt] = \begin{bmatrix}
\omega_0 R_a & -\omega L_q & 0 & \omega L_{aq} & 0 & \omega L_{aq} \\
\omega L_d & \omega_0 R_a & -\omega L_{ad} & 0 & -\omega L_{ad} & 0 \\
0 & 0 & -\omega_0 R_{fd} & 0 & 0 & 0 \\
0 & 0 & 0 & -\omega_0 R_{1q} & 0 & 0 \\
0 & 0 & 0 & 0 & -\omega_0 R_{1d} & 0 \\
0 & 0 & 0 & 0 & 0 & -\omega_0 R_{2q}
\end{bmatrix}$$

$$[Rt] = \begin{bmatrix} \omega_0 & 0 & 0 \\ 0 & \omega_0 & 0 \\ 0 & 0 & \omega_0 \\ 0 & 0 & 0 \\ 0 & 0 & 0 \\ 0 & 0 & 0 \end{bmatrix}$$

Here, the superscript ^{T} means matrix transpose.

The synchronous machine swing equation can be written as:

$$\frac{2H}{\omega_o} \frac{d\omega}{dt} = T_{MECH} - T_{ELEC} \qquad (2.16)$$

$$\frac{d\delta}{dt} = \omega - \omega_o \qquad (2.17)$$

In the above two equations (2.16 and 2.17), ω is in radians per second, the inertia constant H is in seconds, and the load angle δ is in radians, ω_o is the synchronous frequency (377 rad/sec) and the mechanical and electrical torques T_{MECH} and T_{ELEC} are in per unit.

In developing the equations of multi-machine systems, the equations of each synchronous machine expressed in its own d-q reference frame which rotates with its rotor must be expressed in a common reference frame. Usually, a reference frame rotating at synchronous speed is used as the common reference. Axis transformation equations are used to transform between the individual machine (d-q) reference frames and the common (R-I) reference frame [44]

2.3.2   Modeling of the transmission line

A series capacitor-compensated transmission line may be represented by the *RLC* circuit shown in Figure 2.3 [45]. In the voltage phasor diagram shown in Figure 2.4, the rotor angle δ is the angle (in elec. rad) by which the q-axis leads the reference voltage V_b. The differential equations for the circuit elements, after applying Park's transformation [45], can be expressed in the d-q reference frame by the following matrix expressions.

16
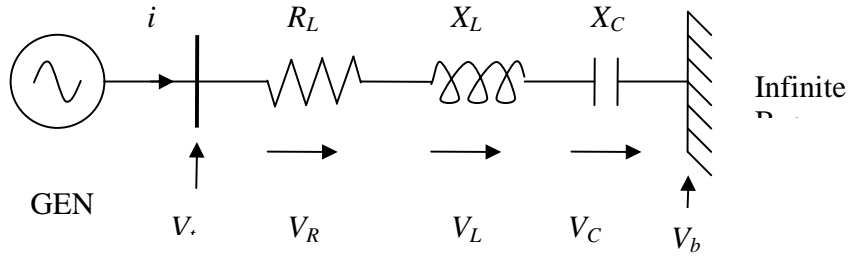
Figure 2.3: A series capacitor-compensated transmission line.
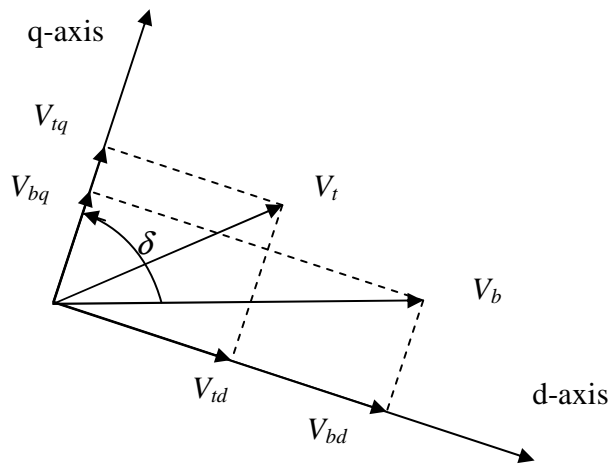
Figure 2.4: Voltage phasor diagram.

The voltage across the resistance:

$$\begin{bmatrix} V_{Rd} \\ V_{Rq} \end{bmatrix} = \begin{bmatrix} R_L & 0 \\ 0 & R_L \end{bmatrix} \begin{bmatrix} i_d \\ i_q \end{bmatrix} \tag{2.18}$$

The voltage across the inductance:

$$\begin{bmatrix} V_{Ld} \\ V_{Lq} \end{bmatrix} = \begin{bmatrix} 0 & -\dfrac{\omega}{\omega_0} X_L \\ \dfrac{\omega}{\omega_0} X_L & 0 \end{bmatrix} \begin{bmatrix} i_d \\ i_q \end{bmatrix} + \begin{bmatrix} \dfrac{X_L}{\omega_0} & 0 \\ 0 & \dfrac{X_L}{\omega_0} \end{bmatrix} \begin{bmatrix} \dfrac{di_d}{dt} \\ \dfrac{di_q}{dt} \end{bmatrix} \tag{2.19}$$

The voltage across the capacitor:

17

$$
\begin{bmatrix} \dfrac{dV_{Cd}}{dt} \\ \dfrac{dV_{Cq}}{dt} \end{bmatrix} = \begin{bmatrix} \omega_0 X_C & 0 \\ 0 & \omega_0 X_C \end{bmatrix} \begin{bmatrix} i_d \\ i_q \end{bmatrix} + \begin{bmatrix} 0 & \omega \\ -\omega & 0 \end{bmatrix} \begin{bmatrix} V_{Cd} \\ V_{Cq} \end{bmatrix}
\tag{2.20}
$$

The overall equations of the transmission line can be written as

$$
\begin{bmatrix} \dfrac{dV_{Cd}}{dt} \\ \dfrac{dV_{Cq}}{dt} \\ V_{td} \\ V_{tq} \end{bmatrix} = [Att]\begin{bmatrix} V_{Cd} \\ V_{Cq} \end{bmatrix} + [Rt1]\begin{bmatrix} \dfrac{di_d}{dt} \\ \dfrac{di_q}{dt} \end{bmatrix} + [Rt2]\begin{bmatrix} i_d \\ i_q \end{bmatrix} + [Btt][V_b]
\tag{2.21}
$$

Where

$$
[Att] = \begin{bmatrix} 0 & \omega \\ -\omega & 0 \\ 1 & 0 \\ 0 & 1 \end{bmatrix}
$$

$$
[Rt1] = \begin{bmatrix} 0 & 0 \\ 0 & 0 \\ \dfrac{X_L}{\omega_0} & 0 \\ 0 & \dfrac{X_L}{\omega_0} \end{bmatrix}
$$

$$
[Rt2] = \begin{bmatrix} \omega_0 X_C & 0 \\ 0 & \omega_0 X_C \\ R_L & -\dfrac{\omega}{\omega_0} X_L \\ \dfrac{\omega}{\omega_0} X_L & R_L \end{bmatrix}
\tag{2.22}
$$

$$[Btt] = \begin{bmatrix} 0 \\ 0 \\ \sin\delta \\ \cos\delta \end{bmatrix}$$

2.3.3 Excitation system

The block diagram representation of the excitation system used in this study is shown in Figure 2.5, and the corresponding data are given in Appendix A [45].
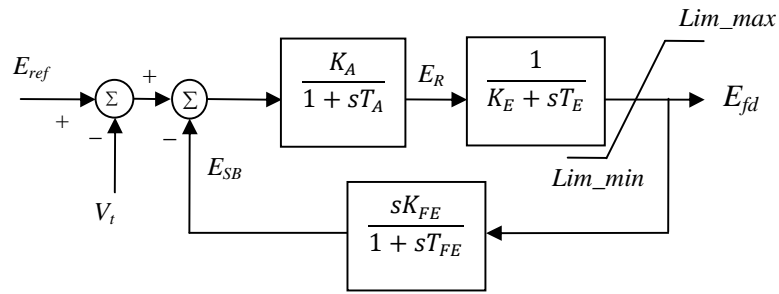
Figure 2.5: Block diagram of the excitation system.

Utilizing the relationship between the excitation system output voltage and the field voltage given by $E_{fd} = \dfrac{L_{ad}}{R_{fd}} e_{fd}$, the state-space equation of the excitation system can be derived from its block diagram and is given by

$$\left[\frac{dX_v}{dt} \right] = [At_v][X_v] + [Bt_v]\begin{bmatrix} V_t \\ E_{ref} \end{bmatrix} \tag{2.23}$$

Where

$$[X_v] = \begin{bmatrix} e_{fd} & E_R & E_{SB} \end{bmatrix}^T$$

$$[At_v] = \begin{bmatrix} -\dfrac{K_E}{T_E} & \dfrac{1}{T_E}\dfrac{R_{fd}}{L_{ad}} & 0 \\[2ex] 0 & -\dfrac{1}{T_A} & -\dfrac{K_A}{T_A} \\[2ex] -\dfrac{K_E K_F}{T_E T_F}\dfrac{L_{ad}}{R_{fd}} & \dfrac{K_F}{T_F T_E} & -\dfrac{1}{T_F} \end{bmatrix} \tag{2.24}$$

$$[Bt_v] = \begin{bmatrix} 0 & 0 \\[2ex] -\dfrac{K_A}{T_A} & \dfrac{K_A}{T_A} \\[2ex] 0 & 0 \end{bmatrix}$$

2.3.4 Modeling of the transformer

The three-phase transformer is constructed by using three single-phase transformers connected in Delta (LV side)/Y grounded (HV side). The transformer leakage and magnetizing reactance as well as the winding resistances and core loss are represented in the model.

2.3.5 Modeling of system loads

The system loads are modeled in these studies by constant impedances. The formula, which is used in calculating the load impedances, is given by [46]:

$$Z_{Load} = \frac{|V_{Load}|^2}{P_{Load} - jQ_{Load}} \tag{2.25}$$

Where

$$Z_{Load} = \text{load impedance.}$$

$$V_{Load} = \text{load voltage.}$$

$$P_{Load} = \text{load real power.}$$

$$Q_{Load} = \text{load reactive power.}$$

2.3.6 DFIG wind turbine model and control

The basic configuration of a DFIG wind turbine is shown in Figure 2.6, where the stator of the induction machine is directly connected to the grid while a back-to-back (BtB) partial-scale power converter (25% to 30% of the generator rating) connects its wound-rotor to the grid. The BtB converter consists of two voltage-sourced converters (Rotor-Side Converter (RSC) and Grid-Side Converter (GSC)) and a common dc bus. The mathematical model of the DFIG wind turbine can be summarized as follows [47]-[51]:
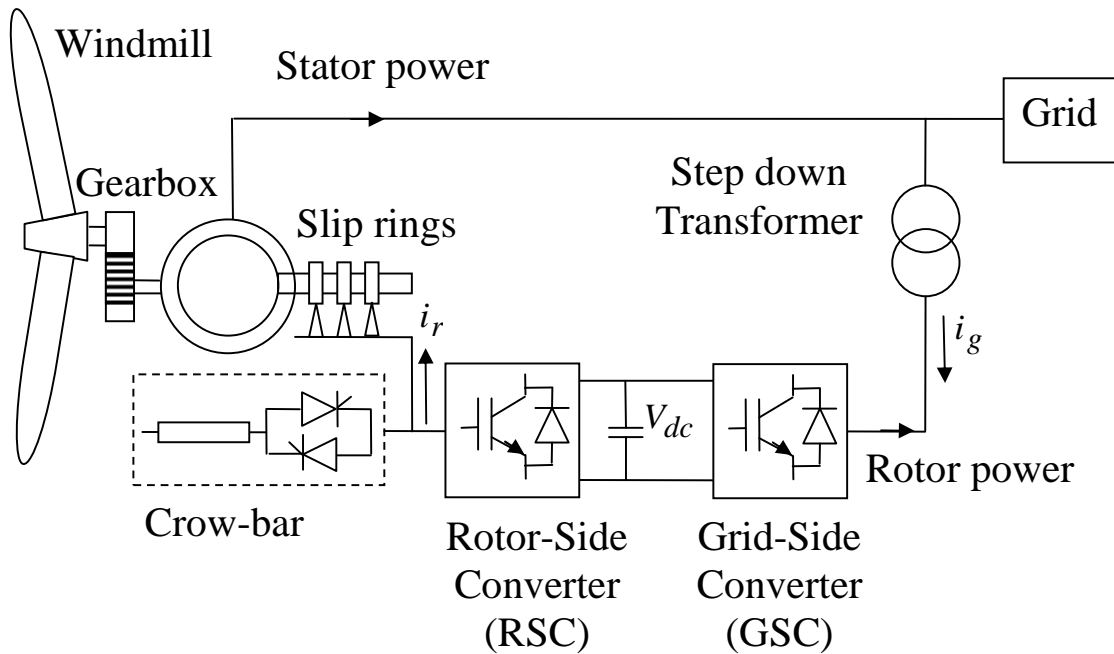
Figure 2.6: Schematic diagram of a DFIG wind turbine.

2.3.7 Wind turbine aerodynamic model

The dynamic output mechanical torque of the wind turbine is expressed as

$$T_{MECH} = \frac{1}{2}\rho A R C_p V_\omega^2 / \lambda \tag{2.26}$$

Where ρ is the air density (kgm^{-3}), A is the blade sweep area (m^2), R is the rotor radius of wind turbine (m), and V_ω is the wind speed (m/s). C_p is the power coefficient of the blade which

is a function of the blade pitch angle θ and the tip speed ratio λ according to the following equation:

$$C_p = \frac{1}{2}\left(\frac{RC_f}{\lambda} - 0.022\theta - 2\right)e^{-0.255\frac{RC_f}{\lambda}} \qquad (2.27)$$

Where C_f is the wind turbine blade design constant and the tip speed ratio λ is given by

$$\lambda = \frac{\Omega_m R}{V_\omega} \qquad (2.28)$$

Where Ω_m is the mechanical angular velocity (rad/s).

The power rotating speed, wind speed and the pitch angle relationships are illustrated in Figure 2.7.
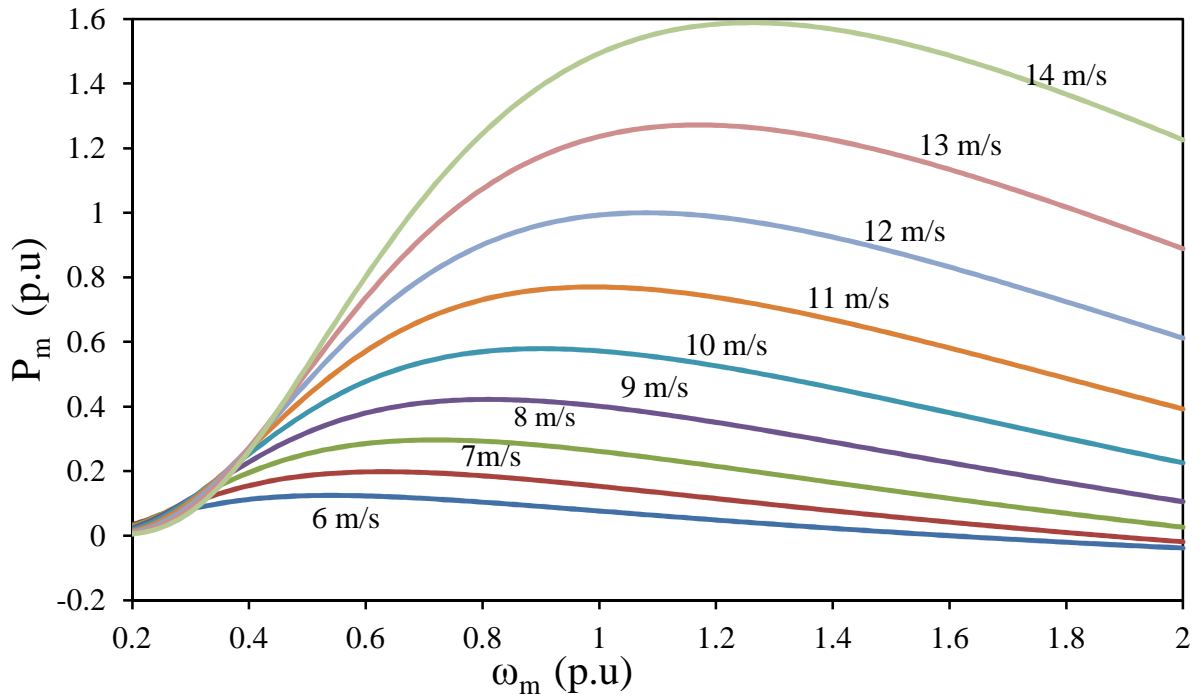
Figure 2.7: Mechanical power, rotor speed and wind speed relationships.

2.3.8 Modeling of the DFIG

Figure 2.8 shows the equivalent circuit of a DFIG in the synchronous qd reference frame, where the $q-$axis leads the $d-$axis by 90°. The stator and rotor voltage equations in qd reference frame can be obtained as follows:
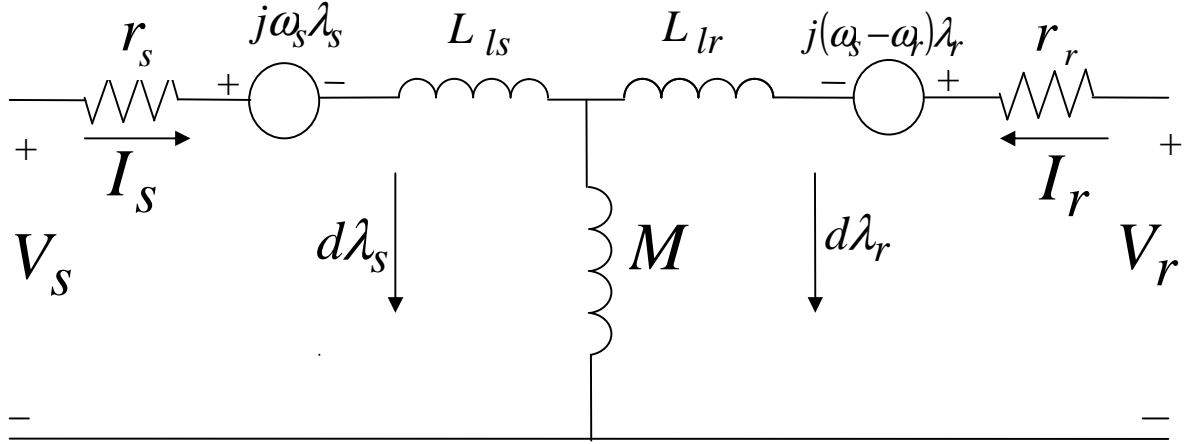
Figure 2.8: Equivalent circuit of the DFIG.

$$\begin{cases} V_s = r_s I_s + j\omega_s \lambda_s + \dfrac{d\lambda_s}{dt} \\ V_r = r_r I_r + j(\omega_s - \omega_r)\lambda_r + \dfrac{d\lambda_r}{dt} \end{cases} \tag{2.29}$$

where $V_s = v_{qs} - jv_{ds}$ and $V_r = v_{qr} - jv_{dr}$. The flux linkage expressions are given as follows:

$$\begin{cases} \lambda_s = L_s I_s + M\, I_r \\ \lambda_r = L_r I_r + M\, I_s \end{cases} \tag{2.30}$$

where $L_s = L_{ls} + M$, $L_r = L_{lr} + M$, $\lambda_s = \lambda_{qs} - j\lambda_{ds}$, $\lambda_r = \lambda_{qr} - j\lambda_{dr}$, $I_s = i_{qs} - ji_{ds}$ and

$I_r = i_{qr} - ji_{dr}$.

From Equations 2.29 and 2.30, a set of differential equations with stator and rotor currents as state variables, stator and rotor voltages as inputs can be established. While the rotor voltages are determined by RSC control scheme, the stator voltages are determined by the network interface.

The electromagnetic torque T_e can be expressed as follows:

$$T_e = \lambda_{qm} i_{dr} - \lambda_{dm} i_{qr} \tag{2.31}$$

23

where λ_{qm} and λ_{dm} are, respectively, the $q-$ and $d-$axes magnetizing flux linkages defined as

$$\lambda_{qm} = \lambda_{qs} - i_{qs} L_{ls} \tag{2.32}$$

$$\lambda_{dm} = \lambda_{ds} - i_{ds} L_{ls}. \tag{2.33}$$

2.3.9 Modeling of the wind turbine shaft system

The detailed investigations reported in [52] have demonstrated that for windmill transient stability studies, a single-mass (lumped mass) model for the wind turbine shaft system cannot provide accurate transient behavior of the system. It has been shown that the critical clearing time calculated using a single-mass model can be 230% higher than the critical clearing time calculated using an adjusted reduced two-mass model. Therefore, for accurate transient stability assessment, the later model should be used. To obtain such an adjusted two-mass model from the three-mass model of the wind turbine shaft shown in Figure 2.9(a), the following steps are performed [53]:

1) Shaft 1 is selected as a reference and the inertias J_2 and J_3 as well as the shaft stiffness k_2 are referred to shaft 1 side using the gear ratio $n = \dfrac{N_1}{N_2}$ as shown in Figure 2.9(b).

2) The differential equations of the rotating system of Figure 2.9(b) are written without including any damping and the state-space matrix $[A]$ given by Equation 2.34 is obtained.

$$\dot{X} = AX \tag{2.34}$$

where

$$X = \begin{bmatrix} \omega_t & \delta_t & \omega_g & \delta_g & \omega_1 & \delta_1 \end{bmatrix}^T$$

3) The imaginary parts of the three eigenvalues of $[A]$ give the two natural torsional frequencies and the frequency of the rigid body mass.

4) The referred gear box and wind turbine masses are lumped and represented by an equivalent mass J_e as shown in Figure 2.9(c).

24

5) Iterative techniques are then used to obtain the value of the single stiffness k_{eq} of Figure 2.9(c) to reproduce accurately the lowest torsional frequency of vibration of the wind turbine shaft system.

$$A = \begin{bmatrix} 0 & \dfrac{-n^2 k_2}{n^2 J_2} & 0 & \dfrac{n^2 k_2}{n^2 J_2} & 0 & 0 \\ 1 & 0 & 0 & 0 & 0 & 0 \\ 0 & \dfrac{n^2 k_2}{J_g} & 0 & \dfrac{-\left(n^2 k_2 + k_1\right)}{J_g} & 0 & \dfrac{k_1}{J_g} \\ 0 & 0 & 1 & 0 & 0 & 0 \\ 0 & 0 & 0 & \dfrac{k_1}{J_1} & 0 & \dfrac{-k_1}{J_1} \\ 0 & 0 & 0 & 0 & 1 & 0 \end{bmatrix}$$
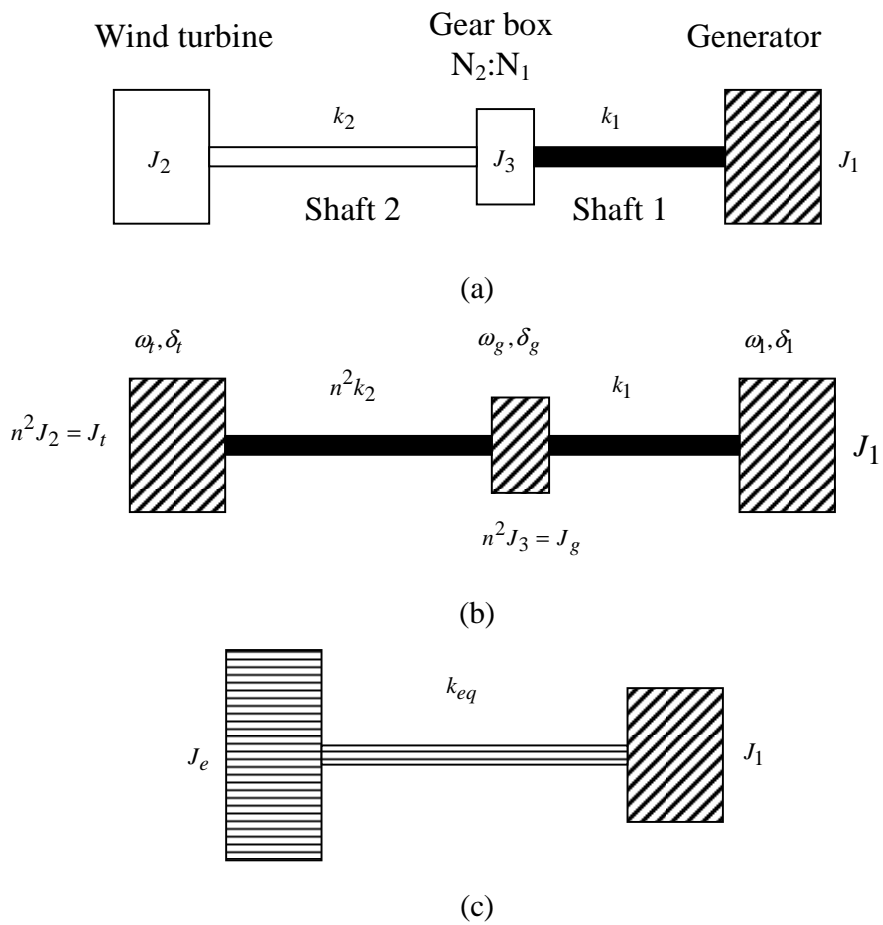
Figure 2.9: Modeling of the wind turbine shaft system.

The inertia constants for the turbine and the generator (the equivalent two-mass model) H_t and H_g are related to J_e and J_l.

2.3.10   Modeling of the BtB dc capacitor link

The dynamics of the BtB dc capacitor link can be described with the help of the equivalent circuit shown in Figure 2.10 as

$$C\frac{dv_{dc}}{dt} = P_r - P_g \tag{2.33}$$

$$\text{where } \begin{cases} P_r = K_1\left(v_{qr}\,i_{qr} + v_{dr}\,i_{dr}\right) \\ P_g = K_2\left(v_{qg}\,i_{qg} + v_{dg}\,i_{dg}\right). \end{cases} \tag{2.34}$$

In Equation 2.34, K_1 and K_2 are constants, P_r, P_g are the active powers of the RSC and the GSC respectively, v_{qr}, v_{dr} are the quadrature and direct axes RSC voltages respectively and v_{qg}, v_{dg} are the quadrature and direct axes GSC voltage.
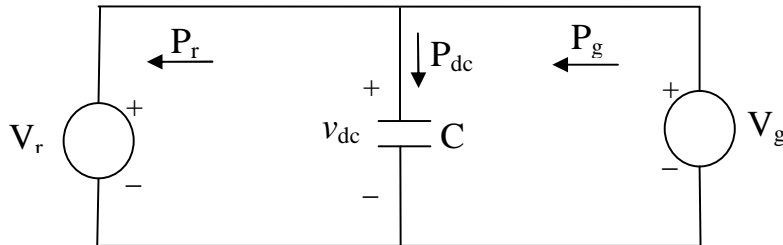
Figure 2.10: Equivalent circuit for the BtB dc capacitor link.

The control of the DFIG wind turbine is achieved by controlling the RSC and GSC converters utilizing vector control techniques. Vector control allows decoupled control of both real and reactive power. The idea is to use a rotating reference frame based on an AC flux or voltage and then to project the currents on this rotating frame. Such projections are usually referred to as the d- and q- components of their respective currents. For flux-based rotating frames, changes in the q- component leads to real power changes, while changes in the d- component leads to reactive power changes. In voltage-based rotating frames (90° ahead of flux-

based frames), the effect is the opposite.

Figure 2.11 shows a general control scheme for the DFIG BtB converter [52] - [54]. In such a scheme, the RSC operates in the stator flux reference frame while the GSC operates in the stator voltage reference frame. The q-axis current of the RSC is used to control the real power while the d-axis current is used for reactive power control. On the other hand, the d-axis current for the GSC is used to control the dc link voltage to a constant level while the q-axis current is used for reactive power control.
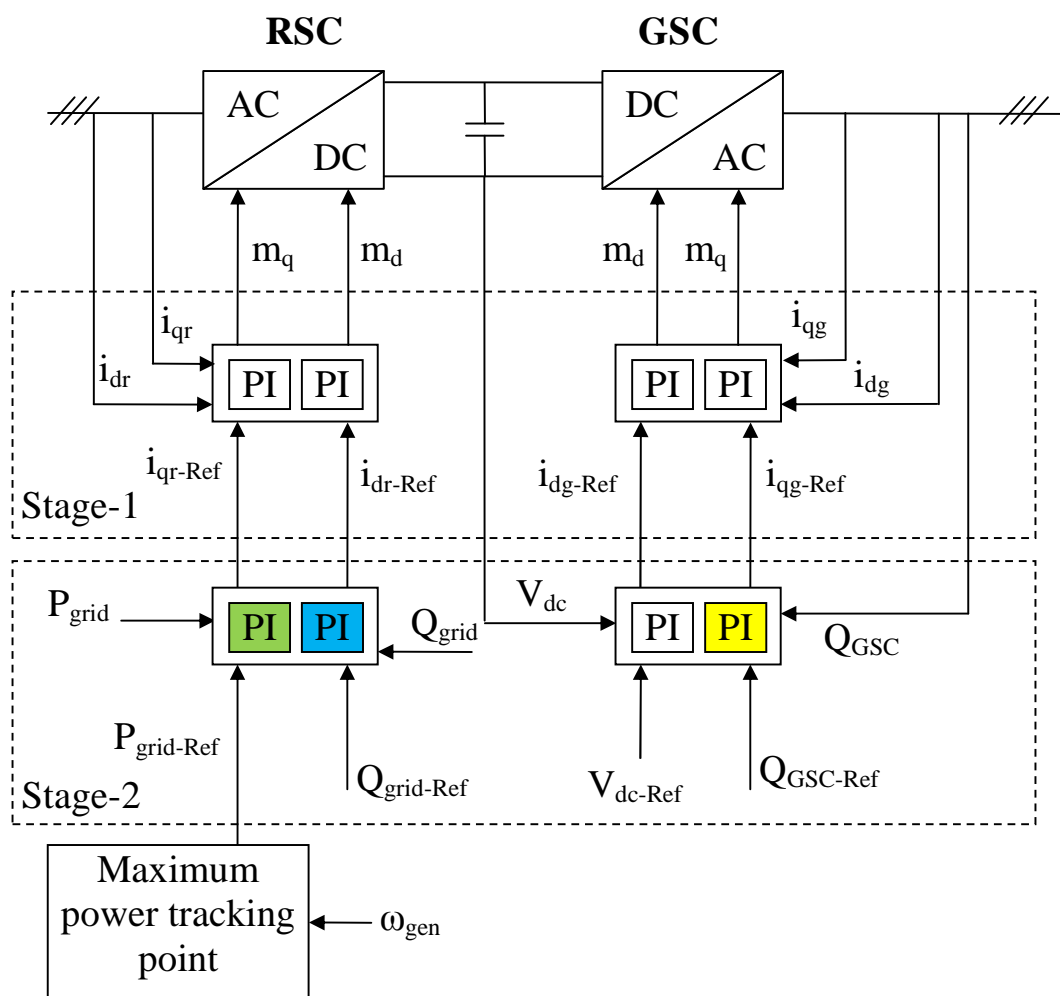
Figure 2.11: Schematic diagram of a general control scheme of DFIG BtB converters.

As illustrated in Figure 2.11, both RSC and GSC are controlled by a two-stage controller. The first stage consists of very fast current controllers regulating the rotor currents to references values that are specified by slower power controllers (Stage-2). In normal operation, the aim of

the RSC is to control independently the real and reactive power on the grid while the GSC has to maintain the dc link capacitor at a set value regardless of the magnitude and direction of the rotor power and to guarantee converter operation with unity power factor (zero reactive power). The reference $P_{grid-Ref}$ for the real power is given by the maximum power tracking point (MPT) look-up table as a function of the optimal generator speed. The reference $Q_{grid-Ref}$ for the reactive power of the RSC can be set to a certain value or to zero according to whether or not the DFIG is required to contribute with reactive power. The reactive power reference for the GSC, $Q_{GSC-Ref}$ is "usually" set to zero. This means that the GSC exchanges only real power with the grid and, therefore, the transmission of reactive power from the DFIG to the grid is done only through the stator. However, the reactive power controllability of the GSC can be useful during the process of voltage reestablishment after clearing a system fault. The reference signal V_{dc-Ref} is set to a constant value that depends on the size of the converter, the stator/rotor voltage ratio and the modulation factor of the power converter.

2.4   A Sample Case Study

In the studies conducted in this thesis, the ElectroMagnetic Transient Program (EMTP-RV) is used for modeling the various system components and producing the time-domain simulation results [55]. Due to the initialization process in the EMTP-RV, simulation results are displayed starting at times equal four seconds. Moreover, faults are assumed to occur at t = 5 seconds.

Figure 2.12 shows the power flow results for the bus voltages and the line real power flows of the system under study. Figure 2.13 shows the transient time responses of the generator load angles and speeds (measured respectively with respect to the load angle and speed of generator 1), the bus voltages and the real power flows in the transmission lines during and after clearing a three-cycle, three-phase fault at the bus 4. The following observations can be made from examining these two figures:

1. The power flow results show heavy power transfers along the two compensated lines L_1 and L_2.

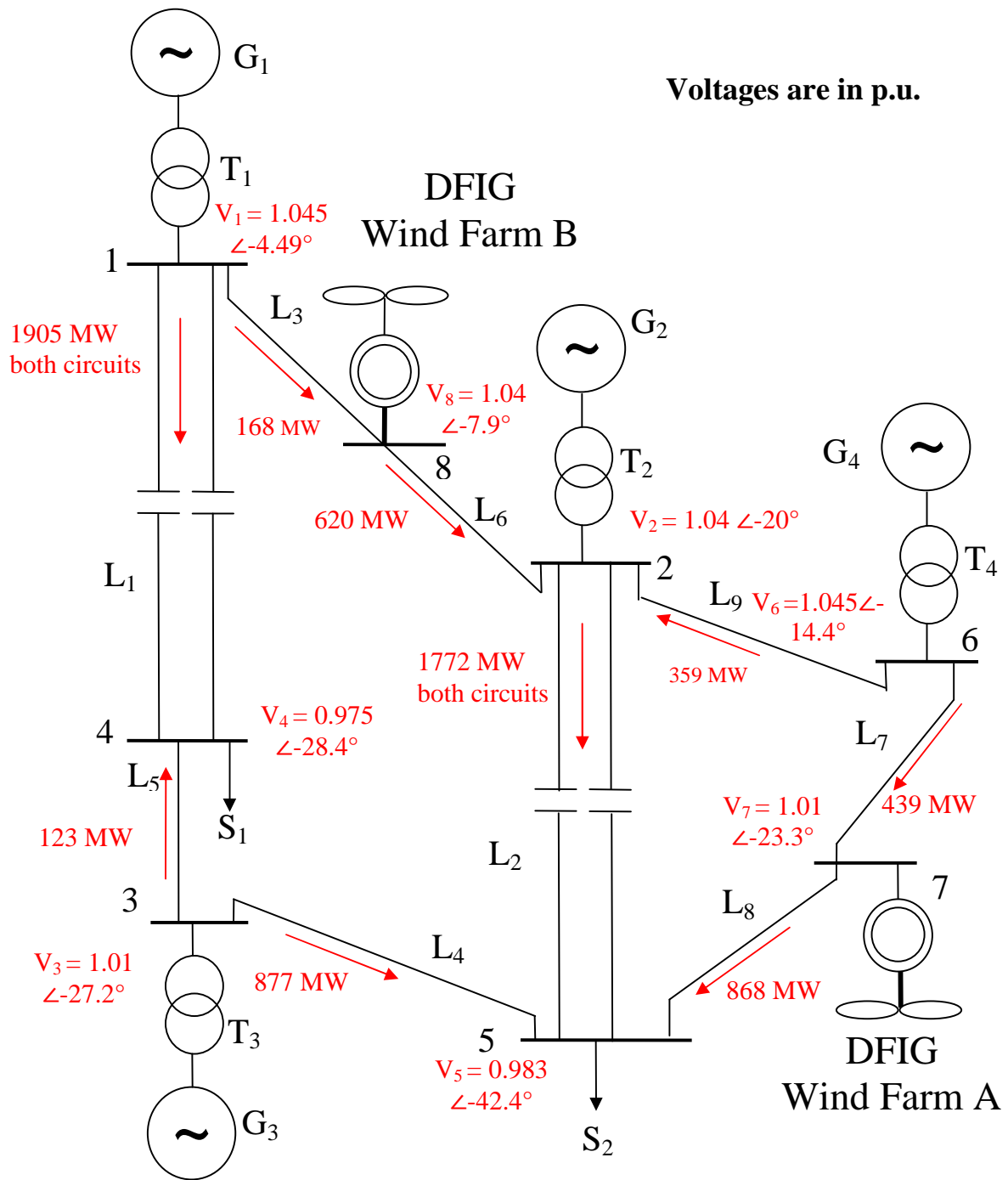**Figure 2.12:** Power flow results of bus voltages and line real power flows of the system under study.
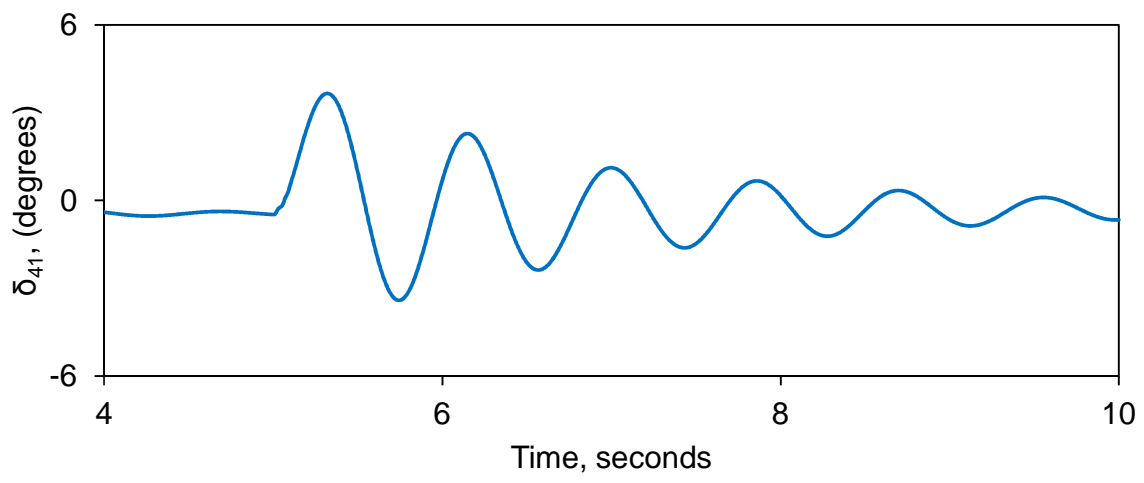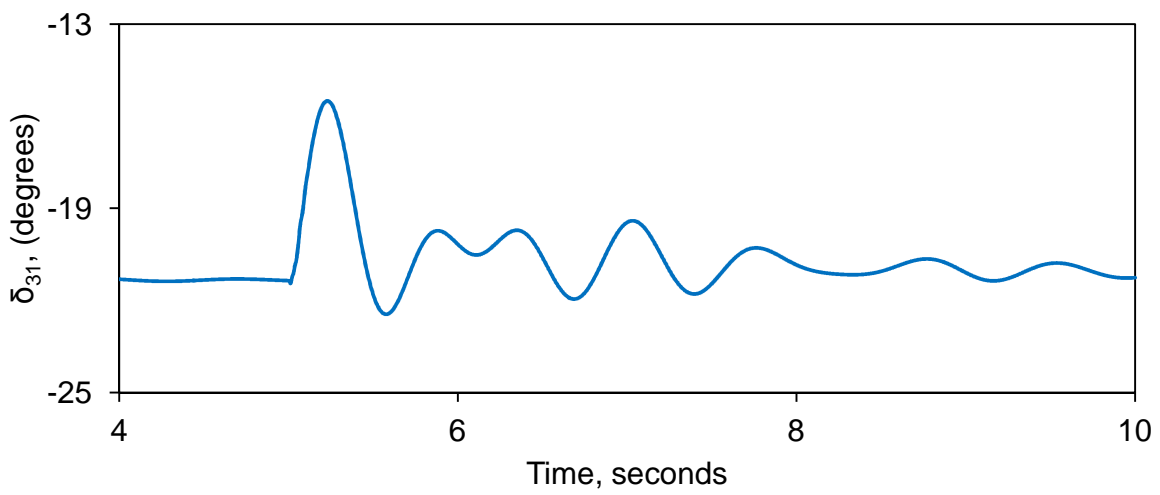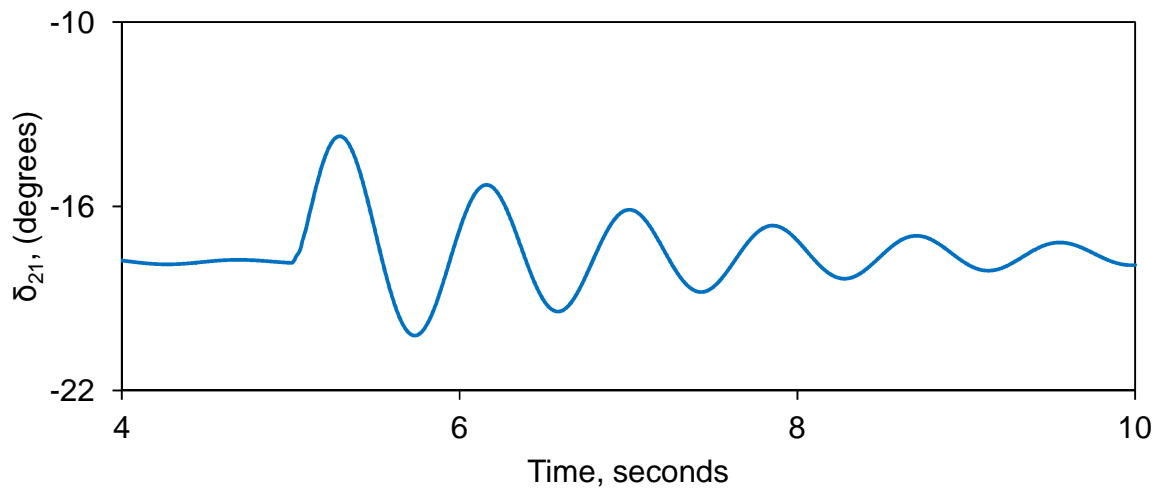
Figure 2.13: Transient time responses of the power system during and after clearing a three-cycle, three-phase fault at bus 4.
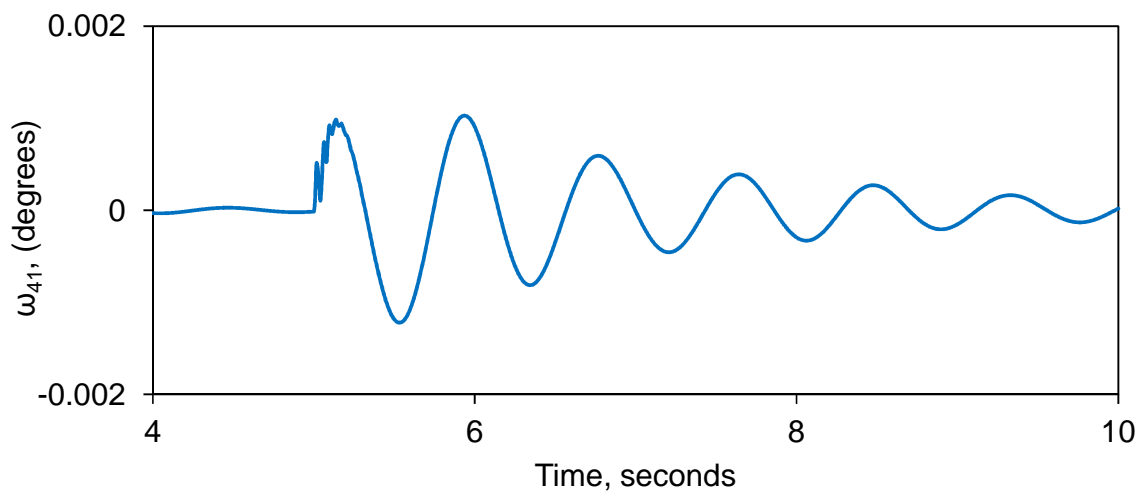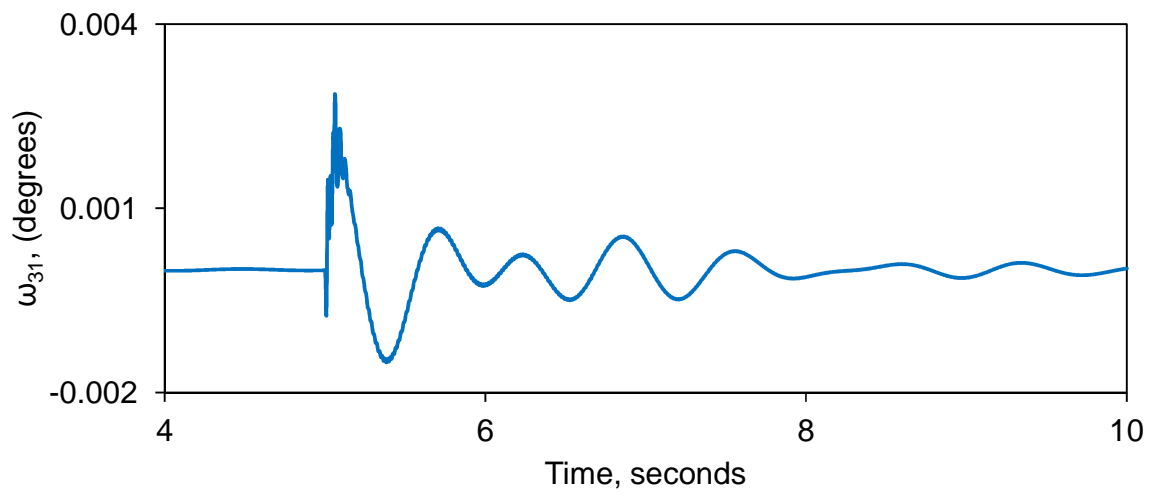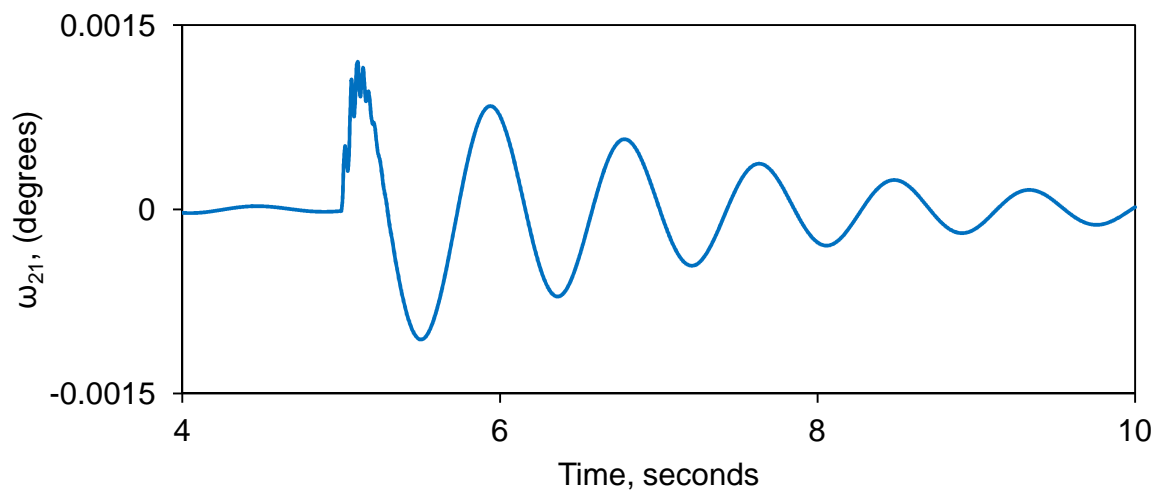
Figure 2.13: continued.
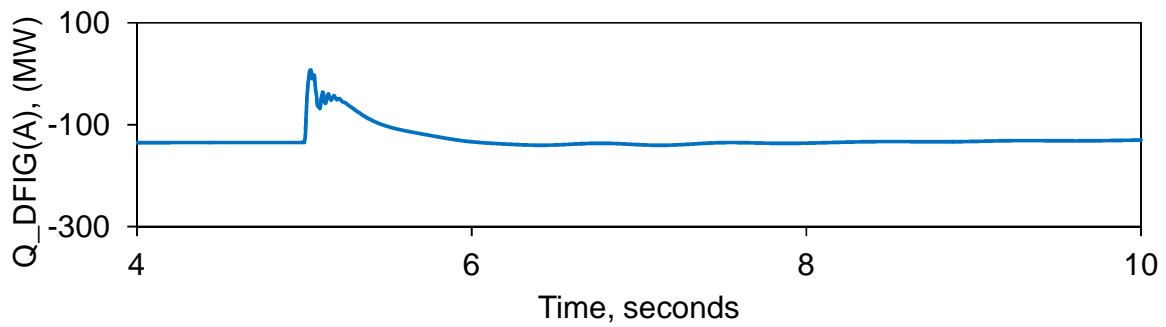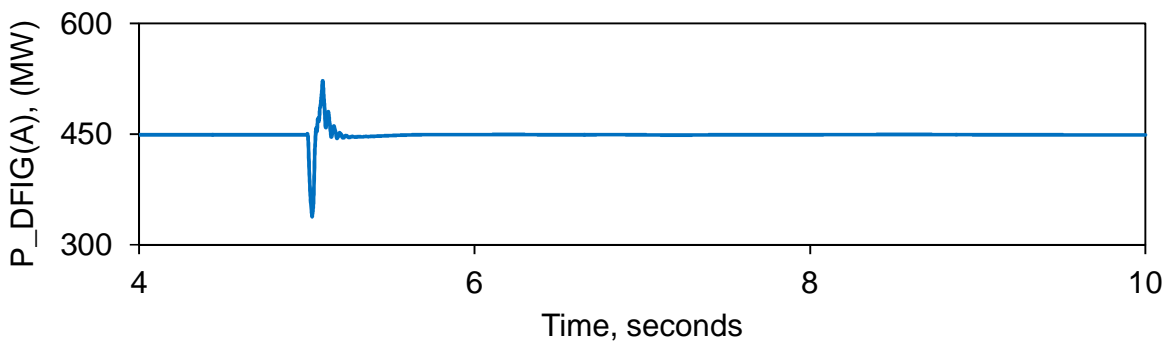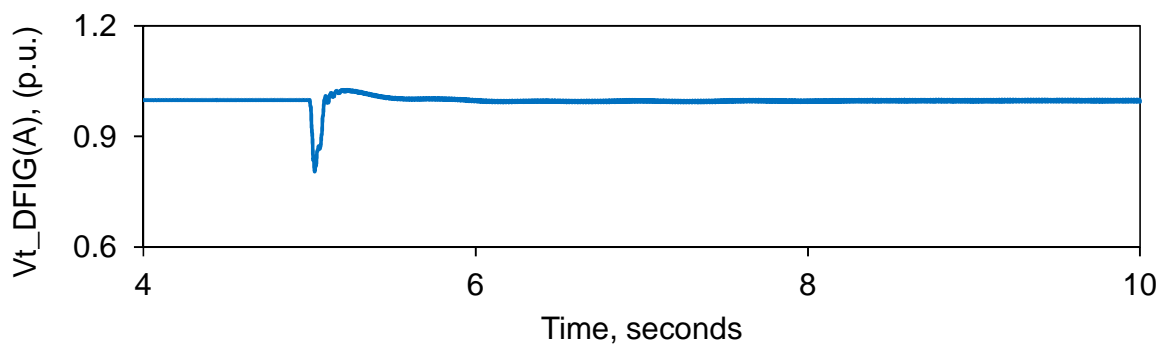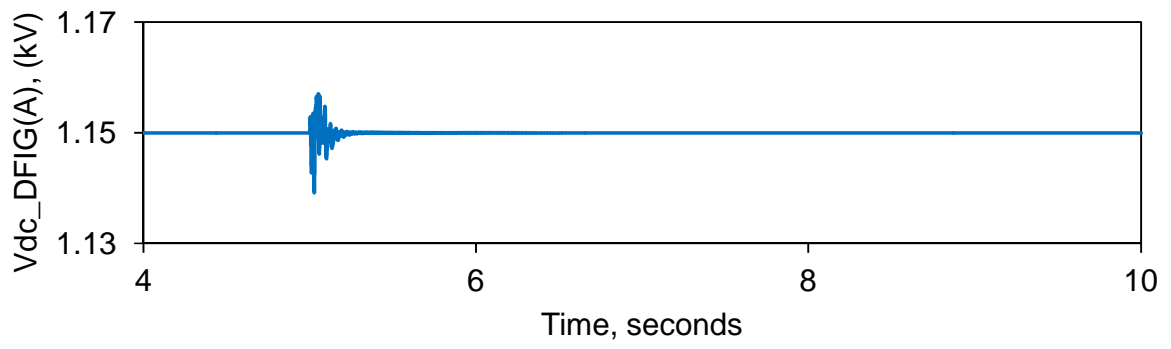
31

Figure 2.13: continued.
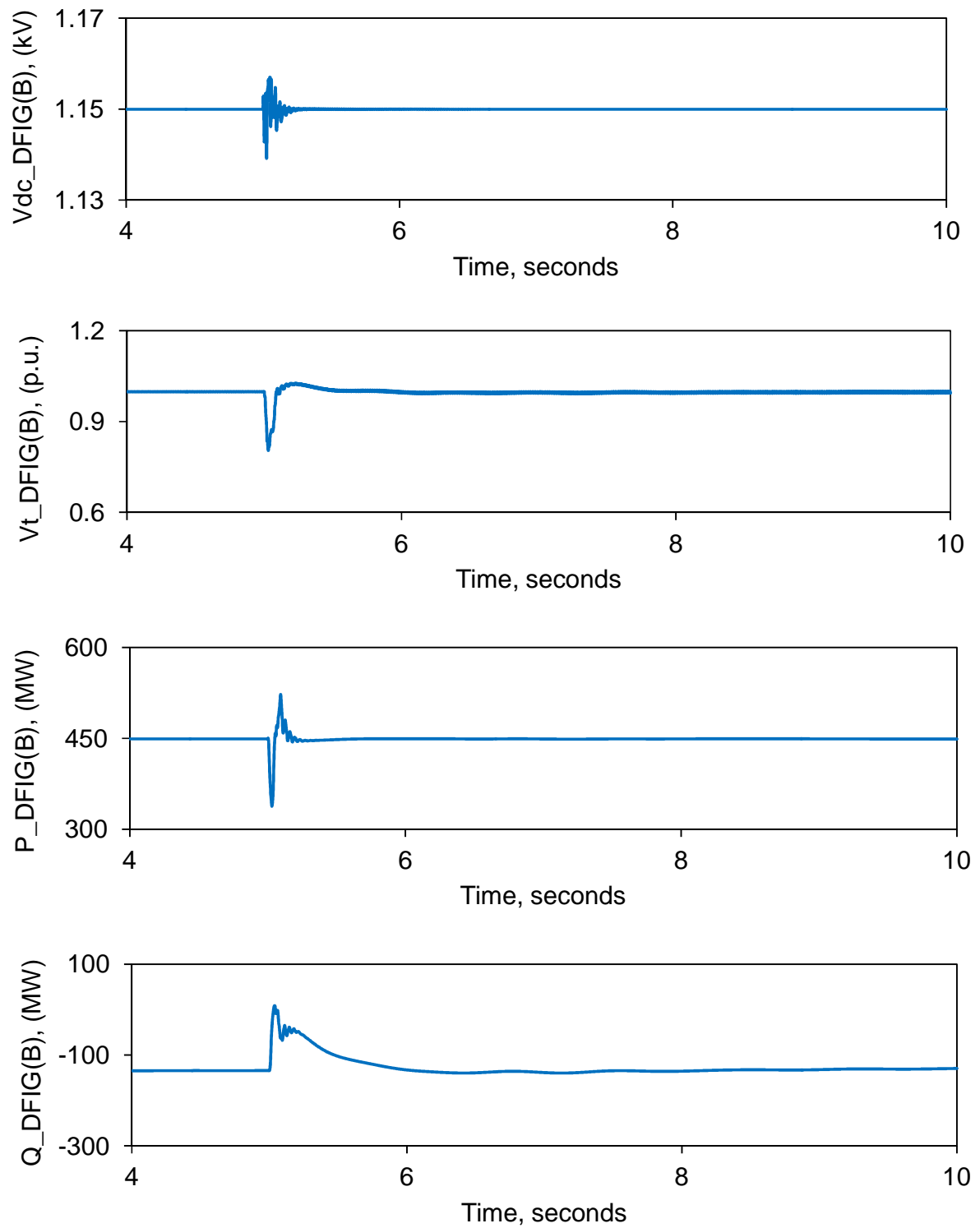
Figure 2.13: continued.
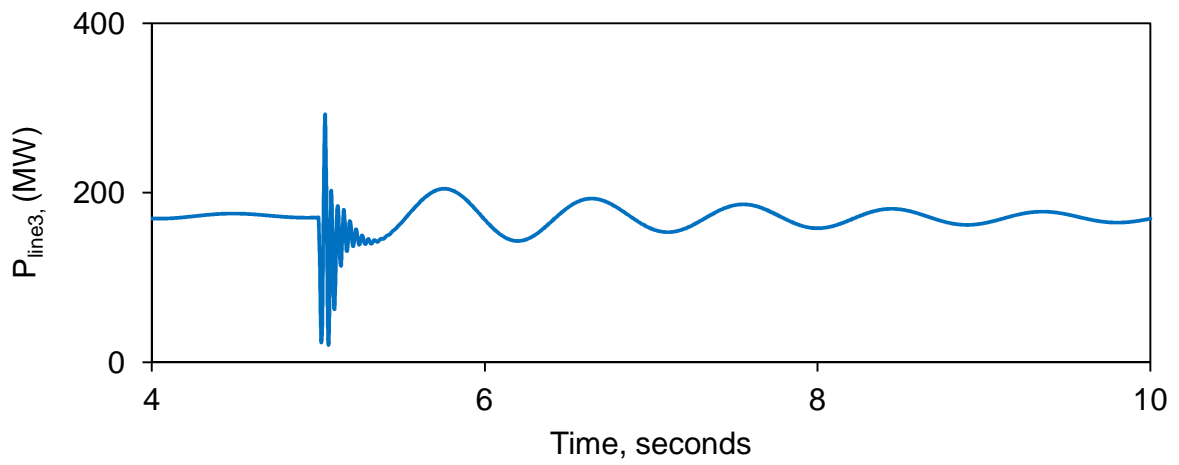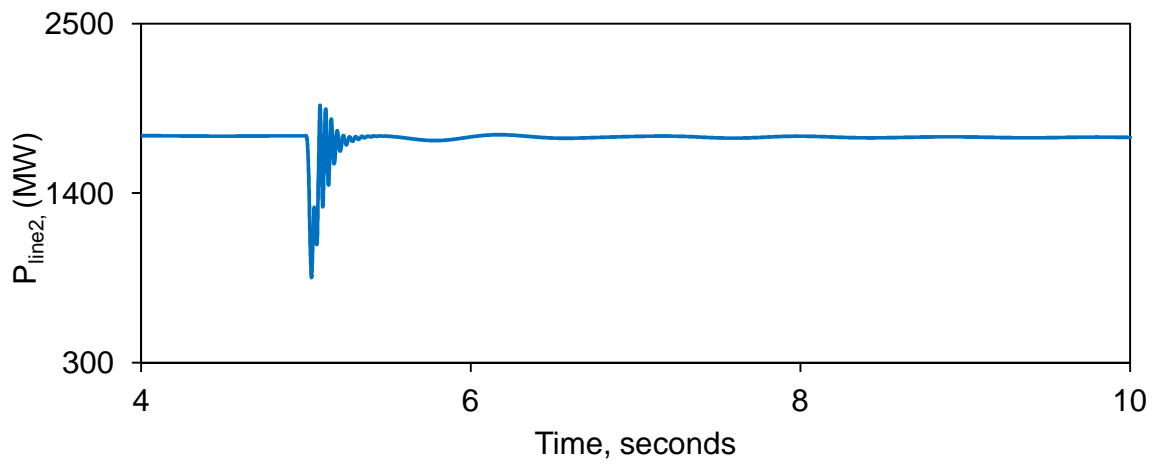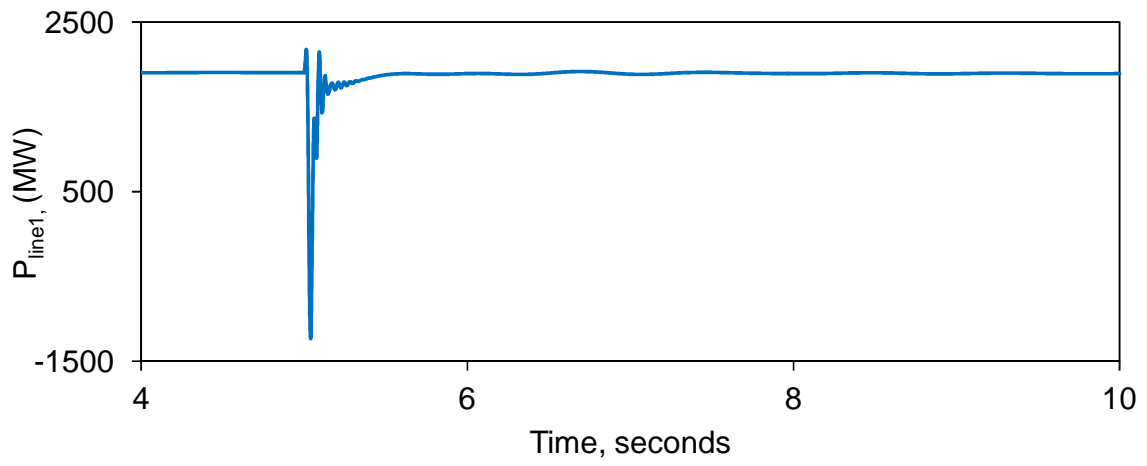
Figure 2.13: continued.
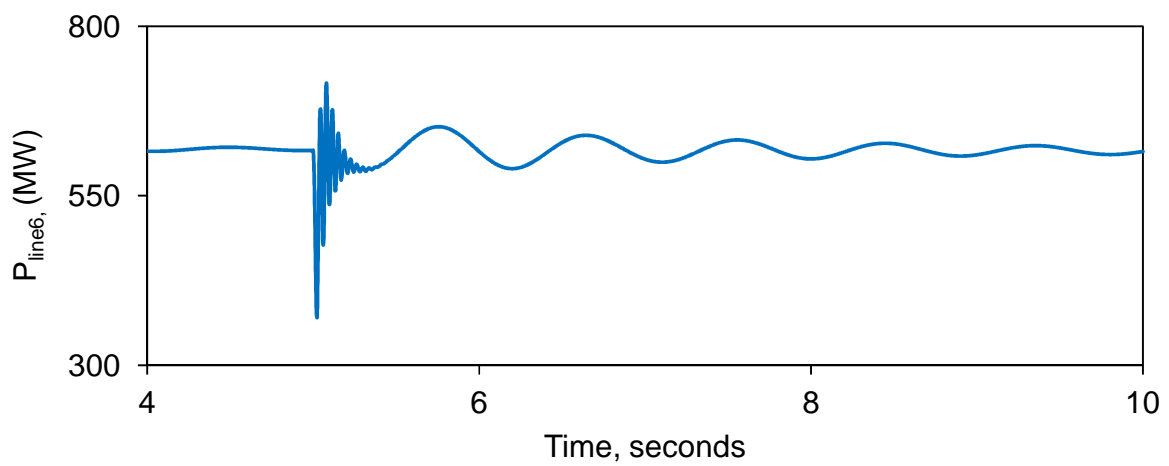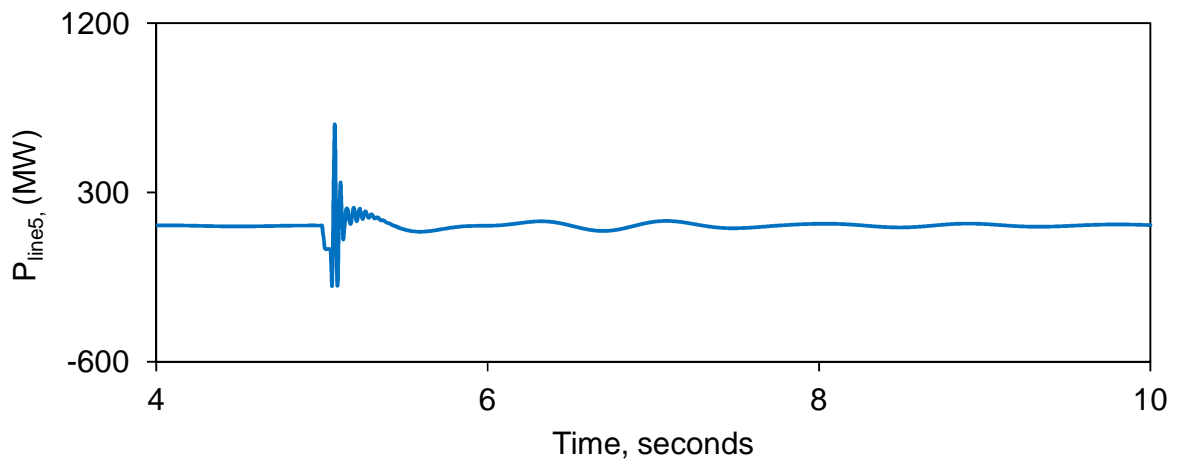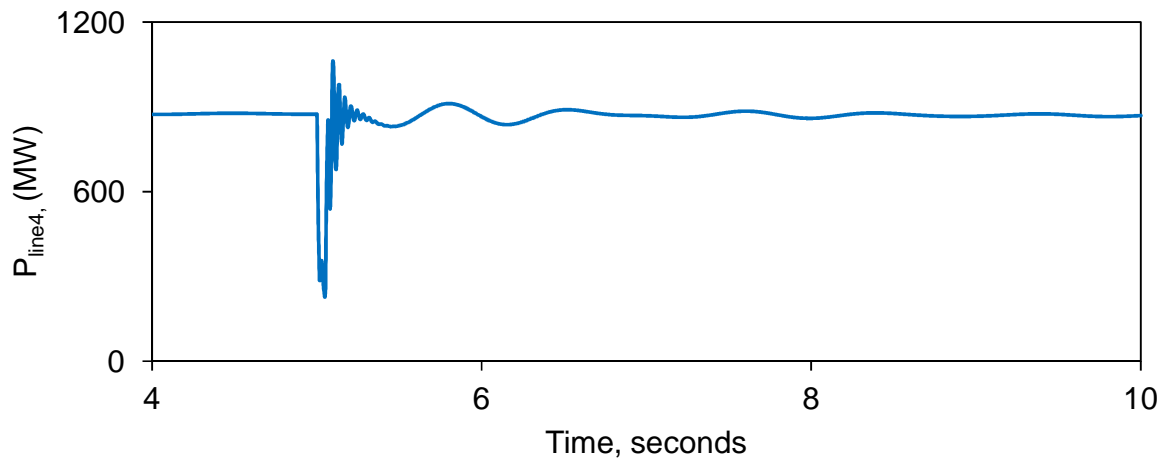
Figure 2.13: continued.
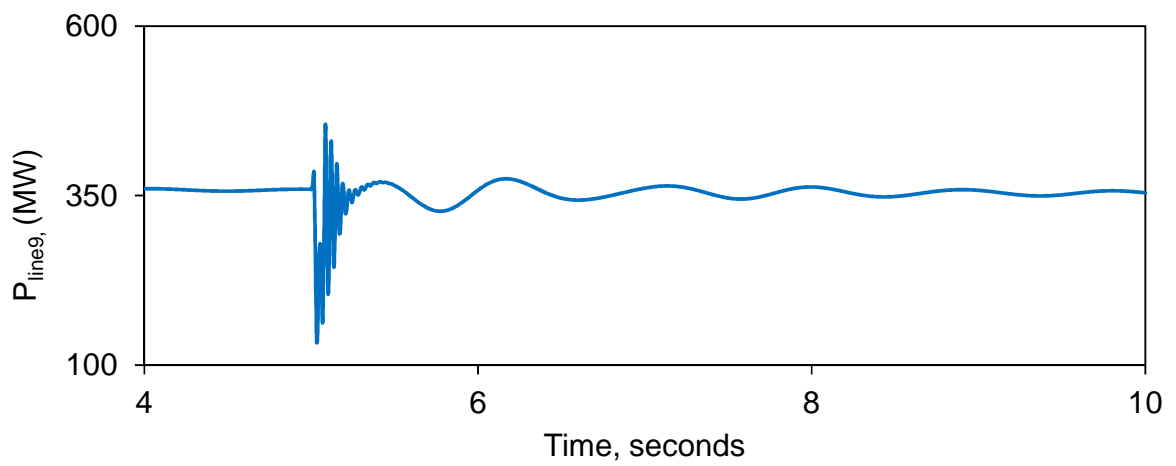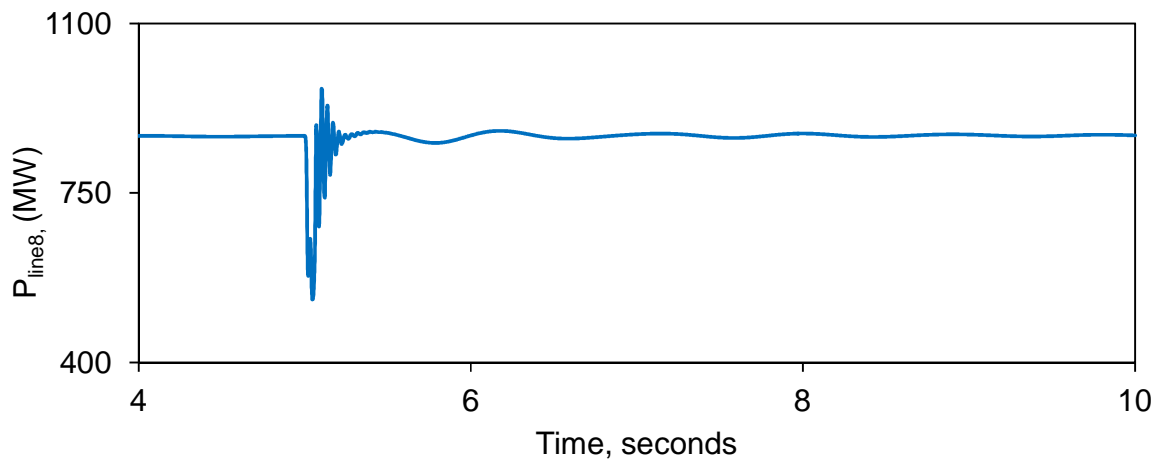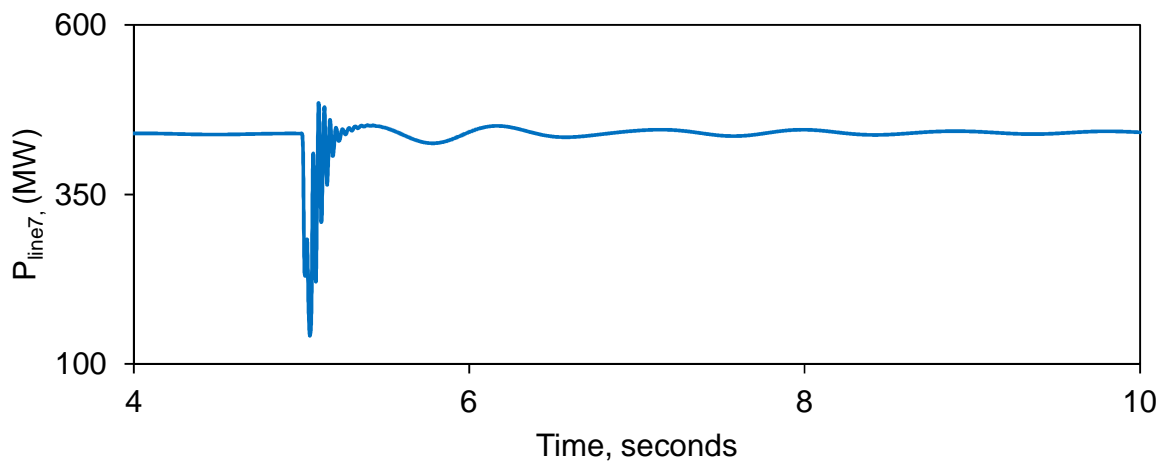
Figure 2.13: continued.

2. The system is stable after fault clearing. The generator load angles and speeds reach steady states. The bus voltages drop immediately at the instant of fault inception but recover after fault clearing.

3. The low frequency oscillations in the generator load angles and speeds are poorly damped.

4. The system under study has four generators; therefore, it has three natural modes of oscillations [27]. In general, synchronous machines respond to disturbances by complex oscillations that involve several natural frequencies, but a particular machine or group of coherent machines may tend to favor one mode over all others [3]. This is the case for generators 2, 3 and 4. As it can be seen from the load angle responses of these three generators, measured with respect to the load angle of generator 1 (Figure 2.13), generators 2, 3 and 4 tend to oscillate at a single frequency (approximately 1.4 Hz).

2.5   Summary

This chapter introduces the system used for the studies reported in this thesis and presents the mathematical models of its various components. A digital time-domain simulation of a case study of the system during a three-phase fault is also presented and some observations are noted.

Chapter 3

THE THYRISTOR CONTROLLED SERIES CAPACITOR AND THE HYBRID SINGLE-PHASE- TCSC COMPENSATION SCHEME

3.1   General

This chapter presents the description and the basic principles of the TCSC as well as the derivation of its mathematical model.   Modeling the hybrid single-phase-TCSC scheme in the ElectroMagnetic Transient Program (EMTP-RV) is also presented.

3.2   Thyristor Controlled Series Capacitor

The TCSC shown in Figure 3.1 consists of a number of series connected modules. In each module, the capacitor bank is provided with a parallel thyristor controlled inductor that circulates current pulses which add in phase with the line current. This boosts the capacitor voltage beyond the level that would be obtained by the line current alone. A Zinc oxide varistor is included in each module for secure overvoltage protection of the TCSC. Each thyristor is triggered once per cycle and has a conduction interval that is shorter than a half-cycle of the rated frequency. If the additional voltage created by the circulating current pulses is controlled to be proportional to the line current, the transmission system will perceive the TCSC as having a virtually increased reactance beyond the physical reactance of the capacitor. This feature which is referred to "vernier control" can be used for short-time transient control. The upper limit for vernier operation is a function of the line current magnitude and time spent at the operating point. Moreover, this scheme can provide an accurate setting of the compensation degree with a high resolution as well as a subsynchronous resonance immune series compensation even at high compensation degrees [55], [56].
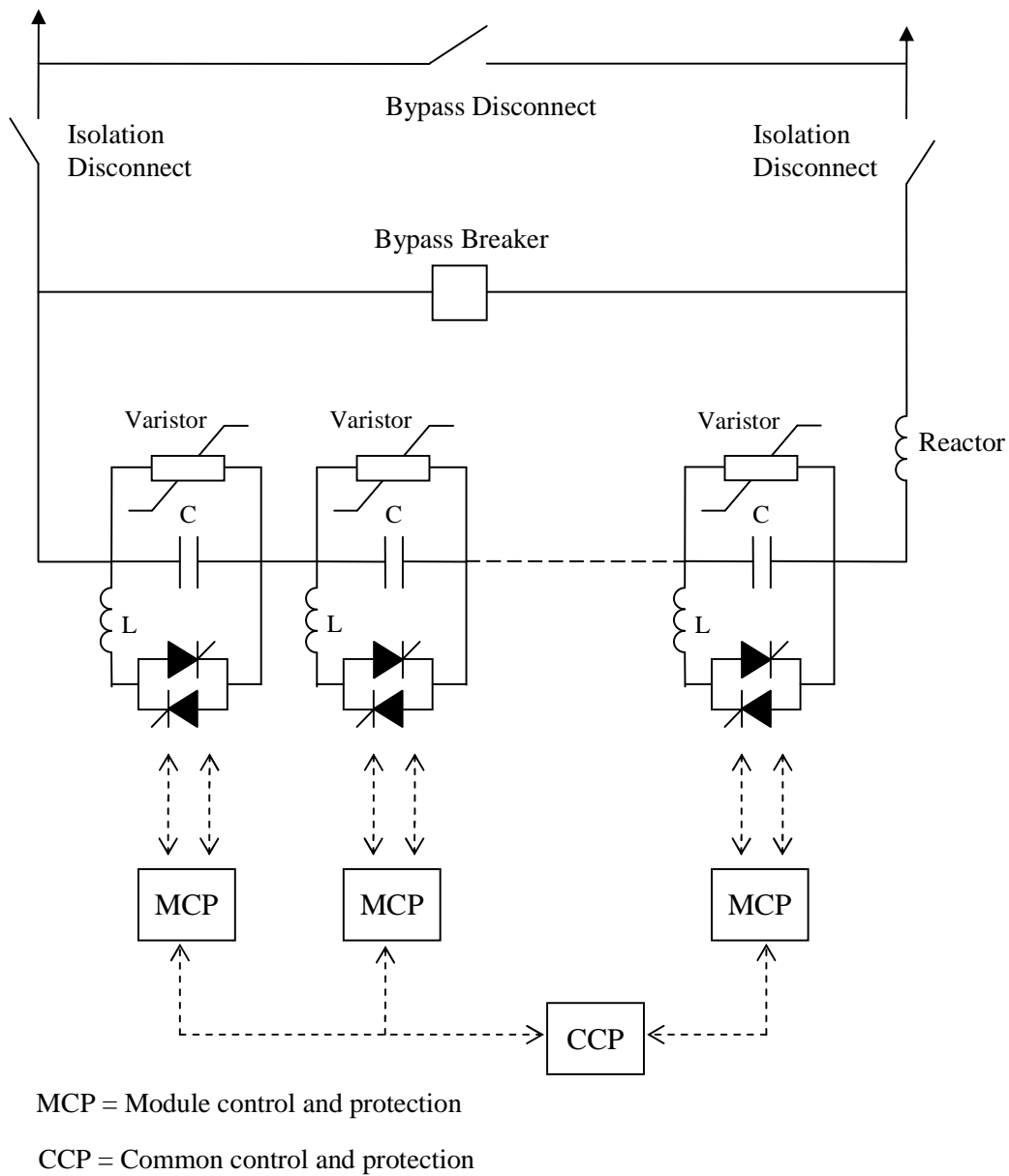
Figure 3.1: A multi-module TCSC.

The control and protection of TCSC are partitioned in two levels; common and module. Commands for both control and protective operations flow from the common level to the module levels. Status information is sent back from each module level. The design concept is to permit any module or combination of modules to be out of service while still being able to operate the remaining modules to benefit the power system.

The common-level protection detects problems affecting all modules, and as such, generally requires bypassing all modules with the bypass breaker. The module-level protection detects problems affecting a single-module and as such, may only initiate protective actions within the affected module. The thyristor switches allow for bypassing individual modules by continuous gating the thyristors, and this is an effective protective action for many potential internal failures (e.g., capacitor failure). However, for some serious problems within a module (e.g., varistor failure), protective actions may involve bypassing all modules with the bypass breaker.

3.3 Operation of the TCSC

3.3.1 Basic principles [56]

A simple understanding of TCSC functioning can be realized by analyzing the behavior of the circuit shown in Figure 3.2 which consists of a variable inductor connected in parallel with a fixed capacitor. The equivalent impedance, Z_{eq}, of this LC combination is expressed as:

$$Z_{eq} = -j \frac{1}{\omega C - \dfrac{1}{\omega L}}$$

(3.1)

The impedance of the capacitor alone, however, is given by $X_c = -j\dfrac{1}{\omega C}$.
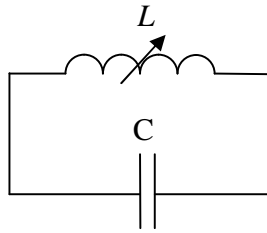
Figure 3.2: A variable inductor connected in parallel with a fixed capacitor.

If $\omega C - \left(\dfrac{1}{\omega L}\right) > 0$ or, in other words, $\omega L > \dfrac{1}{\omega C}$, the reactance of the fixed capacitor is less than that of the parallel-connected variable reactor and that this combination provides a variable-capacitive reactance are both implied. Moreover, this inductor increases the equivalent-capacitive reactance of the LC combination above that of the fixed capacitor.

If $\omega C - \left(\dfrac{1}{\omega L}\right) = 0$, a resonance develops that results in an infinite-capacitive impedance.

If, however, $\omega C - \left(\dfrac{1}{\omega L}\right) < 0$, the LC combination provides inductance above the value of the fixed inductor. This situation corresponds to the inductive-vernier mode of the TCSC operation.

In the variable-capacitive mode of the TCSC, as the inductive reactance of the variable inductor is increased, the equivalent-capacitive reactance is gradually decreased. The minimum equivalent-capacitive reactance is obtained for extremely large inductive reactance or when the variable inductor is open-circuited, in which the value is equal to the reactance of the fixed capacitor itself.

The behavior of the TCSC is similar to that of the parallel LC combination. The difference is that the LC-combination analysis is based on the presence of pure sinusoidal voltage and current in the circuit, whereas in the TCSC, the voltage and current are not sinusoidal because of the thyristor switchings. The analysis in this case is presented in Section 3.4.

3.3.2 Modes of TCSC operation

There are three modes of TCSC operation:

1. Bypassed-Thyristor Mode: the thyristors are made to fully conduct resulting in a continuous sinusoid of flow current through the thyristor valves (Figure 3.3(a)). The TCSC module behaves like a parallel capacitor-inductor combination. The net current through the module, however, is inductive, for the susceptance of the reactor is chosen to be greater than that of the capacitor.

2. Blocked-Thyristor Mode: the firing pulses of the thyristor valves are blocked. The TCSC module is reduced to a fixed capacitor (Figure 3.3(b)).

3. Partially Conducting Thyristor or Vernier Mode: This mode allows the TCSC to behave either as a continuously controllable capacitive reactance or as a continuously controllable inductive reactance. It is achieved by varying the thyristor-pair firing angle in an appropriate range. In practice, the TCSC operates only in the *capacitive-vernier-control* mode. In such a mode, the thyristors are fired when the capacitor voltage and the capacitor current have opposite polarity. This condition causes the reactor current to have a direction opposite to that of the capacitor current, thereby, resulting in a loop-

current flow in the TCSC controller. The loop current increases the voltage across the fixed capacitor, effectively enhancing the equivalent capacitive reactance and the series compensation level for the same value of line current. To preclude resonance, the firing angle α of the forward facing thyristor, as measured from the positive reaching a zero crossing of the capacitor voltage, is constrained in the range $\alpha_{\min} \leq \alpha \leq 180^{\circ}$. This constraint provides a continuous vernier of the TCSC module reactance. The loop current increases as α is decreased from 180° to $\alpha_{\min}$. The maximum TCSC reactance permissible with $\alpha = \alpha_{\min}$ is typically two-and-half to three times the capacitor reactance at fundamental frequency.

(a)

(b)

(c)
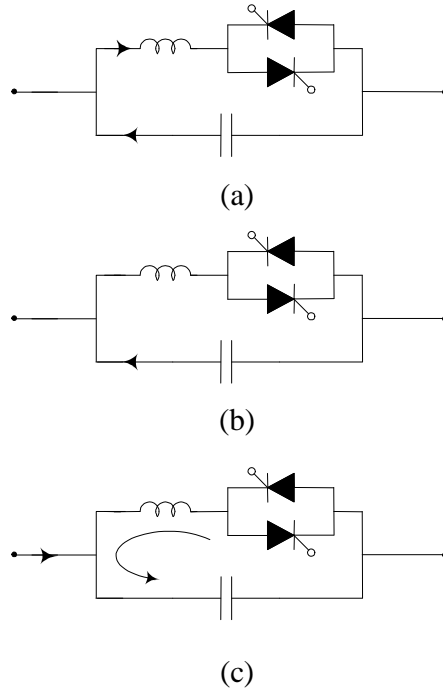
Figure 3.3: TCSC modes of operation: (a) bypassed-thyristor mode, (b) blocked-thyristor mode, (c) vernier mode.

3.4   Analysis of the TCSC

The following "approximate" analysis of TCSC operation in the vernier-control mode is performed based on the simplified TCSC circuit shown in Figure 3.4 [57]. Transmission line current is assumed to be the independent-input-variable and is modeled as an external current source, $i_s(t)$. Moreover, it is assumed that the line current is sinusoidal, as field tests have demonstrated that very few harmonics exist in the line current [13].
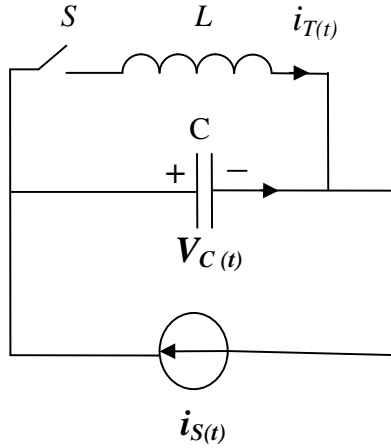
Figure 3.4: A simplified TCSC circuit.

The current through the fixed-series capacitor, C, is expressed as

$$C\frac{dv_c}{dt} = i_s(t) - i_T(t).u \tag{3.2}$$

The switching variable u is equal to 1 when the thyristor valves are conducting (switch S is closed). When the thyristor valves are blocked (switch S is open), $u = 0$. The thyristor current, $i_T(t)$ can be described as

$$L\frac{di_T}{dt} = v_c.u \tag{3.3}$$

Let the line current, $i_s(t)$ be represented by

$$i_s(t) = I_m \cos\omega t \tag{3.4}$$

Equations (3.3) and (3.4) can be solved with the knowledge of the instants of switching. In equidistant firing-pulse control, for balanced TCSC operation, the thyristors are switched on twice in each cycle of the line current at instants t_1 and t_3 given by

$$t_1 = -\frac{\beta}{\omega} \tag{3.5}$$

$$t_3 = \frac{\pi - \beta}{\omega} \tag{3.6}$$

where β is the angle of advance (before the forward voltage becomes zero). Or,

$$\beta = \pi - \alpha; \qquad 0 < \beta < \beta_{max} \tag{3.7}$$

43

The firing angle α is generated using a reference signal that can be in phase with the capacitor voltage. The thyristor switch S turns off at the instant t_2 and t_4 defined as:

$$t_2 = t_1 + \frac{\sigma}{\omega} \tag{3.8}$$

$$t_4 = t_3 + \frac{\sigma}{\omega} \tag{3.9}$$

where σ is the conduction angle and,

$$\sigma = 2\beta \tag{3.10}$$

Solving the TCSC equations (3.2 to 3.4) results in the steady-state thyristor current i_T, as:

$$i_T(t) = \frac{k^2}{k^2 - 1} IMG \left[\cos \omega t - \frac{\cos \beta}{\cos k\beta} \cos \omega_r t \right]; \quad -\beta \leq \omega t \leq \beta \tag{3.11}$$

where

$$\omega_r = \frac{1}{\sqrt{LC}} \tag{3.12}$$

$$k = \frac{\omega_r}{\omega} = \sqrt{\frac{1}{\omega L} \frac{1}{\omega C}} = \sqrt{\frac{X_C}{X_L}} \tag{3.13}$$

and X_C is the nominal reactance of the fixed capacitor only. The steady-state capacitor voltage at the instant $\omega t = -\beta$ is expressed by:

$$v_{C1} = \frac{IMG \ X_C}{k^2 - 1} (\sin \beta - k \cos \beta \tan k\beta) \tag{3.14}$$

At $\omega t = \beta$, $i_T = 0$, and the capacitor voltage is given by:

$$v_C(\omega t = \beta) = v_{C2} = -v_{C1} \tag{3.15}$$

The capacitor voltage is finally obtained as:

$$v_C(t) = \frac{IMG \ X_C}{k^2 - 1} \left[-\sin \omega t + k \frac{\cos \beta}{\cos k\beta} \sin \omega_r t \right]; \quad -\beta \leq \omega t \leq \beta \tag{3.16}$$

$$v_C(t) = v_{C2} + IMG \ X_C(\sin \omega t - \sin \beta); \quad \beta < \omega t < \pi - \beta \tag{3.17}$$

Because the nonsinusoidal capacitor voltage, v_C, has odd symmetry about the axis $\omega t = 0$, the fundamental component, V_{CF}, is obtained as:

44

$$V_{CF} = \frac{4}{\pi} \int_0^{\pi/2} v_c(t) \sin \omega t \, d(\omega t) \tag{3.18}$$

The equivalent TCSC reactance is computed as the ratio of V_{CF} to I_m:

$$
\begin{aligned}
X_{TCSC} = \frac{V_{CF}}{I_m} = X_C &- \frac{X_C^2}{(X_C - X_L)} \frac{2\beta + \sin 2\beta}{\pi} \\
&+ \frac{4X_C^2}{(X_C - X_L)(k^2 - 1)} \frac{\cos^2 \beta \, (k \tan k\beta - \tan \beta)}{\pi}
\end{aligned}
\tag{3.19}
$$

The net reactance of the TCSC in per unit of X_C, denoted by $X_{net} (= X_{TCSC}/X_C$, sometimes called the boost factor) can be expressed as:

$$
\begin{aligned}
X_{net} = 1 &- \frac{X_C}{(X_C - X_L)} \frac{\sigma + \sin \sigma}{\pi} + \frac{4X_C}{(X_C - X_L)} \frac{\cos^2 0.5\sigma}{(k^2 - 1)} \\
&\cdot \frac{(k \tan 0.5\sigma \, k - \tan 0.5\sigma)}{\pi}
\end{aligned}
\tag{3.20}
$$

Because the TCSC is used mainly as a capacitive device, the convention is to define positive reactance as capacitive and negative reactance as inductive. As an example, $X_{net} = +2$ implies that the thyristors are fired so that the resulting circulating current in the fixed capacitor – thyristor controlled reactor loop causes a 60-Hz voltage of $2X_C I_{line}$ p.u. to appear across the fixed capacitor, which lags the line current by 90°.

The traditional boost control method (constant firing angle delay (CFAD)) controls the firing angle $\beta = \pi - \alpha$ of the thyristor. A rather non-linear relationship exists between the boost factor kB and the steady state conduction angle $\sigma = 2\beta$, making kB very sensitive to the instant of triggering when the TCSC operates at a high boost factor. Further, during transients, a complicated dynamic characteristic governs the relationship between the firing angle and the conduction angle. Instead of controlling the thyristor firing angle, another control scheme, named 'Synchronous Voltage Reversal' (SVR), is being used. It aims to control the instant when the capacitor voltage crosses zero [58], [59]. This eliminates the non-linearity in the boost control and results in that the TCSC apparent impedance at subsynchronous frequencies appears as inductive. Furthermore, at low boost factors, SVR controlled TCSC can provide much better SSR damping than conventional CFAD control [60]. In the studies conducted in this thesis, the SVR control is used.

3.5 The Hybrid Single-Phase-TCSC Compensation Scheme

Figure 3.5 shows a phase imbalanced hybrid series capacitive compensation scheme using a TCSC [29], [61]. In such a scheme, the series capacitive compensation in one phase is created using a single-phase TCSC in series with a fixed capacitor (C_c), and the other two phases are compensated by fixed series capacitors (C). The TCSC control is initially set such that its equivalent compensation at the power frequency combined with the fixed capacitor C_c yield a resultant compensation equal to the other two phases. Thus, the phase balance is maintained at the power frequency while at any other frequency, a phase imbalance is created. Mathematically, this can be explained as follows:

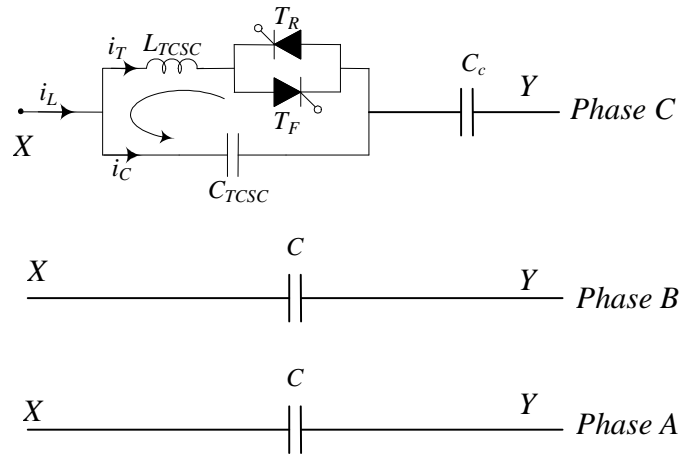**Figure 3.5:** The hybrid single-phase TCSC compensation scheme.

1) At the power frequency, the series reactance between buses X and Y, in Figure 3.5, in phases a, b, and c are given by:

$$X_a = X_b = \frac{1}{j\omega_o C} \tag{3.21}$$

$$X_c = \frac{1}{j\omega_o C_c} - jX_{TCSCo} \tag{3.22}$$

where $-jX_{TCSCo}$ is the effective capacitive reactance of the TCSC at the power frequency such that $X_a = X_b = X_c$.

2) During any other frequency, f_e, including subsynchronous frequencies,

$$X_c = \frac{1}{j\omega_e C_c} - jX_{TCSC_o} - j\Delta X_{TCSC} \tag{3.23}$$

The first terms in (3.22) and (3.23) are different because of the difference in frequency. The third term in (3.23) represents the change in the effective capacitive reactance of the TCSC due to the action of the TCSC supplemental controller.

3.6   Modeling of the Single-Phase TCSC in the EMTP-RV

The single-phase TCSC is modeled in the EMTP-RV as a single module using an ideal thyristor pair and an RC snubber circuit as shown in Figure 3.6. A Phase Locked Loop (PLL) is used to extract phase information of the fundamental frequency line current, which will be used to synchronize TCSC operation. The thyristor gating control is based on the Synchronous Voltage Reversal (SVR) technique [58] - [60]. The TCSC impedance is measured in terms of a boost factor kB, which is the ratio of the apparent reactance of the TCSC seen from the line to the physical reactance of the TCSC capacitor bank. A positive value of kB is considered for capacitive operation. A low-pass filter based estimation algorithm is used to estimate the voltage and the current phasors. A boost measurement block performs complex impedance calculations for the boost factor of the TCSC as $kB = \text{Imag}\{\hat{v}_C / \hat{i}_C\}/ X_{CTCSC}$, where, $\hat{v}_C$ and $\hat{i}_C$ are the estimated phase voltage and current and X_{CTCSC} is the capacitive reactance of the TCSC capacitor branch at the fundamental frequency. A proportional-integral (PI) control based boost level controller is implemented to control the TCSC boost level to the desired value by adjusting the instant of the expected capacitor voltage zero crossing. The integral part of the controller helps in removing the steady state errors. The controller parameters were determined by performing repeated time domain simulations for the different operating conditions. This algorithm uses the difference between the actual boost level and the reference boost level (*err*) shown in Figure 3.6 as an objective function. The algorithm starts with arbitrary initial values for the control parameters and calculates the values of the objective function each time. The control parameters are incremented for the next iteration and the procedure is repeated until the objective function approaches a minimum value (below a threshold value). The procedure described above is widely used by industry for   tuning of controller parameters. The multiple simulations run

based tuning procedure similar to the above was reported in [62], [63]. The optimum values of the parameters obtained for the different compensation degrees are given in Appendix B.
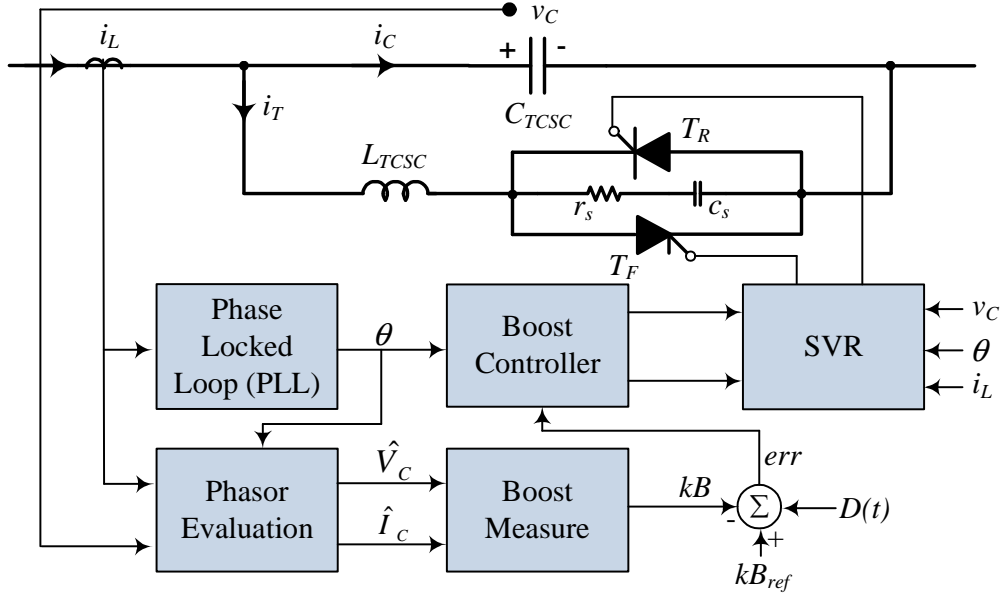

Figure 3.6: Block diagram of a TCSC controller.

In Figure 3.6, kB_{ref} is the TCSC boost level set point and $D(t)$ is the supplementary control signal for damping low frequency oscillations. The Synchronous Voltage Reversal block solves for angle γ from the non-linear relation, $u_{CZ} = X_o i_{LM}[\lambda\gamma - \tan(\lambda\gamma)]$, where u_{CZ} is the estimated capacitor voltage at the desired instant when the capacitor voltage zero crossing occurs, i_{LM} is the measured value of the line current i_L, X_0 is the TCSC capacitor reactance at the TCSC resonance frequency, λ is the ratio between the TCSC resonance frequency and the system fundamental frequency and γ is the angle difference between the firing time and the voltage zero-crossing. The value of γ is used to calculate the exact firing instants of the individual thyristors. The non-linear relationship between the boost factor and the thyristor firing angle α is shown in Figure 3.7.
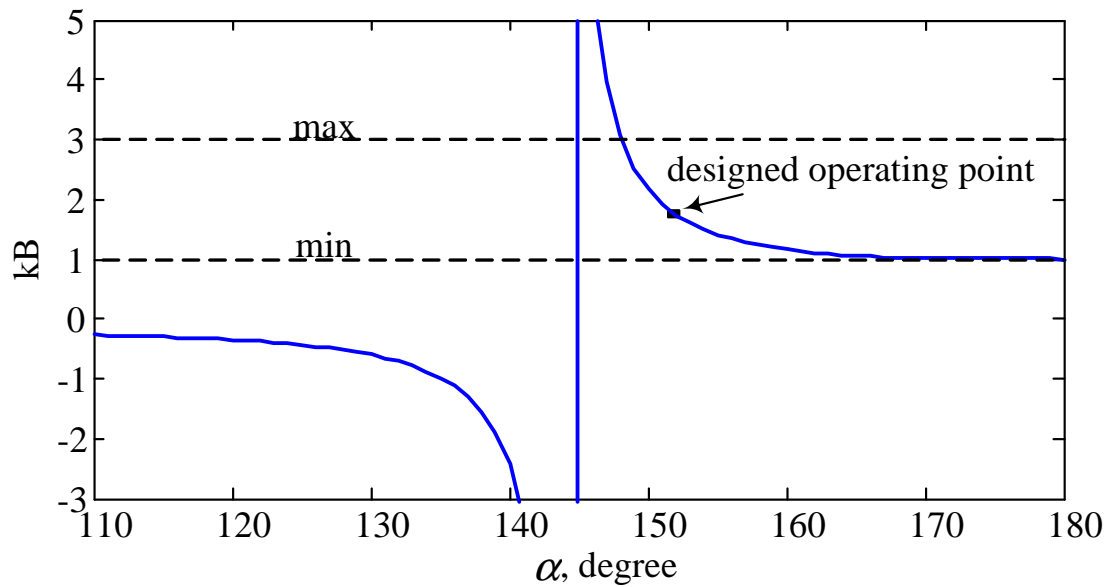
Figure 3.7: TCSC boost factor as a function of the thyristor firing angle α.

The most striking feature of the TCSC is that it behaves like an inductor at subsynchronous frequencies. This prevents the occurrence of a series resonance within a certain critical frequency band. On the other hand, the TCSC behaves like a capacitor at the power frequency. The transition of the virtual reactance of the TCSC from inductive to capacitive outside the subsynchronous frequency band is achieved by means of a reactance controller (like the SVR technique), providing a controllable capacitive reactance around the power frequency as shown in Figure 3.8 [64]. The details of the SVR algorithm are given in [58], [59].
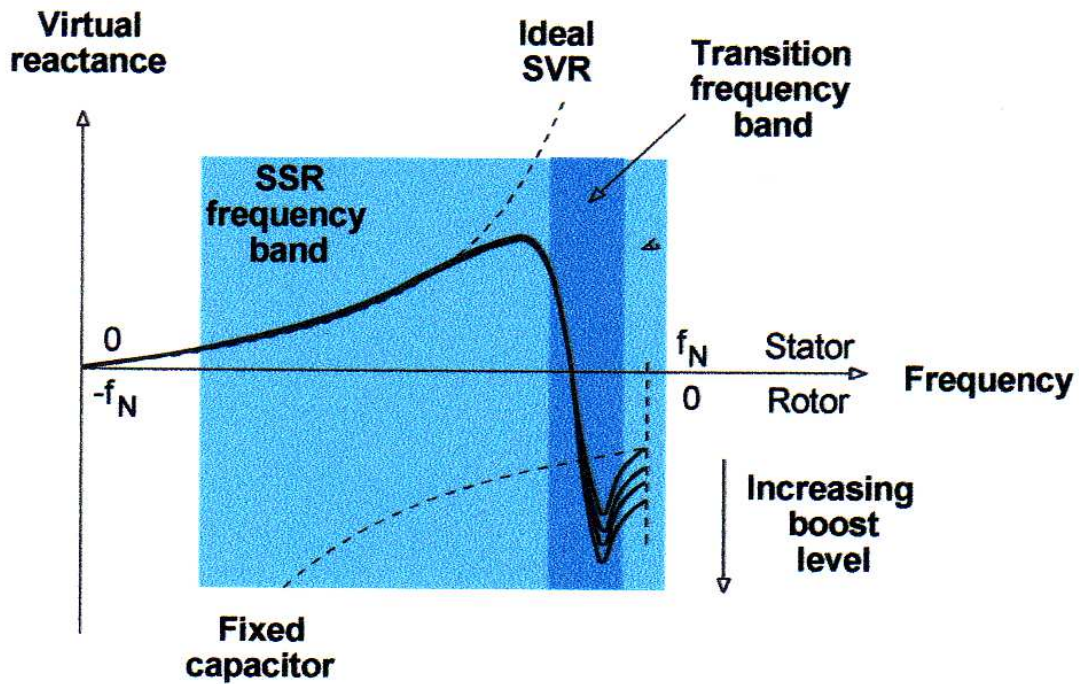
Figure 3.8: Effect of the SVR technique on the virtual reactance of the TCSC.

3.7 Summary

This chapter presents the description, basic principles and the derivation of the mathematical model of the TCSC. Modeling the hybrid single-phase TCSC in the ElectroMagnetic Transient Program (EMTP-RV) is also presented. This model is incorporated in the system under study (Figure 2.1) replacing the fixed compensations in lines L_1 and L_2. The effectiveness of the hybrid single-phase compensation scheme in damping power system oscillations is investigated in the next chapter.

Chapter 4

DAMPING POWER SYSTEM OSCILLATIONS USING PHASE IMBALANCE SERIES CAPACITIVE COMPENSATION SCHEME AND DFIG-BASED WIND FARMS

4.1   General

The control offered by the TCSC is an 'impedance' type control, i.e. the inserted voltage is proportional to the line current. This type of control normally is best suited to applications in power flow corridors, where a well-defined phase angle difference exists between the ends of the transmission line to be compensated and controlled. As a result, transient stability improvement and the increase in the maximum real power transmitted can be achieved. The TCSC and the BtB converters of DFIG-based wind farms can also be used, however, to provide additional damping to the electromechanical (0.5 - 2 Hz) power oscillations as they provide fast speed of response and executes any switching patterns without such restrictions that might apply for mechanical switches. This is accomplished by providing these devices with supplemental controls.

In this chapter, the effectiveness of supplemental controls of the DFIG-based wind farms and the hybrid single-phase-TCSC compensation scheme (Scheme I) in damping power system oscillations is investigated. For this purpose, Scheme I is assumed to be installed in the double circuits of lines L_1 near bus 1 replacing the fixed series capacitor compensation as shown in Figure 4.1. Moreover, it is assumed that, normally, each TCSC provides 50% of the total capacitive compensation and the disturbance is a three-cycle, three-phase fault at bus 4. Furthermore, the performance of the scheme and the DFIG-based wind farm supplemental controllers will be compared to the case with only fixed capacitor compensation in L_1 and L_2

(Fixed C) as well as to the case when the DFIG-based wind farm supplemental controllers are not activated (TCSC only).
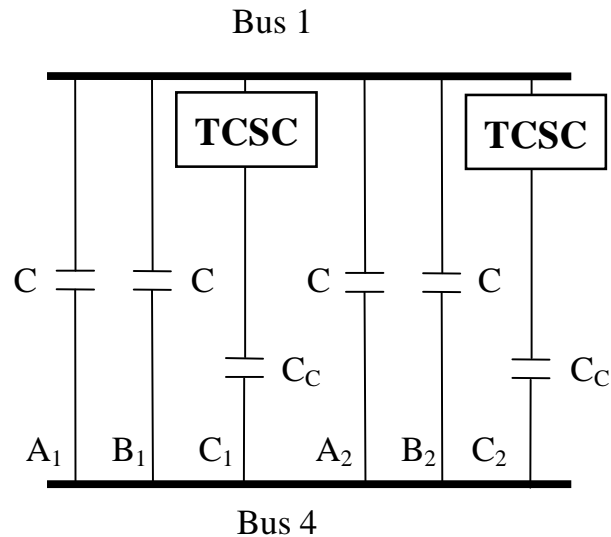
Bus 1

Figure 4.1: Scheme I is installed in the double circuits of L_1.

4.2 TCSC and DFIG-Based Wind Farm Power Oscillations Damping Controllers

As the real power flow in a transmission line is proportional to the inverse of the total line reactance, power oscillations damping can be achieved by properly modulating the TCSC reactance. In the DFIG-based wind farms, damping is achieved by adding a supplementary signal, U_S, in either the real power control loop of the RSC or in the reactive power control loops of the RSC/GSC as shown in Figure 4.2 [65].
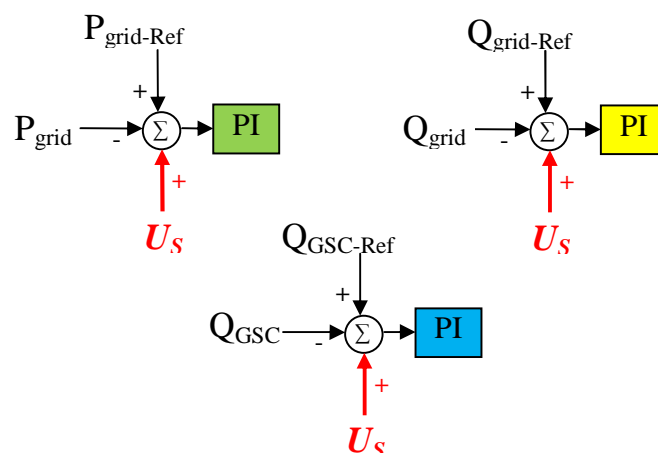
Figure 4.2: Introducing an SSR supplementary control signal in the real control loop of the RSC or in the reactive power control loops of the RSC/GSC.

The traditional type of controller for Power Oscillations Damping (POD) purposes uses cascade-connected washout filters and linear lead-lag compensators to generate the desired reactance modulation signal. The purpose of the wash-out filters is to eliminate the average and extract the oscillating part of the input signal. The lead-lag compensators provide the desired phase shift at the oscillations frequency. Such a controller is illustrated in Figure 4.3 [25], [66], [67]. In some situations, a simple controller consists of only the washout filters can have a better performance than that of the lead-lag controller. Such a controller, shown in Figure 4.4 can be regarded as a proportional type controller.
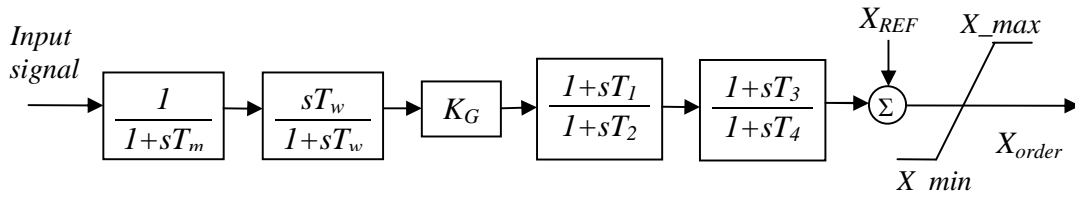
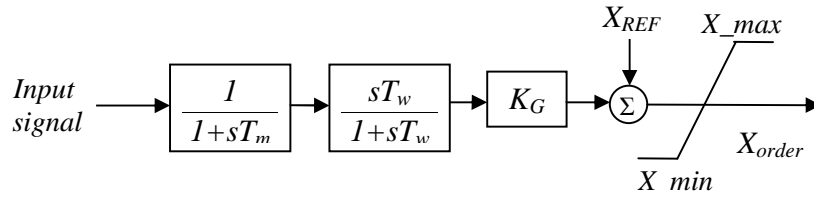**Figure 4.3:** Structure of a lead-lag POD controller.

Figure 4.4: Structure of a simple POD controller.

The selection of the appropriate input (stabilizing) signal is an important issue in the design of an effective and robust controller. The selected input signal must yield correct control action when a severe fault occurs in the system. As an example, it was reported in [68] that if the real power is used as input signal of a pure derivative controller, the output control signal may cause negative damping effects in the presence of disturbances involving large changes in the generator power angles.

The input signals could be local (e.g. real power flows) or remote (e.g. load angles or speed deviations of remote generators). If a wide-area network of Synchronized Phasor Measurement (SPM) units is available, then the remote signals can be downloaded at the controller in real time without delay [69] - [73]. In the studies conducted in this thesis, it is assumed the availability of a wide-area network of Synchronized Phasor Measurement (SPM) units where the supplemental controller input (stabilizing) signals can be downloaded at the

controllers in real time without delay [70] - [73]. In this regard, generators 2 and 4 load angles, measured with respect to generator 1 (δ_{21} and δ_{41}) are selected, for "most" of the study cases, as the supplemental controller stabilizing signals for the TCSC and DFIG-based wind farms respectively. The selection of the stabilizing δ_{21} for the TCSC supplemental control is based on the detailed studies reported in [31] that conclude that such a stabilizing signal is the best one among other signals (other relative load angles, relative speeds and transmission line real power flows).

It is worth noting here that due to the inherent imbalance nature of hybrid single-phase-TCSC compensation scheme during transients, the design of supplemental controllers using classical linear control techniques would be very difficult, if not, virtually impossible to achieve. However, nonlinear control theories for Voltage-Sourced Converters and TCSC applications have been found to have a significant potential in recent years [74]. Some of the examples are; variable-structure controllers (VSCs), model reference adaptive controllers and self-tuning controllers.   VSCs are capable of maintaining a desired response characteristic almost independently of the system structure. The design of any of such controllers is, however, beyond the level of being a part of a Master's research project. In the studies conducted in this thesis, the supplemental controller parameters are determined by performing multiple time domain simulations with the aim of improving the transient responses of the system. In the case of multiple controllers, simultaneous tuning of the parameters of the controllers is performed to ensure that satisfactory dynamic and steady-state performances are met whilst minimizing or preventing undesirable interactions among controllers.

4.3 Effect of the Ratio X_{TCSC}/X_{Cc} (DFIG-Based Wind Farm Supplemental Controllers are Disabled)

The impact of the proportion of the single-phase-TCSC to the fixed capacitor reactance of its phase on the damping of the system oscillations is examined by changing the ratio X_{TCSC}/X_{Cc}. Table 4.1 shows the transfer function of the TCSC supplemental control after final tuning. Figure 4.5 illustrates the generator load angles and speeds, measured with respect to generator 1 load angle and speed and the transmission line real power flow transient time responses during and after fault clearing. As it can be seen from this figure, increasing the proportion of the single-phase-TCSC to the fixed capacitor reactance of its phase results in improving the damping of the system oscillations.   Choosing the value of such a proportion can
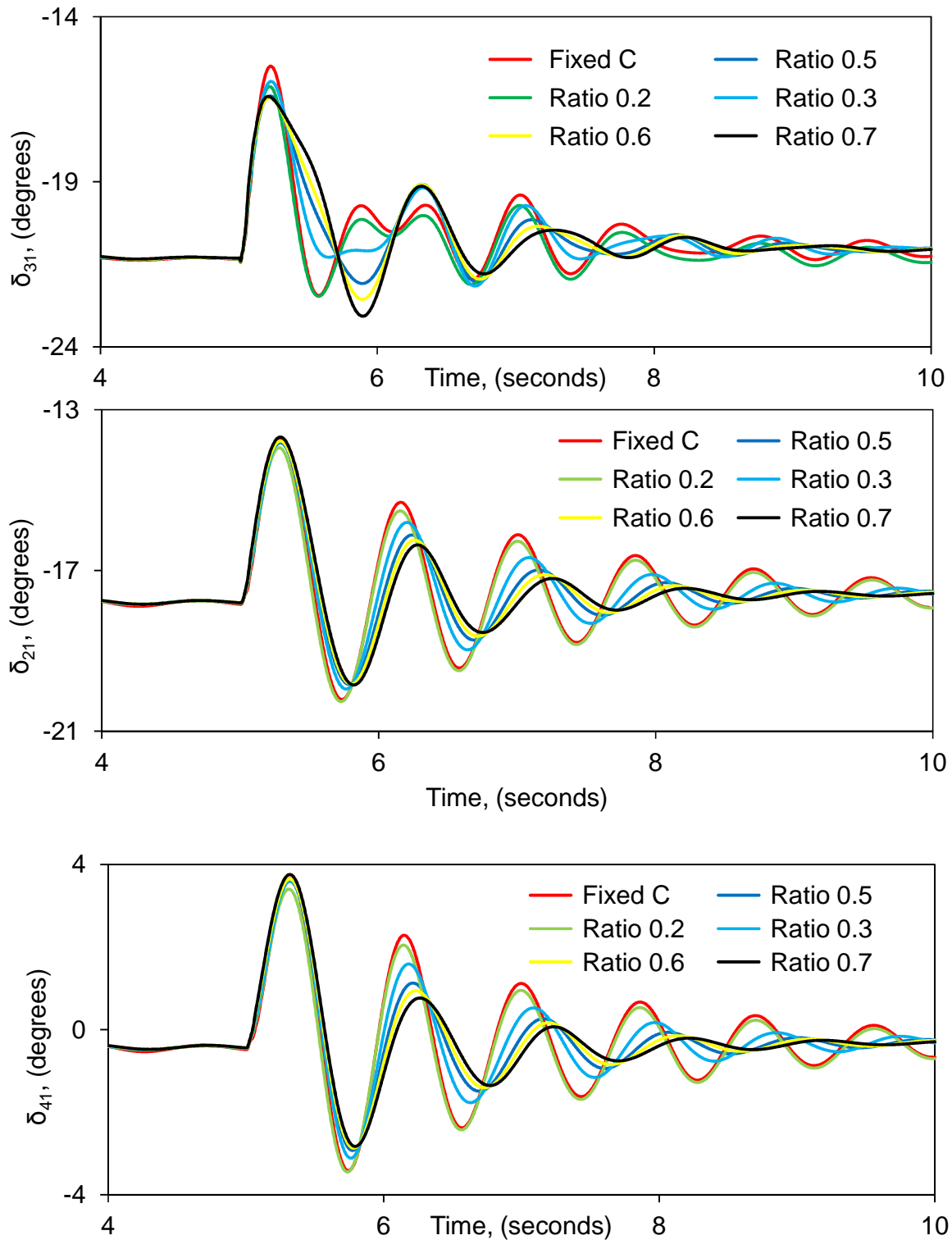
Figure 4.5: Effect of the ratio X_{TCSC}/X_{Cc} on the generator load angles and speeds, measured with respect to generator 1 load angle and speed as well as on the transmission line real power flows during and after clearing a 3-cycle, three-phase fault at bus 4.
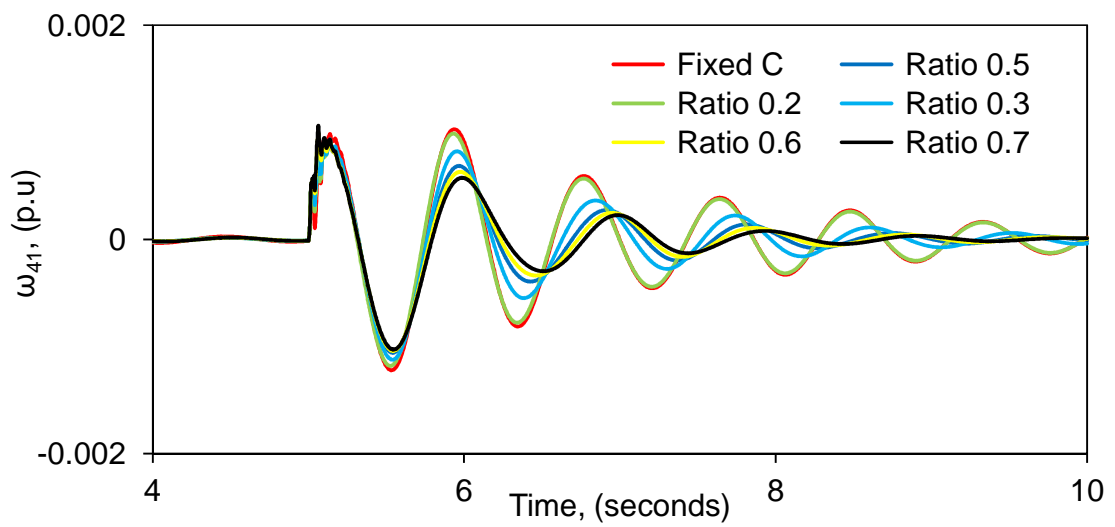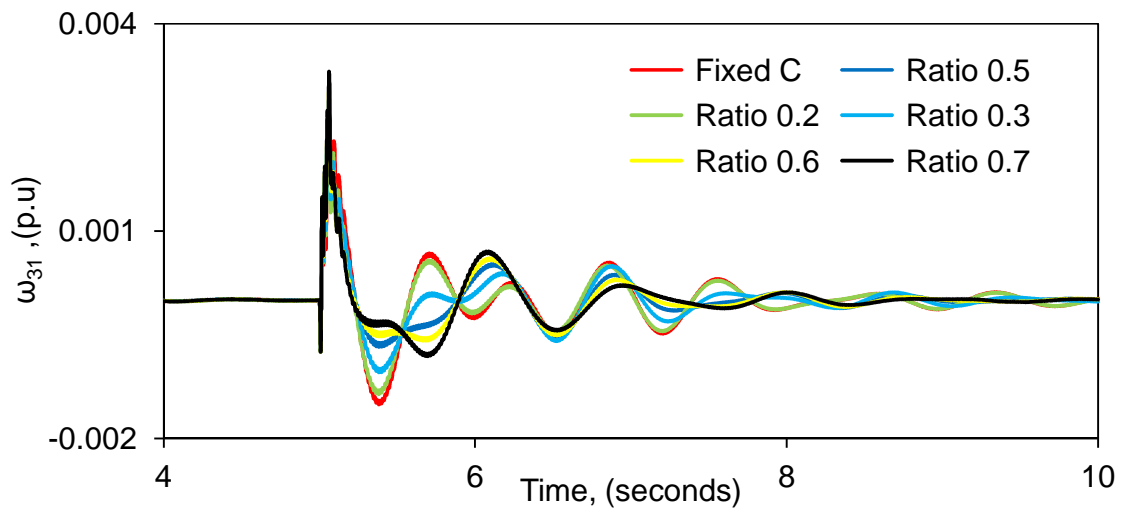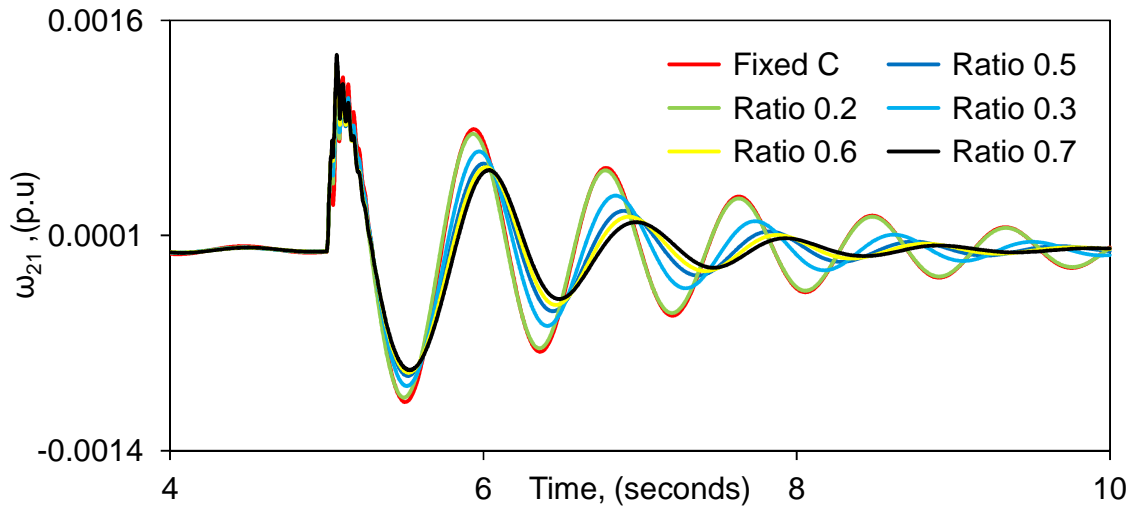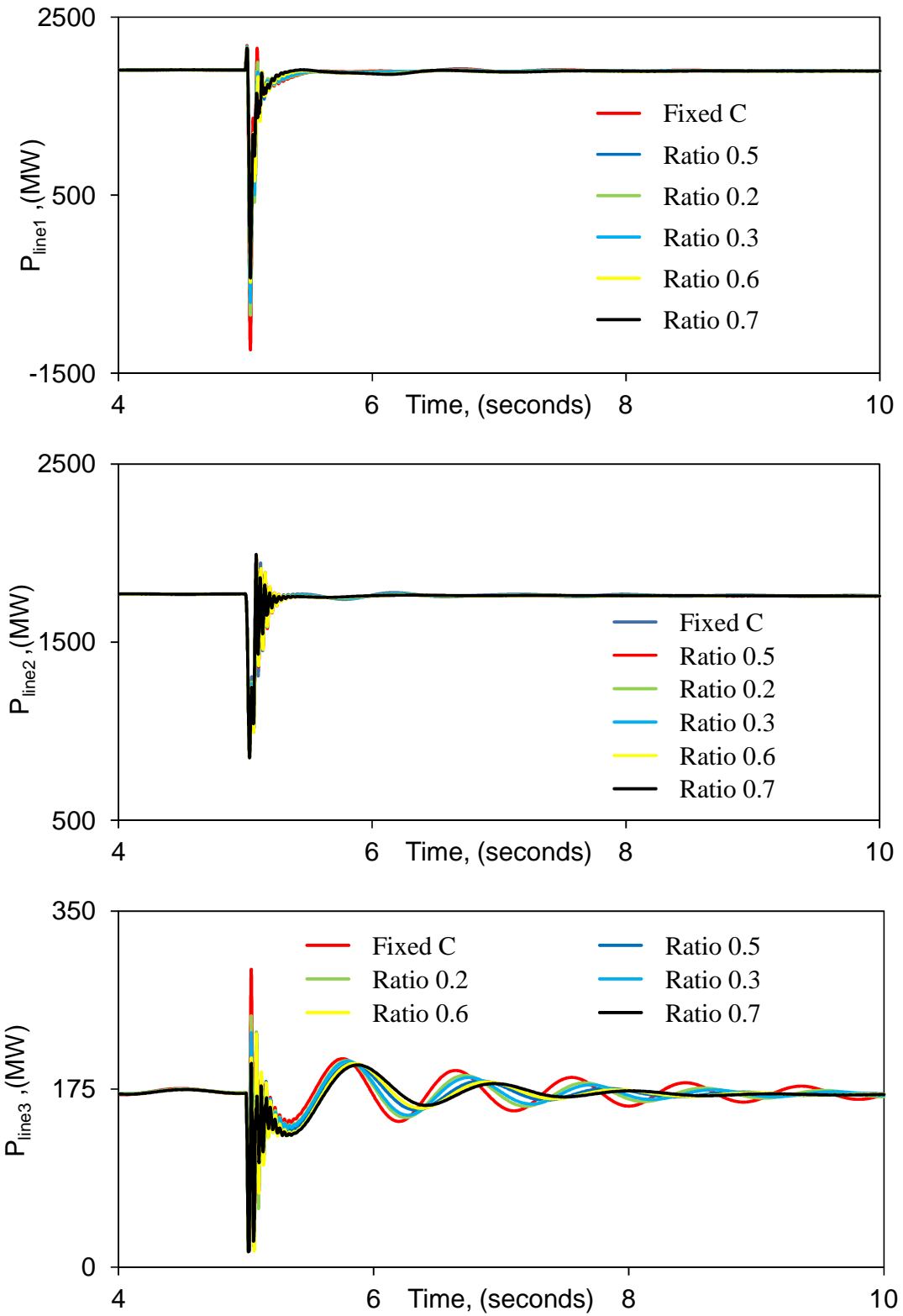
Figure 4.5: continued.
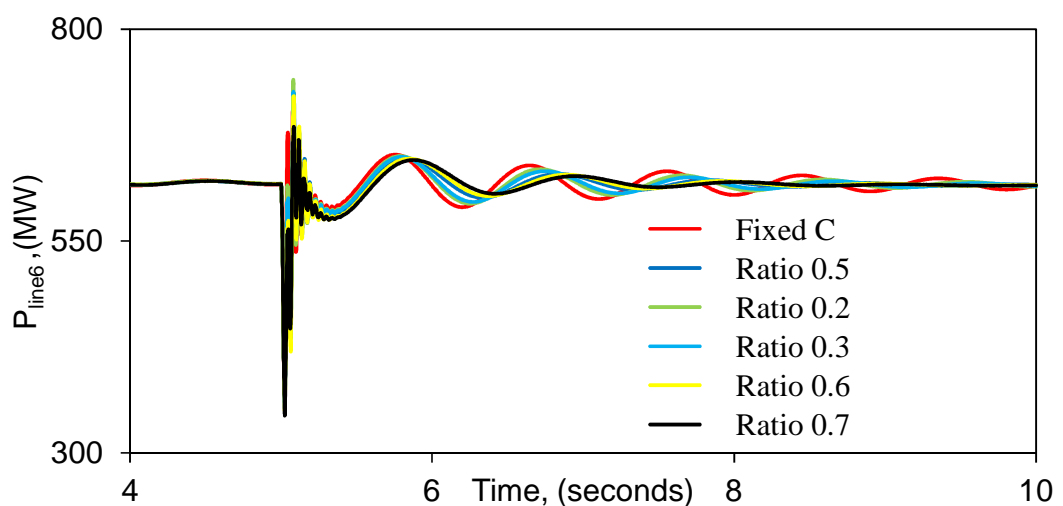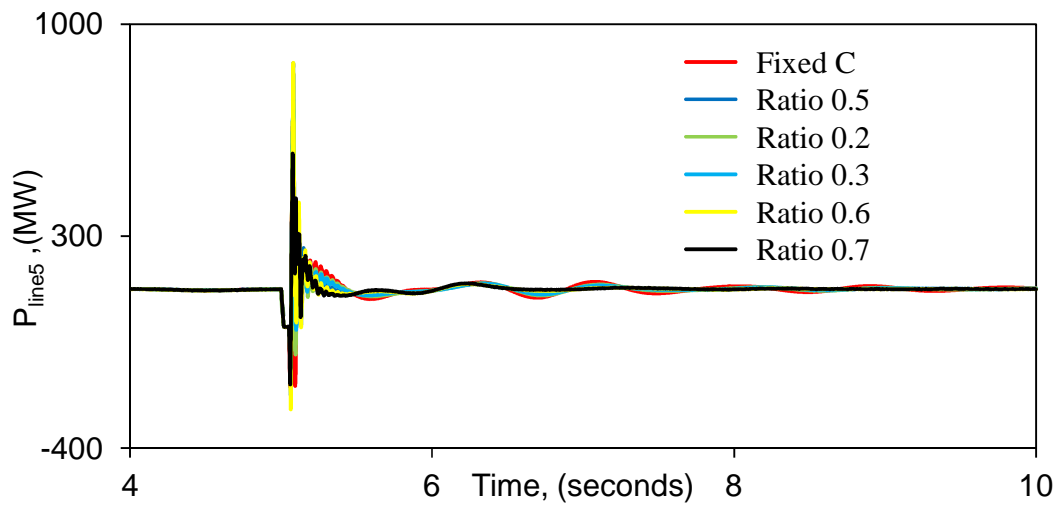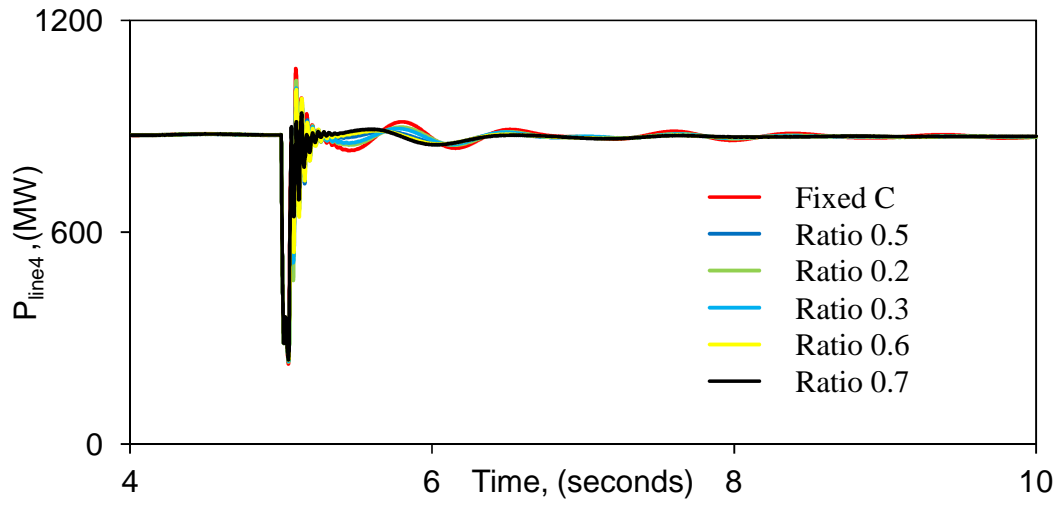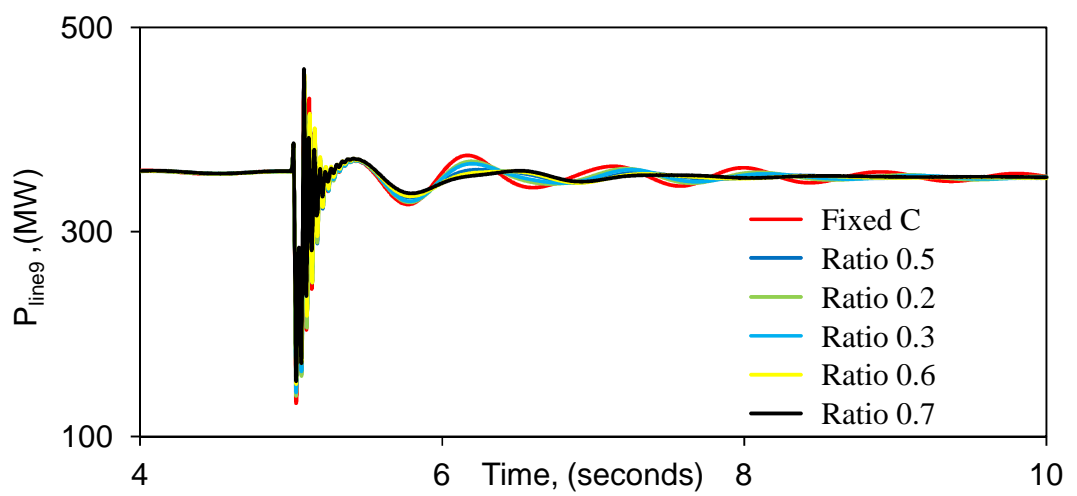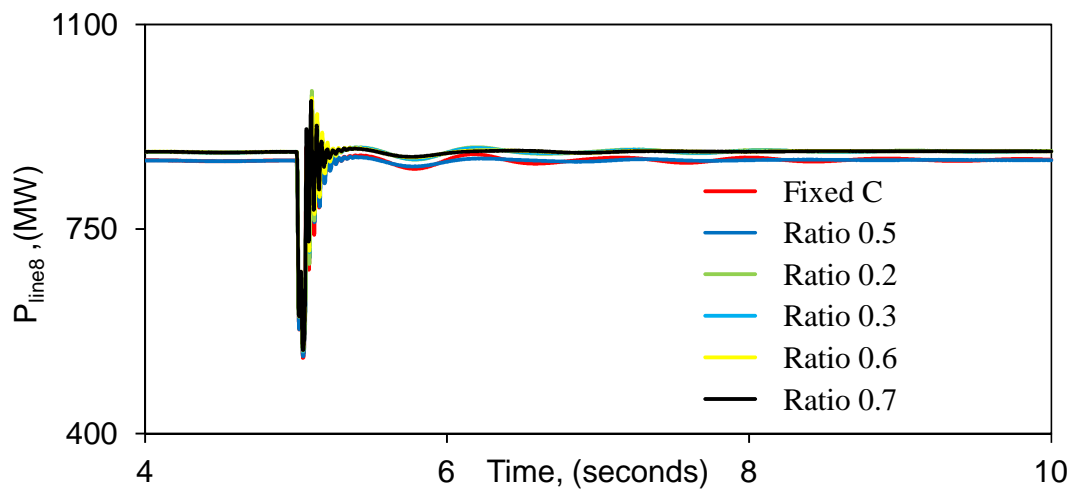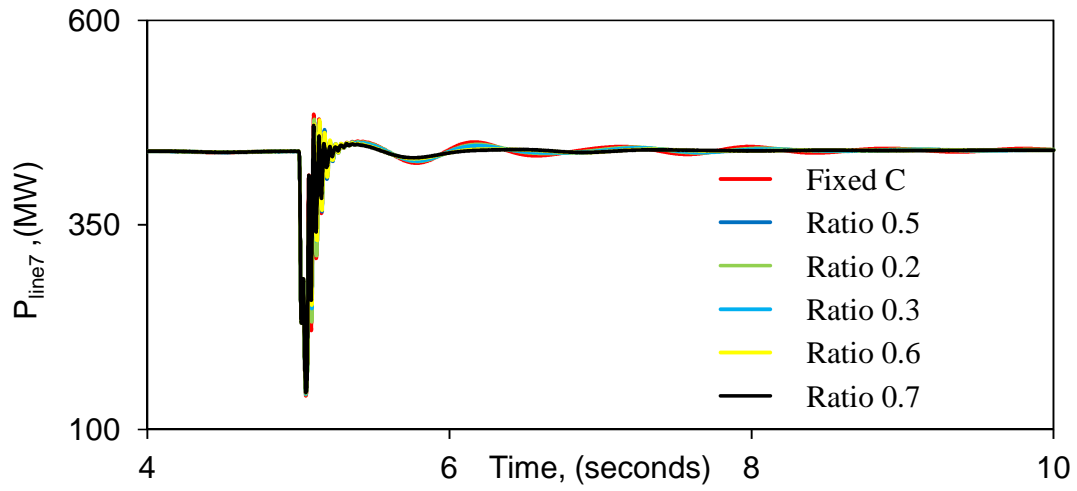
56

Figure 4.5: continued.

Figure 4.5: continued.

Figure 4.5: continued.

be considered as an optimization task between dynamic stability improvements and economical and reliability advantages of fixed series capacitors.

Table 4.1: Transfer functions of the hybrid TCSC compensation scheme supplemental controller.

X_{TCSC}/X_{Cc}	Transfer Function
0.2, 0.3, 0.5, 0.6, 0.7	$G_{TCSC}(s) = 0.25 \dfrac{10}{(s+10)} \dfrac{3s}{(3s+1)}$

4.4 DFIG-Based Wind Farm Supplemental Control is in the Reactive Power Control Loop of the GSC of Wind Farm A

Figure 4.6 illustrates the generator load angles and speeds, measured with respect to generator 1 load angle and speed, and the transmission line real power flow transient time responses during and after fault clearing. Figure 4.7 illustrates the time responses of wind farms A and B real and reactive powers, terminal voltage and the BtB dc voltage for the same case. Table 4.2 shows the transfer functions of the TCSC and wind farm A supplemental controls after final tuning. Comparing the responses for the case of Scheme I supplemental control alone (TCSC) to those for the case of Scheme I and the DFIG-based wind farm supplemental controls in Figure 4.6, the positive contribution of wind farm A supplemental control to the damping of the system oscillations is very clear. Moreover, comparing the reactive power responses of wind farms A and B in Figure 4.7, the supplemental control action is noticeable in the reactive power response of wind farm A.

Table 4.2: Transfer functions of the hybrid TCSC compensation scheme and wind farm A supplemental controllers (wind farm controller is in the Q control loop of the GSC).

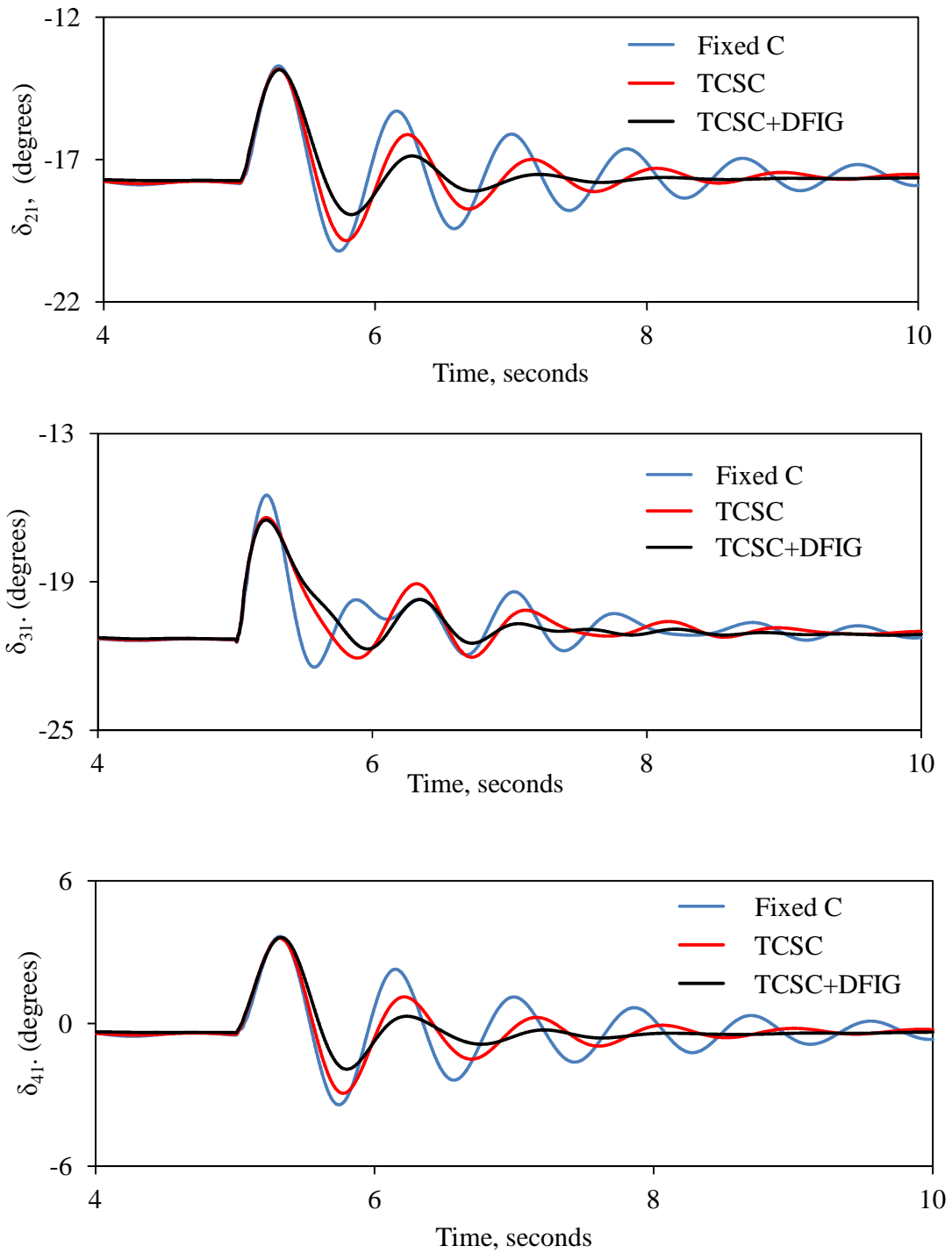|	Transfer Function
Hybrid TCSC Compensation Scheme	$G_{TCSC}(s) = 0.25 \dfrac{10}{(s+10)} \dfrac{3s}{(3s+1)}$
DFIG-Based Wind Farm A	$G_{DFIG\_Q\_Loop\_GSC}(s) = 0.25 \dfrac{s}{(s+1)} \dfrac{1}{(s+5)}$

Figure 4.6: Generator load angles and speeds, measured with respect to generator 1 load angle and speed, and transmission line real power flow transient time responses during and after clearing a 3-cycle, three-phase fault at bus 4 (supplemental control is in the Q control loop of the GSC of wind farm A).
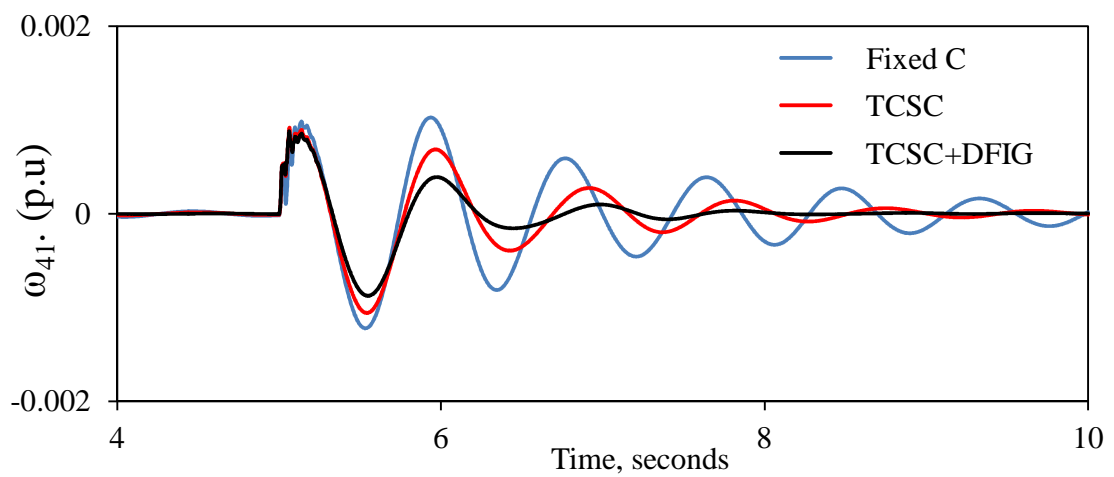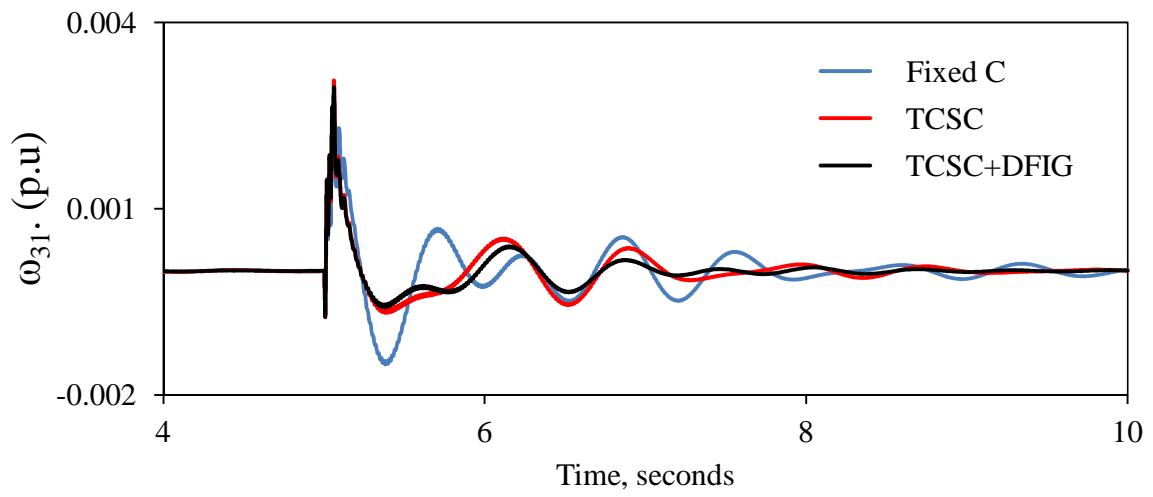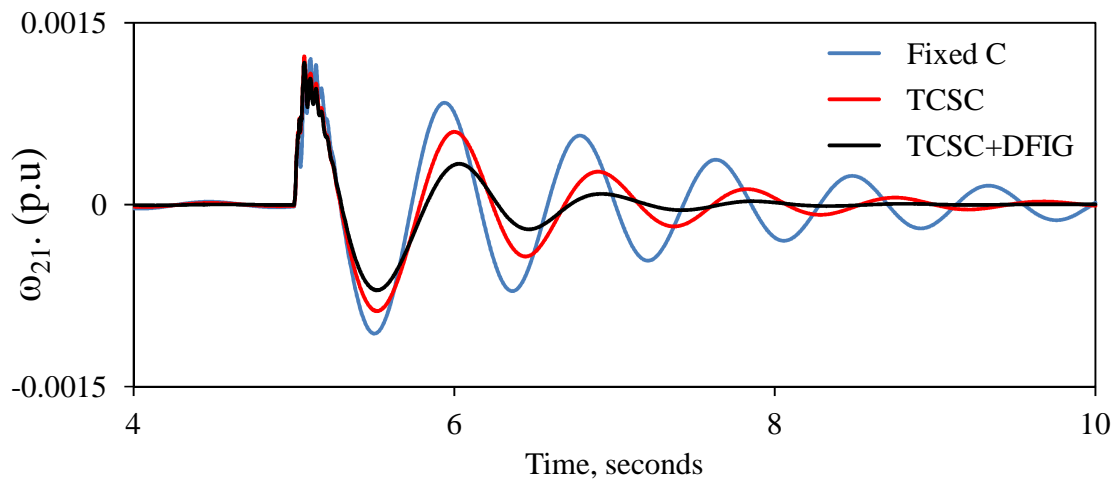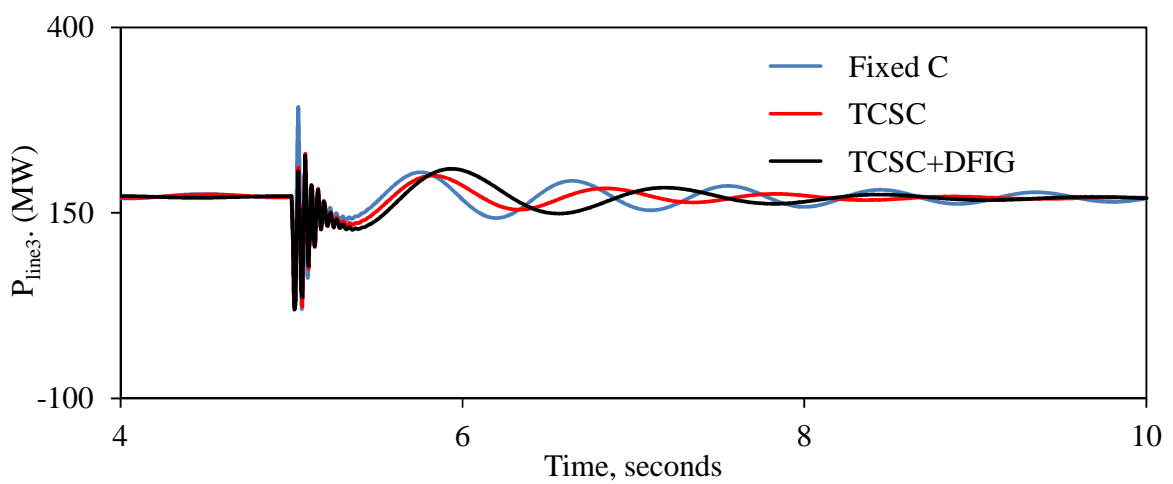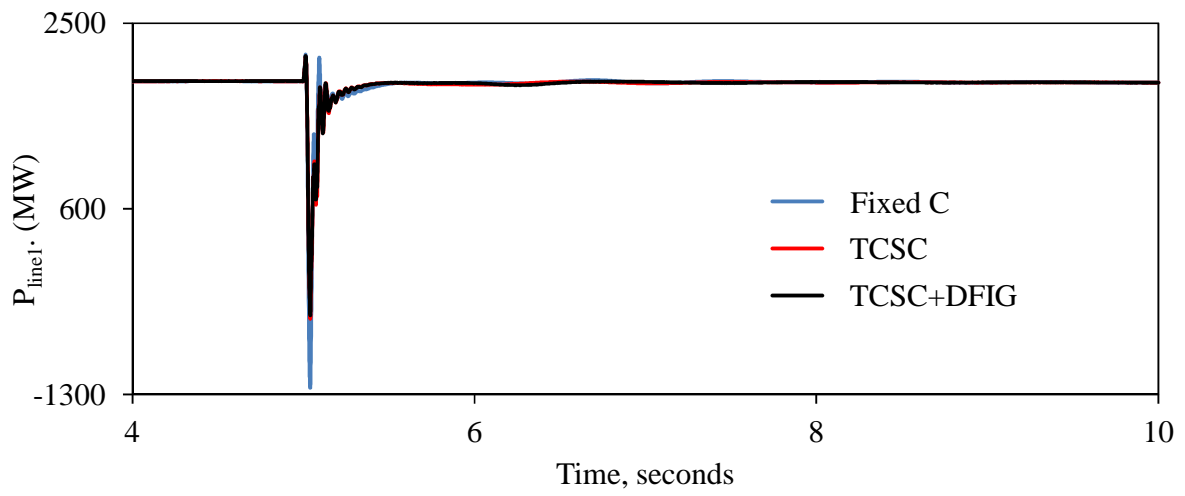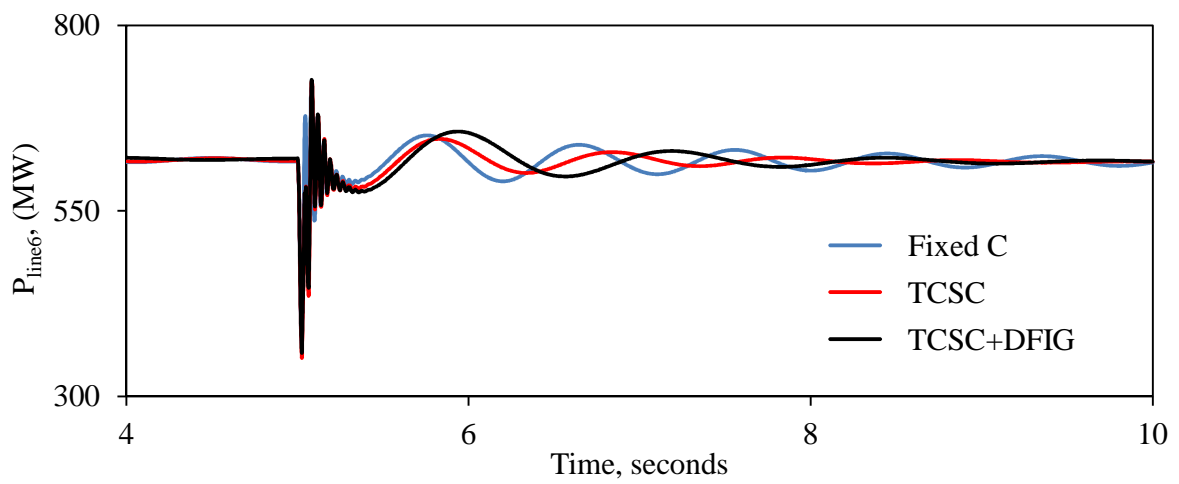
Figure 4.6: continued.
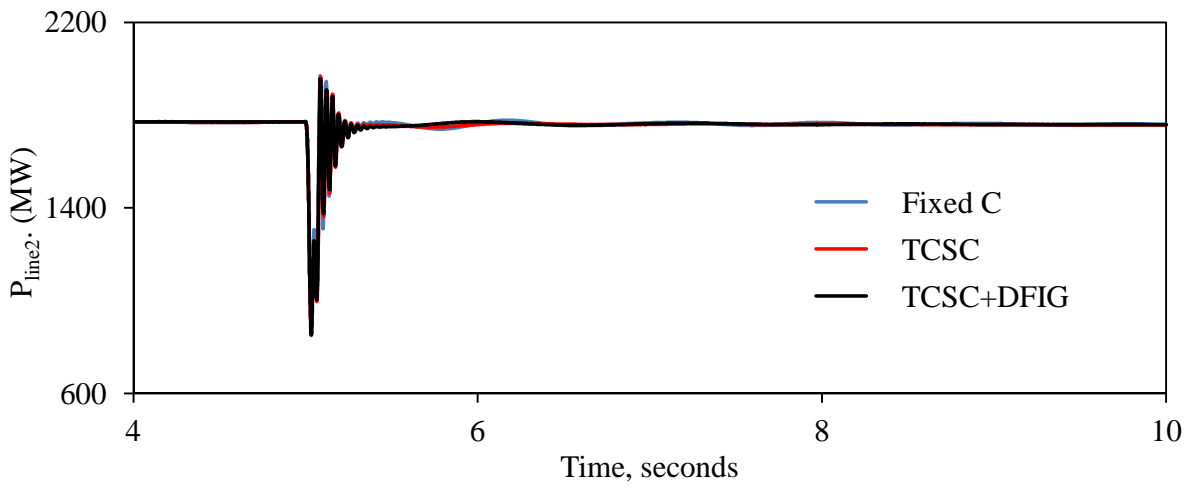
Figure 4.6: continued.
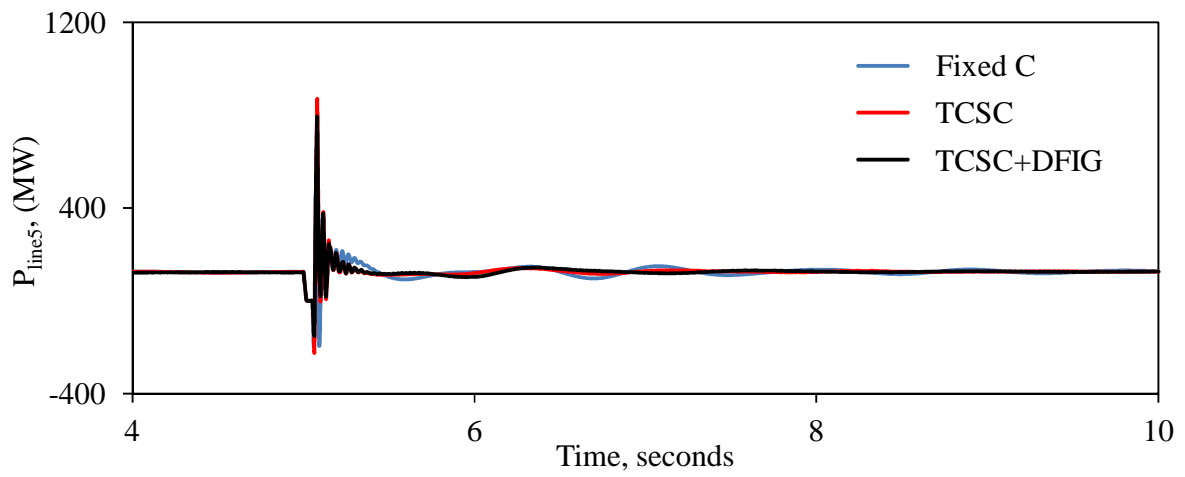
Figure 4.6: continued.

Figure 4.6: continued.

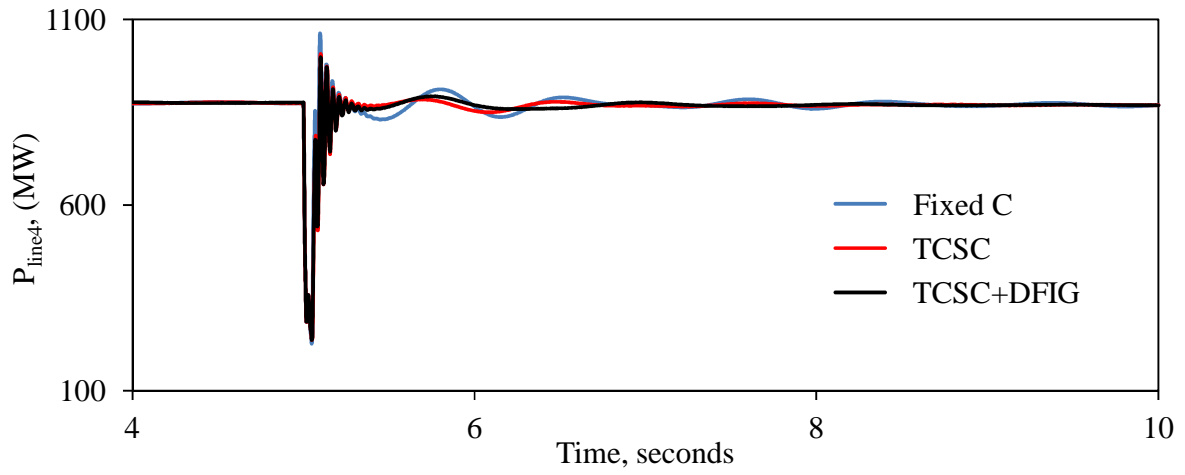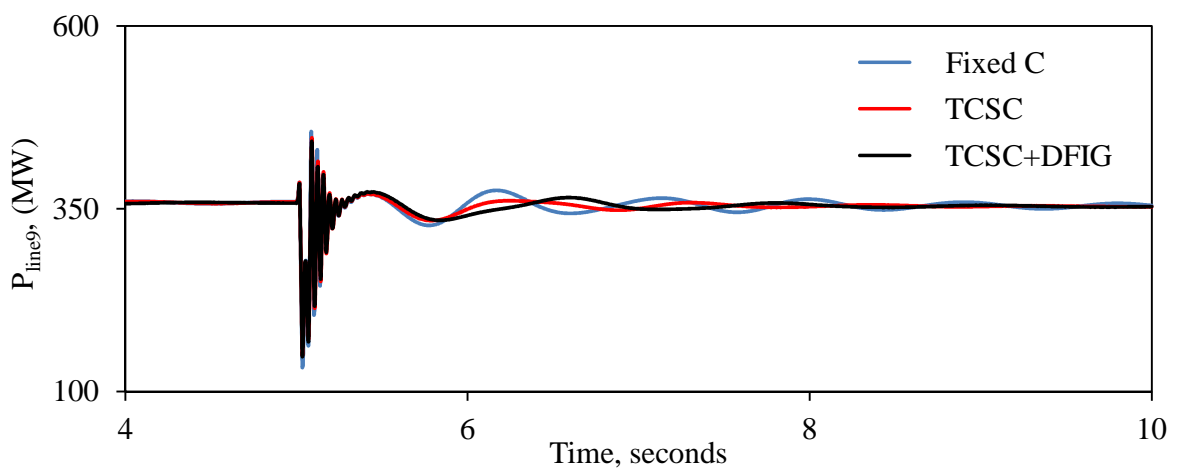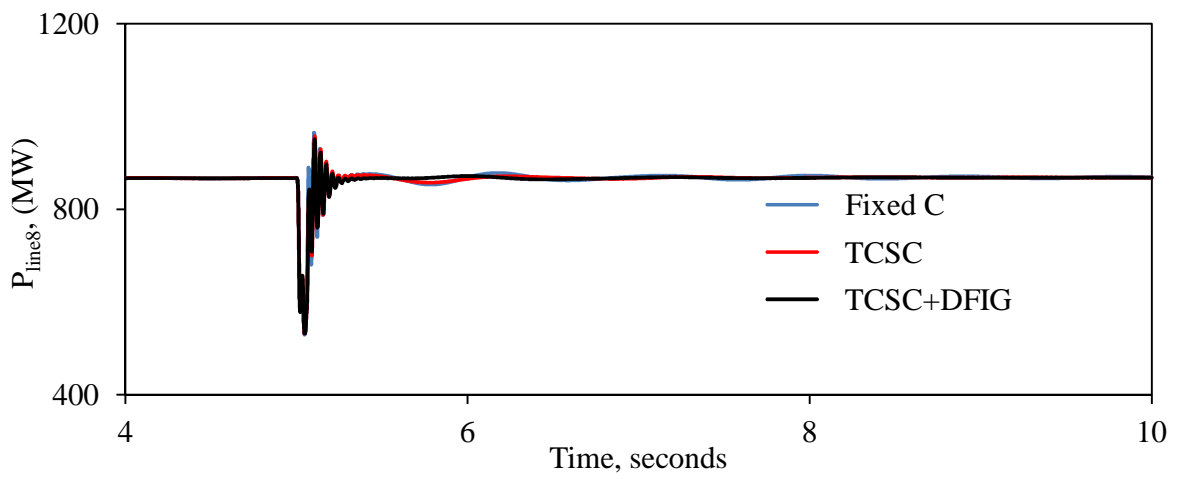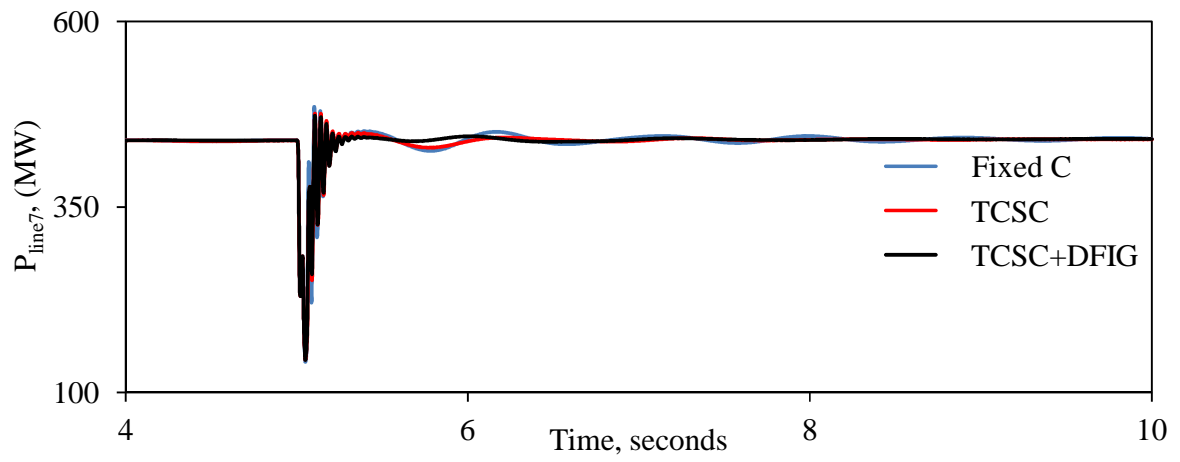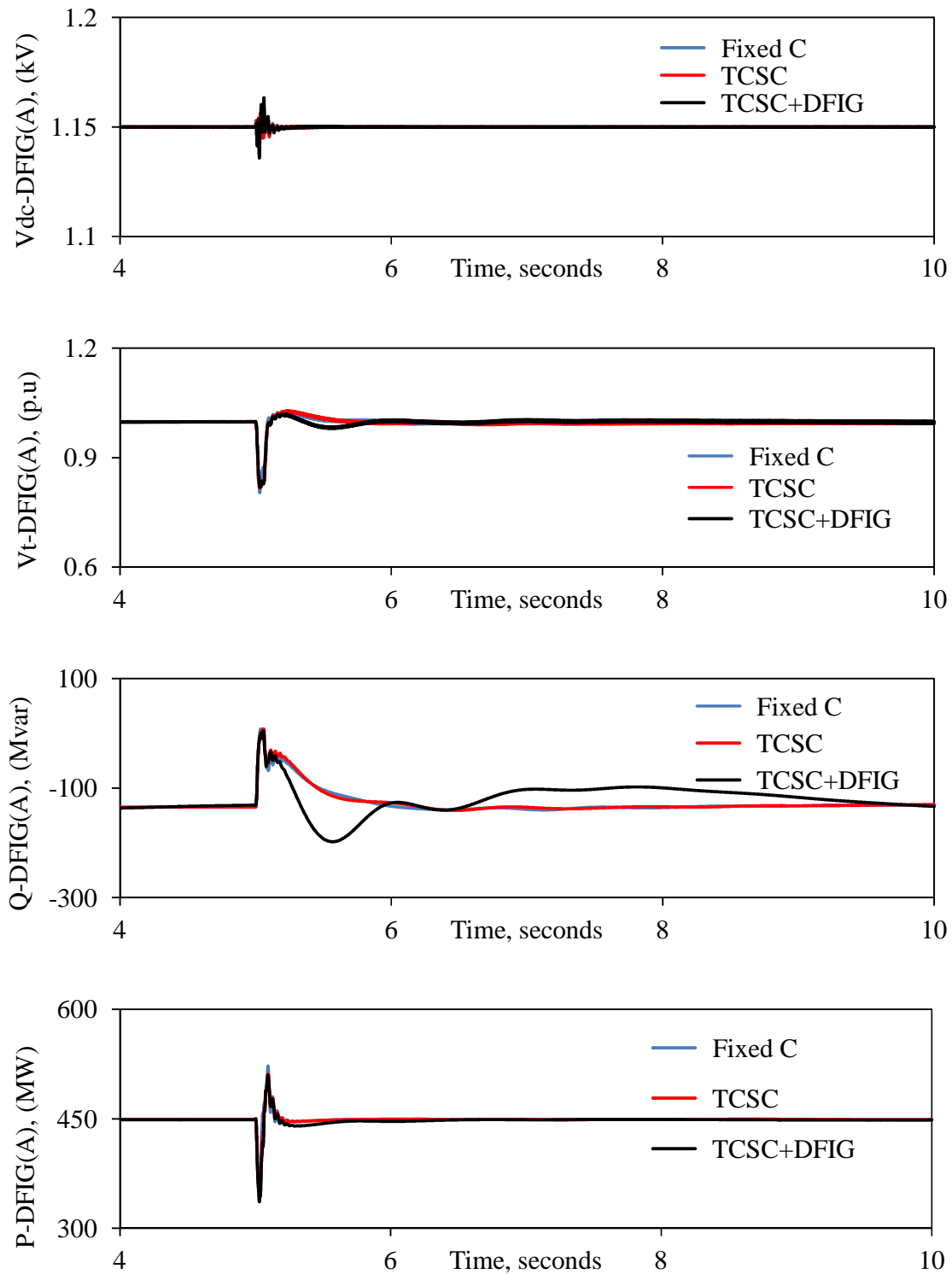**Figure 4.7:** DFIG-based wind farms A and B real and reactive powers, terminal voltages and BtB dc link voltages during and after clearing a 3-cycle, three-phase fault at bus 4. (supplemental control is in the Q control loop of the GSC of wind farm A).
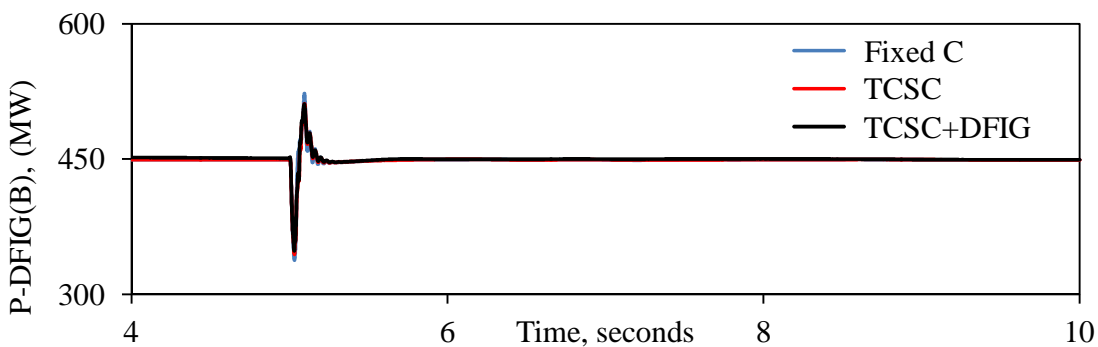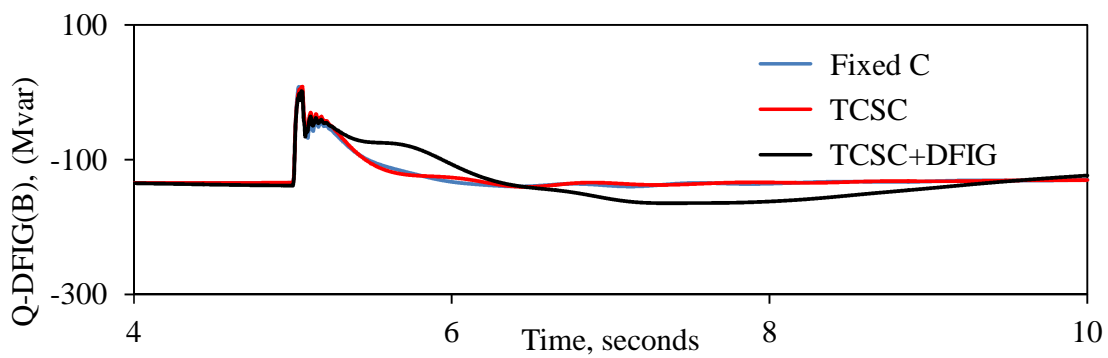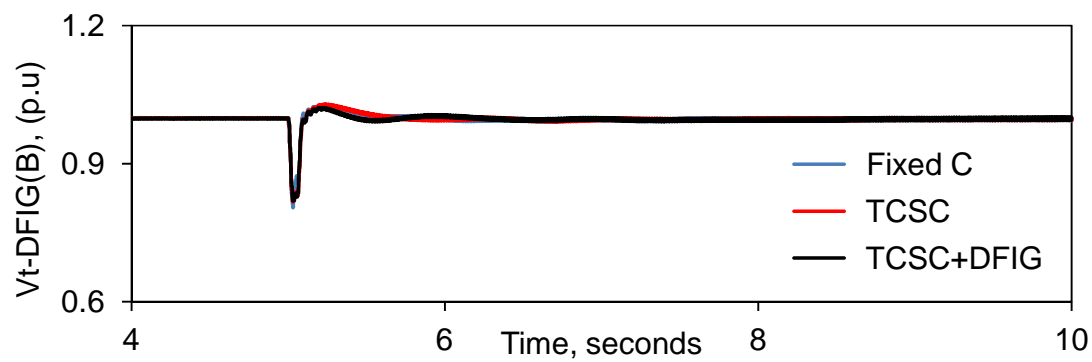
Figure 4.7: continued.

4.5 DFIG-Based Wind Farm Supplemental Control is in the Reactive/Active Power Control Loop of the RSC of Wind Farm A

Figures 4.8 and 4.9 illustrate the generator load angles and speeds, measured with respect to generator 1 load angle and speed, and the transmission line real power flow transient time responses during and after fault clearing. Figures 4.10 and 4.11 illustrate the time responses of wind farms A and B real and reactive powers, terminal voltage and the BtB dc voltage for the same case. Tables 4.3 and 4.4 show the transfer functions of the TCSC and wind farm A supplemental controls after final tuning. Comparing the responses for the case of Scheme I supplemental control alone (TCSC) to those for the case of Scheme I and the DFIG-based wind farm supplemental controls in Figures 4.8 and 4.9, the positive contribution of wind farm A supplemental control, whether it is installed in either the Q or P control loop of the RSC, to the damping of the system oscillations is very clear. It worth noting here that the results of similar studies conducted on wind farm B that are given in Appendix B have shown also an appreciable contribution of wind farm B to the damping of the system oscillations.

Table 4.3: Transfer functions of the hybrid TCSC compensation scheme and wind farm A supplemental controllers (wind farm controller is in the Q control loop of the RSC).

	Transfer Function
Hybrid TCSC Compensation Scheme	$G_{TCSC}(s) = 0.25 \dfrac{10}{(s+10)} \dfrac{3s}{(3s+1)}$
DFIG-Based Wind Farm A	$G_{DFIG\_Q\_Loop\_RSC}(s) = 0.3 \dfrac{s}{(s+15)} \dfrac{1}{(s+2)}$

Table 4.4: Transfer functions of the hybrid TCSC compensation scheme and wind farm A supplemental controllers (wind farm controller is in the P control loop of the RSC).

	Transfer Function
Hybrid TCSC Compensation Scheme	$G_{TCSC}(s) = 0.25 \dfrac{10}{(s+10)} \dfrac{3s}{(3s+1)}$
DFIG-Based Wind Farm A	$G_{DFIG\_P\_Loop\_RSC}(s) = 0.25 \dfrac{s}{(s+1)} \dfrac{1}{(s+8)}$

Figure 4.8: Generator load angles and speeds, measured with respect to generator 1 load angle and speed, and transmission line real power flow transient time responses during and after clearing a 3-cycle, three-phase fault at bus 4 (supplemental control is in the Q control loop of the RSC of wind farm A).
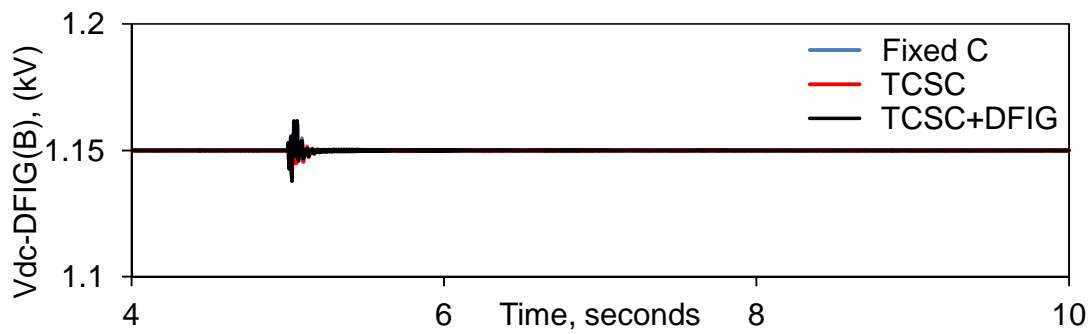
Figure 4.8: continued.

Figure 4.8: continued.

71
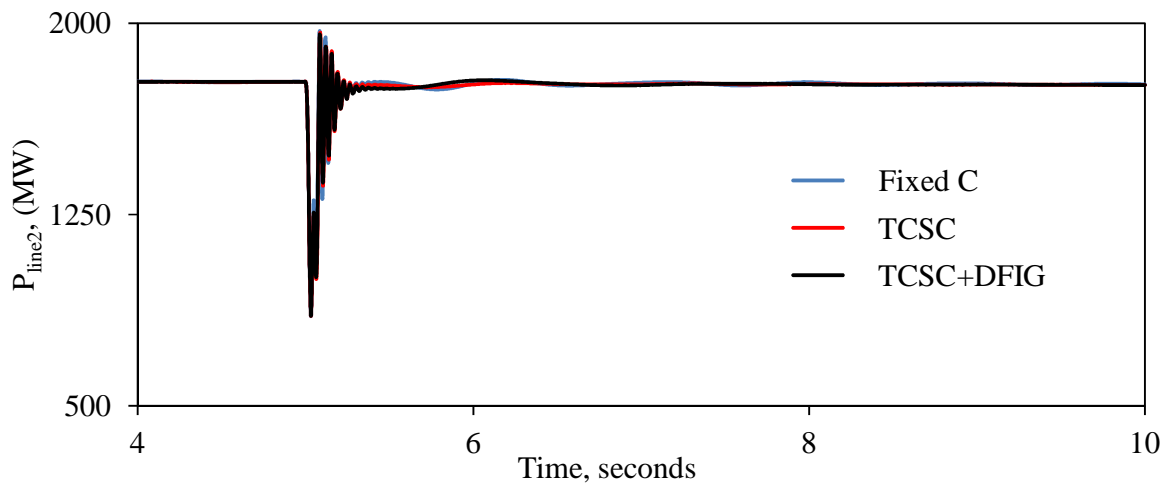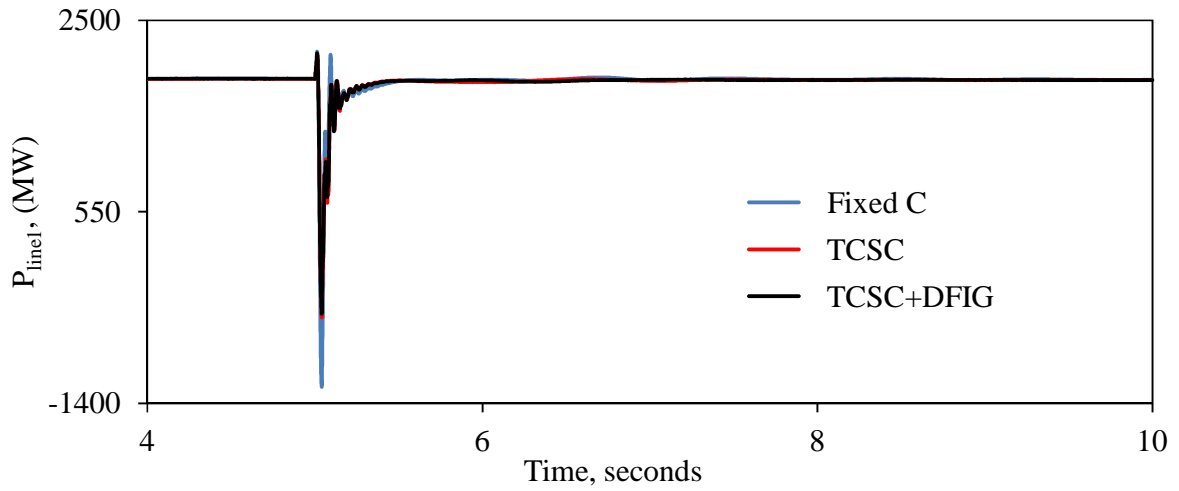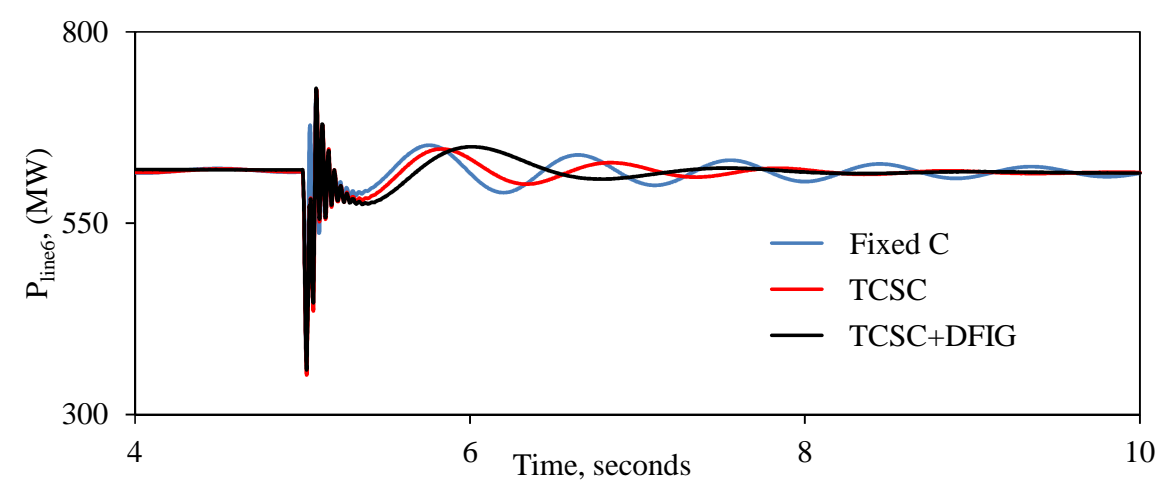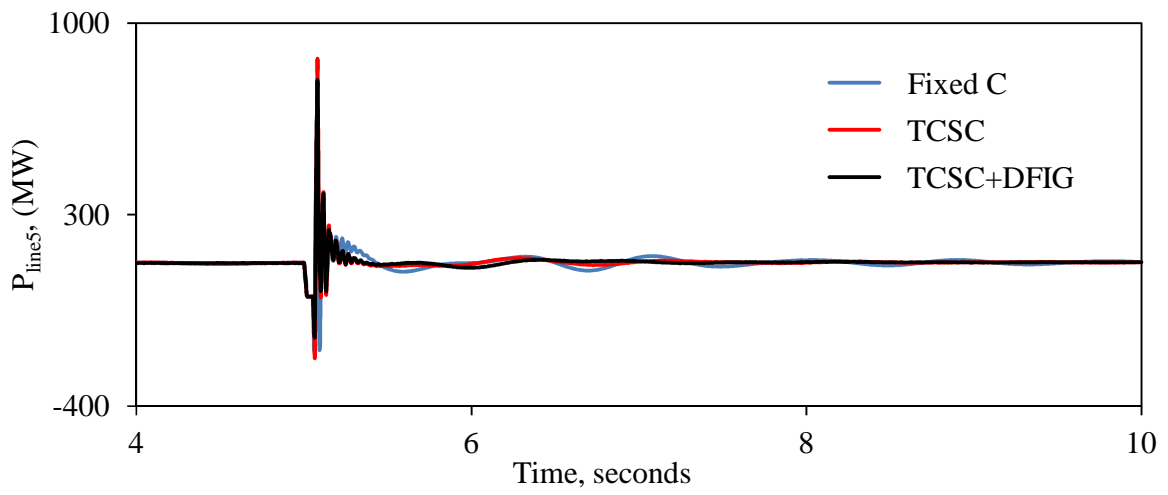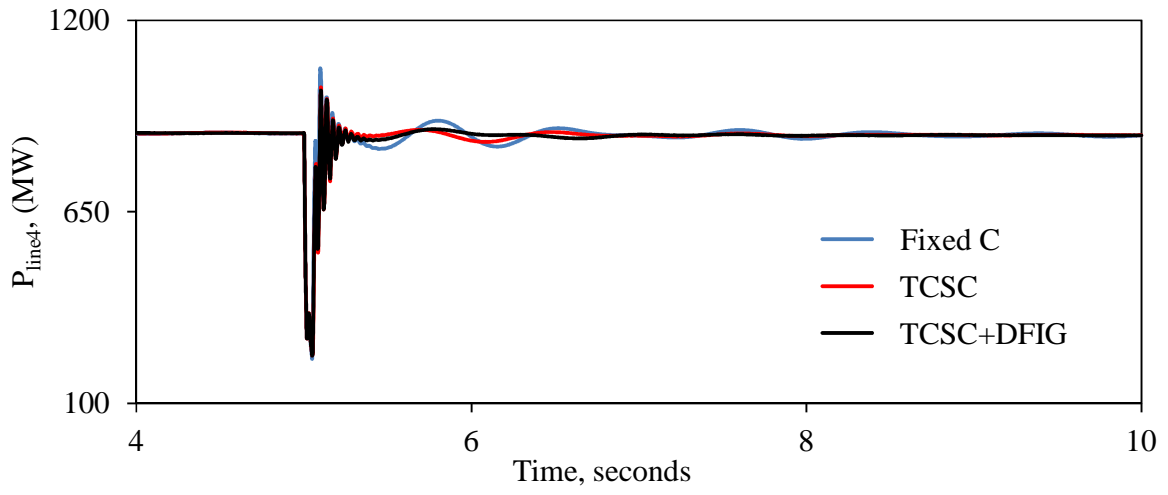
Figure 4.8: continued.
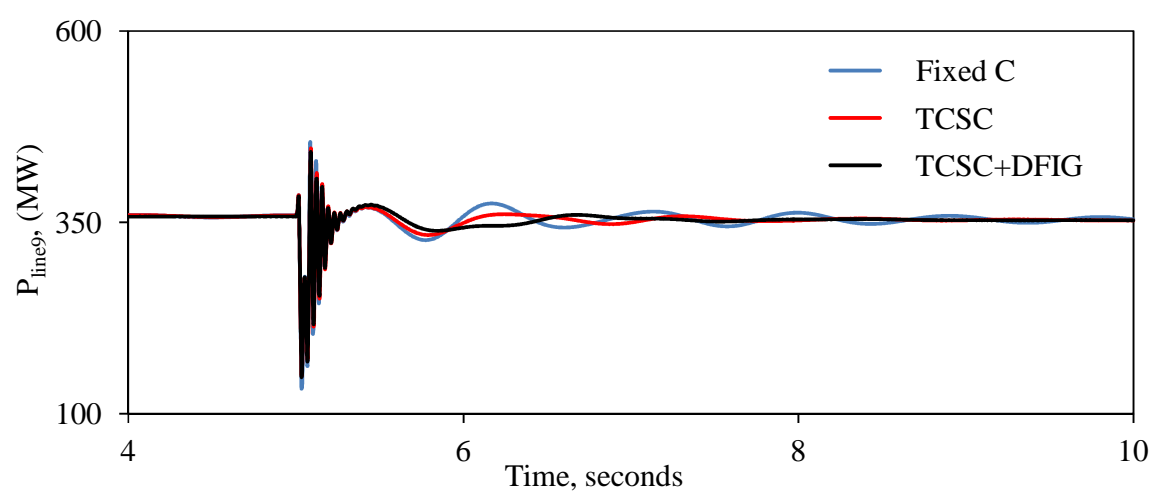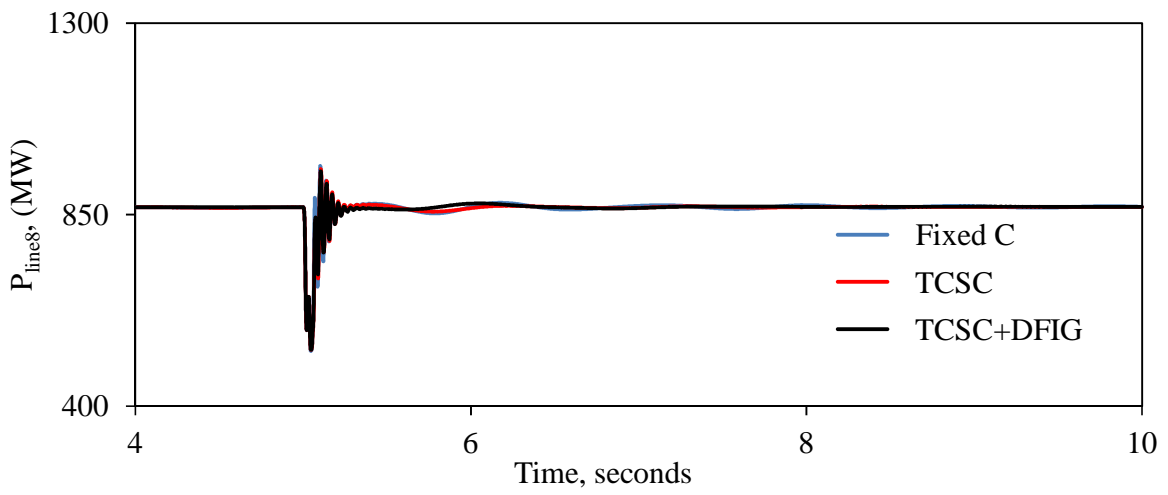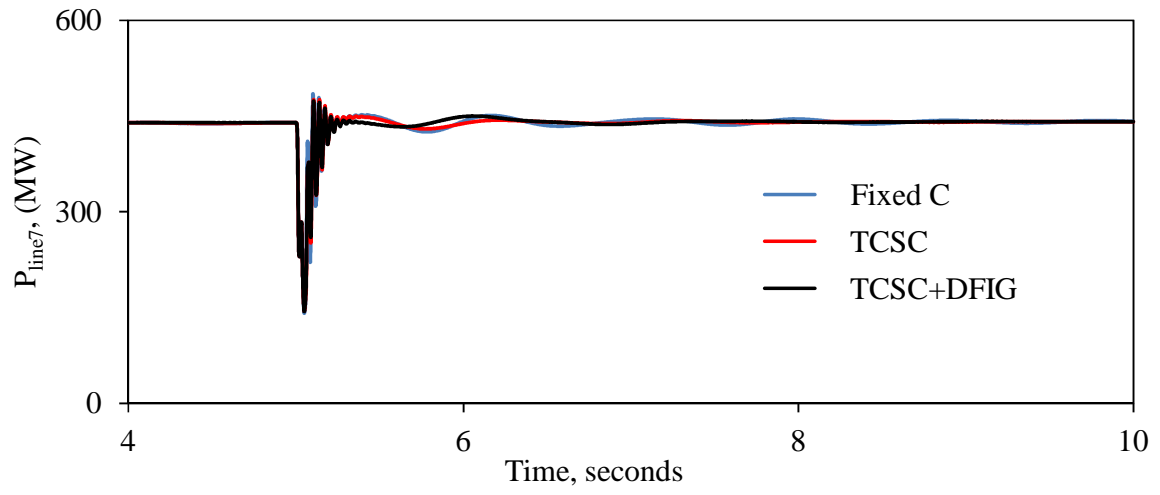
Figure 4.8: continued.
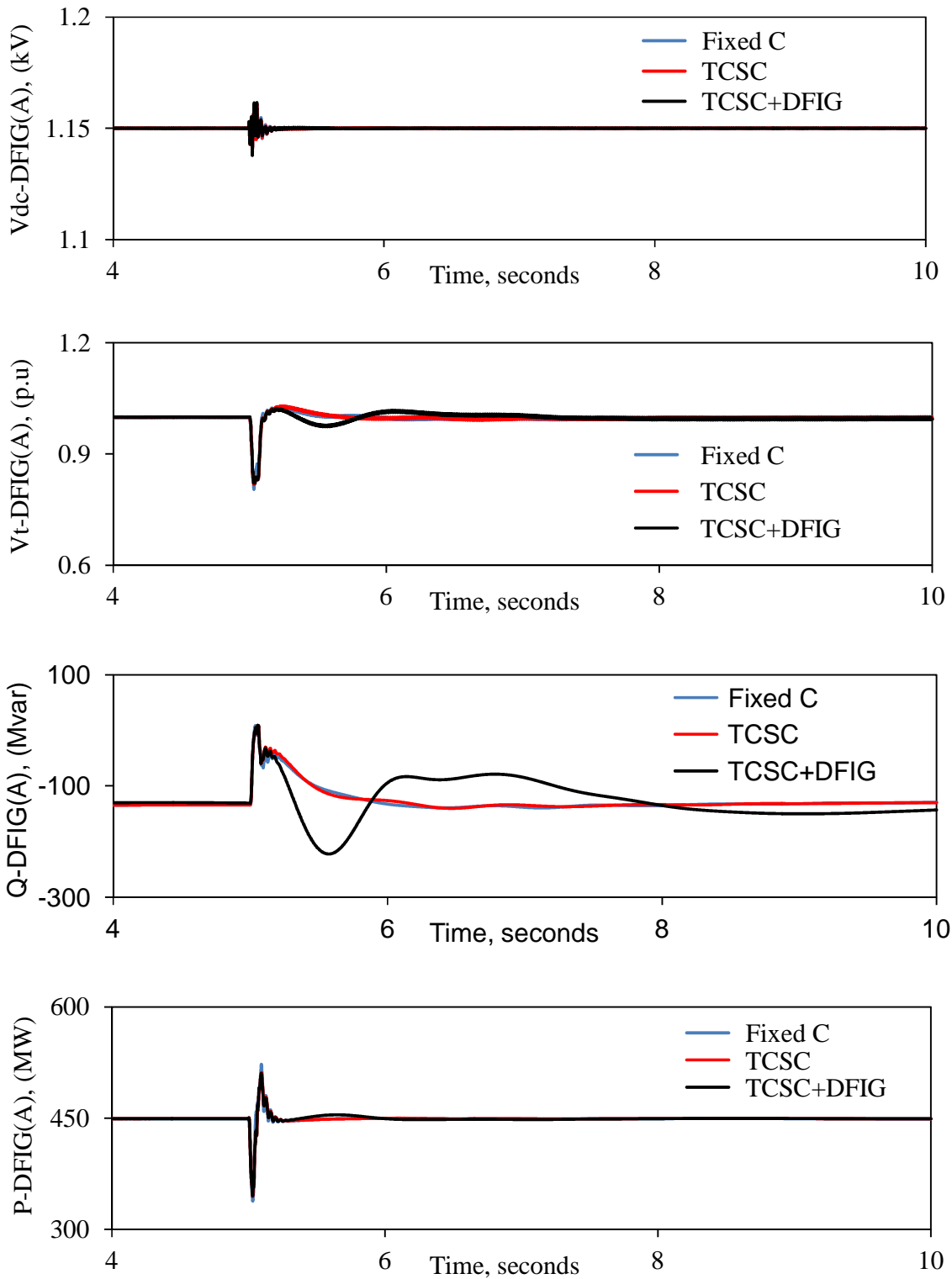
Figure 4.9: DFIG-based wind farms A and B real and reactive powers, terminal voltages and BtB dc link voltages during and after clearing a 3-cycle, three-phase fault at bus 4. (supplemental control is in the Q control loop of the RSC of wind farm A).
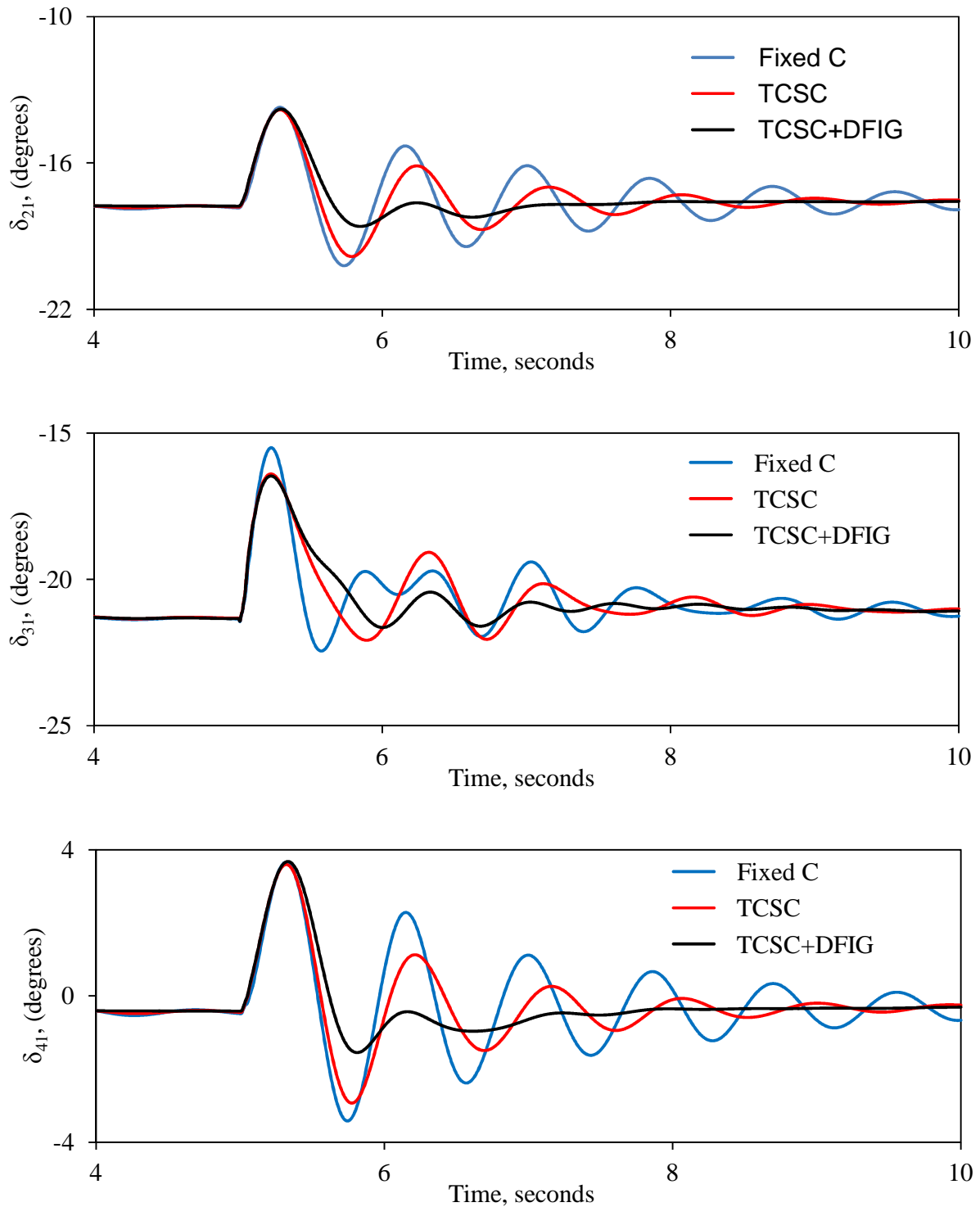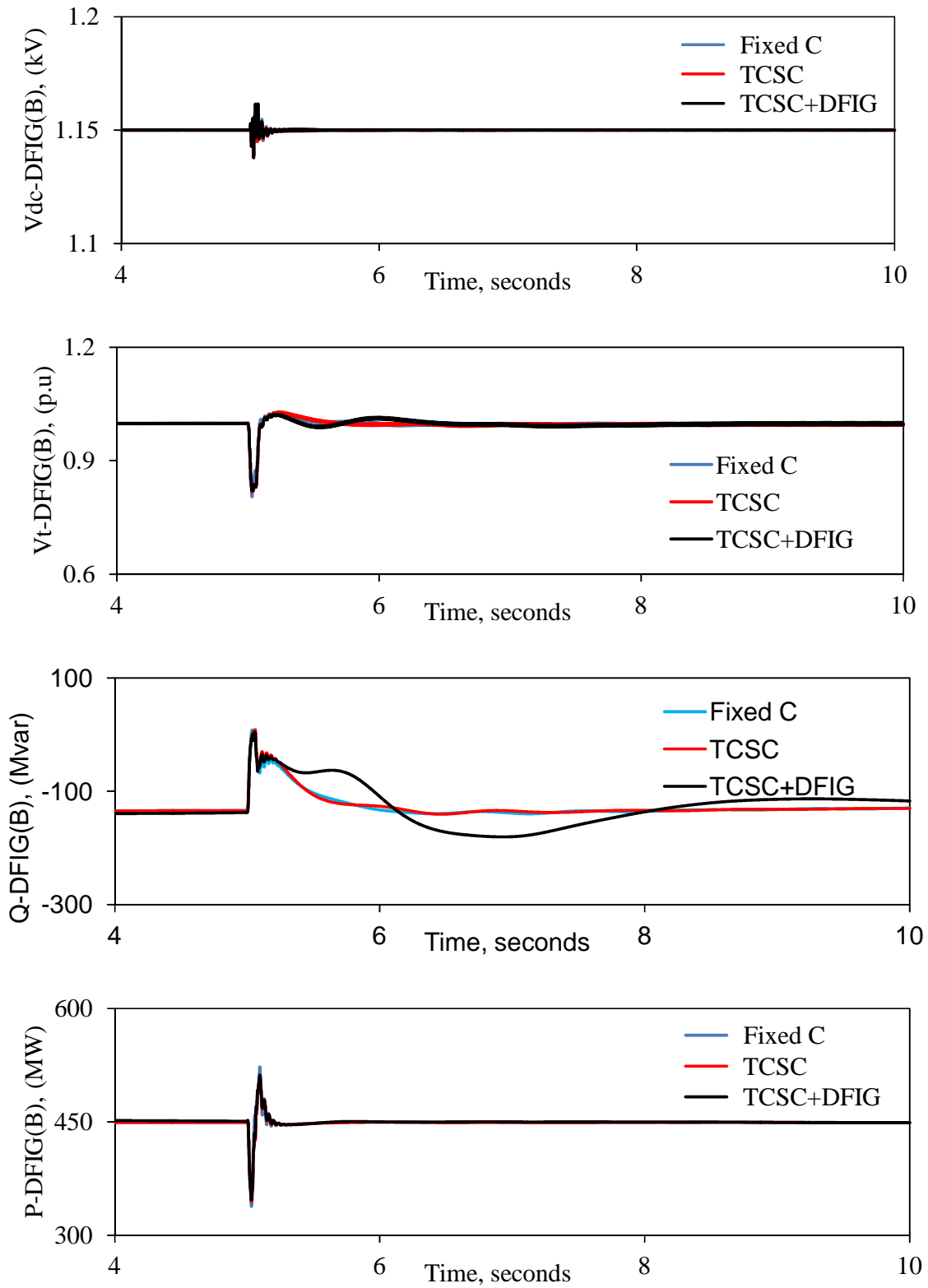
Figure 4.9: continued.
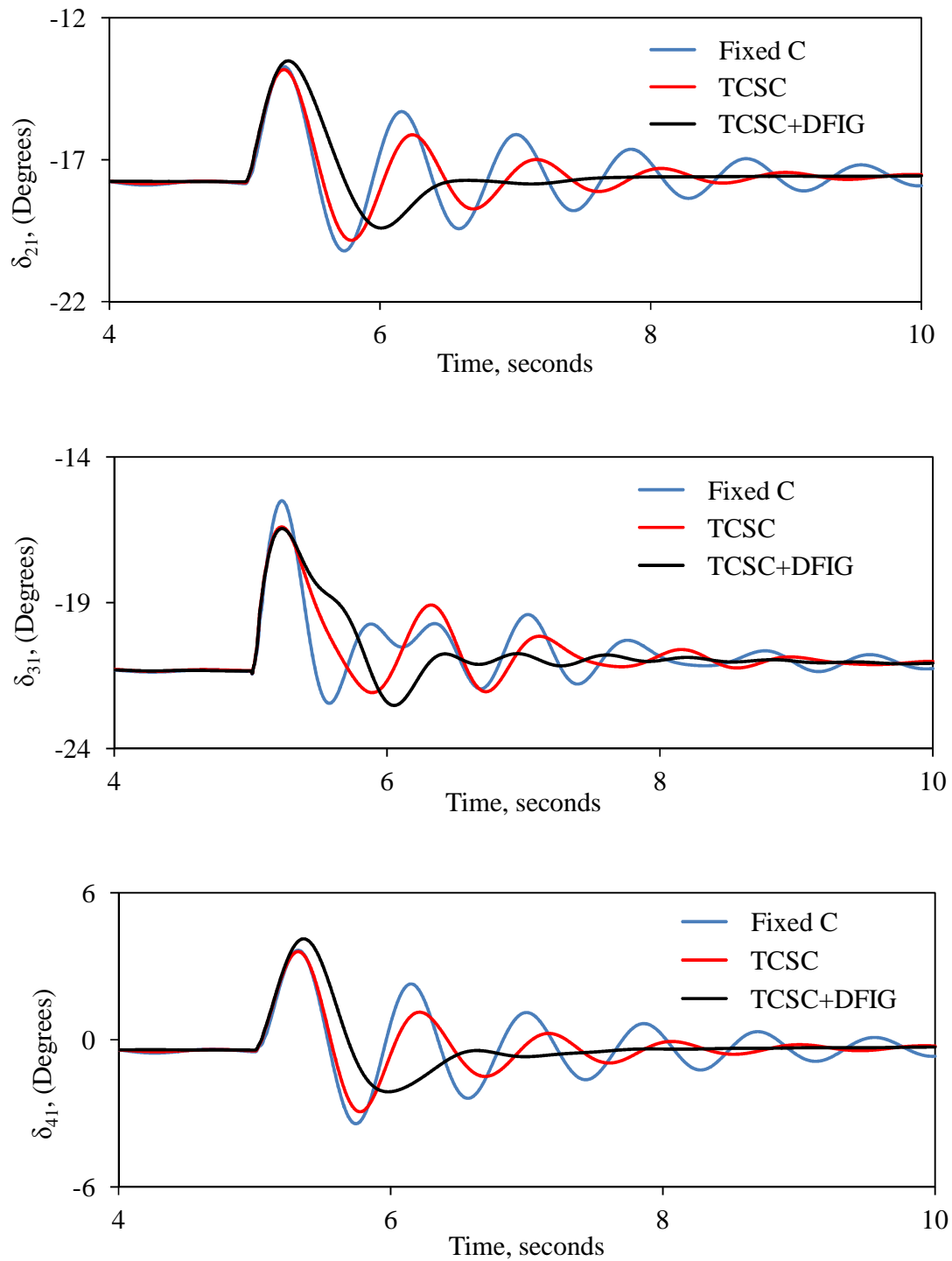
Figure 4.10: Generator load angles and speeds, measured with respect to generator 1 load angle and speed, and transmission line real power flow transient time responses during and after clearing a 3-cycle, three-phase fault at bus 4 (supplemental control is in the R control loop of the RSC of wind farm A).
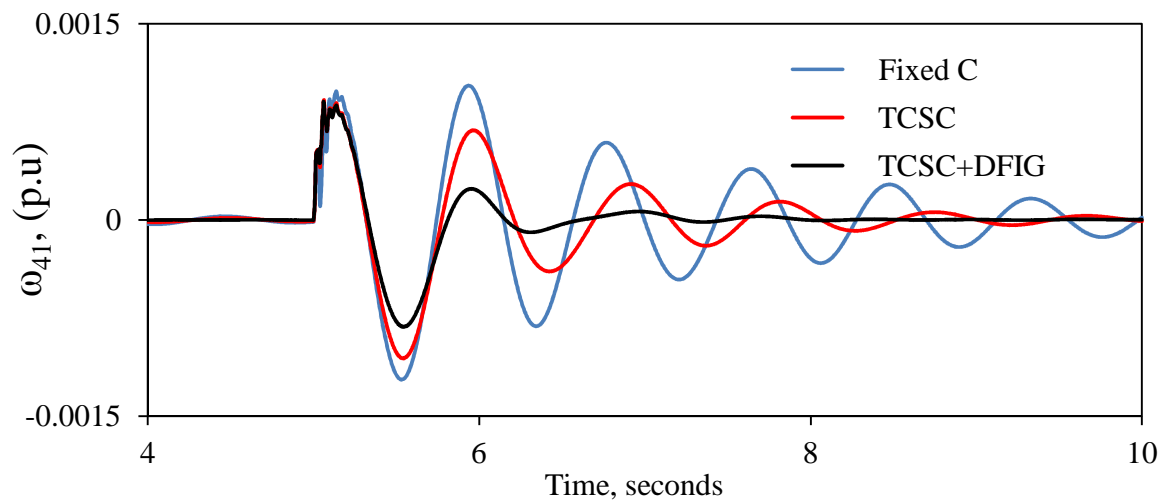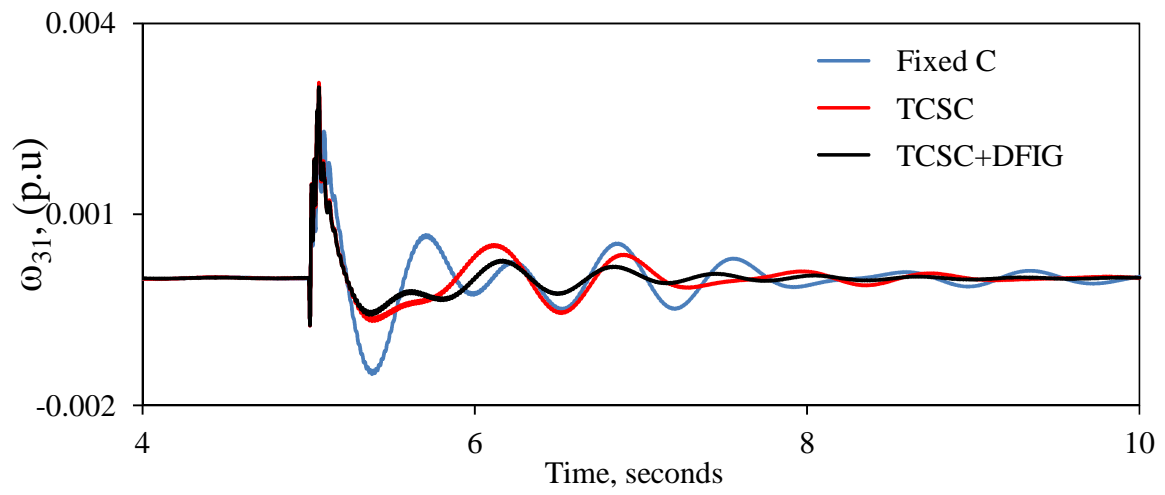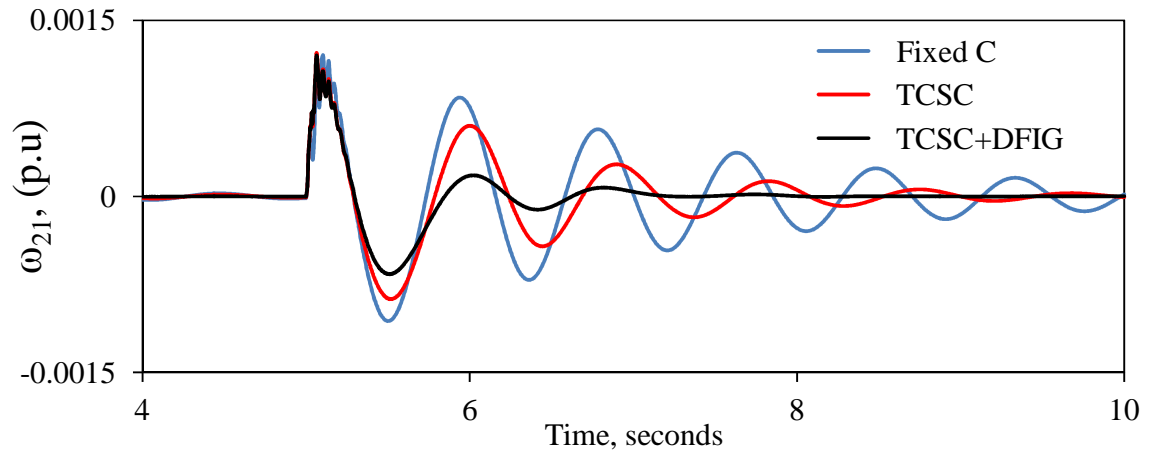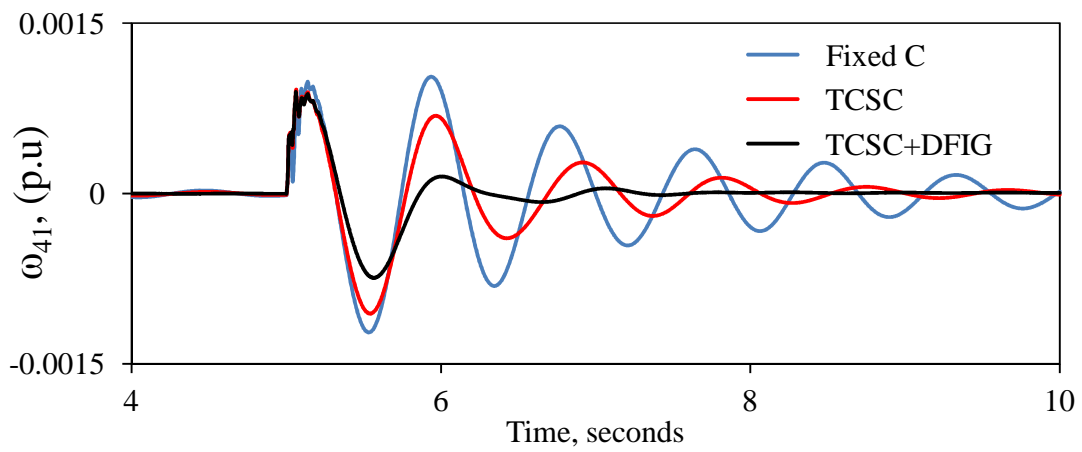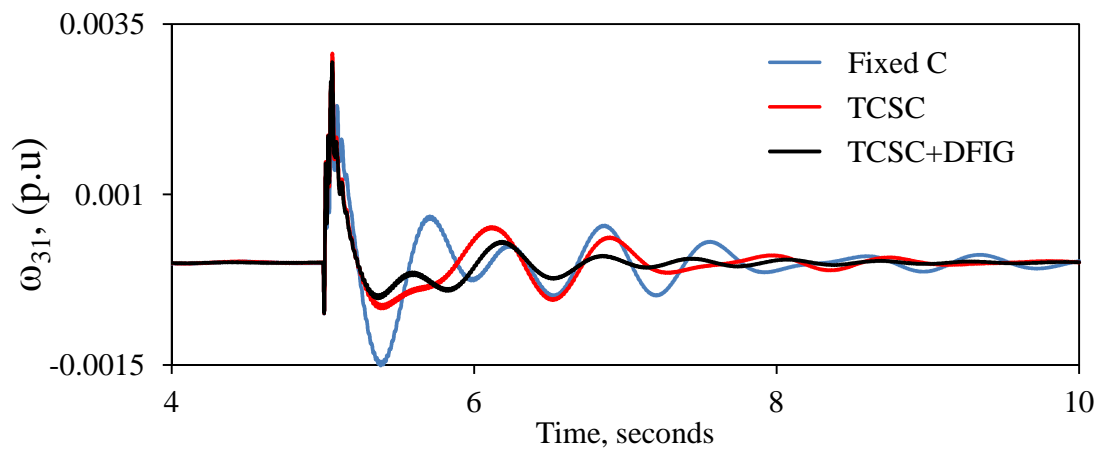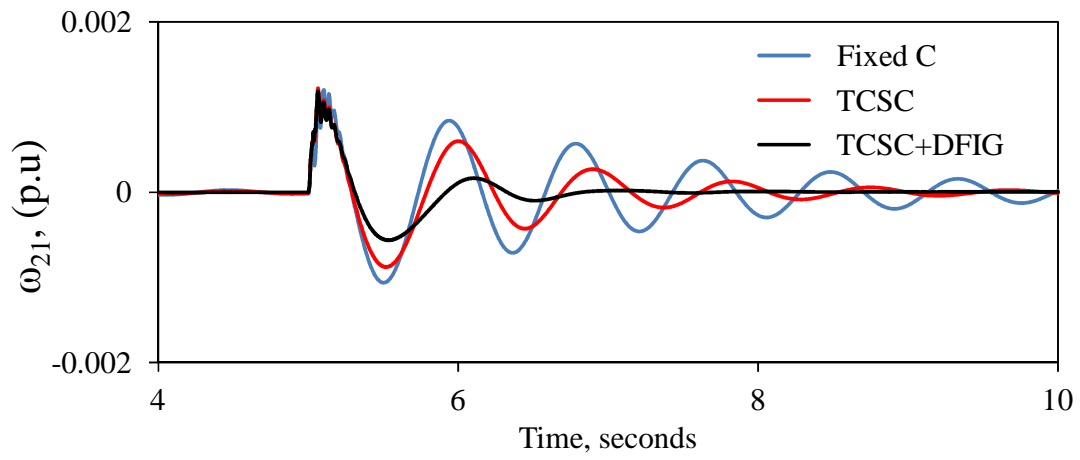
Figure 4.10: continued.

Figure 4.10: continued.

Figure 4.10: continued.

79
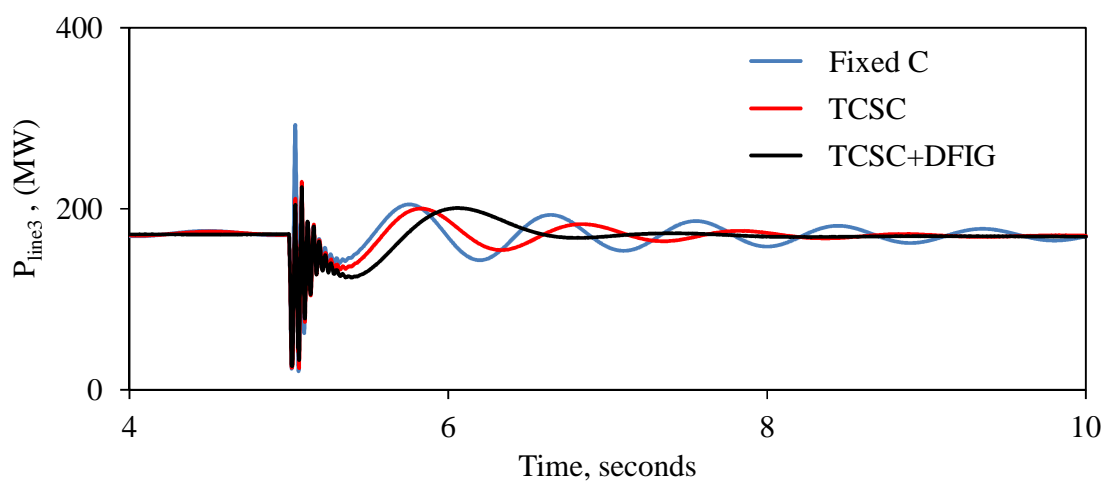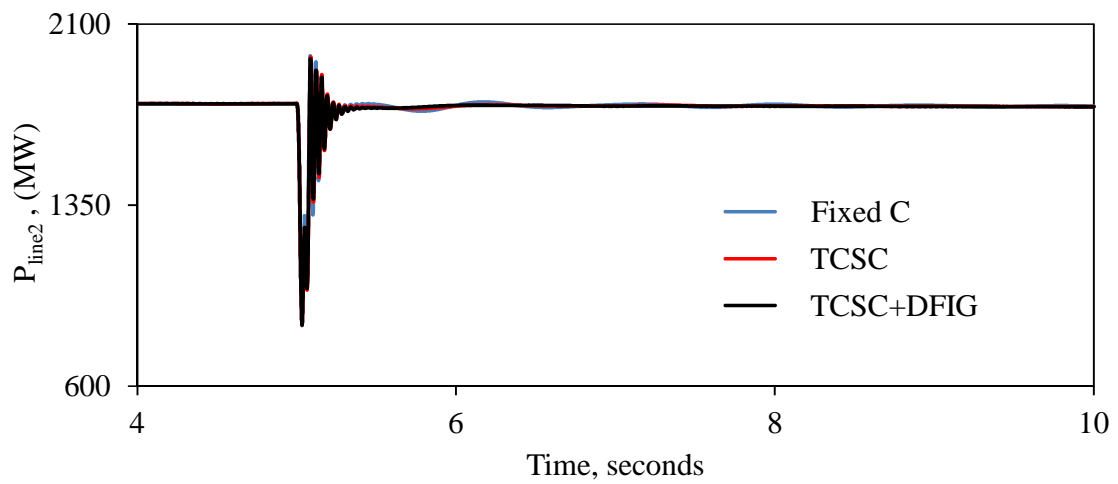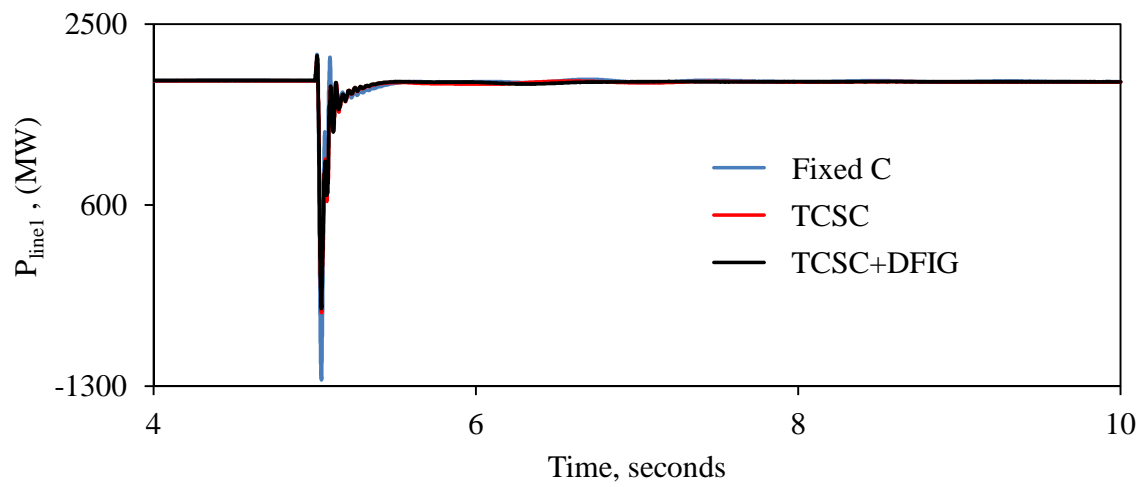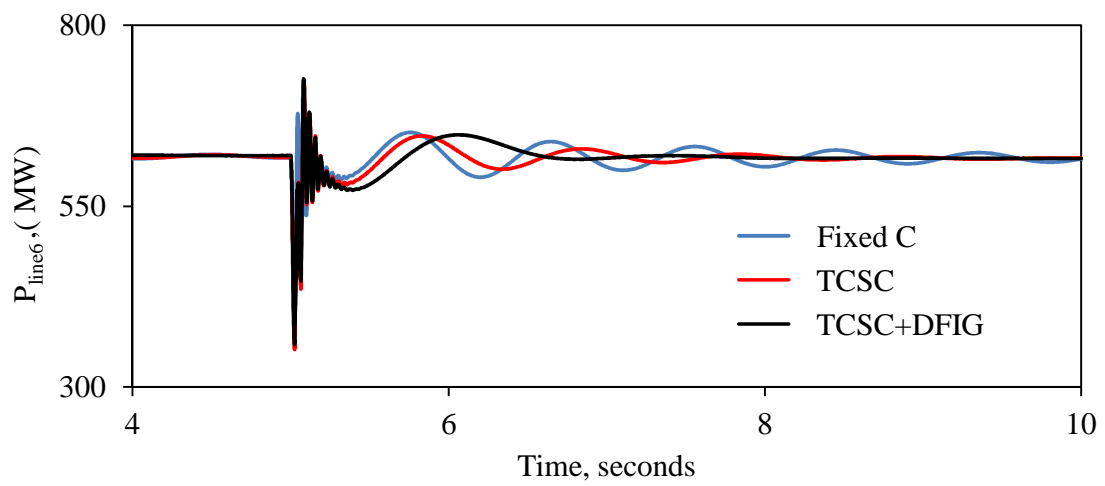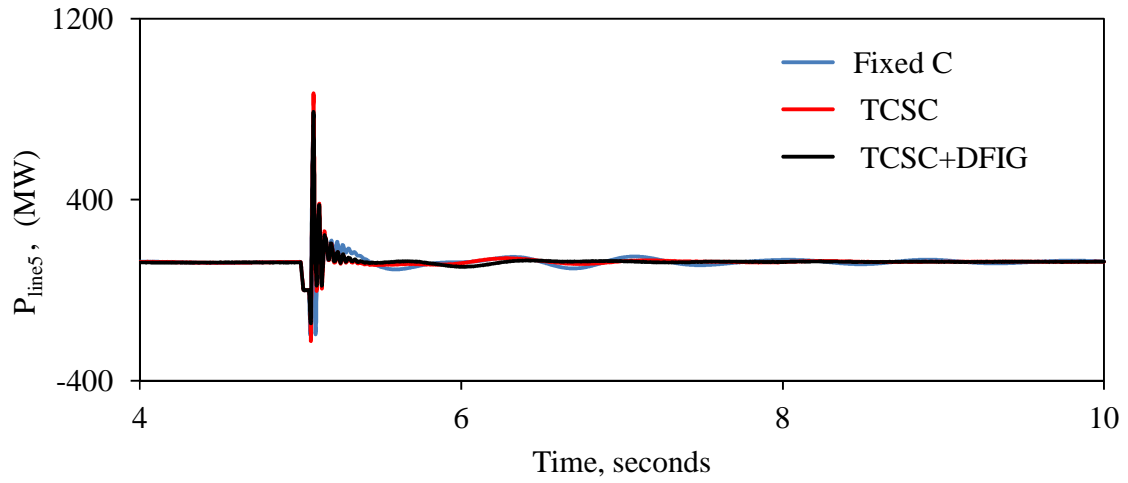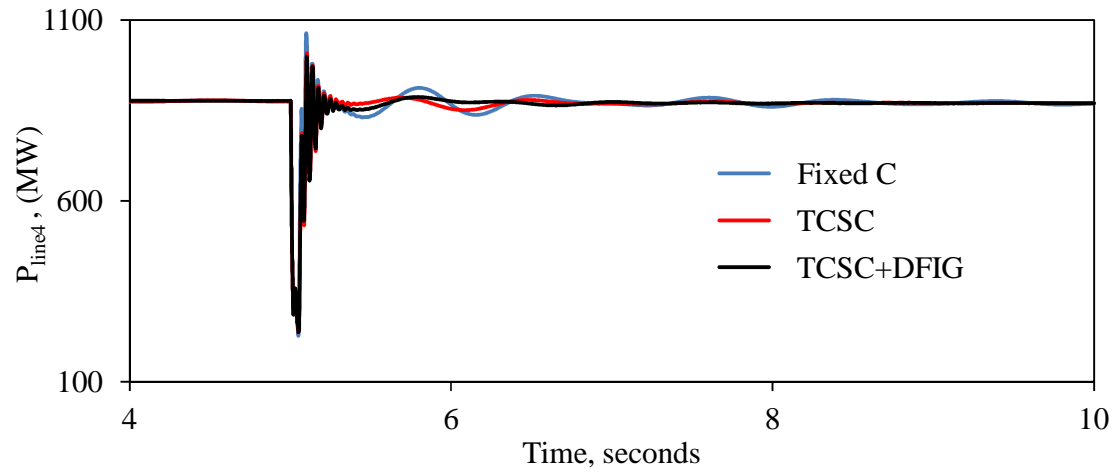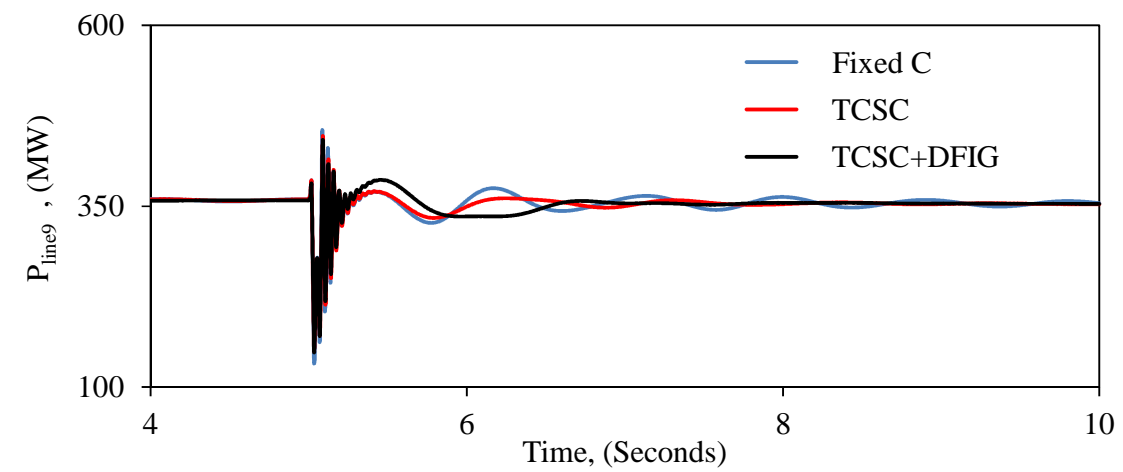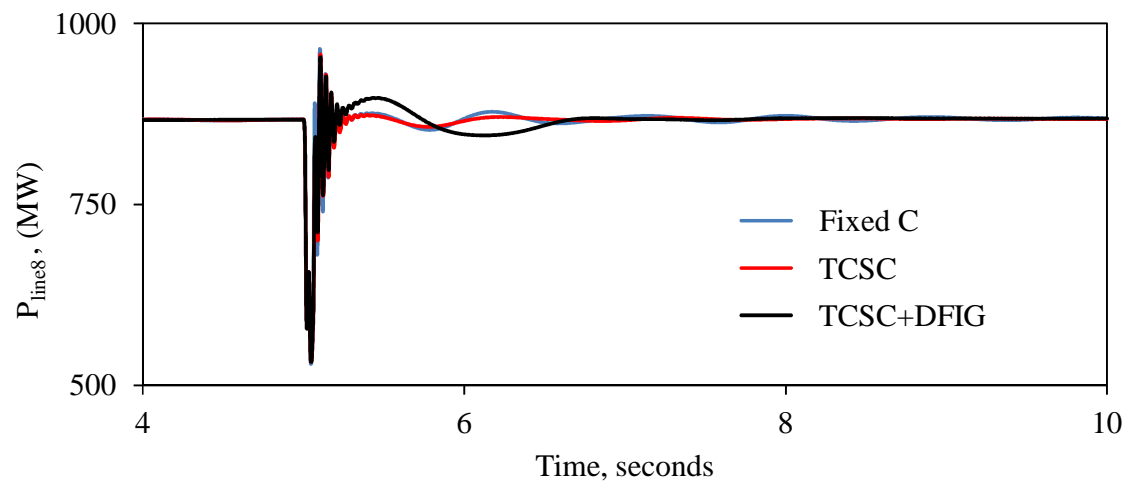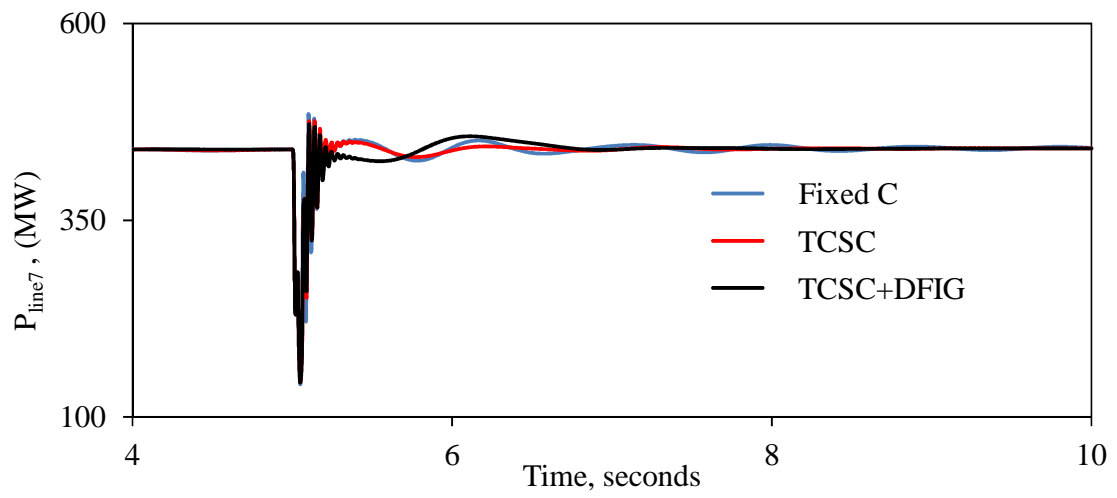
Figure 4.10: continued.
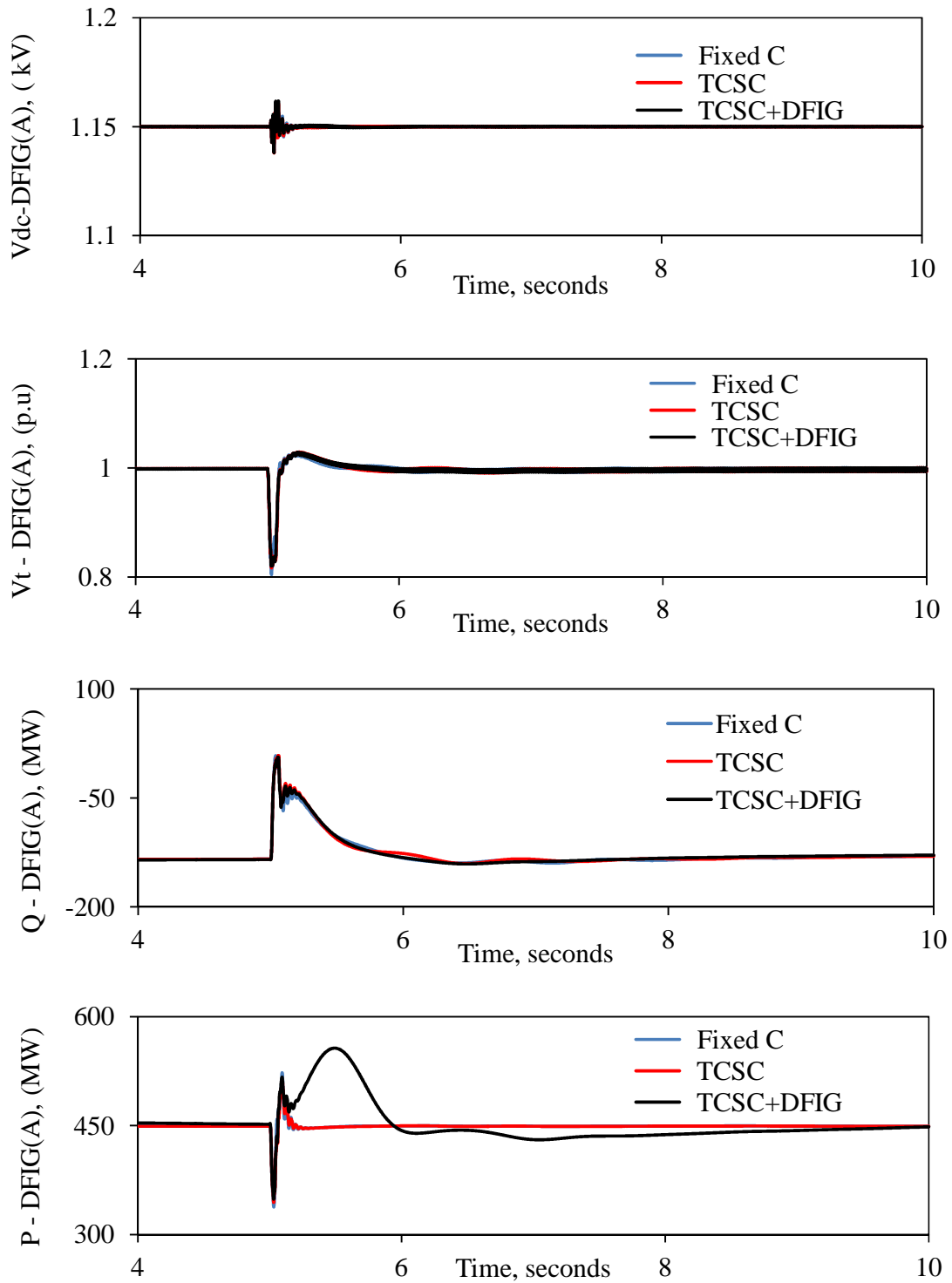
Figure 4.11: DFIG-based wind farms A and B real and reactive powers, terminal voltages and BtB dc link voltages during and after clearing a 3-cycle, three-phase fault at bus 4. (supplemental control is in the P control loop of the RSC of wind farm A).
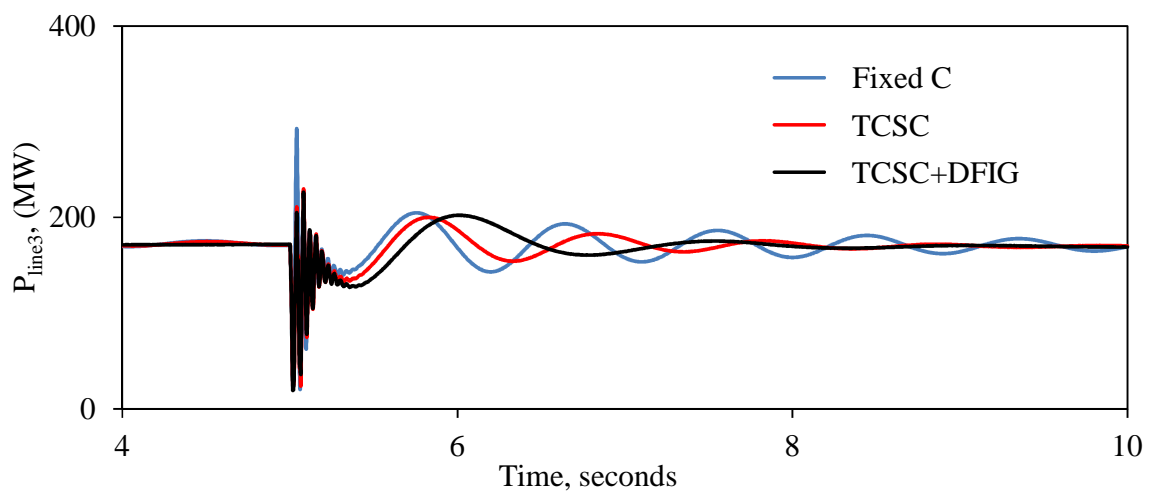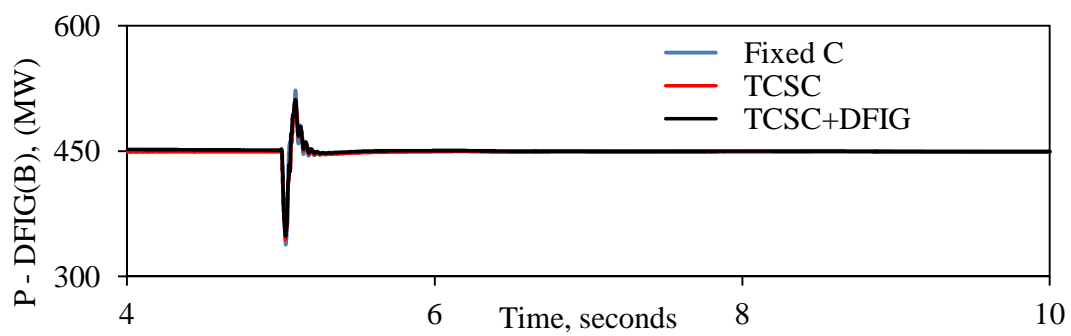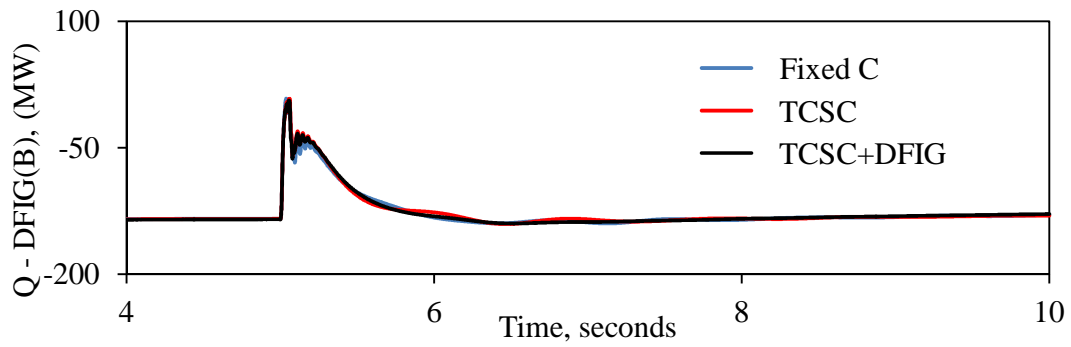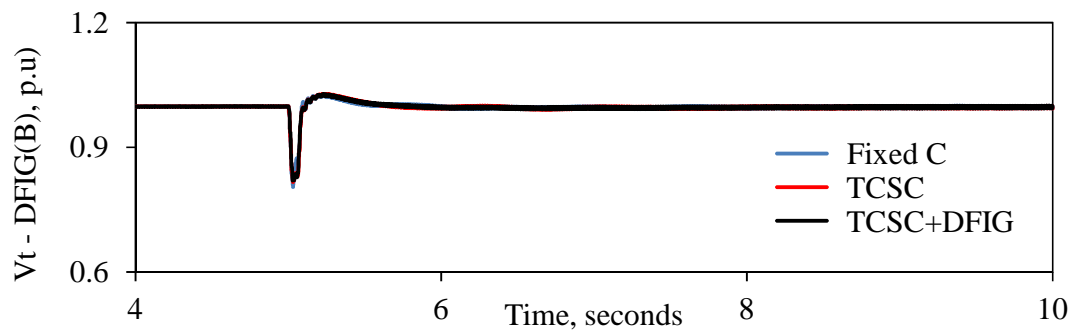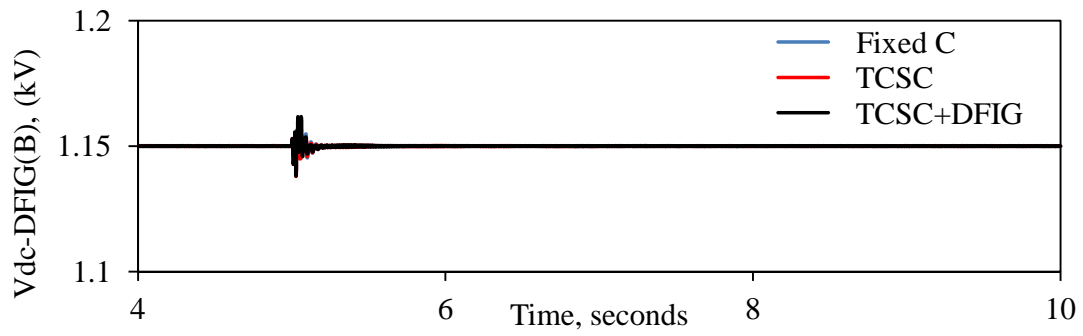
Figure 4.11: continued.

4.6   Impact of Large Share of Wind Power Generation on System Stability

There has been recently a concern over the situation of large share of wind power generation that results in reducing the total inertia of the synchronous generators which results in degrading the system transient stability [75]. The counterargument to this statement, however, is that properly designed supplemental controls for the DFIG back-to-back converters could be an asset in improving the system transient stability rather than degrading it. In order to demonstrate that, investigations are conducted on the system under study in Figure 2.1 for the cases described in Table 4.5.

Table 4.5: Study cases for the impact of large share of wind power on system stability.

Case	Description
No wind farms	Wind farms A and B are removed from the system and their share of power is provided by G_4. G_4 rated MVA is increased by the same amount. Figure 4.12 shows the power flow results for the bus voltages and the line real power flows of the system under study for this study case.
Two wind farms	Supplemental controls of Wind farms A and B are disabled.
Controller at WFA	Supplemental control is only in Wind Farm A
Controller at WFB	Supplemental control is only in Wind Farm B
Two controllers	Supplemental controls of Wind farms A and B are activated.
Scheme I (TCSC) supplemental control is disabled in all the above cases	

Figures 4.13 to 4.15 illustrate the transient time responses of the generator load angles, measured with respect to generator 1 load angle, during and after fault clearing for the cases of Table 4.5. The transfer functions of the TCSC and wind farm supplemental controls after final tuning corresponding to the study cases of Table 4.5 are given in Table 4.6. It can be seen from Figure 4.15 that the system damping in the case of incorporating the wind farms without supplemental controls (two wind farms) is worse than the case of no wind farms. This observation is in a complete agreement with [75]. It can, however, also be seen from Figures 4.13 to 4.15 that supplemental controls installed at wind farms A or/and B can provide significant damping to system oscillations.
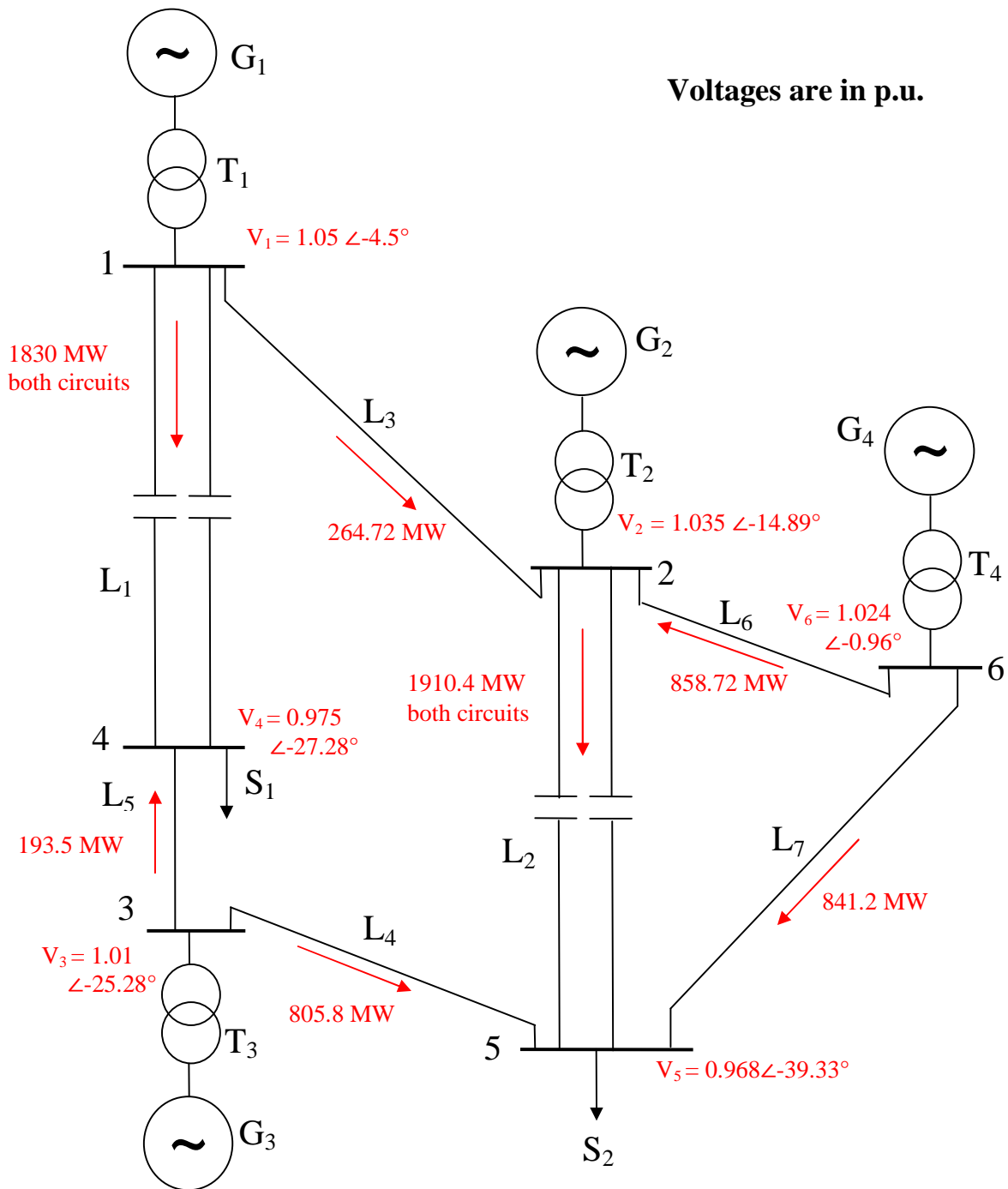
Figure 4.12: Power flow results of bus voltages and line real power flows of the system under study for the no-wind farm study case in Table 4.5.
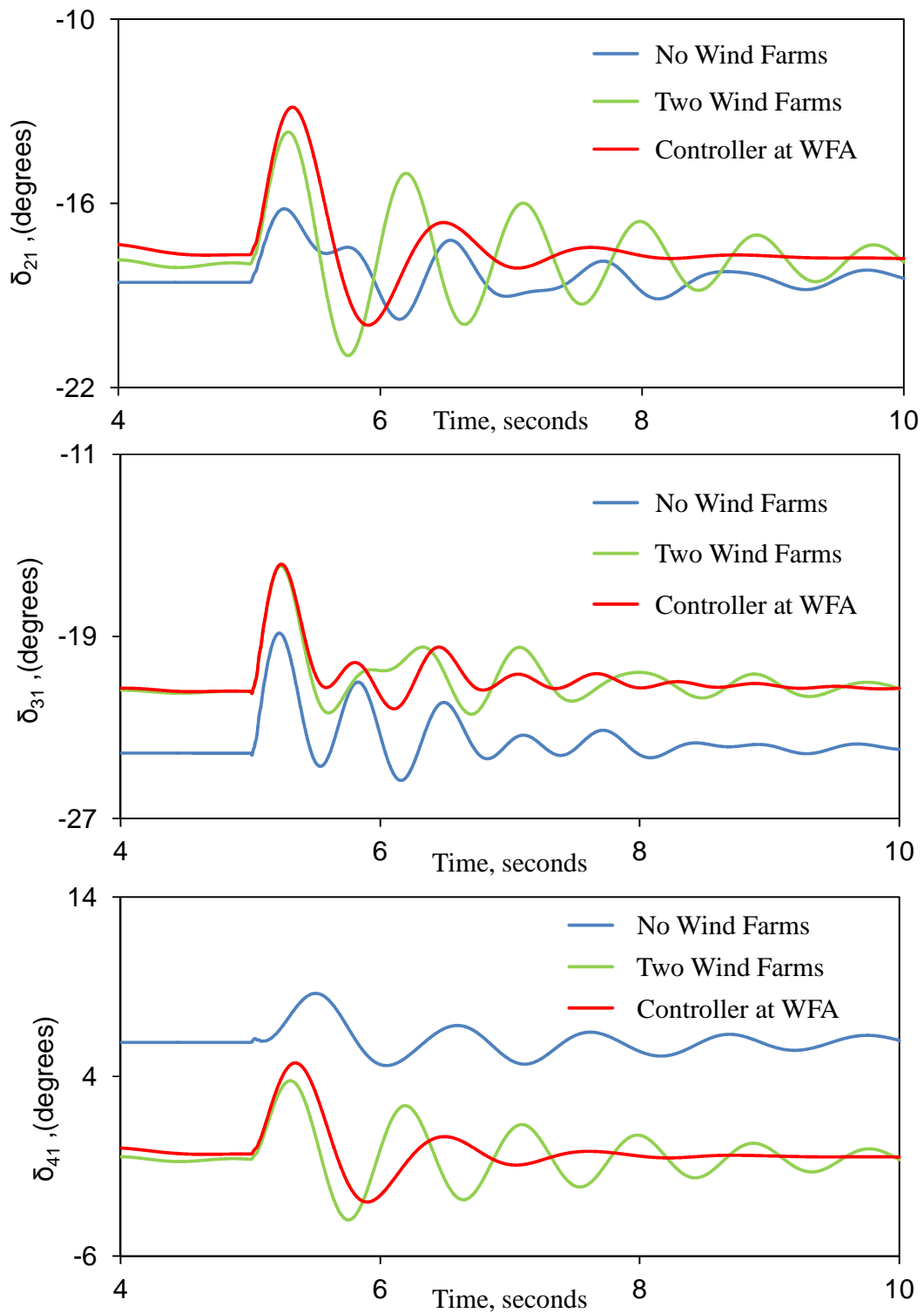
Figure 4.13: Generator load angles, measured with respect to generator 1 load angle, during and after clearing a 3-cycle, three-phase fault at bus 4. (DFIG-based wind farm supplemental controller is in the P control loop of the RSC).

Figure 4.14: Generator load angles, measured with respect to generator 1 load angle, during and after clearing a 3-cycle, three-phase fault at bus 4. (DFIG-based wind farm supplemental controller is in the P control loop of the RSC)

Figure 4.15: Generator load angles, measured with respect to generator 1 load angle, during and after clearing a 3-cycle, three-phase fault at bus 4. (DFIG-based wind farm supplemental controllers are in the P control loops of the RSC).

Table 4.6: Transfer functions of supplemental controls for wind farms A and B.

	Transfer Function
Supplemental Control is in Wind Farm A	$G_{DFIG\_P\_Loop\_RSC}(s) = 0.3 \dfrac{s}{(s+1)} \dfrac{1}{(s+8)}$
Supplemental Control is in Wind Farm B	$G_{DFIG\_P\_Loop\_RSC}(s) = 0.3 \dfrac{s}{(s+1)} \dfrac{1}{(s+5)}$
Supplemental Controls are in Wind Farms A and B	$G_{DFIG\_P\_Loop\_RSC}(s) = 0.3 \dfrac{s}{(s+1)} \dfrac{1}{(s+8)}$ $G_{DFIG\_P\_Loop\_RSC}(s) = 0.3 \dfrac{s}{(s+1)} \dfrac{1}{(s+5)}$

4.7 Effect of the Stabilizing Signal of Wind Farms A and B Supplemental Controls on the Damping of System Oscillations

Four different combinations of stabilizing signals (tabulated in Table 4.7) are examined in order to determine the combination that would result in the best system transient time responses. The final results of the time-domain simulation studies (controller tuning of the TCSC and wind farm A) are shown in Figures 4.16 to 4.18 which illustrates the generator load angles, measured with respect to generator 1 load angle, during and after fault clearing. The corresponding transfer functions of the TCSC and wind farm A supplemental controllers are given in Tables 4.8 to 4.10. Moreover, the final results of the controllers tuning of the TCSC and wind farm B and the associated supplemental control transfer functions are given in Appendix B.

Table 4.7: The four examined combinations of stabilizing signals.

Combination	Stabilizing signals in the TCSC supplemental control	Stabilizing signals in the wind farm supplemental controls
1	δ_{21}	δ_{41}
2	δ_{21}	δ_{31}
3	δ_{31}	δ_{41}
4	δ_{21}	P_{L1}

Table 4.8: Transfer functions of the hybrid TCSC compensation scheme and wind farm A supplemental controllers for the different combinations of stabilizing signals (wind farm controller is in the Q control loop of the GSC).

Combination	Hybrid TCSC Compensation Scheme	DFIG-Based Wind Farm A
1		$G(s) = 0.25 \dfrac{s}{(s+1)} \dfrac{1}{(s+5)}$
2	$G(s) = 0.25 \dfrac{10}{(s+10)} \dfrac{3s}{(3s+1)}$	$G(s) = 0.5 \dfrac{s}{(s+1)} \dfrac{1}{(s+5)}$
3		$G(s) = 0.1 \dfrac{s}{(s+1)} \dfrac{1}{(s+5)}$
4		$G(s) = 0.05 \dfrac{s}{(s+1)} \dfrac{1}{(s+5)}$

Table 4.9: Transfer functions of the hybrid TCSC compensation scheme and wind farm A supplemental controllers for the different combinations of stabilizing signals (wind farm controller is in the Q control loop of the RSC).

Combination	Hybrid TCSC Compensation Scheme	DFIG-Based Wind Farm A
1		$G(s) = 0.3 \dfrac{s}{(s+15)} \dfrac{1}{(s+2)}$
2	$G(s) = 0.25 \dfrac{10}{(s+10)} \dfrac{3s}{(3s+1)}$	
3		$G(s) = 0.3 \dfrac{s}{(s+15)} \dfrac{1}{(s+2)}$
4		$G(s) = 0.1 \dfrac{s}{(s+15)} \dfrac{1}{(s+2)}$

Table 4.10: Transfer functions of the hybrid TCSC compensation scheme and wind farm A supplemental controllers for the different combinations of stabilizing signals (wind farm controller is in the P control loop of the RSC).

Combination	Hybrid TCSC Compensation Scheme	DFIG-Based Wind Farm A
1		$G(s) = 0.5 \dfrac{s}{(s+1)} \dfrac{1}{(s+8)}$
2	$G(s) = 0.25 \dfrac{10}{(s+10)} \dfrac{3s}{(3s+1)}$	
3		$G(s) = 0.2 \dfrac{s}{(s+1)} \dfrac{1}{(s+4)}$
4		$G(s) = 0.02 \dfrac{s}{(s+1)} \dfrac{1}{(s+2)}$

It can be seen from Figures 4.16 to 4.18 that the best damping of the relative load angle responses are achieved with the δ_{21}- δ_{41} combination. The second best damped responses are obtained with the δ_{21}- δ_{31} combination. Again, these results should be expected due to the direct relationship between the relative load angles and the generators that yield the problem. It can also be seen from figures that the worst damped responses are obtained with δ_{21}-P_{L1} combination. It worth noting here that the time simulation results given in Appendix B (Figure B. 5 to B. 8) show that the best damping of the relative load angle responses are achieved with the δ_{21}- δ_{31} combination for the TCSC and wind farm B supplemental controls respectively.

In order to determine the best location for wind farm A supplemental control, the best responses in Figures 4.16 to 4.18 are plotted together in Figure 4.19. As it can be seen from this figure, although the three time responses are very close, nevertheless, the best location for wind farm A supplemental control tends to be in the Q control loop of the RSC. It is worth noting here that Figure B.8 (Appendix B) yield to the same conclusion for wind farm B supplemental control.

Figures 4.20 to 4.22 show comparisons between the best system responses as a result of a supplemental control installed in wind farm A or B. It can be concluded from these figures that, generally, there is no preference in installing the supplemental control in either wind farm especially if it is installed in the Q control loop of the RSC.
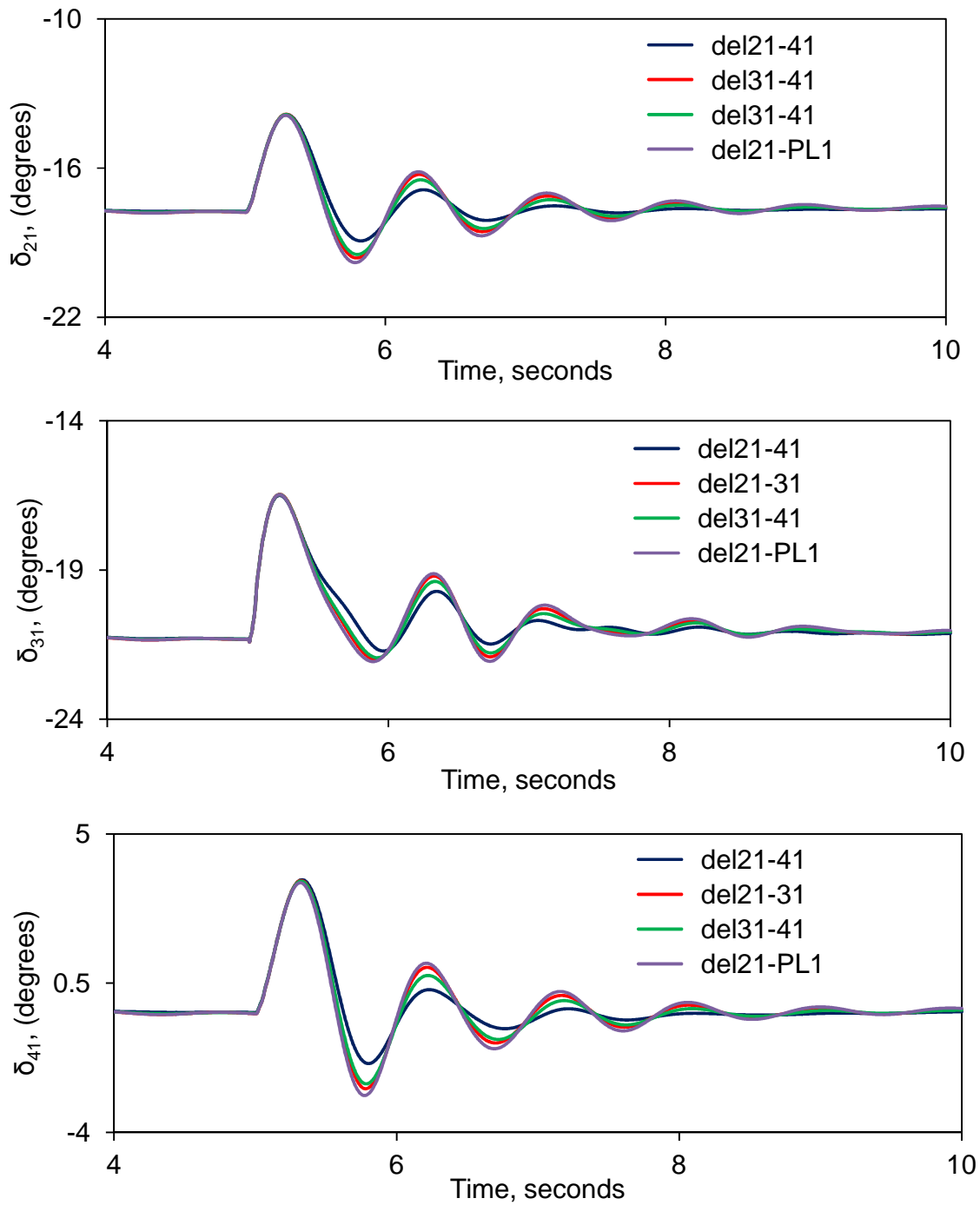
Figure 4.16: Effect of wind farm A supplemental control stabilizing signal on the generator load angles, measured with respect to generator 1 load angle, during and after clearing a 3-cycle, three-phase fault at bus 4. (DFIG-based wind farm supplemental controller is in the Q control loop of the GSC).
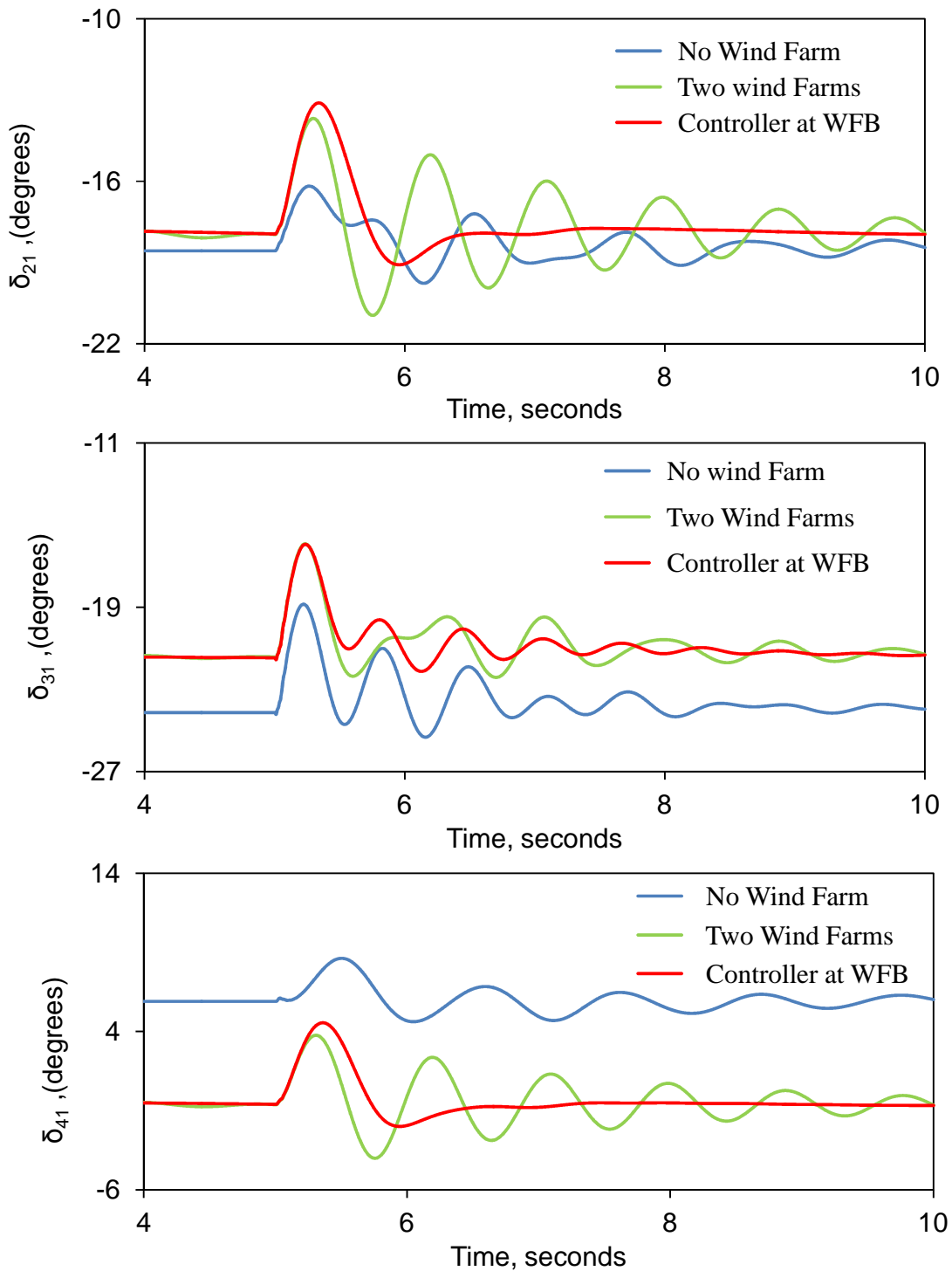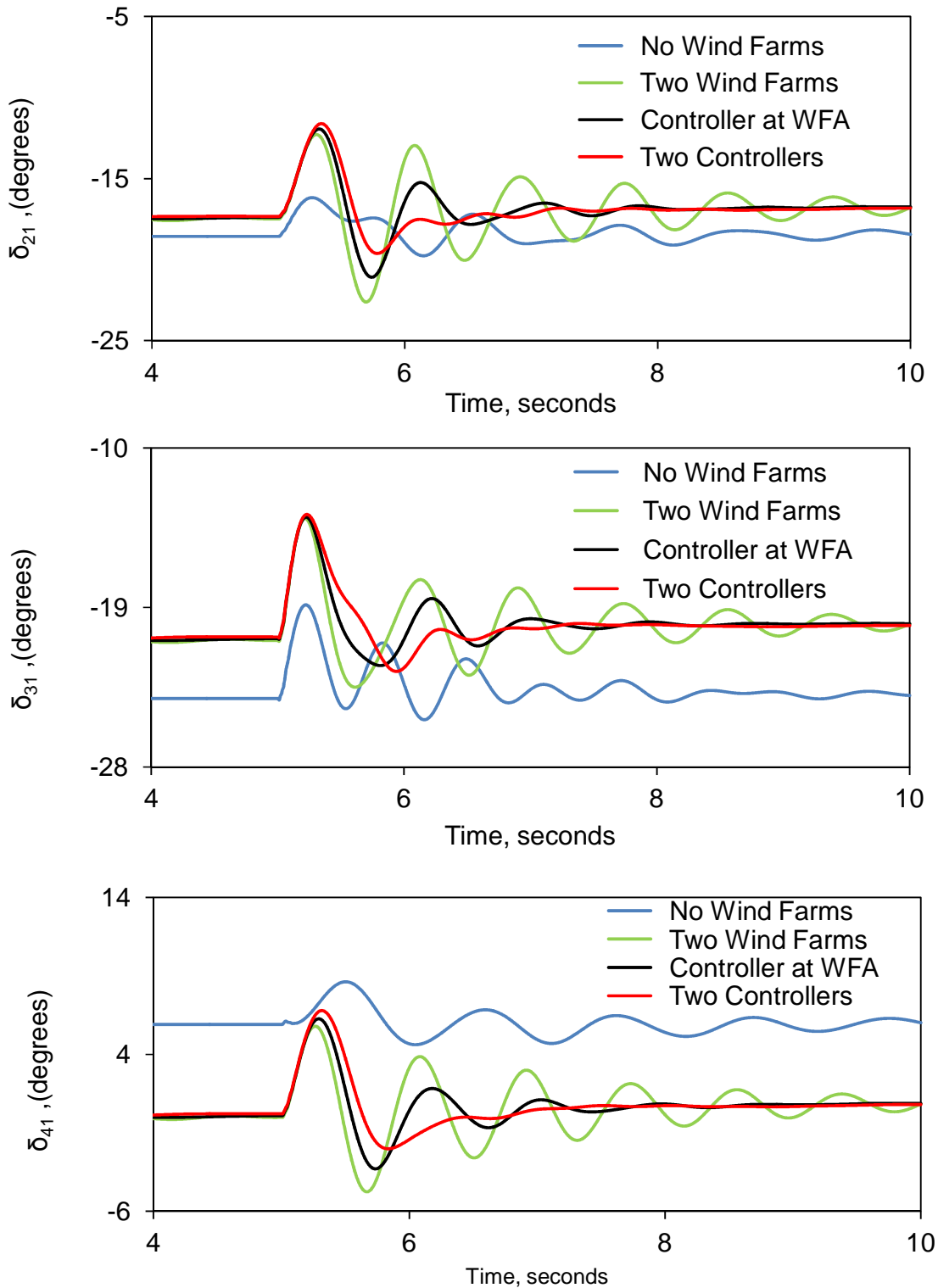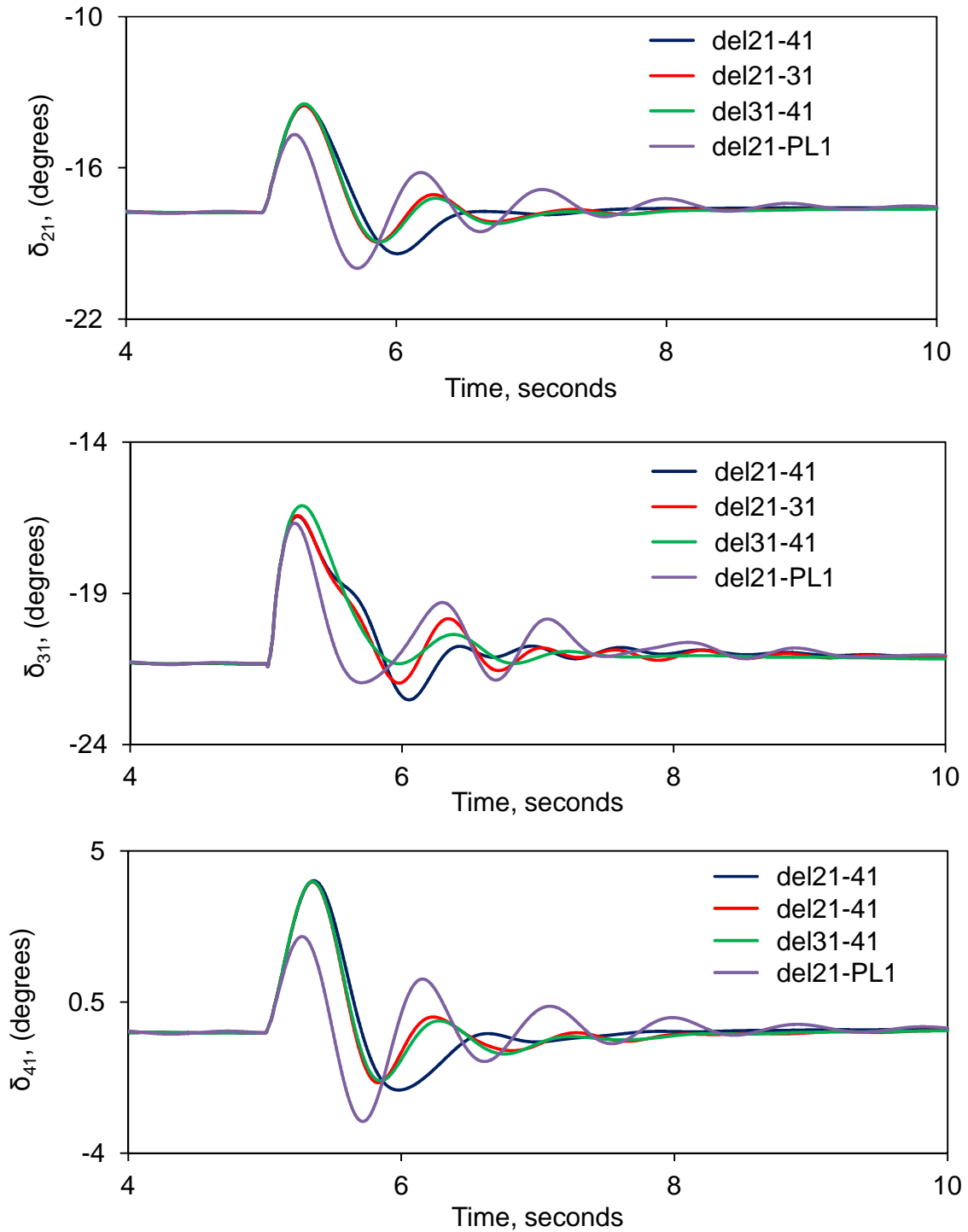
Figure 4.17: Effect of wind farm A supplemental control stabilizing signal on the generator load angles, measured with respect to generator 1 load angle, during and after clearing a 3-cycle, three-phase fault at bus 4. (DFIG-based wind farm supplemental controller is in the P control loop of the RSC).
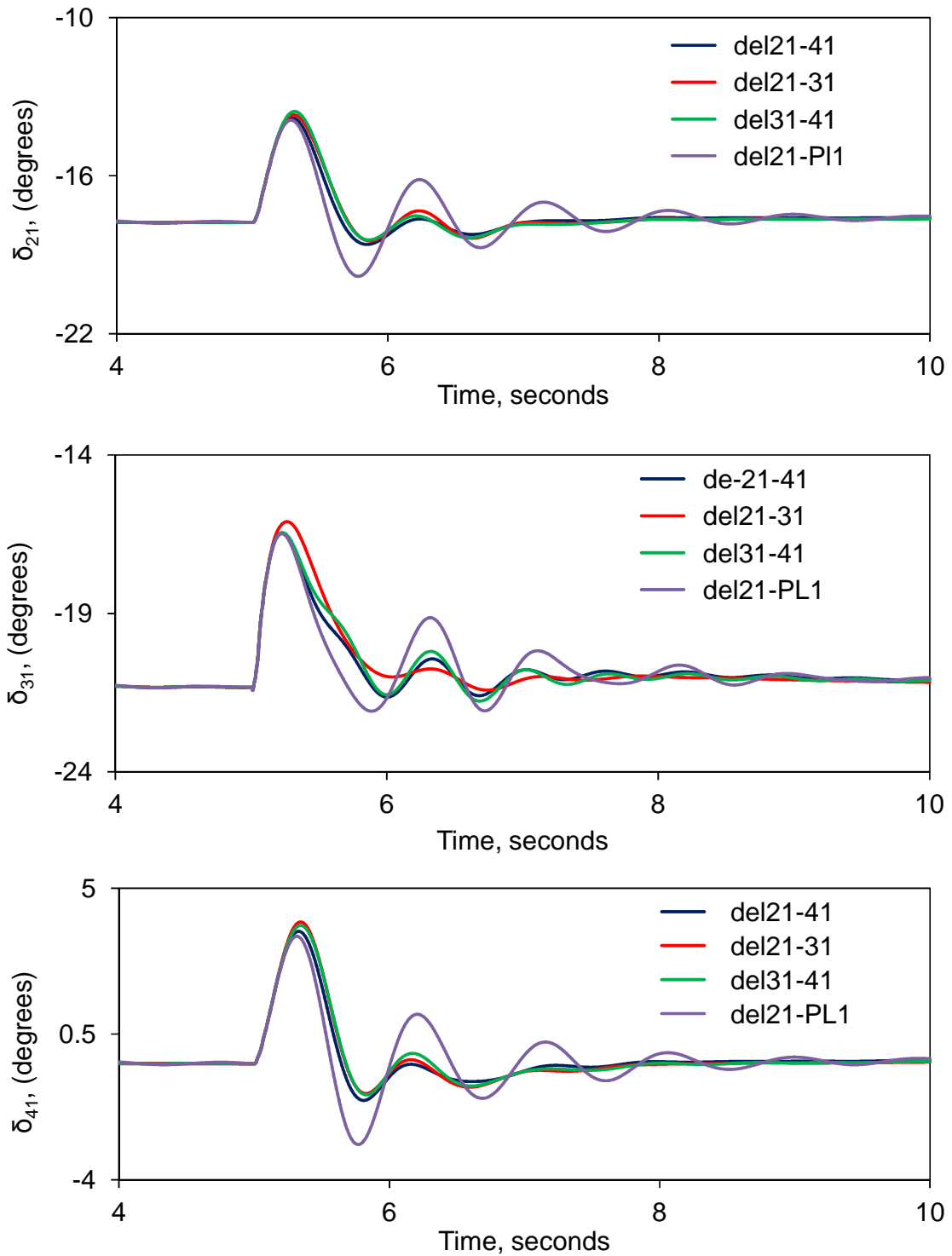
Figure 4.18: Effect of wind farm A supplemental control stabilizing signal on the generator load angles, measured with respect to generator 1 load angle, during and after clearing a 3-cycle, three-phase fault at bus 4. (DFIG-based wind farm supplemental controller is in the Q control loop of the RSC).
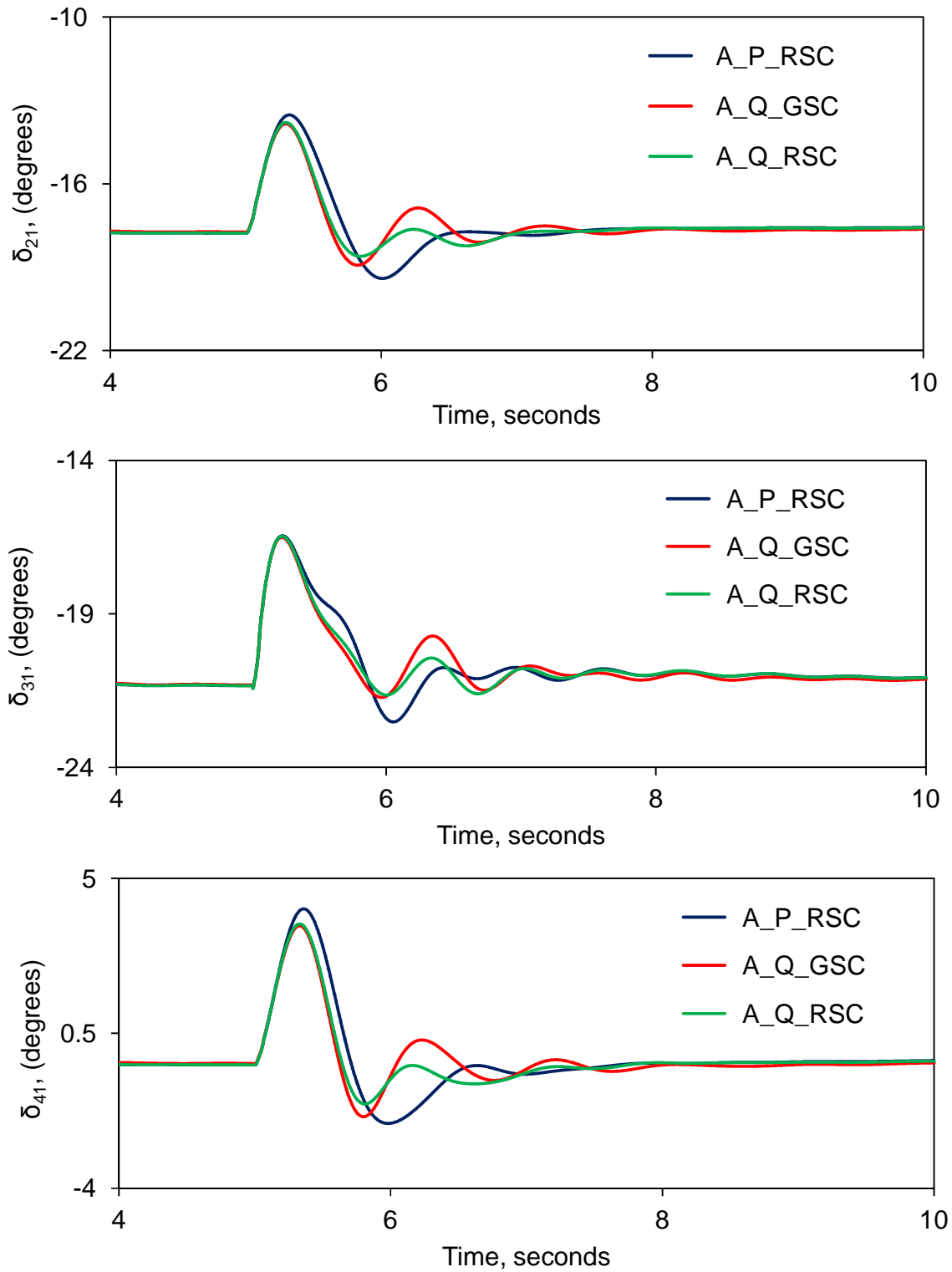
Figure 4.19: Generator load angles, measured with respect to generator 1 load angle, during and after clearing a 3-cycle, three-phase fault at bus 4. (DFIG-based wind farm supplemental controller stabilizing signal is δ_{41}).

94
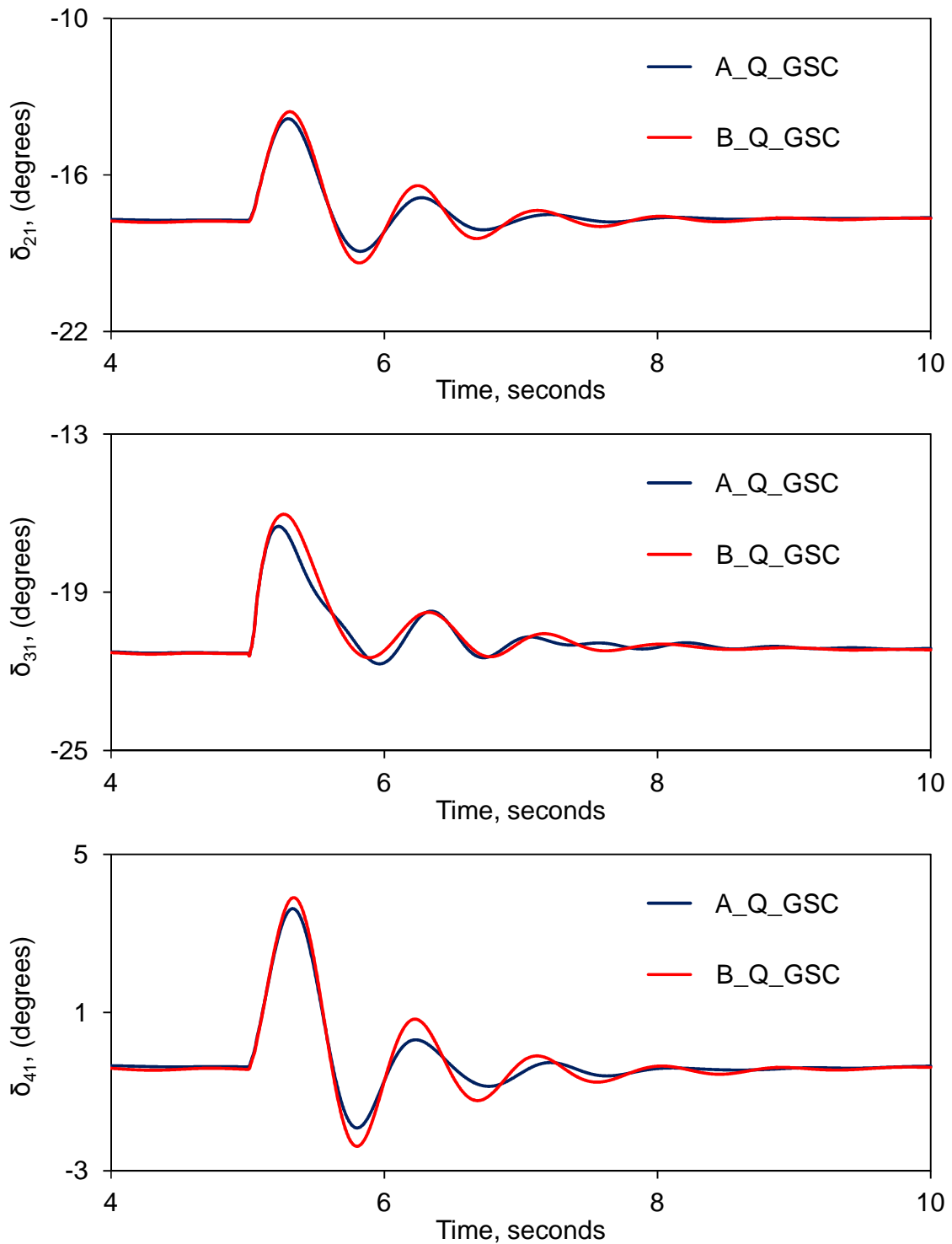
Figure 4.20: Impact of the best stabilizing signals of wind farms A and B GSC supplemental controls on the generator load angles, measured with respect to generator 1 load angle, during and after clearing a 3-cycle, three-phase fault at bus 4. (stabilizing signals for GSC A and B are δ_{41} and δ_{31} respectively).

95
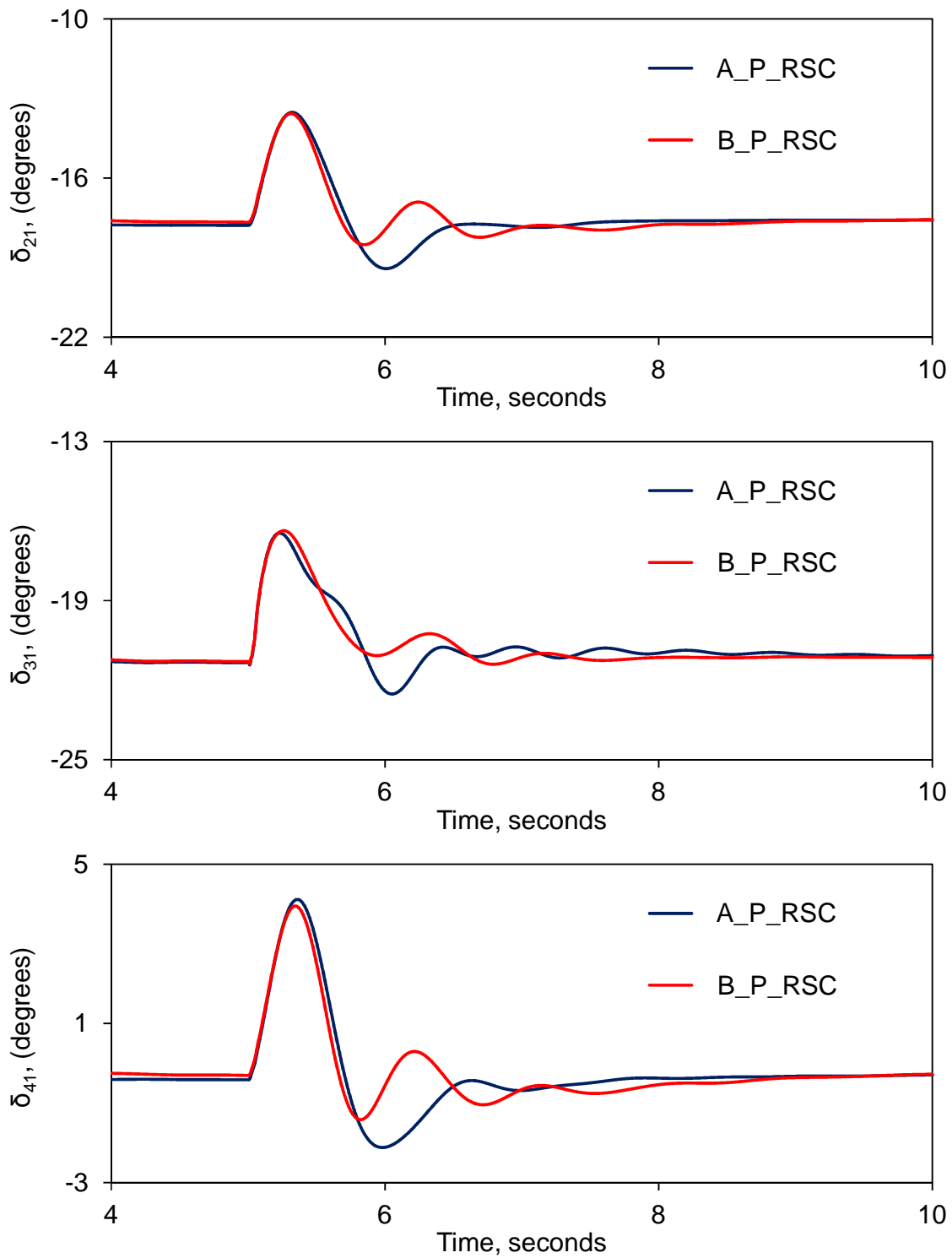
Figure 4.21: Impact of the best stabilizing signals of wind farms A and B RSC supplemental controls on the generator load angles, measured with respect to generator 1 load angle, during and after clearing a 3-cycle, three-phase fault at bus 4. (stabilizing signals for RSC A and B are δ_{41} and δ_{31} respectively).
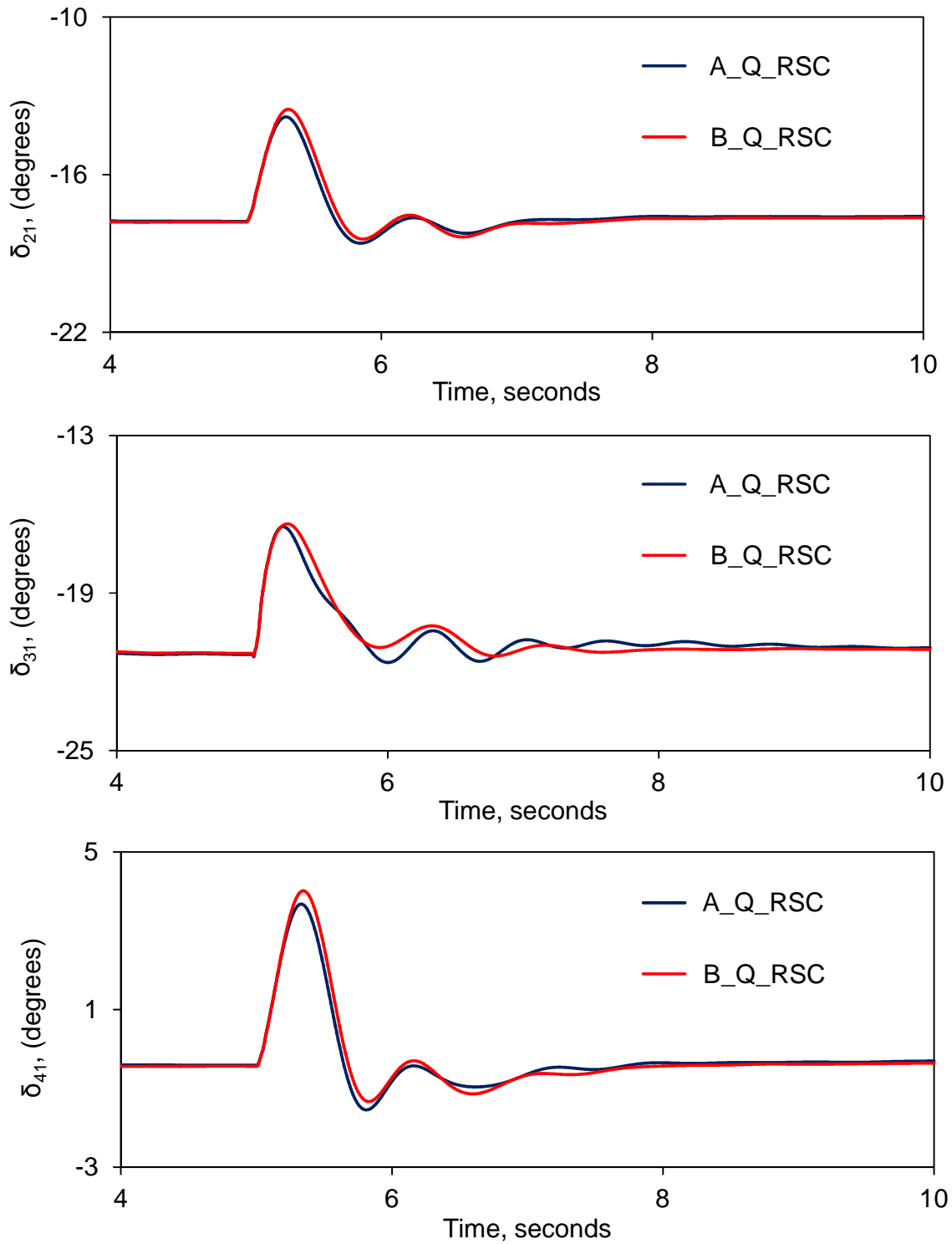
Figure 4.22: Impact of the best stabilizing signals of wind farms A and B RSC supplemental controls on the generator load angles, measured with respect to generator 1 load angle, during and after clearing a 3-cycle, three-phase fault at bus 4. (stabilizing signals for RSC A and B are δ_{41} and δ_{31} respectively).

4.8 Impact of the Fault Clearing Time on the Effectiveness of Wind Farms A and B Supplemental Controls

Figures 4.23 to 4.25 illustrate the generator load angles, measured with respect to generator 1 load angle, transient time responses during and after fault clearing a 4.5 cycle, three-phase fault at bus 4 for the case of wind farm A supplemental control. Table 4.11 shows the transfer functions of the TCSC and wind farm A supplemental controls after final tuning. As it can be seen from these figures, wind farm A supplemental control is still capable of providing significant damping to the system oscillations at the new fault clearing time. It can also be seen from the same figures that the Q control loop of the RSC is still the best location for the wind farm supplemental control. It is worth noting here that the results of similar studies conducted on wind farm B supplemental control, that are not reported in this thesis, have led "almost" to the above observations and conclusions.

Table 4.11: Transfer functions of the hybrid TCSC compensation scheme and wind farm A supplemental controls for a fault duration of 4.5 cycles.

Hybrid TCSC Compensation Scheme	DFIG-Based Wind Farm A
$G(s) = 0.25 \dfrac{10}{(s+10)} \dfrac{3s}{(3s+1)}$	$G_{DFIG\_P\_Loop\_RSC}(s) = 0.5 \dfrac{s}{(s+1)} \dfrac{1}{(s+8)}$
	$G_{DFIG\_Q\_Loop\_RSC}(s) = 0.3 \dfrac{s}{(s+15)} \dfrac{1}{(s+2)}$
	$G_{DFIG\_Q\_Loop\_GSC}(s) = 0.1 \dfrac{s}{(s+1)} \dfrac{1}{(s+5)}$
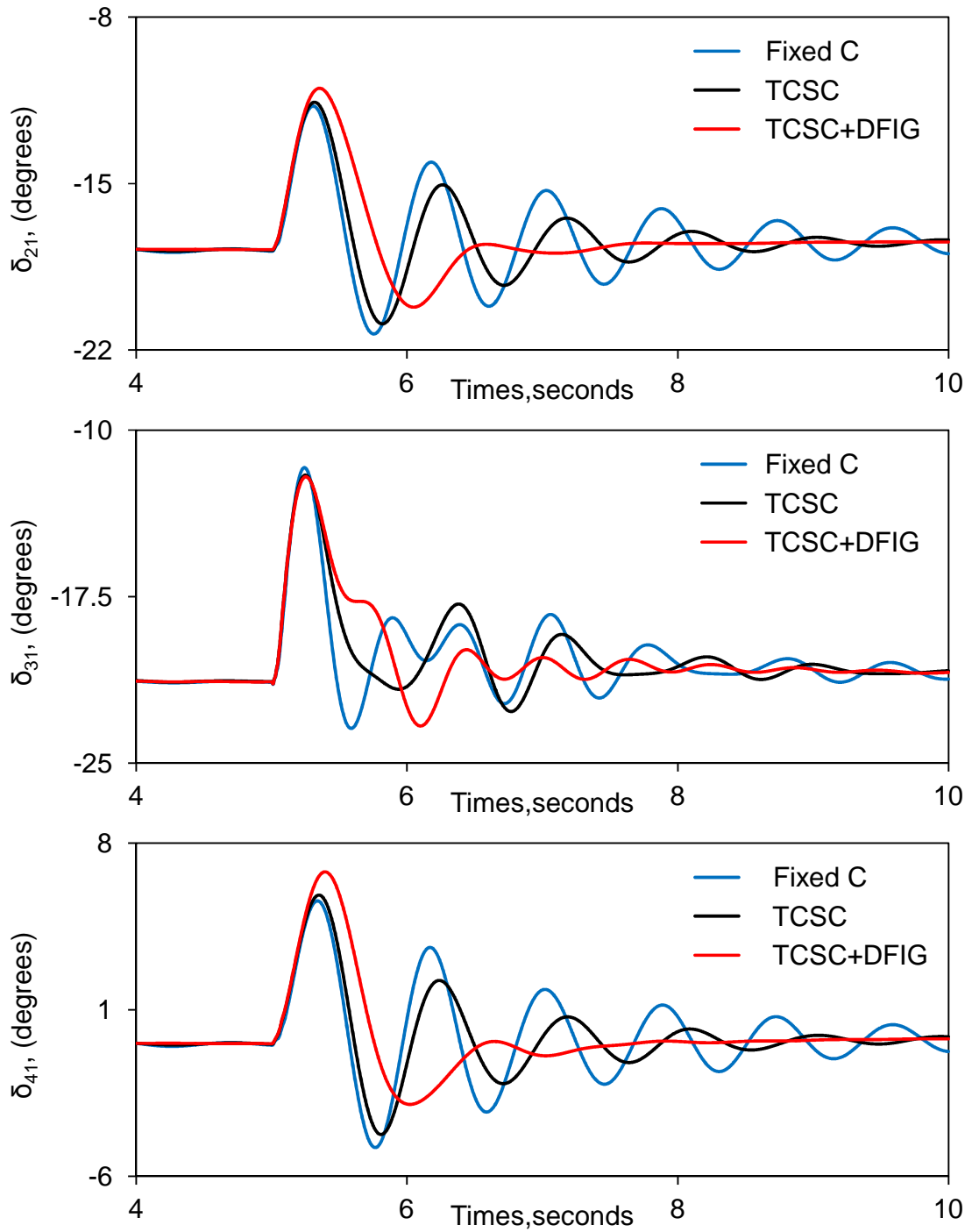
Figure 4.23: Generator load angles and speeds, measured with respect to generator 1 load angle and speed, and transmission line real power flow transient time responses during and after clearing a 4.5-cycle, three-phase fault at bus 4 (supplemental control is in the P control loop of the RSC of wind farm A).
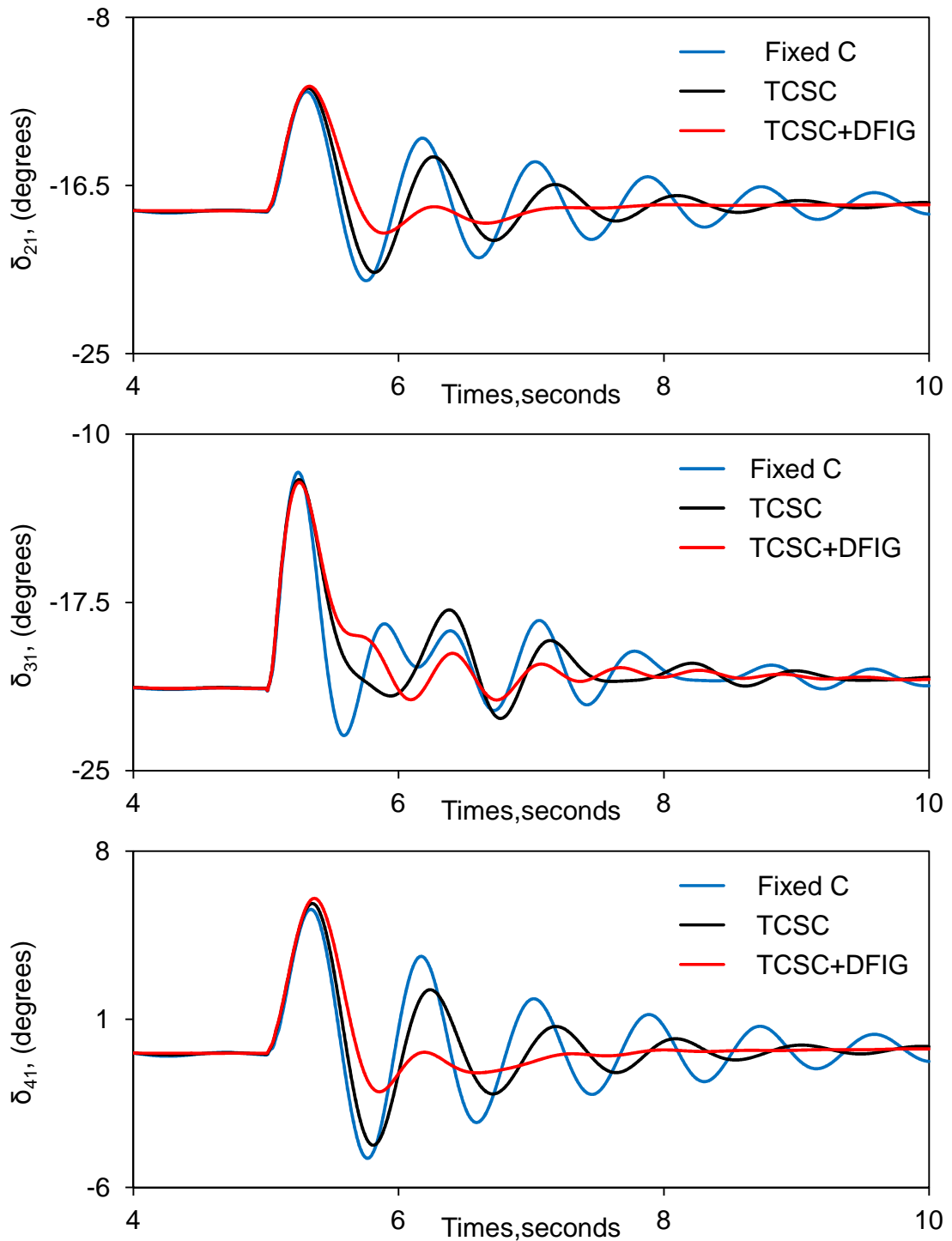
**Figure 4.24:** Generator load angles and speeds, measured with respect to generator 1 load angle and speed, and transmission line real power flow transient time responses during and after clearing a 4.5-cycle, three-phase fault at bus 4 (supplemental control is in the Q control loop of the RSC of wind farm A).

100
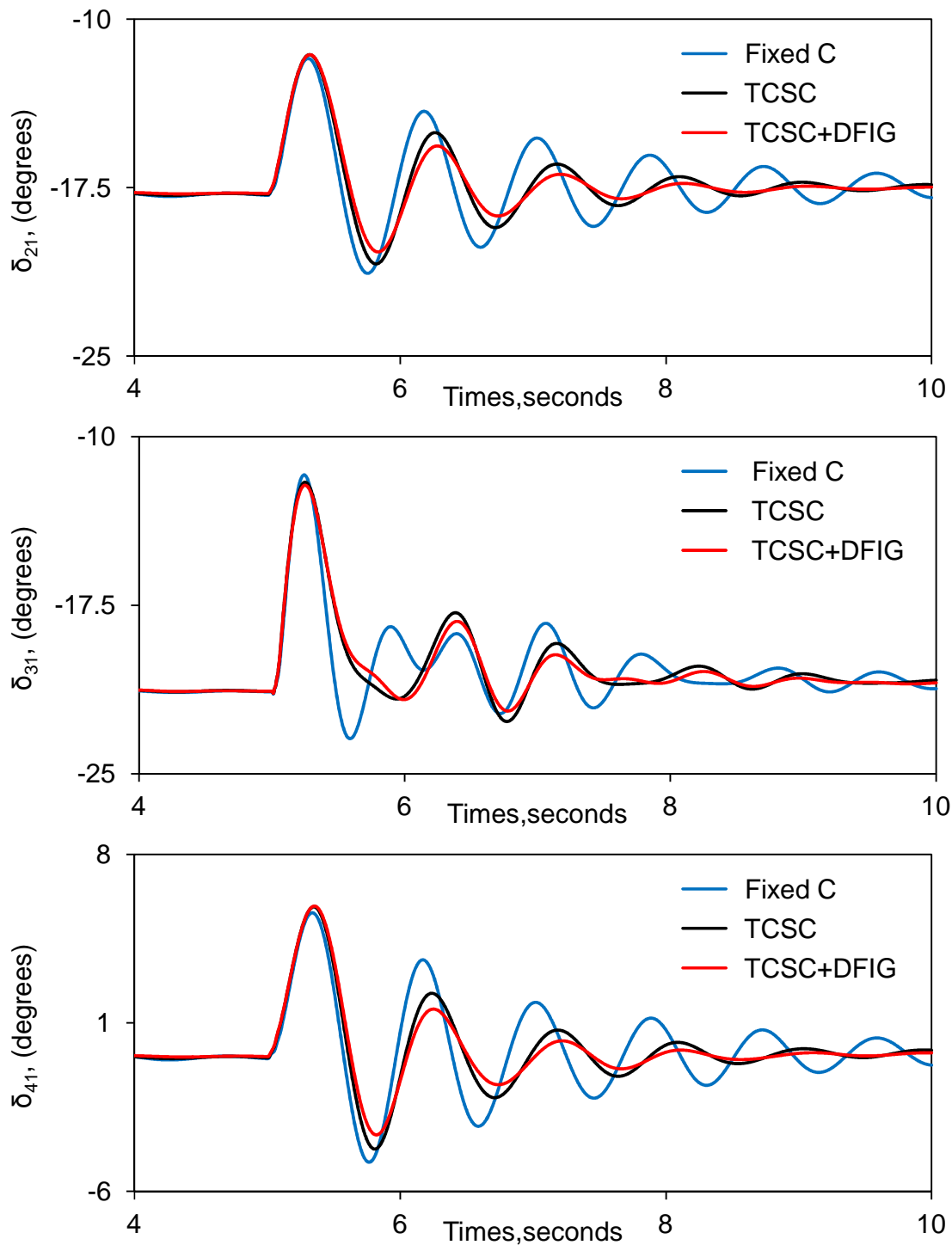
Figure 4.25: Generator load angles and speeds, measured with respect to generator 1 load angle and speed, and transmission line real power flow transient time responses during and after clearing a 4.5-cycle, three-phase fault at bus 4 (supplemental control is in the Q control loop of the GSC of wind farm A).

4.9   Summary

In this chapter, the effectiveness of supplemental controls for hybrid single-phase-TCSC compensation scheme and DFIG-based wind farms in damping power system oscillations resulting from clearing system faults is investigated through several case studies of time-domain simulations. In this context, the effects of the proportion of the single-phase-TCSC to the fixed capacitor reactance of its phase, the location of the wind farm supplemental controls and their stabilizing signals as well as the fault clearing time on damping power system oscillations are explored. The main conclusions drawn from the results of these studies are presented in the next chapter.

Chapter 5

SUMMARY AND CONCLUSIONS

5.1   Summary

Wind, which is a sustainable source of clean power, is the world's fastest growing energy source with sustained worldwide growth rates in excess of 30% annually. The innovative research and developments of efficient wind turbines during the last decade have lowered the cost of wind generated power, so that today, it became an integral part of the electric grid. Although there are different types of wind turbines, most of large wind farms in North America employ Doubly-Fed Induction Generator (DFIG) wind turbines because of the great flexibility of their converter controls.

A problem of interest in the power industry at which DFIG-based wind farms controllers could play a role in it is the mitigation of low frequency oscillations that often arise between areas in a large interconnected power network. These oscillations are due to the dynamics of inter-area power transfer and often exhibit poor damping when the aggregate power transfer over a corridor is high relative to the transmission strength. Inter-area oscillations can severely restrict system operations by requiring the curtailment of electric power transfers as an operational measure. These oscillations can also lead to widespread system disturbances if cascading outages of transmission lines occur due to oscillatory power swings.

This thesis reports the results of the investigations that were carried out to explore the potential use of supplemental controls of a phase imbalance hybrid single-phase-TCSC compensation scheme and DFIG-based wind farms in damping power system oscillations in multi-machine power systems.

A brief review of the benefits of series compensation of transmission lines is presented in Chapter 1. The inability of series capacitors in providing adequate damping to power system oscillations as well as their contribution to the subsynchronous resonance phenomenon are also discussed in this chapter.

In Chapter 2, the system used in the studies conducted in this thesis is introduced and the mathematical models of its components are presented. The results of digital time-domain simulations of a case study for the system with no supplemental controls during a three-phase fault are also presented in this chapter.

In Chapter 3, comprehensive descriptions of the TCSC, its three modes of operation and the analysis of its net reactance are presented. The phase imbalanced hybrid single-phase-TCSC compensation scheme and its modeling in the ElectroMagnetic Transient Program (EMTP-RV) are also presented.

In Chapter 4, several case studies investigating the effects of the proportion of the single-phase-TCSC reactance to the reactance of the fixed capacitor of its phase, the wind farm supplemental control stabilizing signals and their locations in the reactive power control loop of the GSC or in the real or the reactive power control loops of the RSC on the damping of power system oscillations are documented. These studies are intended to demonstrate the effectiveness of the phase imbalance hybrid single-phase-TCSC compensation scheme and DFIG-based wind farm supplemental controls in damping power system oscillations resulting from clearing system faults.

5.2   Conclusions

The studies conducted in this thesis yield the following conclusions for the system under study:

1.   The series capacitor compensated system is first swing stable for three-phase faults, but the post-contingency oscillations are not well damped.

2.   Although the system has three natural modes of oscillation, generators 2, 3 and 4 tend to oscillate at a single frequency (approximately 1.4 Hz).

3.   Increasing the proportion of the single-phase-TCSC to the fixed capacitor of its phase results in improving the damping of system oscillations. Choosing the value of such a proportion can be considered as an optimization task between dynamic stability improvements and economical and reliability advantages of fixed series capacitors.

4.   In the majority of the case studies, adequate power system oscillations damping is obtained with proportional-type TCSC and wind farm supplemental controllers.

5. The best damping of the relative load angle responses are achieved when the stabilizing signals for the hybrid single-phase-TCSC and wind farm A supplemental controllers are respectively, the deviations of generators 2 and 4 load angles, both with respect to generator 1 load angle. On the other hand, the best damping of the relative load angle responses are achieved when the stabilizing signals for the hybrid single-phase-TCSC and wind farm B supplemental controllers are respectively, the deviations of generators 2 and 3 load angles, both with respect to generator 1 load angle.

6. The supplemental controls of the DFIG-based wind farms are very effective in enhancing the damping of power system oscillations whether they are installed in the reactive power control loop of the GSC or in the real or the reactive power control loops of the RSC. Of these three options, the reactive power control loop of the RSC tends to provide "relatively" a better damping for the system oscillations. In the studies conducted in this thesis, no attempt has been made to install supplemental controls simultaneously at the P and Q control loops of the RSC. It is the author's belief that such an arrangement is not necessary.

7. The hybrid single-phase-TCSC and wind farm supplemental controllers are effective in damping system oscillations resulting from clearing system faults with different fault durations.

8. Slight (insignificant) increases in the first swing of some generators are occurred in the case of supplemental controls of the hybrid TCSC compensation scheme and the DFIG-based wind farms. It should be emphasized here that the main task of these supplemental controllers is to damp power system oscillations in the "already stable" system under study. For transient stability control of marginally stable power systems, different TCSC control methodologies are usually used.

9. With regard to the concern over the case of large share of wind power generation which results in reducing the total inertia of the synchronous generators and degrading the system transient stability, it has been shown that in such a case; properly designed supplemental controllers for the wind farm converters could be an asset in improving the system transient stability rather than degrading it.

This thesis is one step towards highlighting the potential of the damping capability of renewable energy systems that could be sold as ancillary service. The ultimate objective is to combine wind farms with conventional power plants and FACTS controllers so that together, they provide the real and reactive modulating powers in wide-area control of large power systems.

REFERENCES

[1]   American Wind Energy Association, web site: http://www.awea.org/.

[2]   P.M. Anderson, *Subsynchronous resonance in power systems,* New York, IEEE Press, 1990.

[3]   P.M. Anderson and R.G. Farmer, *Series Compensation of Power Systems*, PBLSH!, 1996.

[4]   R. Billinton, M. Fotuhi-Firuzabad and S.O. Faried, "Power System Reliability Enhancement using a Thyristor Controlled Series Capacitor," IEEE Transactions on Power Systems, Vol. 14, No. 1, February 1999, pp. 369-374.

[5]   J.L. Batho, J.E. Hardy and N. Tolmunen, "Series Capacitor Installations in the B.C. Hydro 500 kV System," IEEE Transactions on Power Apparatus and Systems, Vol. PAS-96, No. 6, November/December 1977, pp. 1767.1776.

[6]   "Increased Power Transmission Capacity on 500 kV Grid by Installation and Refurbishing of Series Capacitors," ABB online web site, [http://www05.abb.com/global/scot/scot221.nsf/veritydisplay/7f8d670d8379cc50c1256fd a003b4d0a/$File/McLeese%20A02-0159E.pdf].

[7]   D.N. Kosterev, C.W. Taylor, W.A. Mittelstadt, "Model Validation for the August 10, 1996 WSCC System Outage," IEEE Transactions on Power Systems, Vol. 14, No. 3, August 1999, pp. 967-979.

[8]   R. Witzmann, Damping of Interarea Oscillations in Large Interconnected Power Systems," Proceedings of the International Conference on Power Systems Transients (IPST01), Rio de Janeiro, Brazil, June 24-28, 2001, paper No. 197.

[9]   Y.H. Song and A.T. Johns, *Flexible AC Transmission Systems (FACTS)*, London, Institution of Electrical Engineers, 1999.

[10]   N.G. Hingorani and L. Gyugyi, *Understanding FACTS: Concepts and Technology of Flexible AC Transmission Systems,* New York, IEEE Press, 2000.

[11]   C. Gama, "Brazilian North-South Interconnection Control-Application and Operating Experience with a TCSC," Proceedings of the 1999 IEEE PES Summer meeting, Edmonton, Alberta, Canada, July 18-22, 1999, Vol. 2, pp. 1103-1108.

[12]   C. Gama and L. Angquist, "Commissioning and Operative Experience of TCSC for Damping Power Oscillation in the Brazilian North-South Interconnection," CIGRE, Session 2000, Paris, France, paper No. 14-104.

[13]   H.A. Othman and L. Angquist, "Analytical Modeling of Thyristor-Controlled Series Capacitors for SSR Studies," IEEE Transactions on Power Systems, Vol. 11, No. 1, February 1996, pp. 119-127.

[14]   B.K. Perkins and M.R. Iravani, "Dynamic Modeling of a TCSC with Application to SSR Analysis" IEEE Transactions on Power Systems, Vol. 12, No. 4, pp. 1619-1625, 1997.

[15] R.J. Piwko, C.W. Wegner, S.J. Kinney and J.D. Eden, "Subsynchronous Resonance Performance Tests of the Slatt Thyristor-Controlled Series Capacitor," IEEE Transactions on Power Delivery, Vol. 11, No. 2, April 1996, pp. 1112-1119.

[16] W. Zhu, R. Spee, R.R. Mohler, G.C. Alexander, W.A. Mittelstadt and D. Maratukulam, "An EMTP Study of SSR Mitigation Using the Thyristor- Controlled Series Capacitor," IEEE Transactions on Power Delivery, Vol. 10, No. 3, July 1995, pp. 1479-1485.

[17] Naoto Kakimoto and Anan Phongphanphanee, "Subsynchronous Resonance Damping Control of Thyristor-Controlled Series Capacitor," IEEE Transactions on Power Delivery, Vol. 18, No. 3, July 2003, pp. 1051-1059.

[18] R. Rajaraman, I. Dobson, R. H. Lasseter, and Y. Shern, "Computing the Damping of Subsynchronous Oscillations due to a Thyristor Controlled Series Capacitor", IEEE Transactions on Power Delivery, Vol. 11, No. 2, April 1996, pp. 1120–1127.

[19] P. Mattavelli, A.M. Stankovic`, and G.C. Verghese, "SSR Analysis with Dynamic Phasor Model of Thyristor-Controlled Series Capacitor," IEEE Transactions on Power Systems, Vol. 14, No. 1, February 1999, pp. 200–208.

[20] Alireza Daneshpooy and A.M. Gole, "Frequency Response of the Thyristor Controlled Series Capacitor," IEEE Transactions on Power Delivery, Vol. 16, No. 1, January 2001, pp. 53-58.

[21] J.F. Hauer, W.A. Mittelstadt, R.J. Piwko, B.L. Damsky, J.D. Eden, "Modulation and SSR Tests Performed on the BPA 500 kV Thyristor Controlled Series Capacitor Unit at Slatt Substation," IEEE Transactions on Power Systems, Vol. 11, No. 2. May 1996, pp. 801-806.

[22] P.S. Dolan, J.R. Smith and W.A. Mittelstadt, "A Study of TCSC Optimal Damping Control Parameters for Different Operating Conditions," IEEE Transactions on Power Systems, Vol. 10, No. 4, November 1995, pp. 1972-1978.

[23] J. Urbanek, R.J. Piwko, E.V. Larsen, B.L. Damsky, B.C. Furumasu and W. Mittlestadt, "Thyristor Controlled Series Compensation Prototype Installation at the Slatt 500 kV Substation," IEEE Transactions on Power Delivery, Vol. 8, No. 3, July 1993, pp. 1460-1469.

[24] S. Nyati, C.A. Wegner, R.W. Delmerico, R.J. Piwko, D.H. Baker and A. Edris, "Effectiveness of Thyristor Controlled Series Capacitor in Enhancing Power System Dynamics: An Analog Simulator Study," IEEE Transactions on Power Delivery, Vol. 9, No. 2, April 1994, pp. 1018-1027.

[25] X. R. Chen, N.C. Pahalawaththa, U.D. Annakkage and C.S. Kumble, "Design of Decentralised output Feedback TCSC Damping Controllers by Using Simulated Annealing," IEE Proceedings, Generation, Transmission and Distribution, Vol. 145, No. 5, September 1998, pp. 553-558.

[26] Y.Y. Hsu and T.S. Luor, "Damping of Power System Oscillations using Adaptive Thyristor-Controlled Series Compensators Tuned by Artificial Neural Networks," IEE Proceedings, Generation, Transmission and Distribution, Vol. 146, No. 2, March 1999, pp. 137-142.

[27] X.X. Zhou and J. Liang, "Nonlinear Adaptive Control of TCSC to Improve the Performance of Power Systems," IEE Proceedings, Generation, Transmission and Distribution, Vol. 146, No. 3, May 1999, pp. 301-305.

[28] D. Rai, S.O. Faried, G. Ramakrishna, and A. Edris," Damping Inter-Area Oscillations using Phase Imbalanced Series Compensation Schemes," IEEE Transactions on Power Systems, Vol. 26, No. 3, August 2011, pp. 1753-1761.

[29] D. Rai, G. Ramakrishna, S.O. Faried and A. Edris," Enhancement of Power System Dynamics Using a Phase Imbalanced Series Compensation Scheme," IEEE Transactions on Power Systems, Vol. 25, No. 2, May 2010, pp. 966-974.

[30] D. Rai, Power System Dynamics Enhancement Through FACTS Devices and Adaptive Control, Ph.D. thesis, University of Saskatchewan, 2012.

[31] S. Pan, Damping Power System Oscillations Using a Phase Imbalanced Hybrid Series Capacitive Compensation Scheme, M.Sc. Thesis, University of Saskatchewan, 2010.

[32] Z. Miao, L. Fan, D. Osborn and S. Yuvarajan," Control of DFIG-Based Wind Generation to Improve Interarea Oscillation Damping," IEEE Transactions on Energy Conversion, Vol. 24, No. 2, June 2009, pp. 415-422.

[33] L. Fan, H. Yin and Z. Miao," On Active/Reactive Power Modulation of DFIG-Based Wind Generation for Interarea Oscillation Damping," IEEE Transactions on Energy Conversion, Vol. 26, No. 2, June 2011, pp. 513-521.

[34] N. Kshatriya, U.D. Annakkage, F.M. Hughes and A.M. Gole, "Optimized Partial Eigenstructure Assignment-Based Design of a Combined PSS and Active Damping Controller for a DFIG," IEEE Transactions on Power Systems, Vol. 25, No. 2, May 2010, pp. 866-876.

[35] T. Knuppel, J.N. Nielsen, K.H. Jensen, A. Dixon and J. Ostergaard," Power Oscillation Damping Controller for Wind Power Plant Utilizing Wind Turbine Inertia as Energy Storage," 2011 IEEE Power and Energy Society General meeting, Detroit, MI, July 24-28, 2011, Paper No. 2011GM0059.

[36] L. Wang, K-H Wang, "Dynamic Stability Analysis of a DFIG-Based Offshore Wind Farm Connected to a Power Grid Through an HVDC Link," IEEE Transactions on Power Systems, Vol. 26, No. 3, August 2011, pp. 1501-1510.

[37] Y. Lei, A. Mullane, G. Lightbody and R. Yacamini, "Modeling of the Wind Turbine with a Doubly Fed Induction Generator for Grid Integration Studies," IEEE Transactions on Energy Conversion, Vol. 21, No. 1, March 2006, pp. 257-264.

[38] C. Zhu, L. Fan and M. Hu, "Control and Analysis of DFIG-Based Wind Turbines in a Series Compensated Network for SSR Damping," 2010 IEEE Power and Energy Society General Meeting, Minneapolis, MN, July 25-29, 2010, Digital Object Identifier: 10.1109/PES.2010.5590091.

[39] L. Yang, Z. Xu, J. Ostergaard, Z.Y. Dong, K.P. Wong and X. Ma, "Oscillatory Stability and Eigenvalue Sensitivity Analysis of a DFIG Wind Turbine System," IEEE Transactions on Energy Conversion, Vol. 26, No. 1, March 2011, pp. 328-339.

[40] L. Fan, R. Kavasseri, Z. Lee Miao and C. Zhu, "Modeling of DFIG-Based Wind Farms for SSR Analysis," IEEE Transactions on Power Delivery, Vol. 25, No. 4, October 2010, pp. 2073-2082.

[41] L. Xu, L. Yao and C. Sasse," Grid Integration of Large DFIG-Based Wind Farms Using VSC Transmission," IEEE Transactions on Power Systems, Vol. 22, No. 3, August 2007, pp. 976-984.

[42] W. Qiao, G. Harley and G.K. Venayamoorthy," Coordinated Reactive Power Control of a Large Wind Farm and a STATCOM Using Heuristic Dynamic Programming," IEEE Transactions on Energy Conversion, Vol. 24, No. 2, June 2009, pp. 493-503.

[43] S.O. Faried, I. Unal, D. Rai, and J. Mahseredjian, "Utilizing DFIG-Based Wind Farms for Damping Subsynchronous Resonance in Nearby Turbine-Generators," IEEE Transactions on Power Systems, Vol. 28, No. 1, February 2013, pp. 452-459.

[44] P. Kundur, *Power System Stability and Control,* New York, McGraw-Hill, 1994.

[45] Y. Yu, *Electric Power System Dynamics,* New York, Academic Press, 1983.

[46] O.I. Elgerd, *Electrical Energy Systems Theory*, McGraw-Hill, 1971.

[47] L. Wang, K-H Wang, "Dynamic Stability Analysis of a DFIG-Based Offshore Wind Farm Connected to a Power Grid Through an HVDC Link," IEEE Transactions on Power Systems, Vol. 26, No. 3, August 2011, pp. 1501-1510.

[48] Y. Lei, A. Mullane, G. Lightbody and R. Yacamini, "Modeling of the Wind Turbine with a Doubly Fed Induction Generator for Grid Integration Studies," IEEE Transactions on Energy Conversion, Vol. 21, No. 1, March 2006, pp. 257-264.

[49] C. Zhu, L. Fan and M. Hu, "Control and Analysis of DFIG-Based Wind Turbines in a Series Compensated Network for SSR Damping," 2010 IEEE Power and Energy Society General Meeting, Minneapolis, MN, July 25-29, 2010, Digital Object Identifier: 10.1109/PES.2010.5590091.

[50] L. Yang, Z. Xu, J. Ostergaard, Z.Y. Dong, K.P. Wong and X. Ma, "Oscillatory Stability and Eigenvalue Sensitivity Analysis of a DFIG Wind Turbine System," IEEE Transactions on Energy Conversion, Vol. 26, No. 1, March 2011, pp. 328-339.

[51] L. Fan, R. Kavasseri, Z. Lee Miao and C. Zhu, "Modeling of DFIG-Based Wind Farms for SSR Analysis," IEEE Transactions on Power Delivery, Vol. 25, No. 4, October 2010, pp. 2073-2082.

[52] L. Xu, L. Yao and C. Sasse," Grid Integration of Large DFIG-Based Wind Farms Using VSC Transmission," IEEE Transactions on Power Systems, Vol. 22, No. 3, August 2007, pp. 976-984.

[53] W. Qiao, G. Harley and G.K. Venayamoorthy," Coordinated Reactive Power Control of a Large Wind Farm and a STATCOM Using Heuristic Dynamic Programming," IEEE Transactions on Energy Conversion, Vol. 24, No. 2, June 2009, pp. 493-503.

[54] A.D. Hansen, G. Michalke, P. Sorensen, T. Lund and Florin Iov, "Co-ordinated Voltage Control of DFIG Wind Turbines in Uninterrupted Operation during Grid Faults," Wind

Energy, Vol. 10, No. 1, January/February 2007, pp. 51-68, published online, DOI: 10.1002/we.207.

[55] A. Daneshpooy and A.M. Gole," Frequency Response of the Thyristor Controlled Series Capacitor," IEEE Transactions on Power Delivery, Vol. 16, No. 1, January 2001, pp. 53-58.

[56] K. Kabiri, S. Henschel and H.W. Dommel, "Resistive Behavior of Thyristor-Controlled Series Capacitors at Subsynchronous Frequencies," IEEE Transactions on Power Delivery, Vol. 19, No. 1, January 2004, pp. 374-379.

[57] R.M. Mathur and R.K. Varma, *Thyristor-Based FACTS Controllers for Electrical Transmission Systems,* Piscataway, NJ, IEEE, 2002.

[58] H. Xie and L. Ängquist, "Synchronous Voltage Reversal control of TCSC – impact on SSR conditions," Proceedings of the Nordic Workshop on Power and Industrial Electronics (NORPIE), 2004.

[59] Lennart Ängquist, "Synchronous Voltage Reversal Control of Thyristor Controlled Series Capacitor," Royal Institute of Technology, TRITA-ETS-2002-07, ISSN 1650-674X.

[60] L. Angquist and C. Gama, "Damping Algorithm based on Phasor Estimation," Proceedings of the IEEE Power Engineering Society Winter Meeting, Columbus, Ohio, January 28 – February 1, 2001, Vol. 3, pp. 1160-1165.

[61] D. Rai, S.O. Faried, G. Ramakrishna, and A. Edris, "Hybrid Series Compensation Scheme Capable of Damping Subsynchronous Resonance," IET Generation, Transmission and Distribution, Vol. 4, No. 3, March 2010, pp. 456-466.

[62] A.M. Gole, S. Filizadeh, R.W. Menzies, and P.L. Wilson, "Optimization-enabled Electromagnetic Transient Simulation," IEEE Transactions on Power Delivery, Vol. 20, No. 1, January 2005, pp. 512–518.

[63] A.M. Gole, S. Filizadeh, and P.L. Wilson, "Inclusion of Robustness into Design using Optimization-enabled Transient Simulation," IEEE Transactions on Power Delivery, Vol. 20, No. 3, July 2005, pp. 1991–1997.

[64] R. Grünbaum and Jacques Pernot, "Thyristor Controlled Series Compensation: A State of the Art Approach for Optimization of Transmission over Power Links, ABB online web site:
[http://www05.abb.com/global/scot/scot221.nsf/veritydisplay/d578889d05b3ba01c1256f da003b4cff/$File/SEE_FIILE2001_TCSC.pdf]

[65] I. Unal and S. O. Faried, "Damping Power System Oscillations Using Phase Imbalanced Series Capacitive Compensation and DFIG-Based Wind Farms" Proceedings of the Innovative Smart Grid Technologies Europe 2012, Berlin Germany, October 14-17, 2012.

[66] N. Yang, Q. Liu and J. McCalley, "TCSC Controller Design for Interarea Oscillations," IEEE Transactions on Power Systems, Vol. 13, No. 4, November 1998, pp. 1304-1309.

[67] X. Chen, N. Pahalawaththa, U. Annakkage and C. Kumbe, "Output Feedback TCSC Controllers to Improve Damping of Meshed Multi-Machine Power Systems," IEE

Proceedings, Generation, Transmission and Distribution, Vol. 44, No. 3, May 1997, pp. 243-248.

[68]   J. Machowski, S. Robak and J. Bialek, "Damping of Power Swings by Optimal Control of Series Compensators," Proceedings of the 10th International Conference on Power System Automation and Control *PSAC'97*, Bled, Slovenia, October 1-3, 1997, pp. 39-44.

[69]   J.F. Hauer, M.K. Donnelly, W.A. Mittelstadt, W. Litzenberger and D.J. Maratukulam, "Information Functions and Architecture for Networked Monitoring of Wide Area Power System Dynamics: Experience with the Evolving Western System Dynamic Information Network," Proceedings of the Sixth Symposium of Specialists on Electric Operational and Expansion Planning (VI SEPOPE), Bahia, Brazil, May 24-29, 1998.

[70]   B. Bhargava and A. Salazar, "Use of Synchronized Phasor Measurement System for Monitoring Power System Stability and System Dynamics in Real-Time," Proceedings of the 2008 IEEE PES GM, Pittsburgh, PA, July 20 – 24, 2008, pp. 1-8.

[71]   H. Ni, G.T. Heydt and L. Mili, "Power System Stability Agents using Robust Wide Area Control, "IEEE Transactions on Power Systems, Vol. 17, No. 4, November 2002, pp. 1123-1131.

[72]   X. Xie, J. Xiao, C. Lu and Y. Han, "Wide-Area Stability Control for Damping Interarea Oscillations of Interconnected Power Systems," IEE Proceedings, Generation, Transmission and Distribution, Vol. 153, No. 5, September 2006, pp. 507-514.

[73]   C.W. Taylor, D.E. Erickson, K.E. Martin, R.E. Wilson and V. Venkatasubramanian," WACS-Wide-Area Stability and Voltage Control System: R&D and Online Demonstration," Proceedings of IEEE, Vol. 93, No. 5, May 2005, pp. 892-906.

[74]   X. Zhou and J. Liang, "Overview of Control Schemes for TCSC to Enhance the Stability of Power Systems," IEE Proceedings, Generation, Transmission and Distribution, Vol. 146, No. 2, March 1999, pp. 125-130

[75]   I. Erlich, B. Gessesse, F. Shewarega, "Modeling and Performance Analysis of Wind Farms: A Case Study of the Ashegoda Wind Farm in Ethiopia",   IEEE   PES   Power Africa 2012 Conference and Exposition, Johannesburg, South Africa, 9-13 July 2012

APPENDIX A

DATA OF THE SYSTEM UNDER STUDY

A.1   Synchronous Generators

Table A.1: Synchronous generator data.

	G_1	G_2	G_3	G_4
Rating, MVA	2400	1000	1100	1100
Rated voltage, kV	26	26	26	26
Armature resistance, r_a , p.u.	0	0.0045	0.0045	0.0045
Leakage reactance, x_l , p.u.	0.13	0.14	0.12	0.12
Direct-axis synchronous reactance, x_d , p.u.	1.79	1.65	1.54	1.54
Quadrature-axis synchronous reactance, x_q , p.u.	1.71	1.59	1.5	1.5
Direct-axis transient reactance, x_d' , p.u.	0.169	0.25	0.23	0.23
Quadrature-axis transient reactance, x_q' , p.u.	0.228	0.46	0.42	0.42
Direct-axis subtransient reactance, x_d'' , p.u.	0.135	0.2	0.18	0.18
Quadrature-axis subtransient reactance, x_q'' , p.u.	0.2	0.2	0.18	0.18
Direct-axis transient open-circuit time constant, T_{do}' , s	4.3	4.5	3.7	3.7
Quadrature-axis transient open-circuit time constant, T_{qo}' , s	0.85	0.55	0.43	0.43
Direct-axis subtransient open-circuit time constant, T_{do}'' , s	0.032	0.04	0.04	0.04
Quadrature-axis subtransient open-circuit time constant, T_{qo}'' , s	0.05	0.09	0.06	0.06
Zero-sequence reactance, x_o , p.u.	0.13	0.14	0.12	0.12
Inertia constant, H, s	7	3.7	3.12	3.12

A.2 Transformers

Table A.2: Transformer data.

	T_1	T_2	T_3	T_4
Rating, MVA	2400	1000	1100	1100
Rated voltage, kV	26/500	26/500	26/500	26/500
Resistance, r_T, p.u.	0	0	0	0
Leakage reactance, x_T, p.u.	0.1	0.1	0.1	0.1

A.3 Transmission Lines

All transmission lines have the same series impedance and shunt admittance per unit length.

$$Z_{T.L.series} = 0.01864 + j\,0.3728\ \Omega/km$$

$$Y_{T.L.shunt} = j\,4.4739\ \mu S/km$$

Transmission voltage = 500 kV

A.4 System Loads

$$S_1 = 1950 + j\,200\ MVA$$

$$S_2 = 3437 + j\,250\ MVA$$

A.5 Excitation System

Table A.3: Excitation system data.

$K_A = 2$	$K_E = 1.0$
$K_{FE} = 0.03$	$T_A = 0.04$ s
$T_{FE} = 1.0$ s	$T_E = 0.01$s
$Lim\_max = 4.75$ p.u.	$Lim_min = $ -4.75 p.u.

A.6 Single Phase TCSC Data

Table A.4: TCSC data.

$K_p = 0.5$	$K_I = 5$
$C_{TCSC} = 72.63\ \mu F$	$L_{TCSC} = 15.50\ mH$

APPENDIX B

ADDITIONAL CASE STUDIES

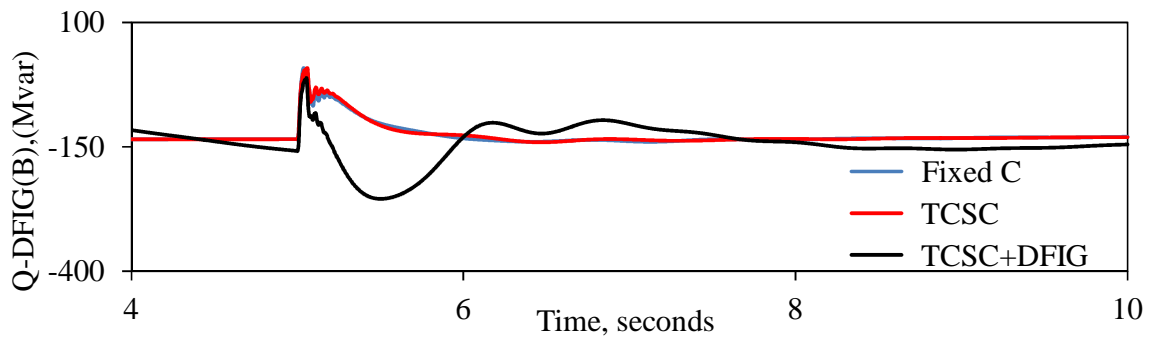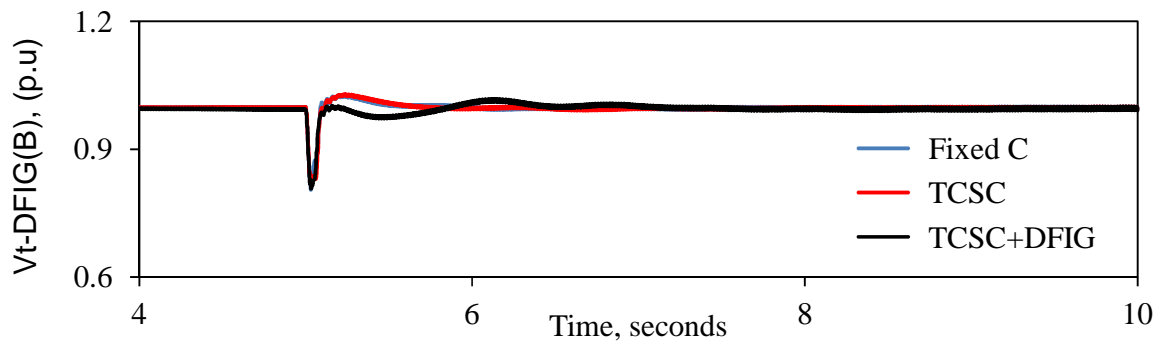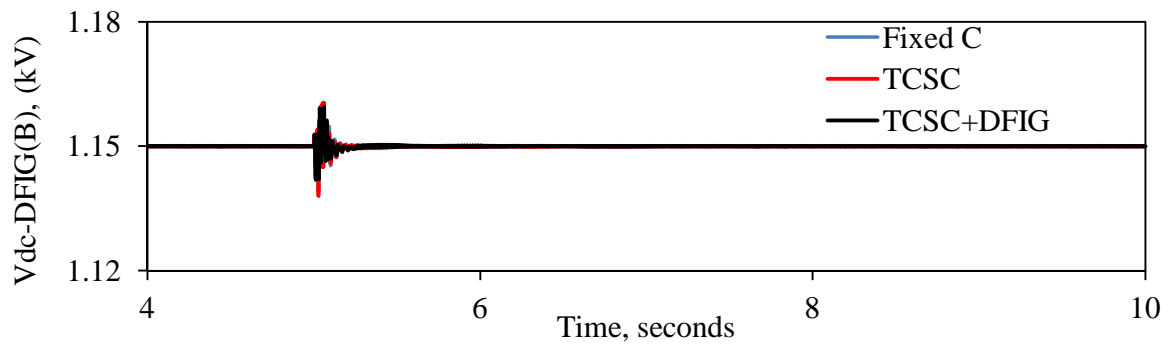## B.1 DFIG-Based Wind Farm Supplemental Control is in the Reactive Power Control Loop of the GSC of Wind Farm B

Figure B.1 illustrates the generator load angles and speeds, measured with respect to generator 1 load angle and speed, and the transmission line real power flow transient time responses during and after fault clearing. Figure B.2 illustrates the time responses of wind farm B real and reactive powers, terminal voltage and the BtB dc voltage for the same case. Table B.1 shows the transfer functions of the TCSC and wind farm B supplemental controls after final tuning. Comparing the responses for the case of Scheme I supplemental control alone (TCSC) to those for the case of Scheme I and the DFIG-based wind farm supplemental controls in Figure B.1, the positive contribution of wind farm B supplemental control to the damping of the system oscillations is very clear.

Table B.1: Transfer functions of the hybrid TCSC compensation scheme and wind farm B supplemental controllers (wind farm controller is in the Q control loop of the GSC).

|	Transfer Function
Hybrid TCSC Compensation Scheme	$G_{TCSC}(s) = 0.25 \dfrac{10}{(s+10)} \dfrac{3s}{(3s+1)}$
DFIG-Based Wind Farm B	$G_{DFIG\_Q\_Loop\_GSC}(s) = 0.15 \dfrac{s}{(s+0.04)} \dfrac{1}{(s+0.1)}$
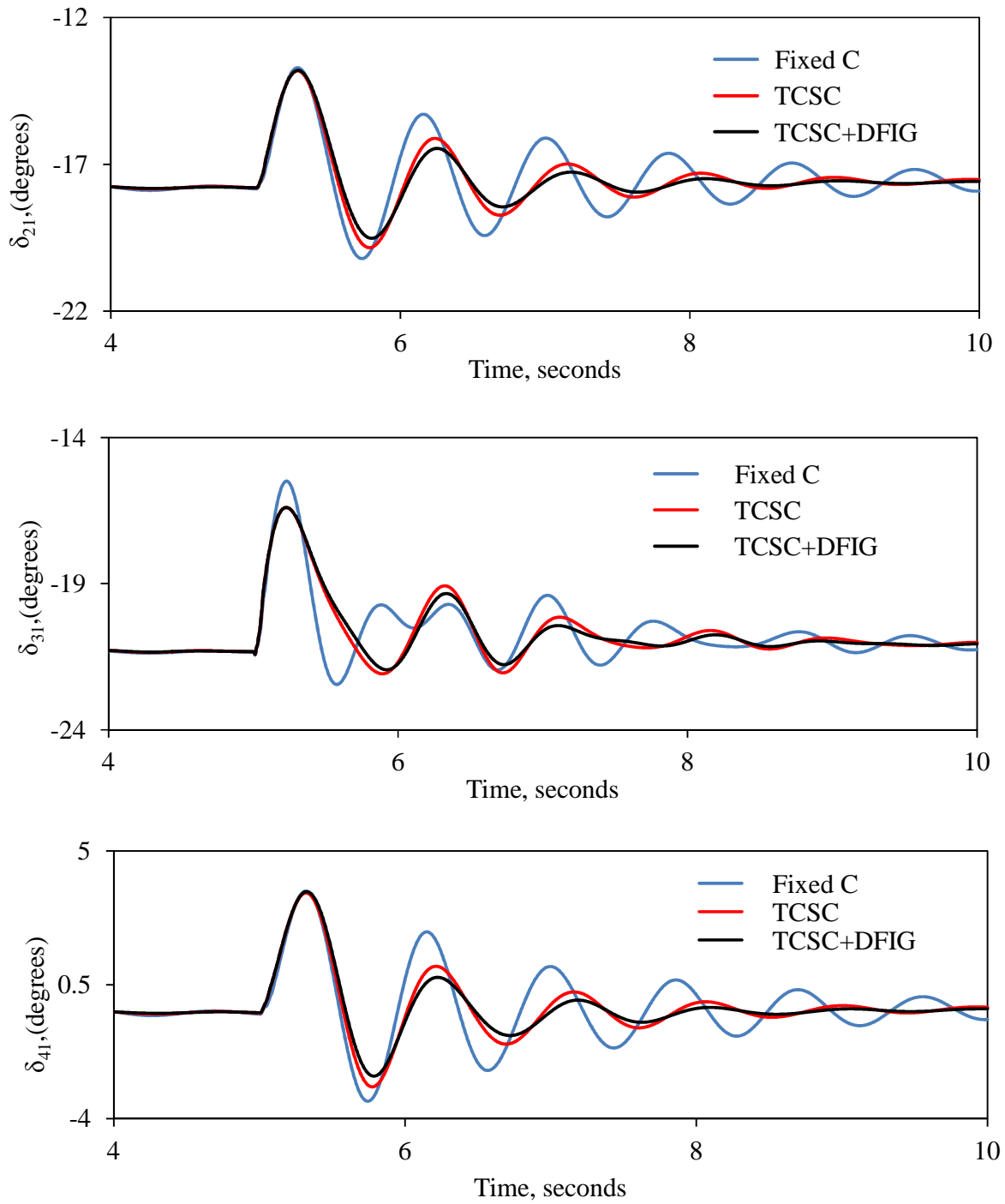
Figure B.1: Generator load angles and speeds, measured with respect to generator 1 load angle and speed, and transmission line real power flow transient time responses during and after clearing a 3-cycle, three-phase fault at bus 4 (supplemental control is in the Q control loop of the GSC of wind farm B).
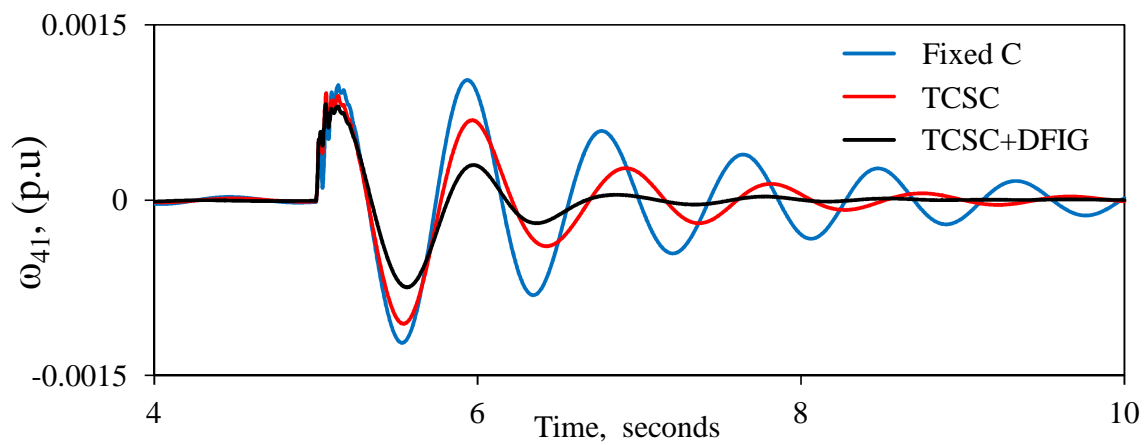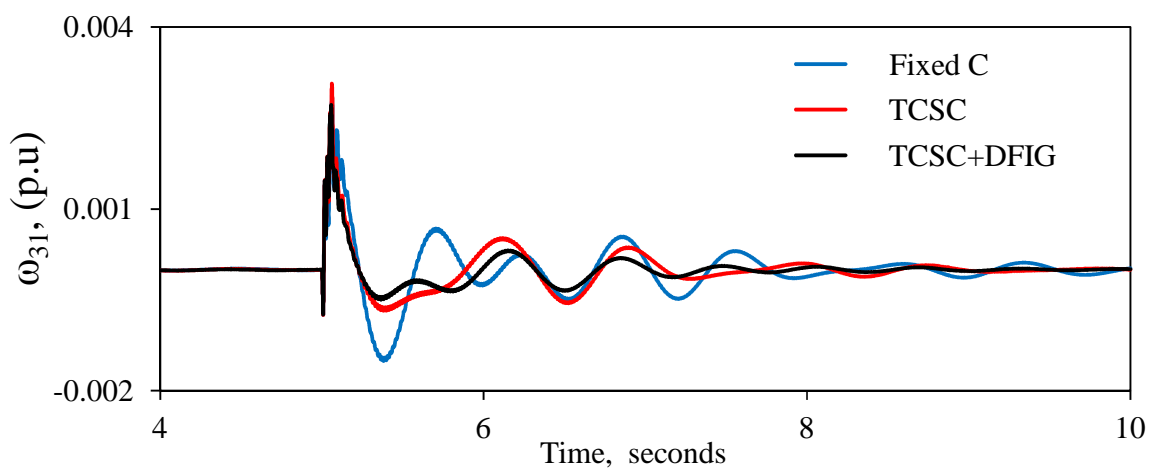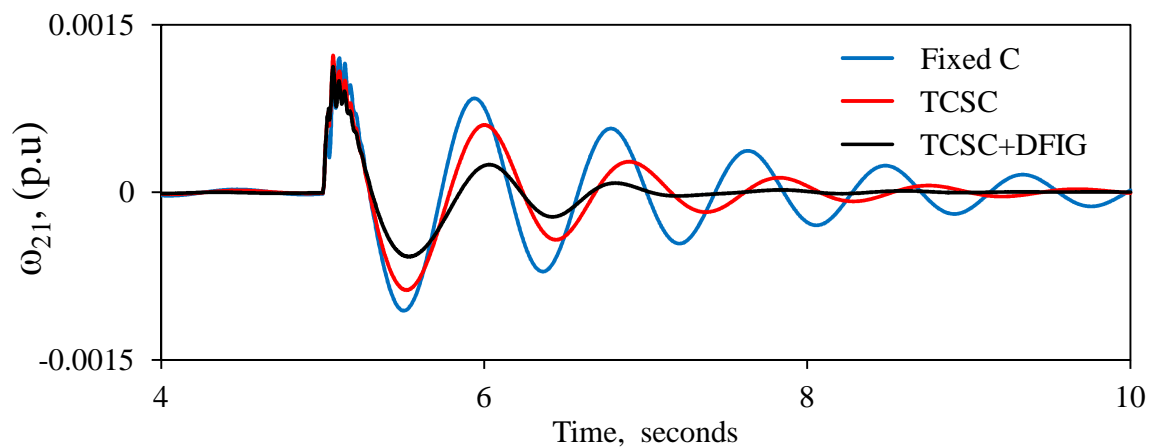
116

Figure B. 1: continued.

Figure B.1: continued.

118
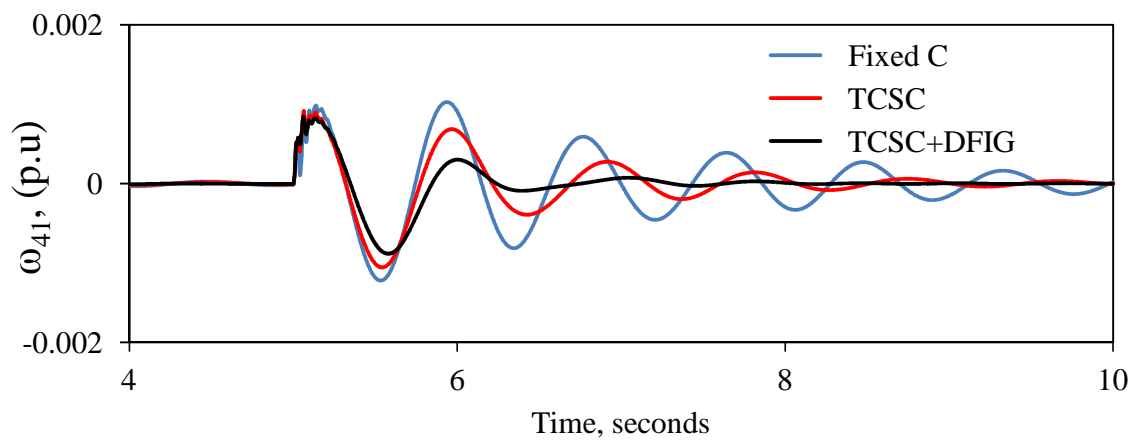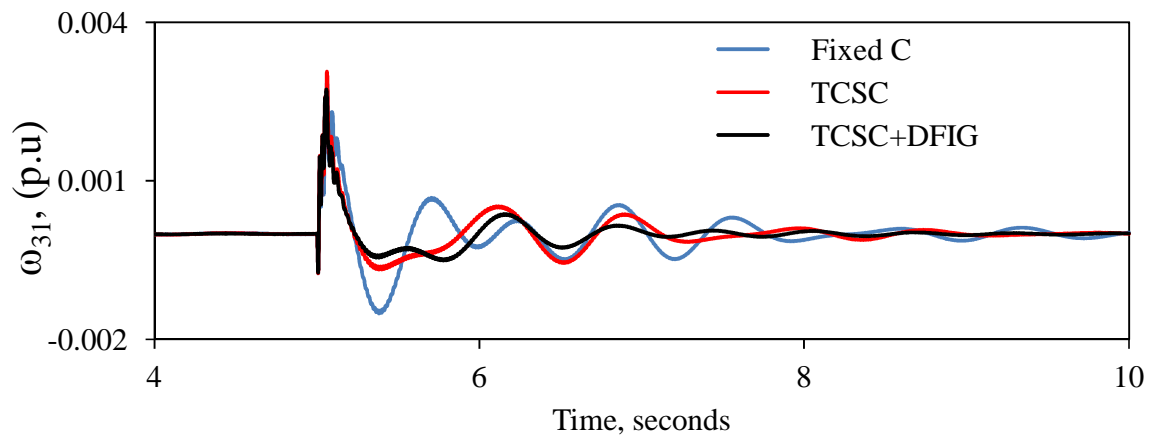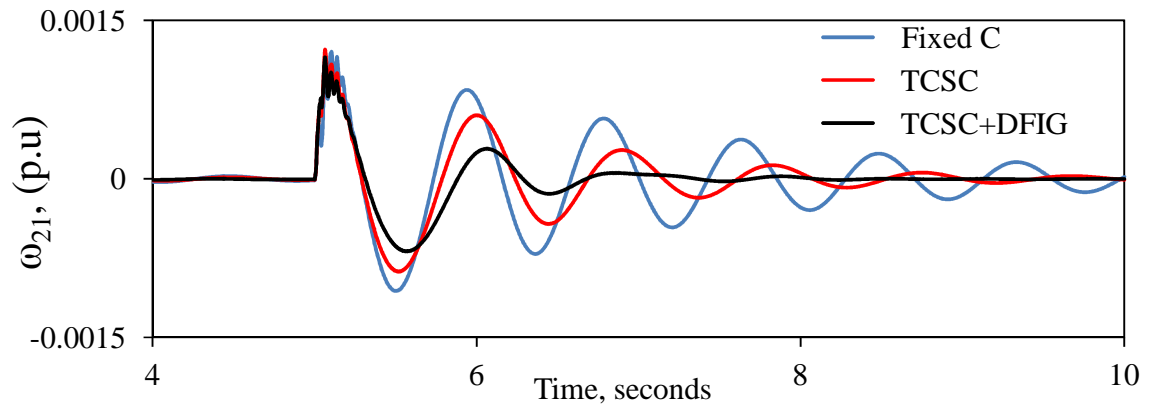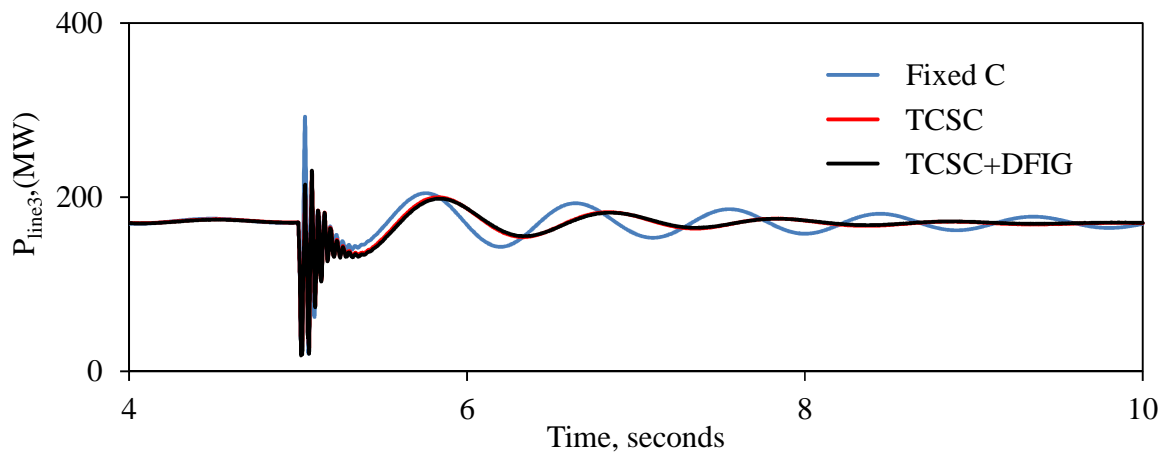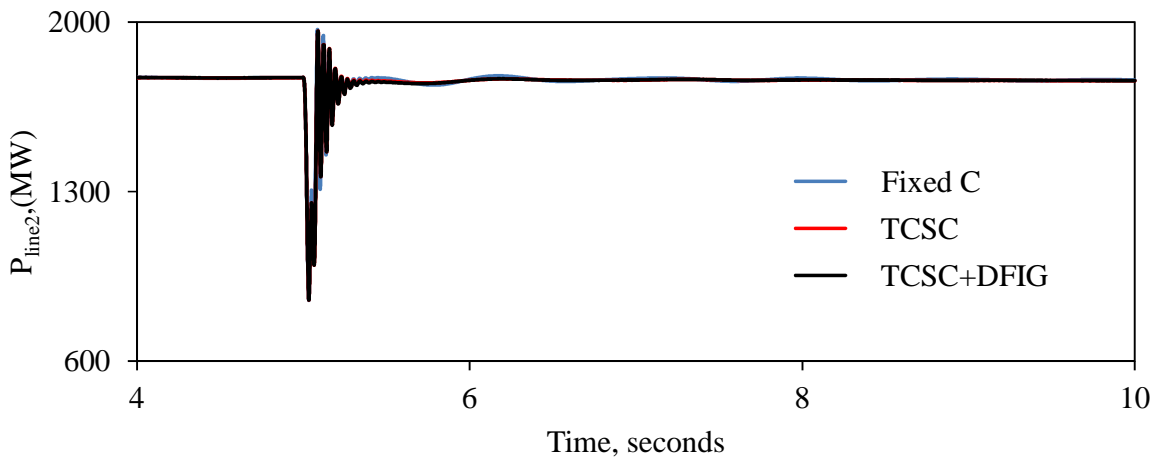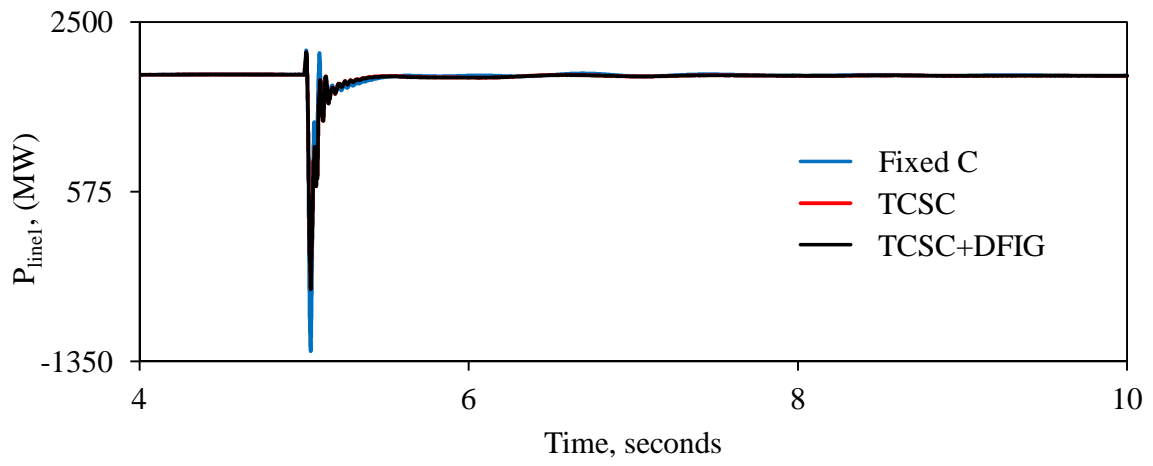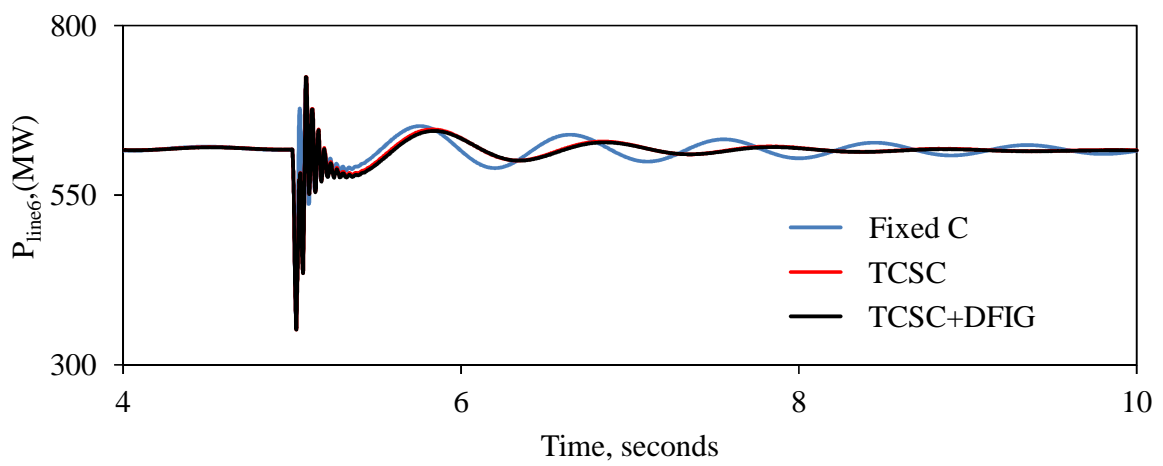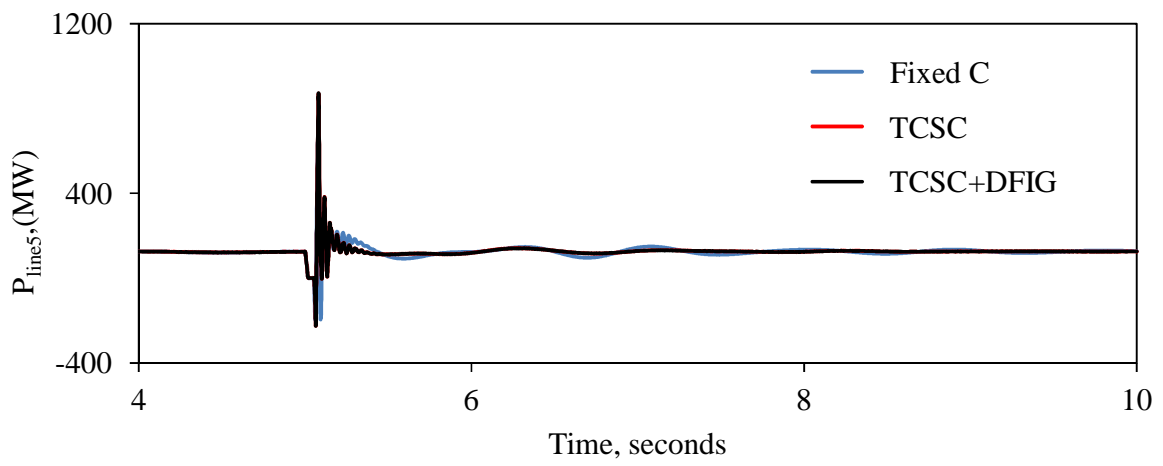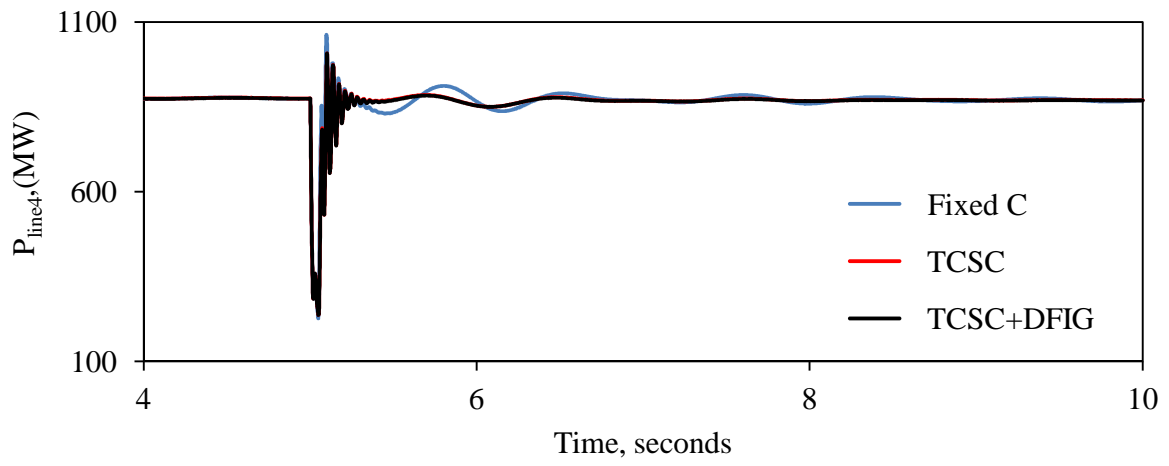
Figure B.1: continued.
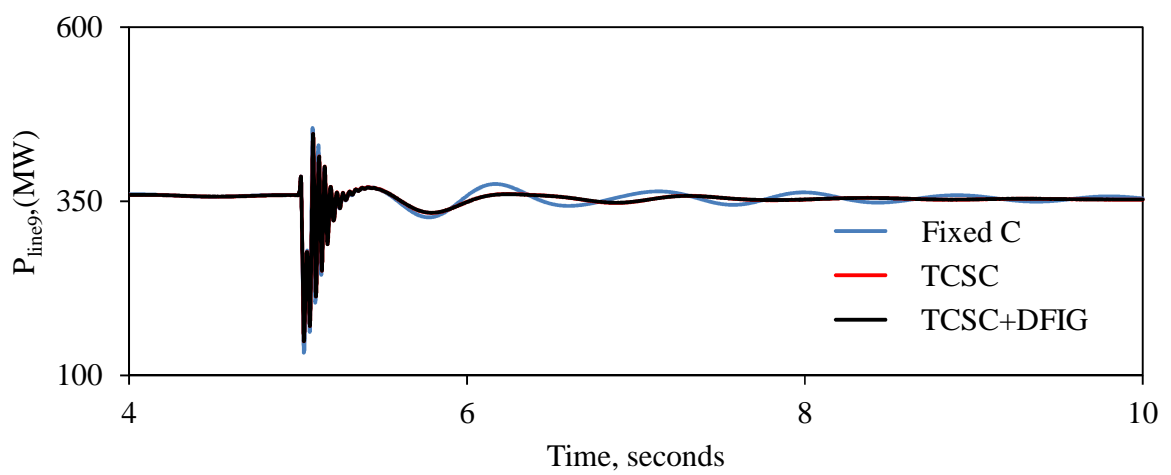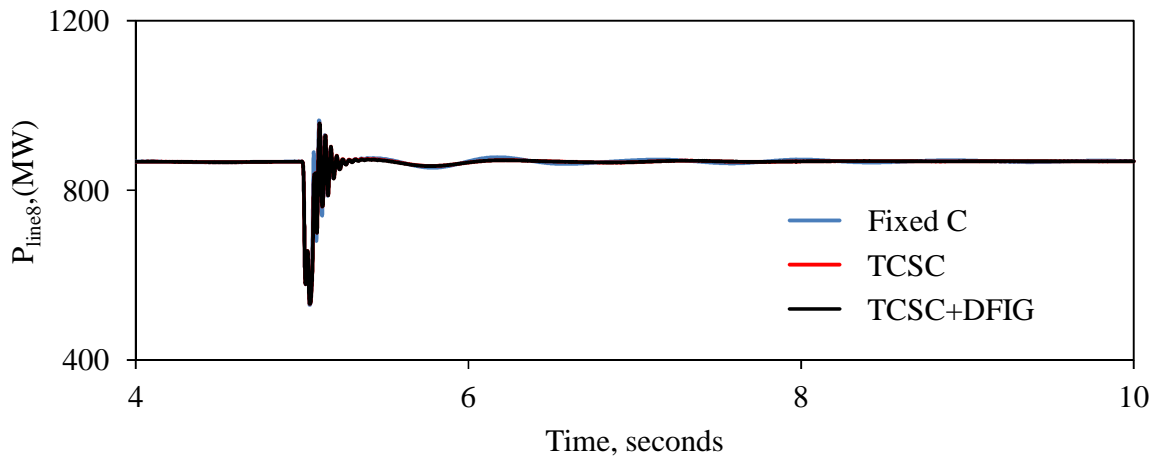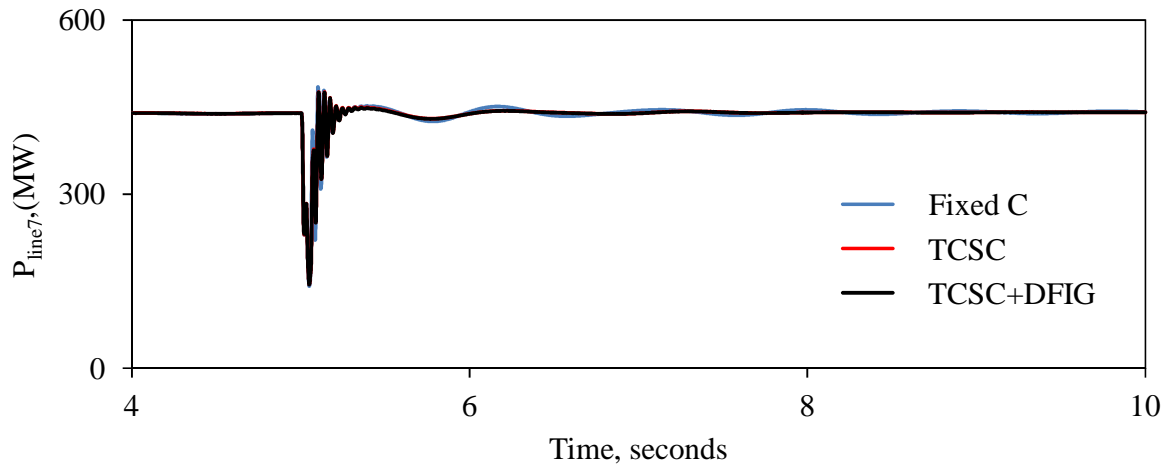
Figure B.1:   continued.
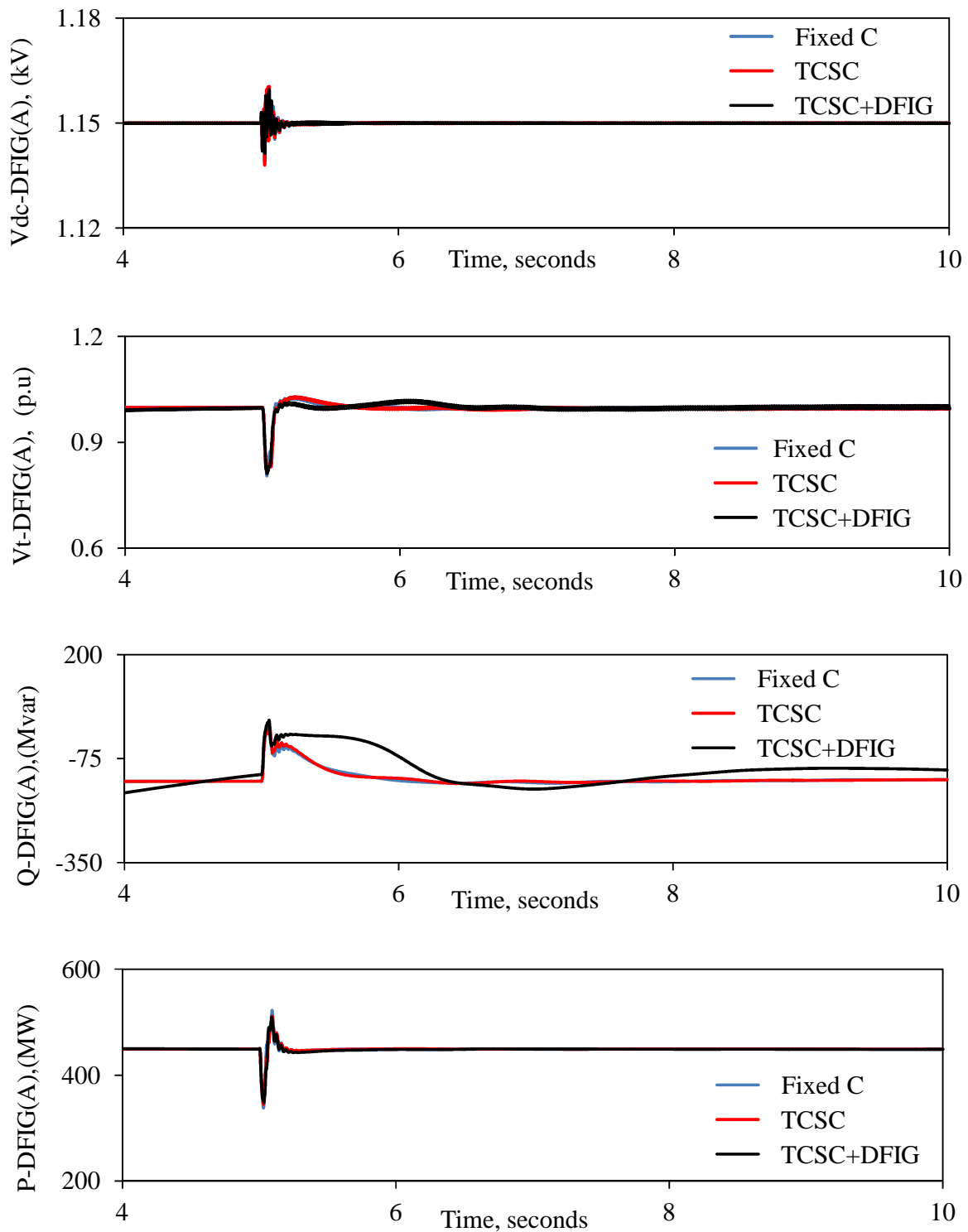
Figure B.2: DFIG-based wind farms A and B real and reactive powers, terminal voltages and BtB dc link voltages during and after clearing a 3-cycle, three-phase fault at bus 4. (supplemental control is in the Q control loop of the GSC of wind farm B).

121
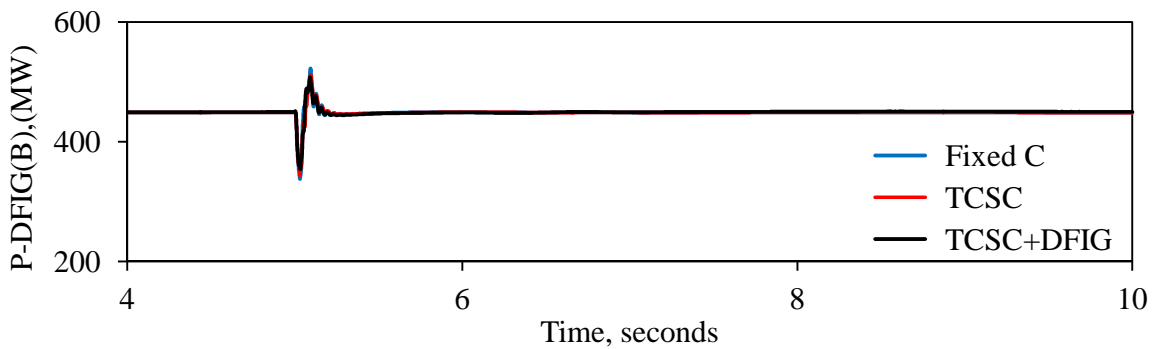
Figure B.2: continued.

B.2 DFIG-Based Wind Farm Supplemental Control is in the Reactive/Active Power Control Loop of the RSC of Wind Farm B
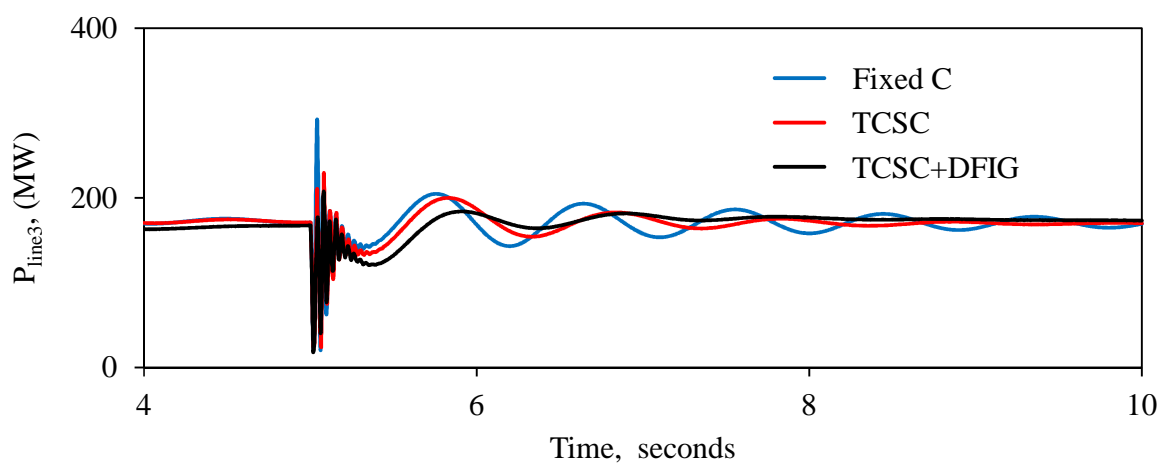
Figures B.3 and B.4 illustrate the generator load angles and speeds, measured with respect to generator 1 load angle and speed, and the transmission line real power flow transient time responses during and after fault clearing. Figures B.5 and B.6 illustrate the time responses of wind farm B real and reactive powers, terminal voltage and the BtB dc voltage for the same case. Tables B.2 and B.3 show the transfer functions of the TCSC and wind farm B supplemental controls after final tuning. Comparing the responses for the case of Scheme I supplemental control alone (TCSC) to those for the case of Scheme I and the DFIG-based wind farm supplemental controls in Figures B.3 and B.4, the positive contribution of wind farm B supplemental control, whether it is installed in either the Q or P control loop of the RSC, to the damping of the system oscillations is very clear.

Table B.2: Transfer functions of the hybrid TCSC compensation scheme and wind farm B supplemental controllers (wind farm controller is in the Q control loop of the RSC).

	Transfer Function
Hybrid TCSC Compensation Scheme	$G_{TCSC}(s) = 0.25 \dfrac{10}{(s+10)} \dfrac{3s}{(3s+1)}$
DFIG-Based Wind Farm A	$G_{DFIG\_Q\_Loop\_RSC}(s) = 0.35 \dfrac{s}{(s+18)} \dfrac{1}{(s+0.8)}$

Table B.3: Transfer functions of the hybrid TCSC compensation scheme and wind farm B supplemental controllers (wind farm controller is in the P control loop of the RSC).

	Transfer Function
Hybrid TCSC Compensation Scheme	$G_{TCSC}(s) = 0.25 \dfrac{10}{(s+10)} \dfrac{3s}{(3s+1)}$
DFIG-Based Wind Farm A	$G_{DFIG\_P\_Loop\_RSC}(s) = 0.15 \dfrac{s}{(s+1)} \dfrac{1}{(s+2)}$
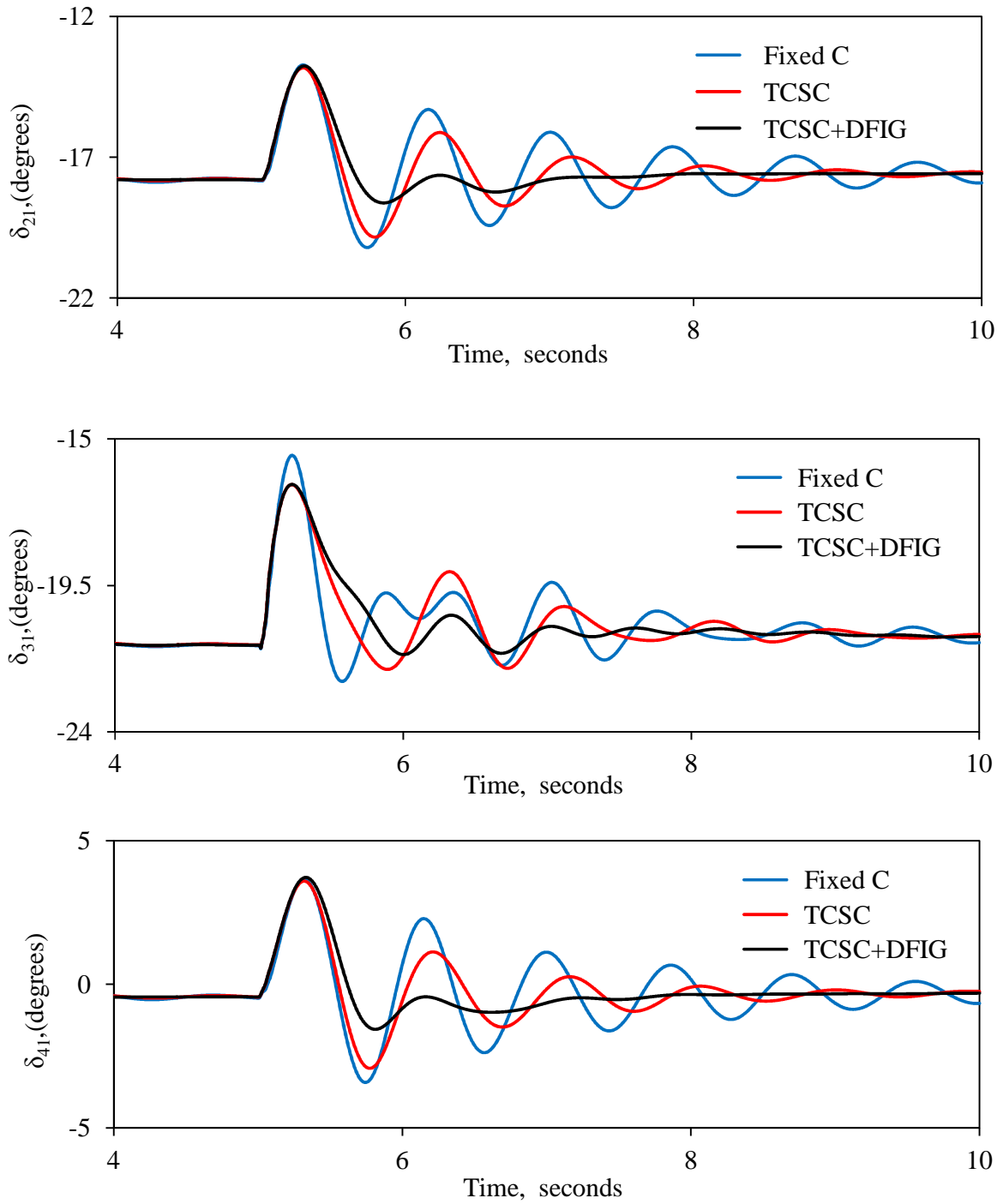
Figure B.3: Generator load angles and speeds, measured with respect to generator 1 load angle and speed, and transmission line real power flow transient time responses during and after clearing a 3-cycle, three-phase fault at bus 4 (supplemental control is in the Q control loop of the RSC of wind farm B).
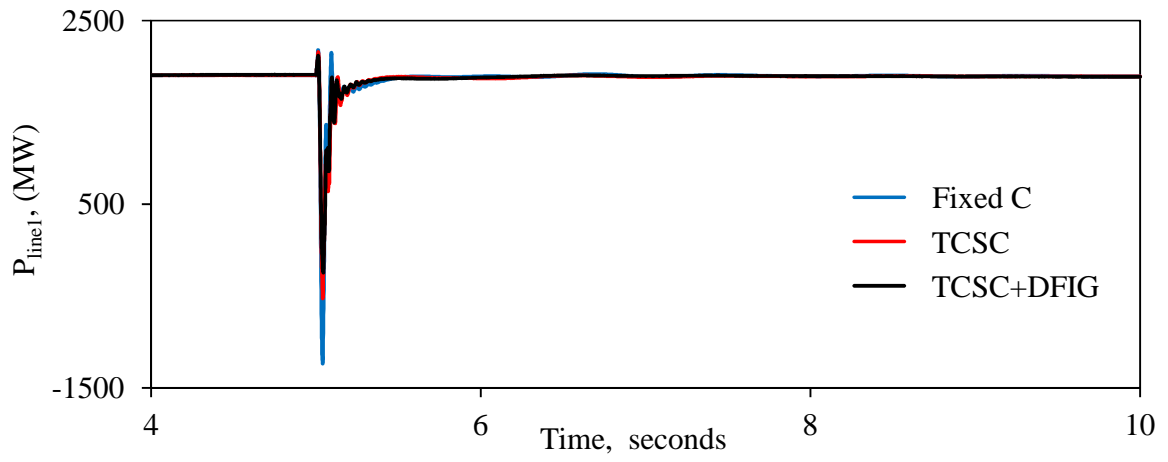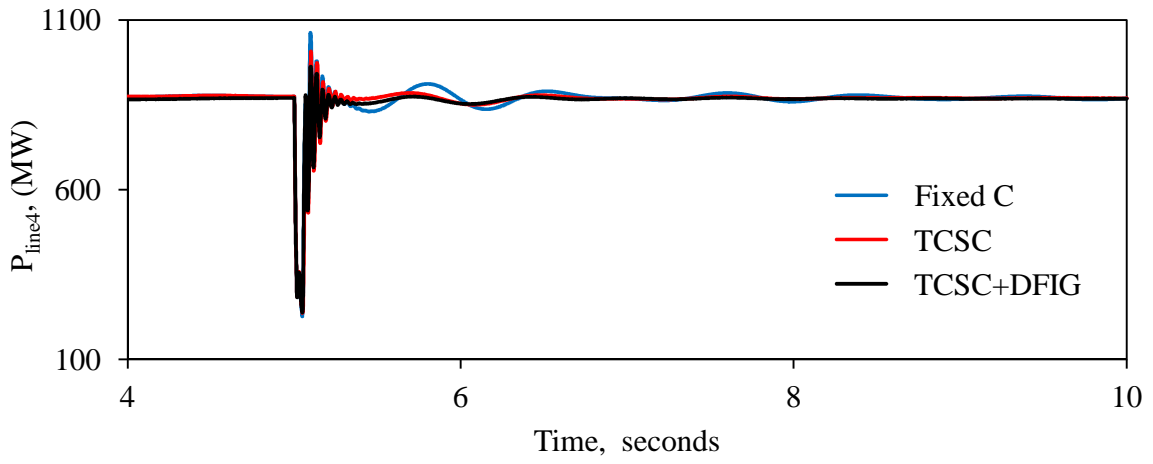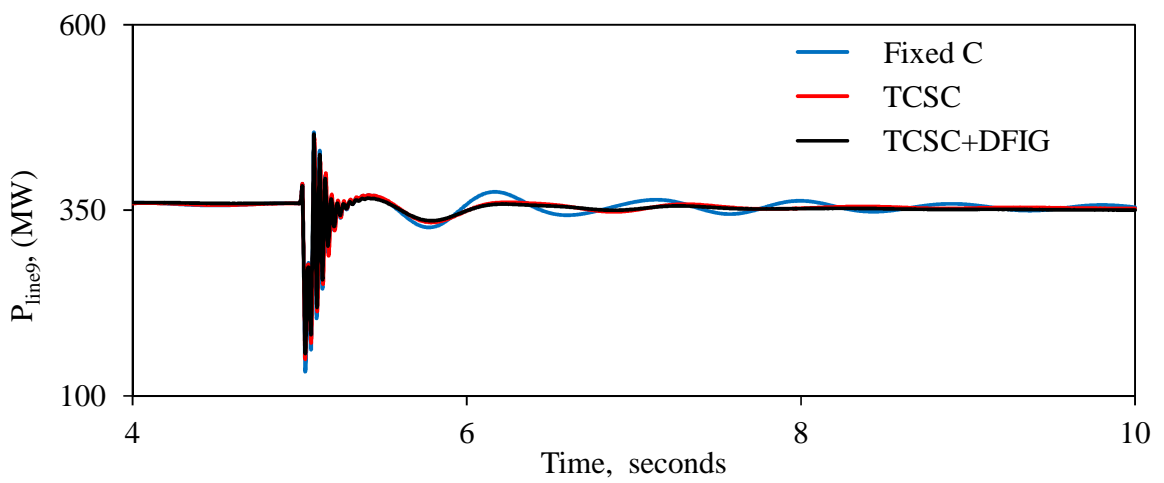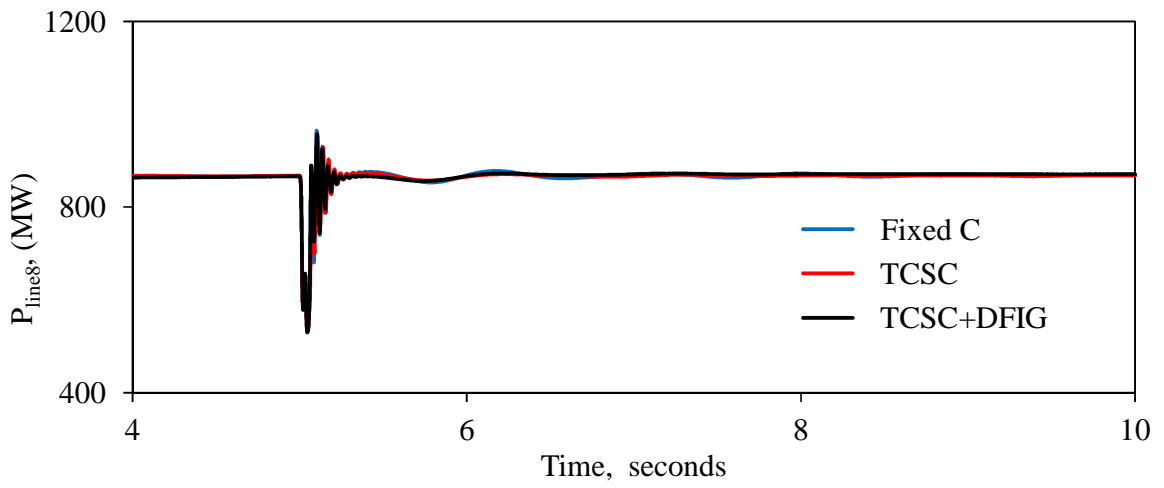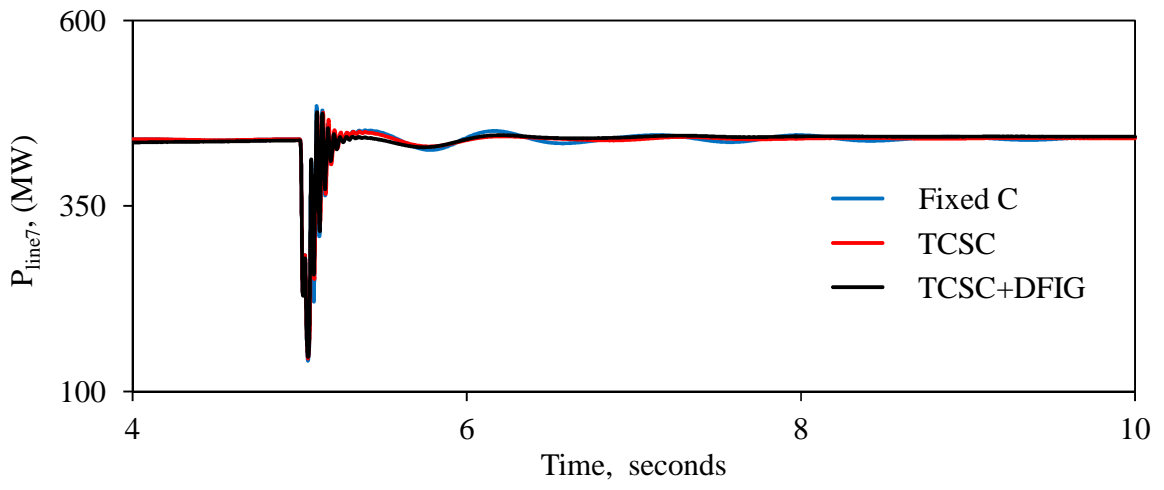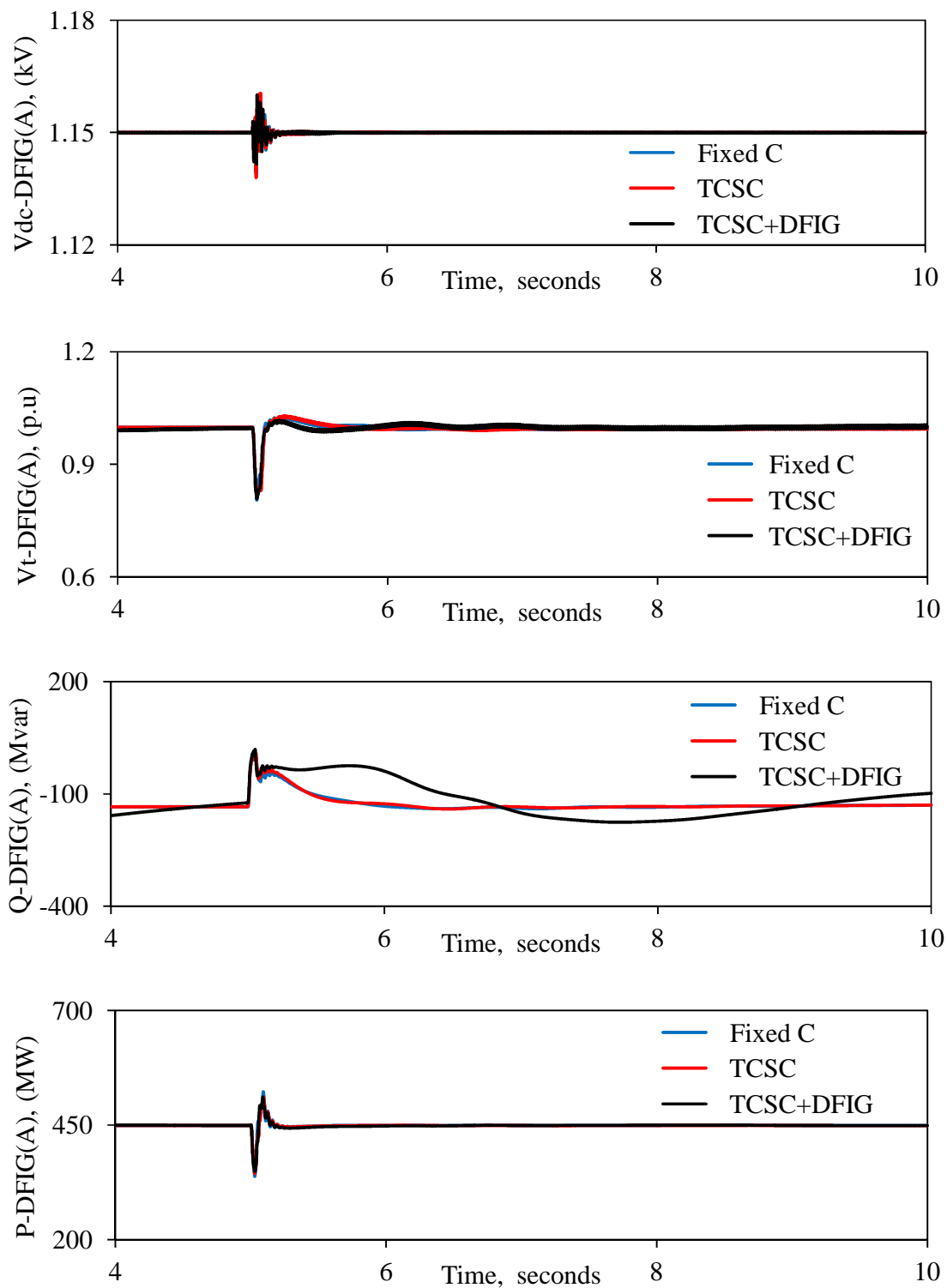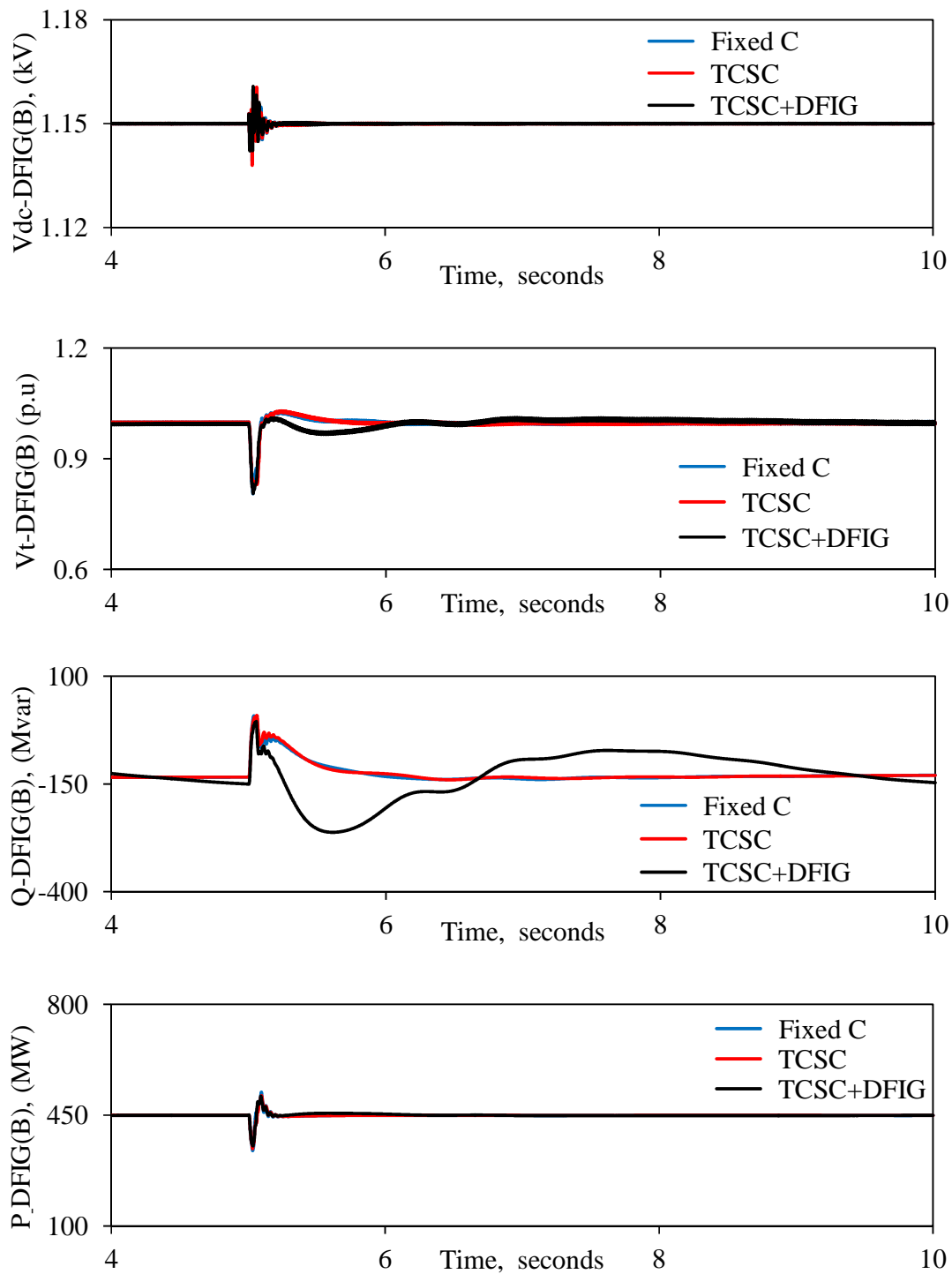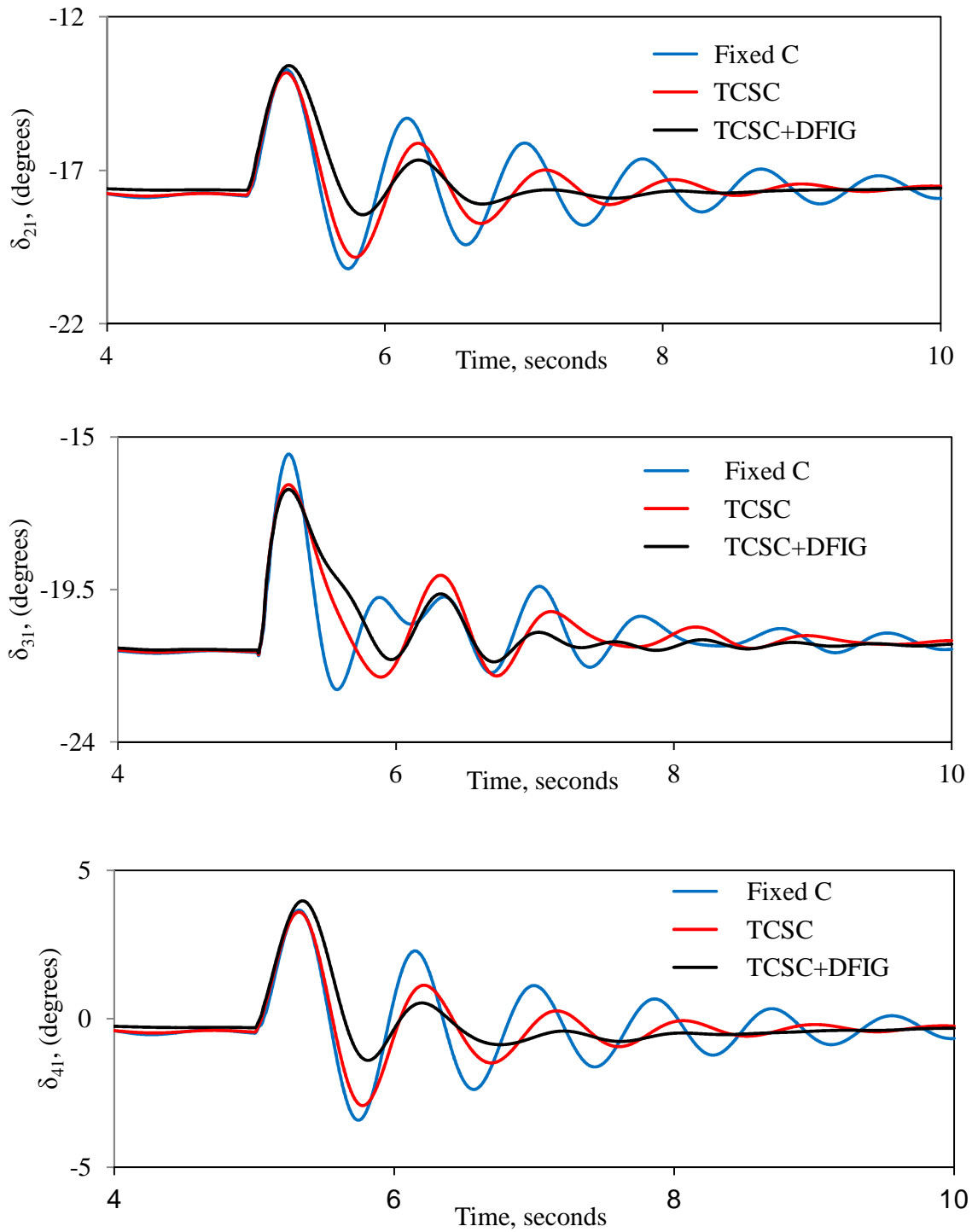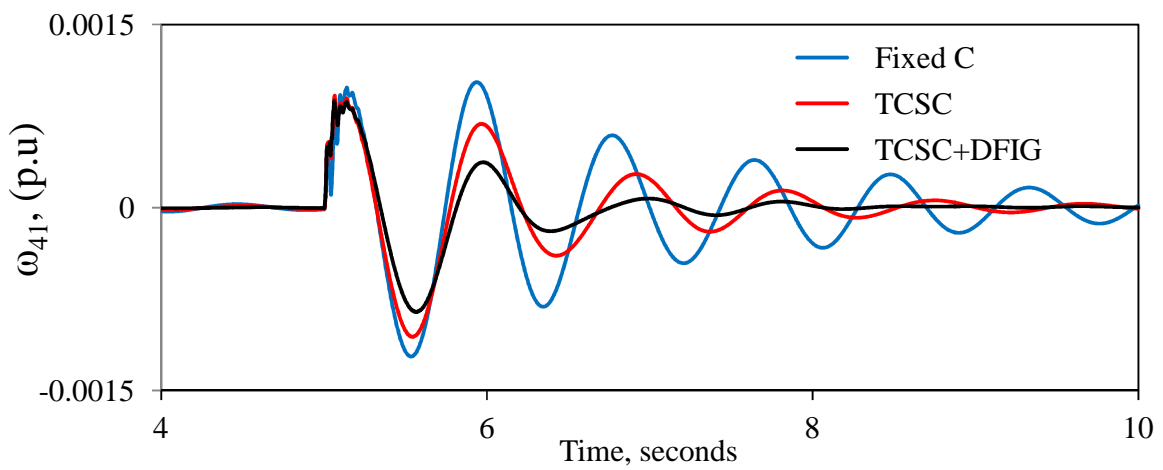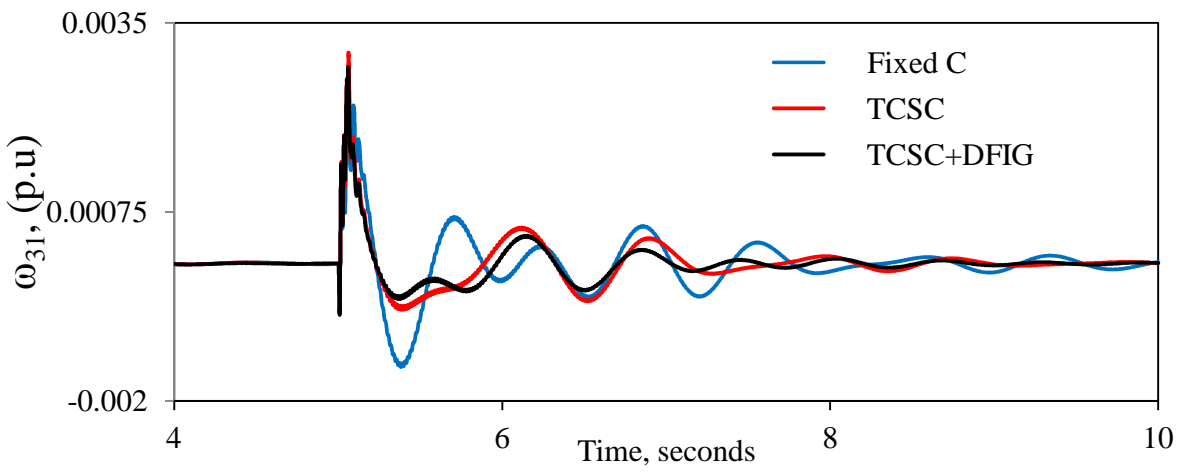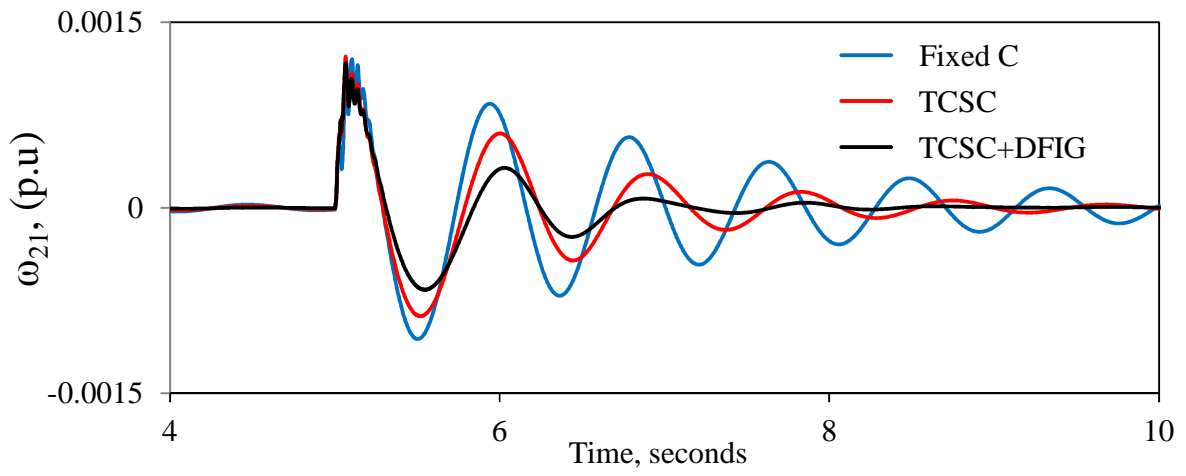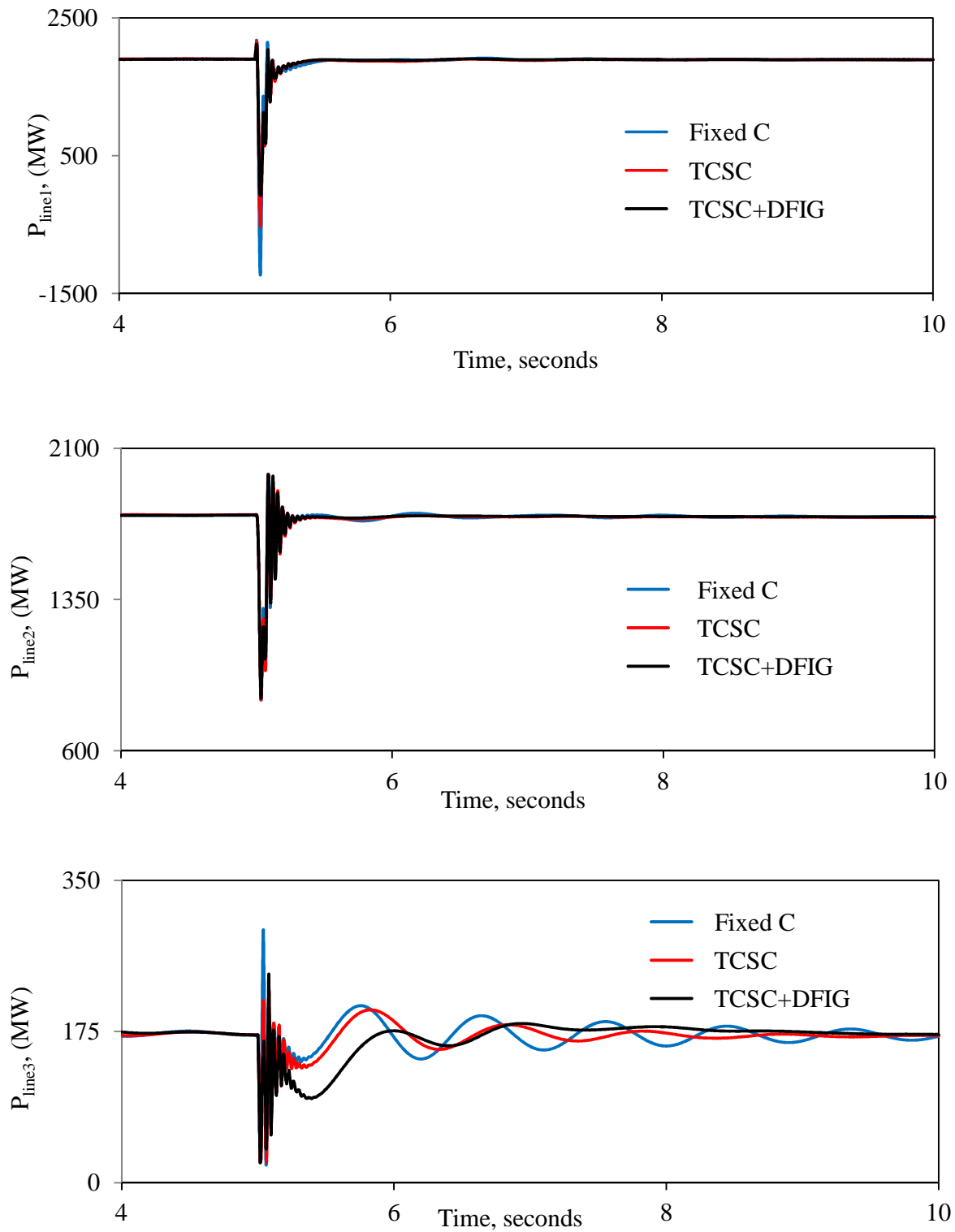
Figure B.3: continued.
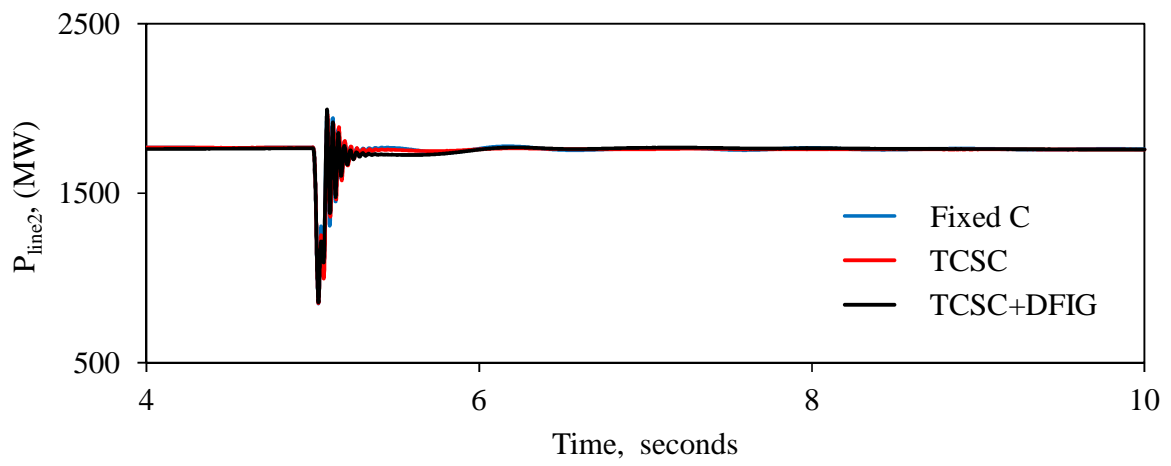
Figure B.3: continued.
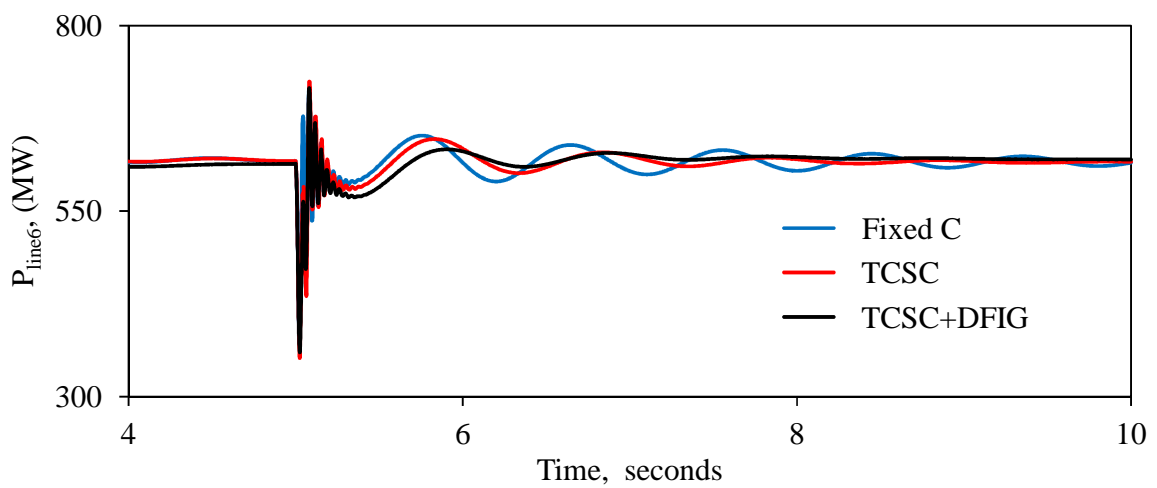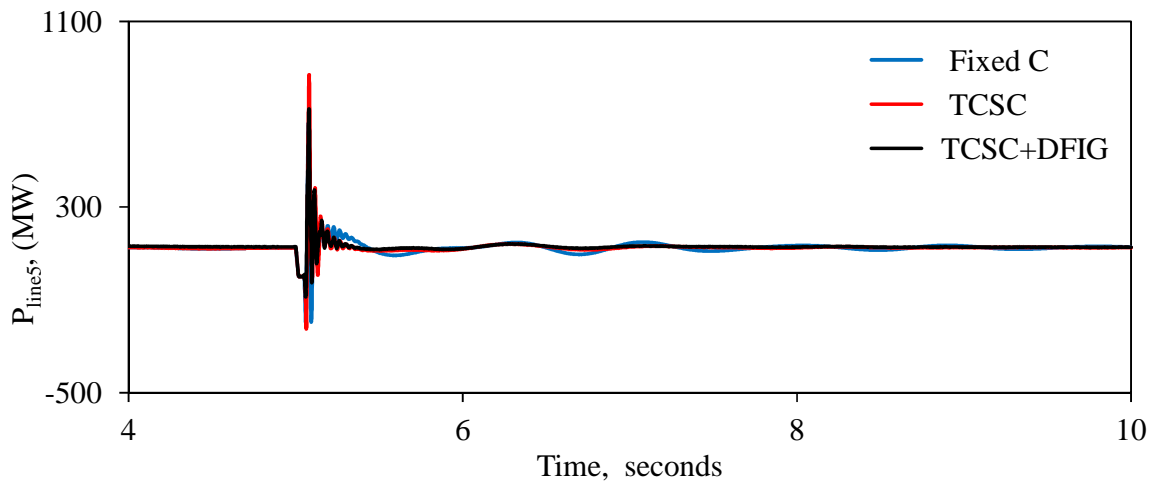
Figure B.3: continued.

Figure B.3: continued.

Figure B.4: DFIG-based wind farms A and B real and reactive powers, terminal voltages and BtB dc link voltages during and after clearing a 3-cycle, three-phase fault at bus 4. (supplemental control is in the Q control loop of the RSC of wind farm B).

129

Figure B.4: continued.

130

Figure B.5: Generator load angles and speeds, measured with respect to generator 1 load angle and speed, and transmission line real power flow transient time responses during and after clearing a 3-cycle, three-phase fault at bus 4 (supplemental control is in the P control loop of the RSC of wind farm B).

Figure B.5: continued.
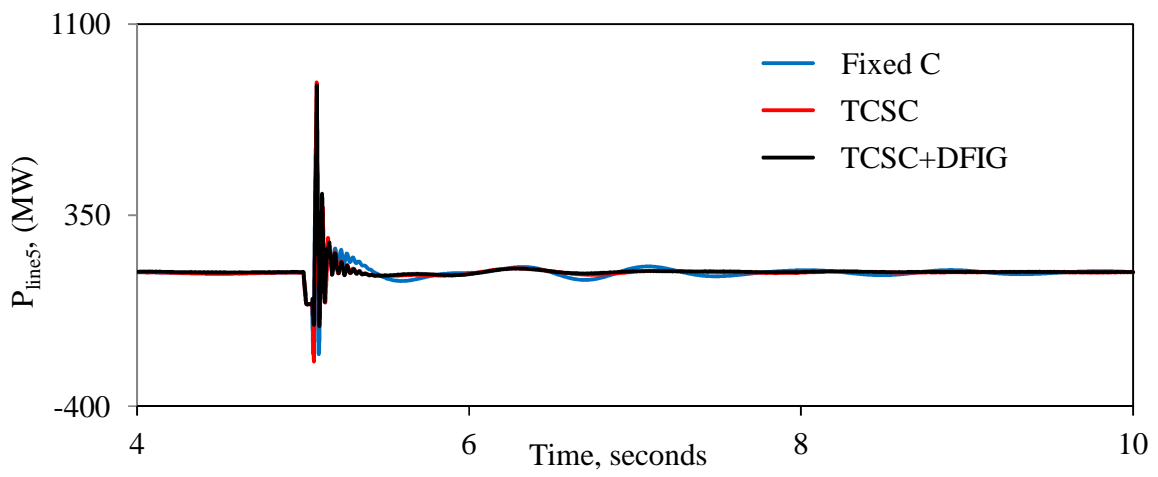
132
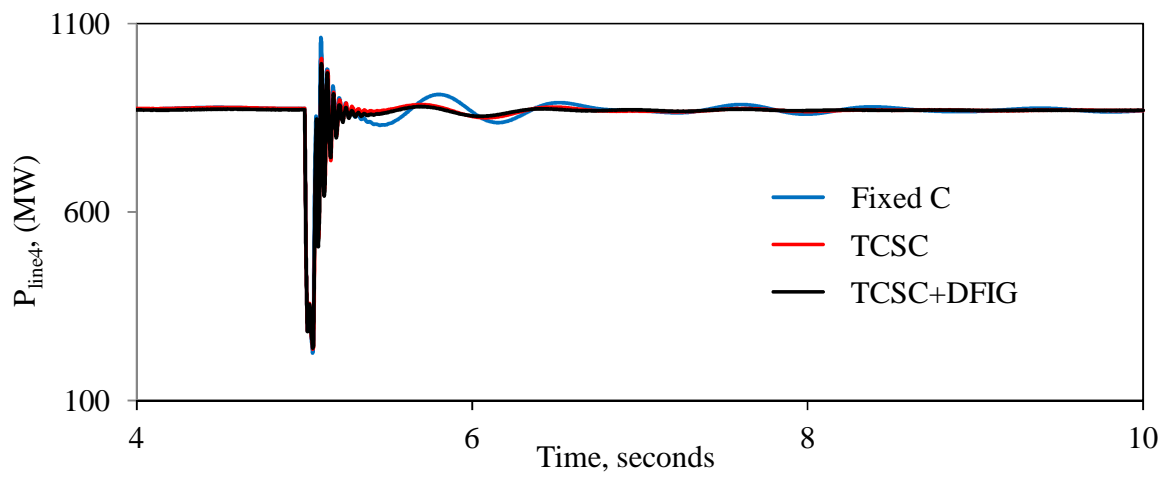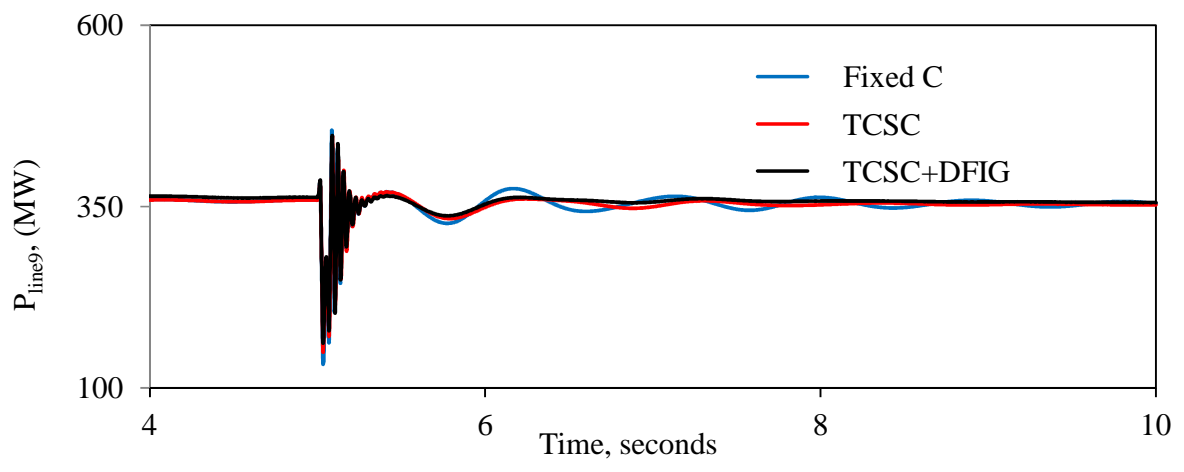
Figure B.5:   continued.
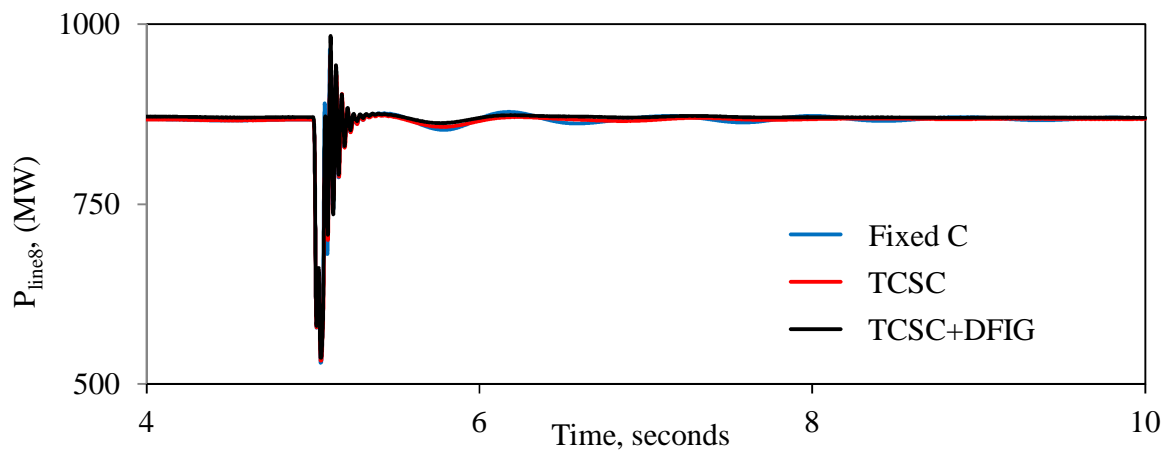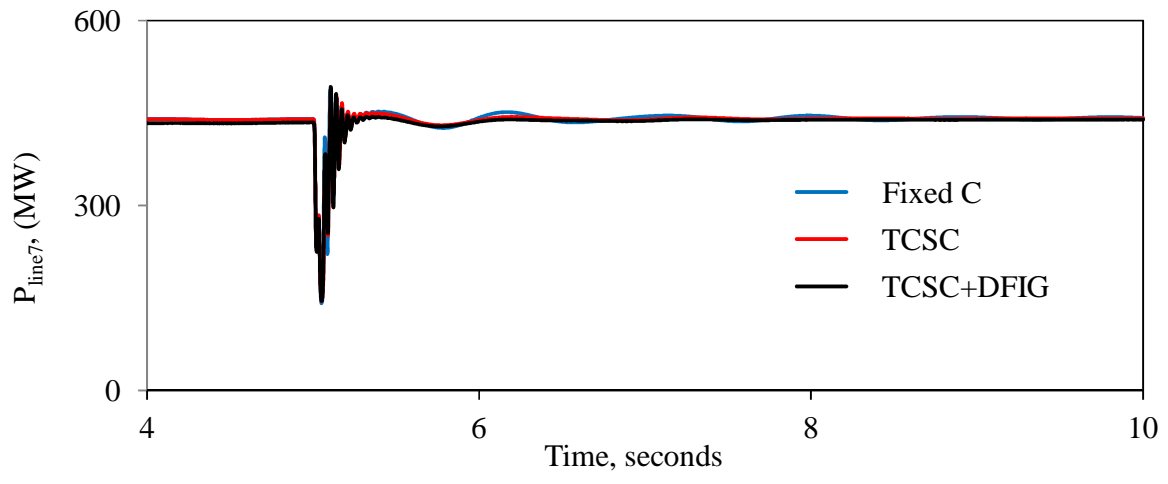
Figure B.5: continued.
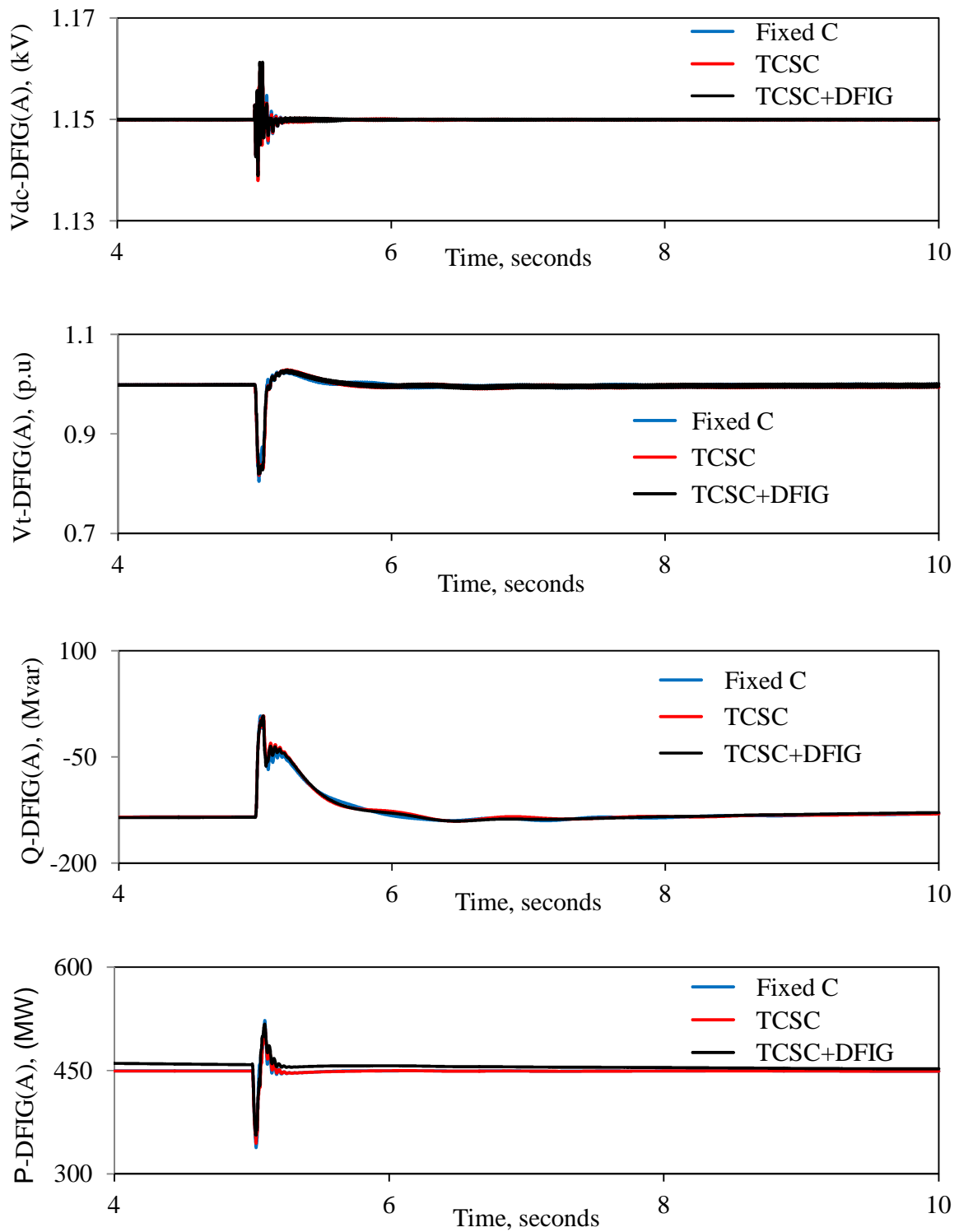
134

Figure B.5: continued.

135

Figure B.6: DFIG-based wind farms A and B real and reactive powers, terminal voltages and BtB dc link voltages during and after clearing a 3-cycle, three-phase fault at bus 4. (supplemental control is in the P control loop of the RSC of wind farm B).
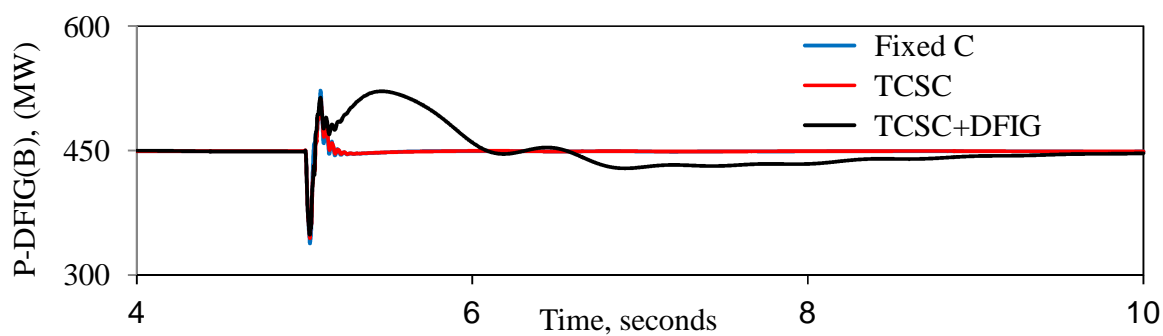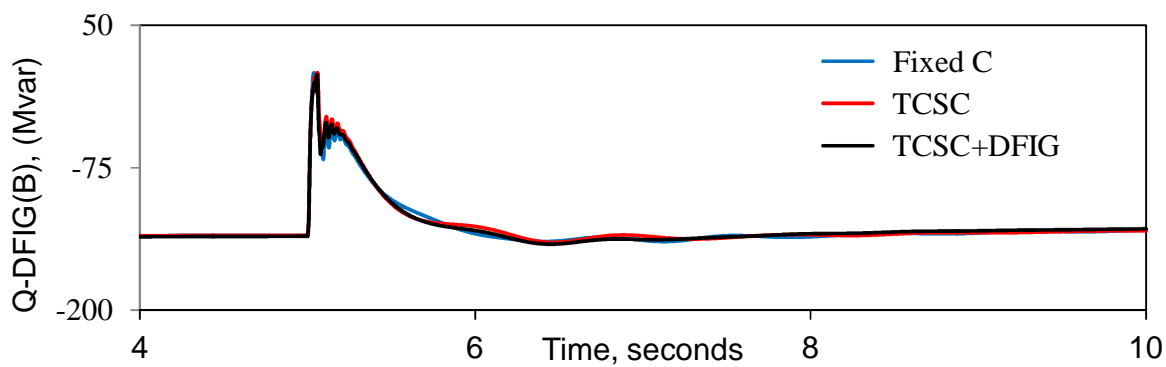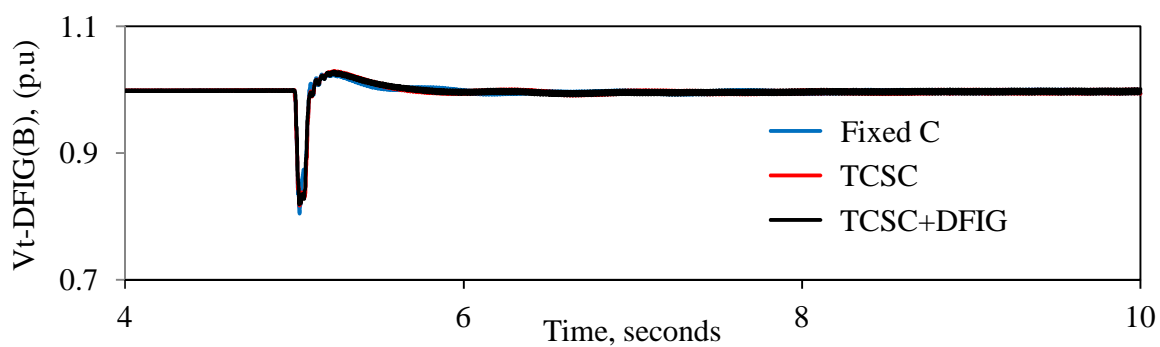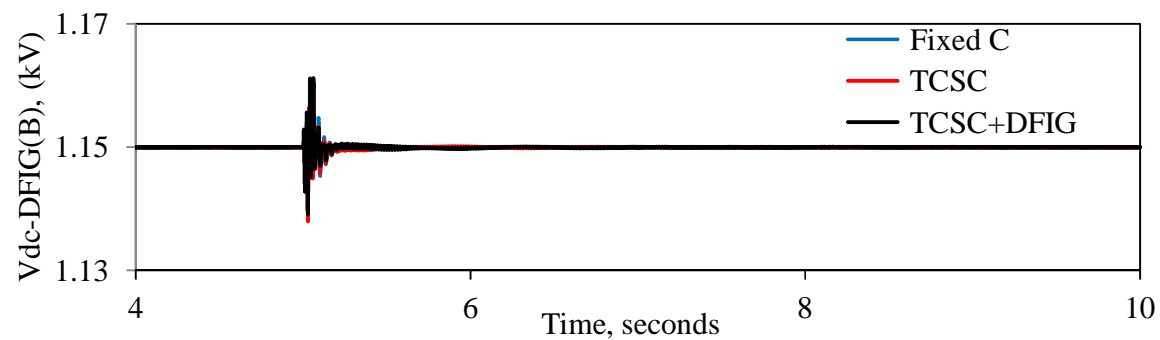
136

Figure B.6: continued.

137

B.3   Effect of the Stabilizing Signal of Wind Farm B Supplemental Controls on the Damping of System Oscillations

The final results of the time-domain simulation studies (controller tuning of the TCSC and wind farm B) are shown in Figures B.7 to B.9 which illustrates the generator load angles, measured with respect to generator 1 load angle, during and after fault clearing.   The corresponding transfer functions of the TCSC and wind farm B supplemental controllers are given in Tables B.4 to B.6.

Table B.4: Transfer functions of the hybrid TCSC compensation scheme and wind farm B supplemental controllers for the different combinations of stabilizing signals (wind farm controller is in the Q control loop of the GSC).

Combination	Hybrid TCSC Compensation Scheme	DFIG-Based Wind Farm B
1		$G(s) = 0.1 \dfrac{s}{(s+0.04)} \dfrac{1}{(s+0.1)}$
2	$G(s) = 0.25 \dfrac{10}{(s+10)} \dfrac{3s}{(3s+1)}$	$G(s) = 0.05 \dfrac{s}{(s+0.04)} \dfrac{1}{(s+0.1)}$
3		$G(s) = 0.1 \dfrac{s}{(s+0.05)} \dfrac{1}{(s+0.2)}$
4		$G(s) = 0.01 \dfrac{s}{(s+0.1)} \dfrac{1}{(s+2)}$

Table B.5: Transfer functions of the hybrid TCSC compensation scheme and wind farm B supplemental controllers for the different combinations of stabilizing signals (wind farm controller is in the Q control loop of the RSC).

Combination	Hybrid TCSC Compensation Scheme	DFIG-Based Wind Farm B
1		$G(s) = 0.35 \dfrac{s}{(s+18)} \dfrac{1}{(s+0.8)}$
2	$G(s) = 0.25 \dfrac{10}{(s+10)} \dfrac{3s}{(3s+1)}$	$G(s) = 0.3 \dfrac{s}{(s+12)} \dfrac{1}{(s+2)}$
3		$G(s) = 0.3 \dfrac{s}{(s+2)} \dfrac{1}{(s+12)}$
4		$G(s) = 0.01 \dfrac{s}{(s+2)} \dfrac{1}{(s+12)}$

Table B.6: Transfer functions of the hybrid TCSC compensation scheme and wind farm B supplemental controllers for the different combinations of stabilizing signals (wind farm controller is in the P control loop of the RSC).

Combination	Hybrid TCSC Compensation Scheme	DFIG-Based Wind Farm B
1		$G(s) = 0.15 \dfrac{s}{(s+2)} \dfrac{1}{(s+1)}$
2	$G(s) = 0.25 \dfrac{10}{(s+10)} \dfrac{3s}{(3s+1)}$	$G(s) = 0.15 \dfrac{s}{(s+1)} \dfrac{1}{(s+2)}$
3		$G(s) = 0.15 \dfrac{s}{(s+1)} \dfrac{1}{(s+2)}$
4		$G(s) = 0.01 \dfrac{s}{(s+1)} \dfrac{1}{(s+2)}$

It can be seen from Figures B.7 to B.9 that the best damping of the relative load angle responses are achieved with the δ_{21}- δ_{31} combination. The second best damped responses are obtained with the δ_{21}- δ_{41} combination. Again, these results should be expected due to the direct relationship between the relative load angles and the generators that yield the problem. It can also be seen from figures that the worst damped responses are obtained with δ_{21}-P_{L1}.

In order to determine the best location for wind farm B supplemental control, the best responses in Figures B.7 to B.9 are plotted together in Figure B.10. As it can be seen from this figure, although the three time responses are very close, nevertheless, the best location for wind farm B supplemental control tends to be in the Q control loop of the RSC.
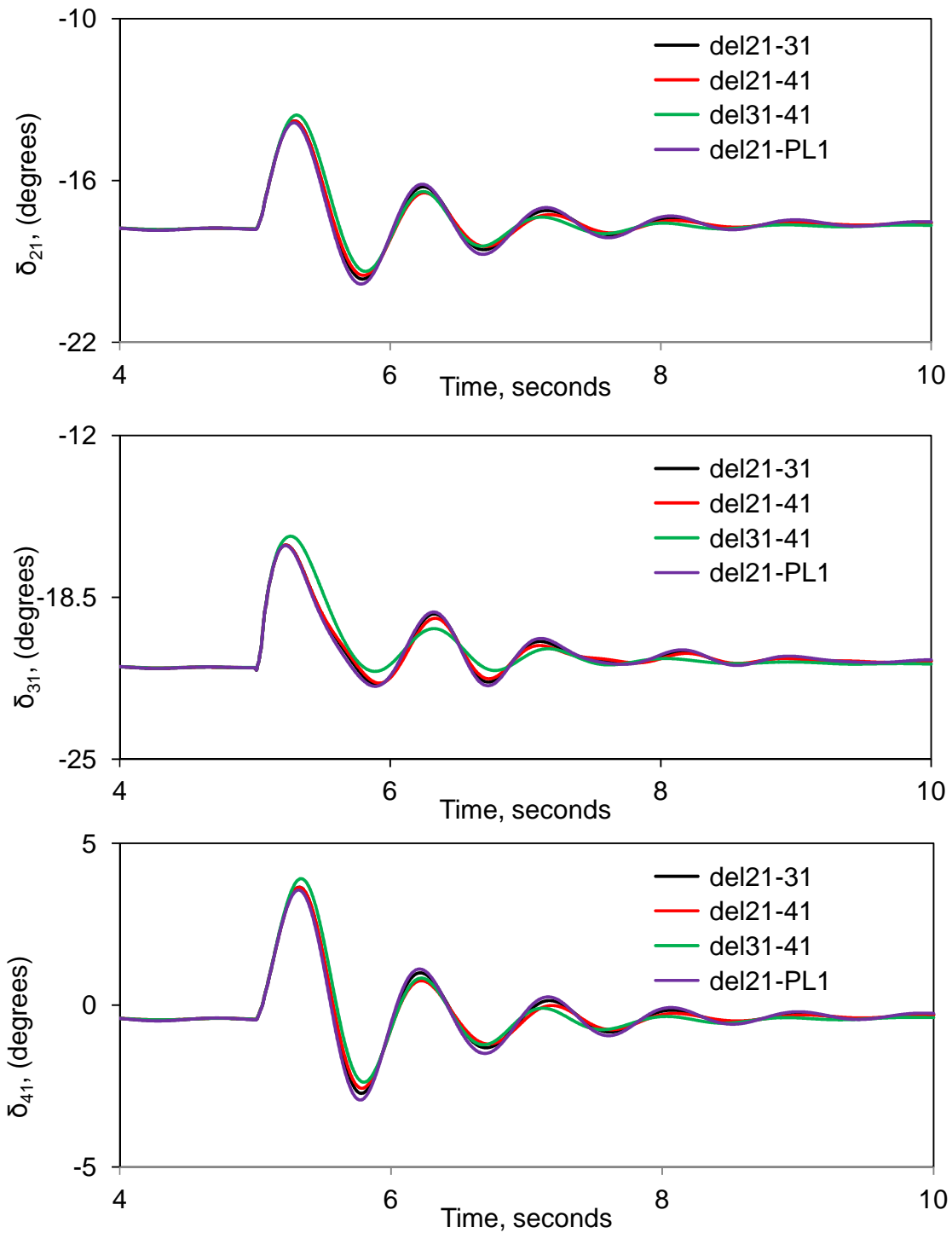
Figure B.7: Effect of wind farm B supplemental control stabilizing signal on the generator load angles, measured with respect to generator 1 load angle, during and after clearing a 3-cycle, three-phase fault at bus 4. (DFIG-based wind farm supplemental controller is in the Q control loop of the GSC).
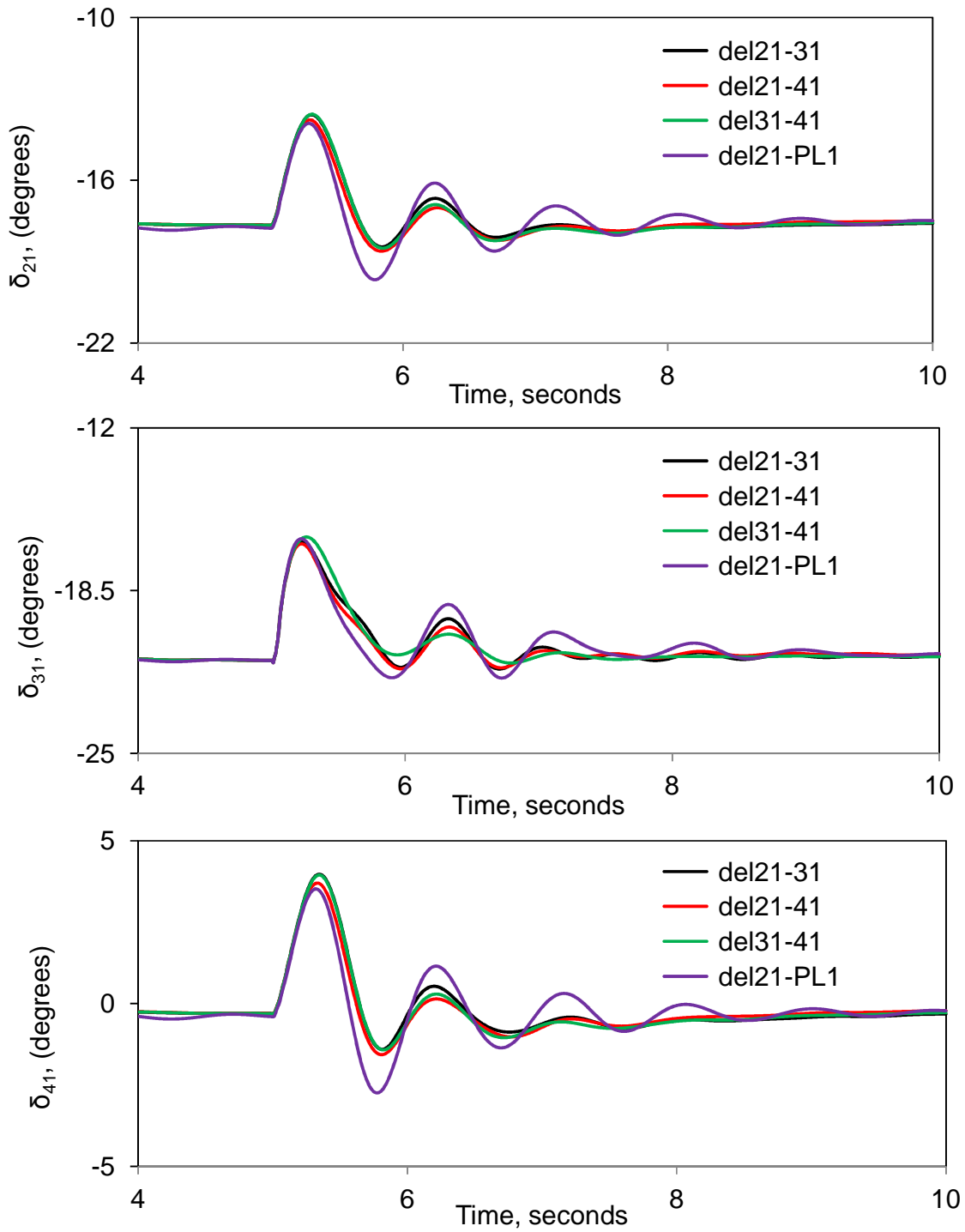
140

Figure B.8: Effect of wind farm B supplemental control stabilizing signal on the generator load angles, measured with respect to generator 1 load angle, during and after clearing a 3-cycle, three-phase fault at bus 4. (DFIG-based wind farm supplemental controller is in the P control loop of the RSC).
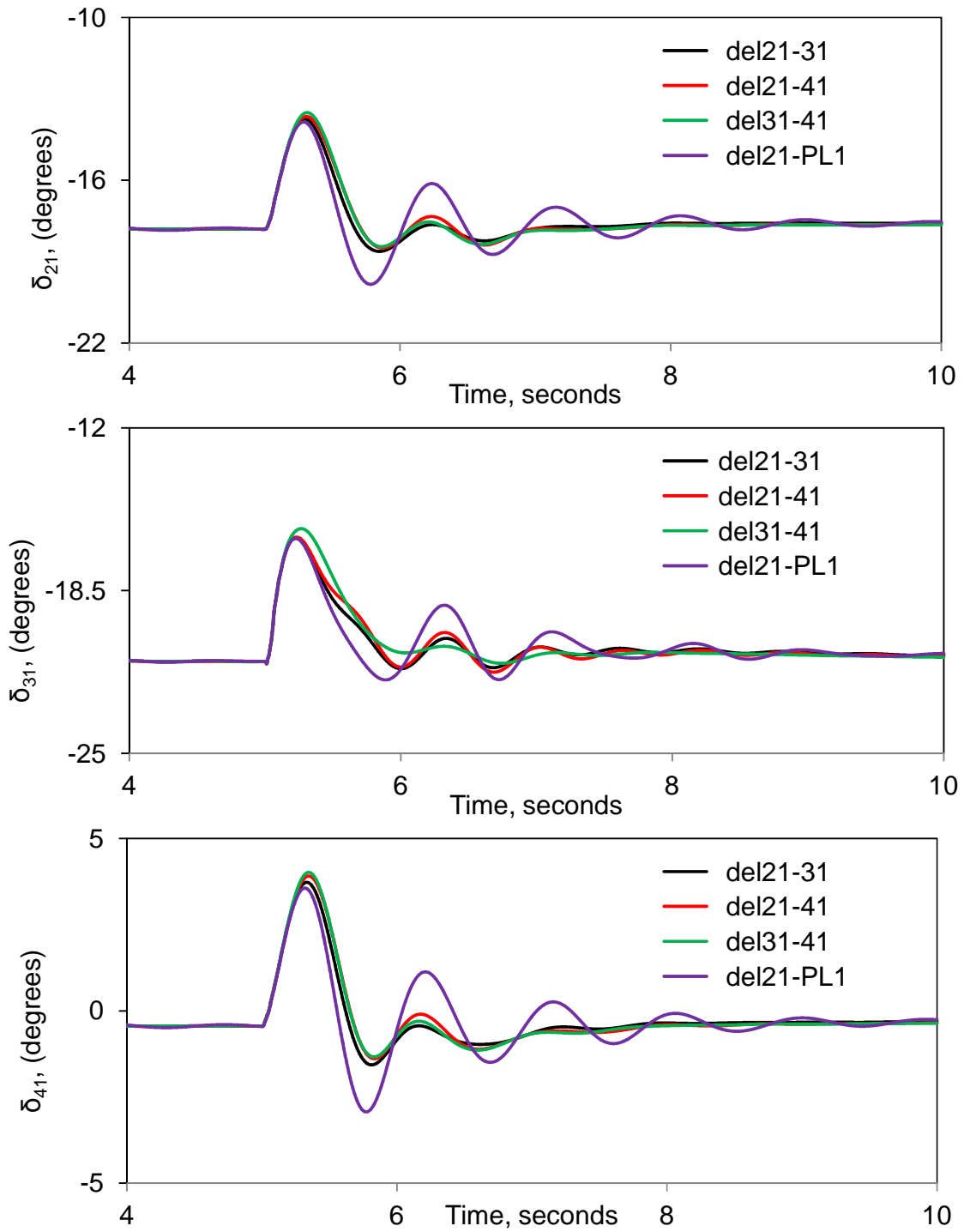
Figure B.9: Effect of wind farm B supplemental control stabilizing signal on the generator load angles, measured with respect to generator 1 load angle, during and after clearing a 3-cycle, three-phase fault at bus 4. (DFIG-based wind farm supplemental controller is in the Q control loop of the RSC).
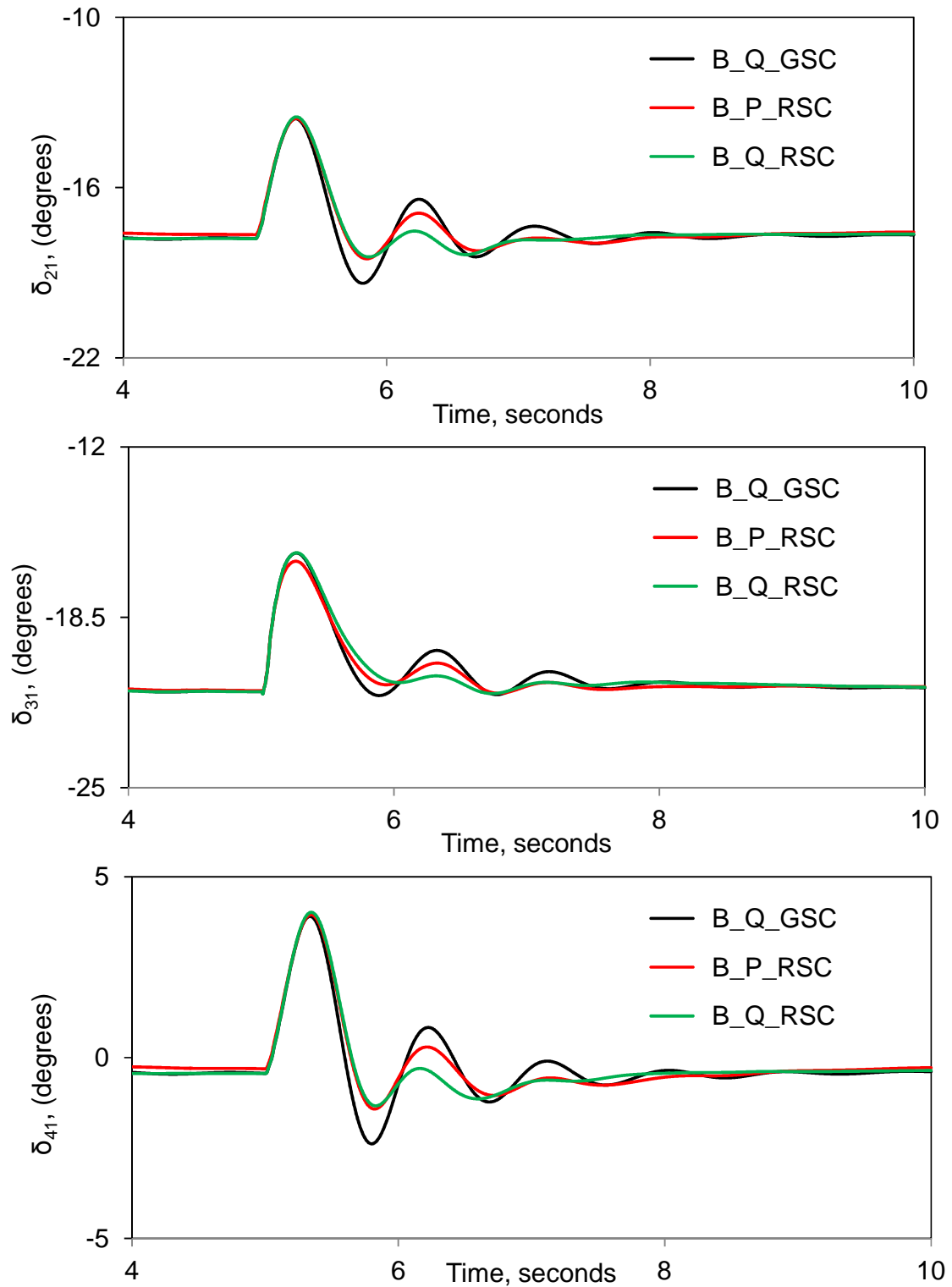
Figure B.10: Generator load angles, measured with respect to generator 1 load angle, during and after clearing a 3-cycle, three-phase fault at bus 4. (DFIG-based wind farm supplemental controller stabilizing signal is δ_{31}).